

---

# **Signatures of correlations and interactions in the optical spectra of localized excitons in carbon nanotubes**

Manuel Nutz

---



München 2020



---

**Signatures of correlations and interactions  
in the optical spectra of localized excitons in  
carbon nanotubes**

Manuel Nutz

---

Dissertation  
an der Fakultät für Physik  
der Ludwig-Maximilians-Universität  
München

vorgelegt von  
Manuel Nutz  
aus Neumarkt i.d.OPf.

München, den 28. Mai 2020

Erstgutachter: Prof. Dr. Alexander Högele  
Zweitgutachter: Prof. Dr. Achim Hartschuh  
Tag der mündlichen Prüfung: 21. Juli 2020

# Zusammenfassung

Kohlenstoffnanoröhren sind Nanostrukturen, deren Form einer einatomigen Lage Graphit, aufgerollt zu einem Hohlzylinder, entspricht. Die Ladungsträger in halbleitenden Kohlenstoffnanoröhren bilden stark gebundene Elektron-Loch-Paare (Exzitonen), die Photolumineszenz vom Rand des sichtbaren Spektrums bis in das Telekom-Band emittieren. Häufig sind Exzitonen in Kohlenstoffnanoröhren lokalisiert, z. B. an künstlichen Kristalldefekten. Ihre physikalischen Eigenschaften werden dann durch die Gesetze der Quantenmechanik bestimmt, was sie in Verbindung mit ihrer variablen Wellenlänge zu vielversprechenden Kandidaten für Anwendungen in der Quanteninformationsverarbeitung macht.

Lokalisierte Exzitonen sind starken Wechselwirkungen mit ihrer Umgebung ausgesetzt, die einen Einblick in ihre physikalischen Eigenschaften erlauben. Die vorliegende Dissertation erarbeitet ein tieferes Verständnis dieser Wechselwirkungen, das auch hilfreich für technische Anwendungen ist. Dafür wurden sowohl schwach gebundene Exzitonen in flachen Potentialmulden als auch an künstlichen Defekten lokalisierte Exzitonen untersucht.

Kohlenstoffnanoröhren werden häufig mit Tensidmolekülen ummantelt, die eine chemische Aufbereitung erlauben. Die spektrale Linienform von schwach lokalisierten Exzitonen in Kohlenstoffnanoröhren mit Tensidhülle ist oft auffallend asymmetrisch. In dieser Arbeit wurde ein quantenmechanisches Modell entwickelt, um die Holstein-Wechselwirkung zwischen dem Dipolmoment des lokalisierten Exzitons und Molekülschwingungen des Tensids zu beschreiben. Charakteristika der relevanten Molekülschwingungen wurden anhand von Dichtefunktionaltheorie berechnet und Photolumineszenzspektren durch die Kombination mit dem Modell simuliert. Simulation und Messdaten stimmten über einen weiten Bereich von Probertemperaturen und Anregungslaserleistungen hervorragend überein.

In kovalent funktionalisierten Kohlenstoffnanoröhren sind Exzitonen an künstlichen Kristalldefekten stark lokalisiert. Zwar ist die Photolumineszenz dieser Zustände ungewöhnlich intensiv, aber zwischen einzelnen Kohlenstoffnanoröhren variieren die Spektren erheblich. Magnetophotolumineszenzmessungen zeigten, dass diese Unterschiede, anders als für freie Exzitonen, nicht durch dunkle Zerfallskanäle erklärbar sind. Durch Photonenkorrelationspektroskopie wurden zwei Arten von Emittlern mit starken bzw. schwachen Korrelationen zwischen den beiden Ladungszuständen der lokalisierten Exzitonen identifiziert. Dieses Resultat ergab Niveauschemata zur Beschreibung der exzitonischen Besetzungsdichte und zeigte, dass häufig mehrere Defektstellen in unmittelbarer Nachbarschaft auftreten und durch Coulomb-Abstoßung miteinander korreliert sind.

Die Ergebnisse dieser Arbeit identifizierten dipolare und elektrostatische Wechselwirkungen als bedeutende Kopplungsmechanismen lokalisierter Exzitonen in Kohlenstoffnanoröhren. Dies bietet eine Orientierung für das Design künftiger Techniken zur Funktionalisierung und Tensidummhüllung von Kohlenstoffnanoröhren, um deren nächste Generation von Anwendungen in der Photonik zu verbessern.



# Abstract

Carbon nanotubes are a one-dimensional allotrope of carbon that can be imagined as a single-atomic layer of graphite rolled up to a hollow cylinder. The charge carriers in semiconducting carbon nanotubes form strongly bound electron-hole pairs (excitons) that support photoluminescence emission ranging from the edge of the visible spectrum into the telecom band. Frequently, the excitons are localized, e. g. at intentional defect sites, and their photophysical properties are then dominated by the laws of quantum mechanics. Along with their wavelength tunability, this feature makes localized excitons in carbon nanotubes promising candidates for quantum information processing applications.

Localized excitons in carbon nanotubes are subject to strong interactions with their environment that provide insights into their fundamental physical properties. This thesis is aimed at providing a deeper understanding of these couplings that is also beneficial for the improvement of carbon nanotube technologies. Both weakly confined excitons in shallow potential minima and excitons localized intentionally at covalent defect sites were studied.

Carbon nanotubes are frequently wrapped with surfactant molecules that enable wet-chemical purification processes. The photoluminescence lineshapes of weakly localized excitons in surfactant-wrapped carbon nanotubes often feature a peculiar asymmetry. In this work, a quantum-mechanical model was developed that describes the Holstein-like interaction between the dipole moment of localized excitons and molecular vibrations of the surfactant. Photoluminescence spectra were simulated by combining this model with the characteristics of the relevant molecular vibrations that were calculated by means of density functional theory. An excellent agreement between the simulations and the data was obtained over a broad range of sample temperatures and excitation laser irradiances.

Covalently functionalized carbon nanotubes host strongly localized excitons confined at intentional lattice defects. While photoluminescence emission from these states is exceptionally bright, the spectral response shows significant variations on the level of individual carbon nanotubes. Magneto-photoluminescence experiments established that in contrast to diffusive excitons these variations cannot be attributed to the presence of nonradiative decay channels. Photon correlation measurements identified two classes of emitters with strongly and weakly pronounced correlations between the two possible charge states of the localized excitons. This finding guided the formulation of level schemes describing the exciton population dynamics and revealed the frequent presence of multiple proximal defect sites that are correlated by repulsive Coulomb interactions.

Both studies in this work identified dipolar and electrostatic interactions as important coupling mechanisms of localized excitons in carbon nanotubes. These results provide guidance in the design of future carbon nanotube functionalization techniques and surfactant wrappings to improve the next generation of carbon nanotube-based photonics applications.



# Contents

<b>1. Introduction</b>	<b>1</b>
<b>2. Fundamentals of photoluminescence spectroscopy of single-walled carbon nanotubes</b>	<b>5</b>
2.1. Graphene – the building block of carbon nanotubes . . . . .	6
2.1.1. Crystal structure and Brillouin zone . . . . .	6
2.1.2. Electronic properties and band structure . . . . .	8
2.2. Chirality and crystal structure of single-walled carbon nanotubes . . . . .	10
2.3. Electronic properties and band structure of single-walled carbon nanotubes .	14
2.4. Excitonic states in single-walled carbon nanotubes . . . . .	18
2.5. Second order time-correlation functions . . . . .	22
<b>3. Experimental methods for confocal microscopy of individual carbon nanotubes</b>	<b>27</b>
3.1. Cryogenic confocal microscope . . . . .	28
3.2. Sample preparation . . . . .	31
<b>4. Photoluminescence lineshapes of localized excitons in polymer-decorated carbon nanotubes</b>	<b>37</b>
4.1. Introduction . . . . .	38
4.2. Origins of the spectral lineshape of localized excitons in cryogenic carbon nanotubes . . . . .	38
4.3. Quantum-mechanical description of exciton-vibron interactions in carbon nanotubes . . . . .	43
4.4. Spectral signatures of exciton-vibron interactions in polymer-decorated carbon nanotubes . . . . .	49
4.5. Temperature dependence of exciton-vibron interactions in polymer-decorated carbon nanotubes . . . . .	57
4.6. Effect of excitation power on spectral characteristics of polymer-decorated carbon nanotubes . . . . .	61
4.7. Conclusion . . . . .	64
<b>5. Excitonic properties of quantum defects in covalently functionalized carbon nanotubes</b>	<b>67</b>
5.1. Introduction . . . . .	68
5.2. Preparation and characterization of hexyl-functionalized carbon nanotubes .	68

---

5.3. Multiplicity of defect states in cryogenic hexyl-functionalized carbon nanotubes	72
5.4. Photon correlation spectroscopy of defect states in cryogenic hexyl-functionalized carbon nanotubes . . . . .	78
5.5. Conclusion . . . . .	90
<b>6. Summary and outlook</b>	<b>93</b>
<b>A. Aspects of density functional theory simulations</b>	<b>97</b>
A.1. Fundamentals of density functional theory . . . . .	97
A.2. Details of density functional theory simulations . . . . .	102
A.3. Conversion between molecular dipole moments and integrated molar absorptivity . . . . .	104
<b>B. Photon emission statistics of carbon nanotube defect sites in the framework of rate models</b>	<b>111</b>
B.1. Blinking single-photon source with one emissive state . . . . .	112
B.2. Blinking single-photon source with two competing emissive states . . . . .	118
B.3. Emission from a single defect site in the presence of a shelving state . . . . .	123
B.4. Emission from a single defect site in the presence of multiple shelving states .	124
B.5. Emission from two correlated defect sites in the presence of a shelving state .	127
<b>List of Abbreviations</b>	<b>133</b>
<b>References</b>	<b>137</b>
<b>List of Publications</b>	<b>169</b>
<b>Danksagung</b>	<b>171</b>

# 1

## Introduction

---

Almost 75 years ago, the first successful construction of a solid-state transistor started a technological revolution [1]. It initiated the success of integrated circuits that continue to grow in complexity following the predictions of Moore's law [2]. This development laid the foundations for the information age that is sometimes also called the silicon age after the enabling raw material [1], putting it in line with the stone age, the bronze age, and the iron age [3, p. V]. Interestingly, the most versatile chemical element is not on this list of names. Carbon forms more than 10 million known chemical compounds compared to "only" about 1.7 million compounds that comprise the other 117 chemical elements [4, p. 308]. Recently, carbon-based technologies have attracted growing attention, e. g. in the field of organic electronics [5–7], for energy storage applications [8–10], for sensing [P6, 11–13], or even in smart textiles [14–17]. It was proposed that the widespread replacement of metals and alloys by carbon composites [18–20] could convert the primary metal production, which is responsible for more than 10 % of world's primary energy consumption, into a climate-neutral fabrication of carbon materials [21]. In view of these advances, it is possible that the next technological revolution will be based on carbon.

One of the most remarkable allotropes of carbon are [carbon nanotubes \(CNTs\)](#) that were first described in 1991 [22], although they had likely been produced and observed much earlier [23, p. 3]. These one-dimensional crystals can be imagined as a single-atomic, two-dimensional layer of graphite – graphene – rolled up to a cylinder with sub-nanometer to few-nanometer diameters [23, p. 35] and reported lengths of up to half a meter [24]. Along with their exceptional aspect ratio, [CNTs](#) feature outstanding electric [25, 26, 27, p. VI] and thermal conductivity [27, p. VI, 28, 29], tensile strength, and hardness [27, p. 5, 30] that promote their application in many technological areas [31]. A peculiar property of [CNTs](#) from the perspective of solid-state physics is the dependence of their electronic band structure on the geometry. Dictated by the crystal structure, [CNTs](#) either show metallic behavior or are semiconductors with diameter-dependent band gaps [23, pp. 61, 69, 32] that correspond to a fundamental [photoluminescence \(PL\)](#) emission wavelength ranging from the edge of

the visible spectrum into the near infrared [33–35]. These properties make CNTs promising candidates for the fields of optoelectronics and photonics [36], where they have been employed in applications such as all-optical sensing [P6, 37, 38], infrared photodetectors [39–41], photovoltaic cells [42–44], light-emitting diodes [45, 46], and quantum light emitters tunable over the entire telecom window [47, 48].

Due to their exceptionally large binding energy the charge carriers in CNTs form bound electron-hole pairs – excitons – that dominate the photophysical properties of CNTs [49–51]. While the excitons may diffuse freely along the CNT axis in pristine samples [52–55], frequently they also become localized at intentional crystal defects [48, 56–59] or in shallow potential traps at low temperatures [60–62]. In this localized regime the exciton dynamics is governed by their quantum nature that make them interesting candidates for quantum information processing applications [47, 63–65]. At the same time, PL emission from localized CNT excitons is subject to strong interactions with the environment [66–68] that give rise to variations in emission energy [60, 61], spectral wandering [P6], and intensity fluctuations [69], amongst others. The study of these coupling mechanisms provides insights into the fundamental physical properties of localized excitons and has evolved to an active field of research [P6, 38, 59, 60, 70, 71]. In addition, a thorough knowledge of the environmental interactions is beneficial for the realization of CNT-based nonclassical devices. Routes towards the deterministic control of the PL properties of localized excitons in CNTs have been identified that include the minimization of environmental influences in freely suspended [67, 72] or polymer-embedded CNTs [73, 74] and the protection of excitonic states in deep potential traps [47, 48, 56, 58, 64]. While these techniques have enabled the realization of many novel device applications for CNTs, however, the control of the experimental parameters to the level required for quantum information processing applications remains challenging [65].

This thesis is aimed at providing a deeper understanding of the most significant environmental interactions of localized excitons in CNTs. Both excitons trapped at intentional crystal defects and unintentionally localized excitons in shallow potential traps have been studied with a combination of complementary spectroscopic techniques. Weakly localized excitons in polymer-wrapped CNTs exhibited a peculiar asymmetric lineshape that was attributed to a previously unreported dipolar coupling mechanism to molecular vibrations of the surfactant molecules. Time-resolved studies of the PL from defect-trapped excitons in covalently functionalized CNTs revealed the presence of electrostatic interactions that modify the exciton population dynamics in the frequent case of multiple defect sites in close proximity. Both effects provide novel insights into the interaction mechanisms of localized excitons in CNTs.

The structure of this work is as follows: **Chapter 2** introduces the crystal structure and electronic properties of CNTs and their building block graphene. The excitonic states in CNTs are given special attention. Furthermore, second order time-correlation functions are introduced and their experimental characteristics are reviewed. In **Chapter 3**, the design and

the specifications of the home-built confocal microscope used for cryogenic PL spectroscopy of individual CNTs and a description of the different detection setups is presented. Also, details of the sample preparation are introduced.

Chapter 4 discusses the influences of surfactants on the PL lineshape of localized excitons in CNTs. After a review of proposed exciton-phonon coupling mechanisms in the literature, a quantum-mechanical description of dipolar interactions between localized excitons and molecular vibrations of surfactants is presented. This model was used to simulate PL spectra by combining it with characteristic quantities of the molecular vibrations calculated by density functional theory (DFT). The excellent agreement between model and data over a broad range of sample temperatures and excitation laser irradiances is illustrated. These results are complemented by an introduction to the DFT method employed in this work and the derivation of a conversion formula between molecular dipole moments and the integrated molar absorptivity in Appendix A.

In Chapter 5, covalently functionalized CNTs are studied that host strongly defect-localized neutral and negatively charged excitons. The exceptional brightness of PL from these states is attributed to the absence of nonradiative decay channels, contrasting the properties of free or weakly localized CNT excitons. Time-resolved PL decay and photon correlation measurements revealed the existence of two different classes of emitters with distinct properties. By comparing with model predictions for the photon correlation data, we identified the two scenarios as solitary and multiple defect sites in the focal spot of our confocal microscope. This result established photon correlation spectroscopy as a powerful tool for the investigation of exciton population dynamics. Appendix B presents the numerical analysis of the relevant rate models that is omitted in Chapter 5 for the sake of brevity.

A summary of the results obtained in this thesis and an outlook that highlights possible future directions of research is given in Chapter 6.



# 2

## Fundamentals of photoluminescence spectroscopy of single-walled carbon nanotubes

---

Single-walled carbon nanotubes can be pictured as a single sheet of graphene rolled to a seamless cylinder. Many characteristics of carbon nanotubes are therefore inherited from the physical properties of the hexagonal graphene lattice that are briefly revisited in this chapter. The electronic band structure of graphene is obtained in a tight-binding description of the carbon  $\pi$  orbitals, resulting in a linear, Dirac-like dispersion at the  $K$  and  $K'$  points of the Brillouin zone. The geometric structure of a single-walled carbon nanotube is determined by the chiral vector that represents the displacement of two carbon atoms that coincide after the imagined rolling process. The chiral vector accordingly also determines a number of properties like the carbon nanotube diameter, the rolling angle, and the shape of the unit cell. The electronic band structure of carbon nanotubes is obtained from the graphene band structure in a zone-folding approach. The quantization of momentum in the circumferential direction gives rise to discrete energy bands that yield metallic or semiconducting behavior depending on the chiral vector. In one-dimensional systems, the density of states exhibits a peculiar divergent behavior, resulting in the concentration of optical transitions to the band edges in semiconducting carbon nanotubes. In addition, pronounced Coulomb interactions give rise to the formation of bound electron-hole pairs (excitons) that dominate the photoluminescence response of carbon nanotubes. Of the 16 possible exciton configurations only one state may decay radiatively in the absence of symmetry breaking. Since this optically bright state is not the lowest in energy, the optical quantum yield of carbon nanotubes is low, particularly at cryogenic temperatures. Magnetic fields parallel to the nanotube axis brighten the optical response of carbon nanotubes due to the breaking of time-reversal symmetry. Time-resolved measurements of photoluminescence light are often characterized by the analysis of correlations in the photon emission. The definition and properties of the second order time-correlation function are briefly revisited and experimental differences to the temporal correlation of single-photon detection events are highlighted.

## 2.1. Graphene – the building block of carbon nanotubes

Single-walled carbon nanotubes (CNTs) can be imagined as a sheet of graphene that is rolled to a seamless cylinder (cf. Figs. 2.1 (a)–(c)). For that reason, many physical characteristics of CNTs are inherited from graphene. This section provides a short review of the crystal structure and the electronic properties of graphene that serve as the starting point for the subsequent discussion of these aspects for single-walled CNTs.

### 2.1.1. Crystal structure and Brillouin zone

From the 118 chemical elements, there exist more than 10 million known compounds containing carbon – organic compounds – compared to “only” about 1.7 million inorganic compounds [4, p. 308]. Part of the reason for this wealth of organic chemical species is the ability of carbon to form several distinct types of chemical bonds depending on the hybridization of its electronic orbitals [23, p. 1]. Of the six electrons of carbon, two electrons each occupy the  $1s^2$ , the  $2s^2$ , and the  $2p^2$  orbital in the electronic ground state. While the  $1s^2$  electrons are strongly bound to the atomic core, the more weakly bound  $2s^2 2p^2$  valence electrons participate in chemical reactions [23, p. 5]. Since the  $\sim 4$  eV energy separation between the  $2s$  and the  $2p$  electrons is smaller than chemical bond energies, one of the  $2s$  electrons can be excited to the  $2p$  state to enhance the binding energy of a carbon atom with its neighboring atoms [23, p. 9].

When carbon forms chemical bonds, the wave functions of the  $2s$  and  $2p$  states mix and form either  $sp$ ,  $sp^2$ , or  $sp^3$  hybrid orbitals that are given by the linear combination of the remaining single  $2s$  electron with one, two, or three of the  $2p$  electrons, respectively [23, pp. 5–9]. The  $sp$ ,  $sp^2$ , or  $sp^3$  hybridized electrons form  $\sigma$  bonds with the neighboring atoms that obtain their strength from an increased electron density between the atomic nuclei. By contrast, unpaired  $2p$  electrons form weaker  $\pi$  bonds in which two lateral lobes of electron density overlap [76, pp. 321–324]. In the absence of steric interactions the  $\sigma$  bonds adopt orientations that maximize their respective distance. For  $sp$  orbitals this results in linear

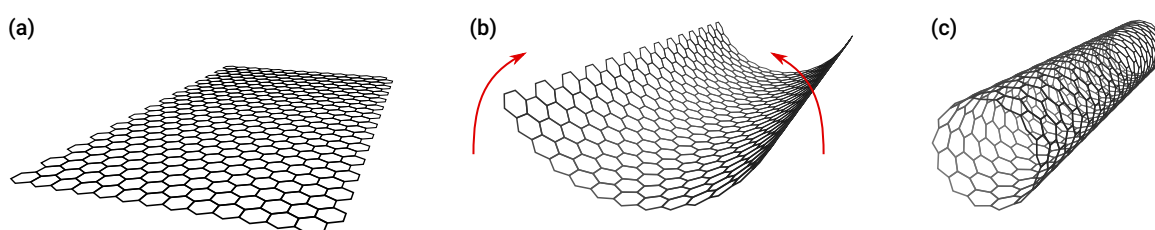


**Figure 2.1.:** Illustrative sketch of the formation of a single-walled CNT starting from (a) a flat sheet of graphene that is (b) being rolled up in order to (c) form a seamless cylinder. Graphics (a)–(c) are reproduced from [75].

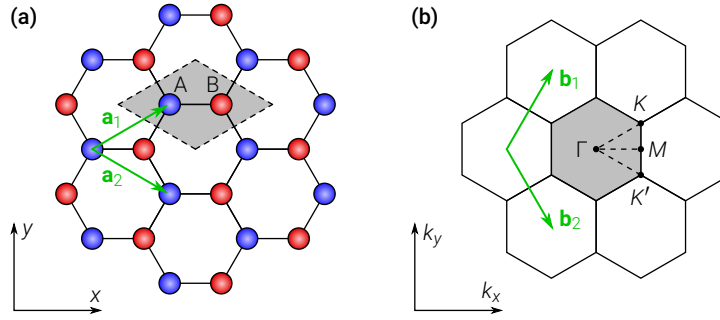


**Figure 2.2.:** Real and reciprocal-space lattice of graphene. **(a)** Hexagonal real-space lattice of graphene spanned by the unit vectors  $\mathbf{a}_1$  and  $\mathbf{a}_2$  (green). The unit cell (gray shaded area) comprises two carbon atoms A and B that belong to the two graphene sublattices colored in blue and red, respectively. **(b)** Corresponding reciprocal-space lattice spanned by the reciprocal unit vectors  $\mathbf{b}_1$  and  $\mathbf{b}_2$  (green). The hexagonal first BZ is highlighted in gray and features the high-symmetry points  $\Gamma$ ,  $M$ ,  $K$ , and  $K'$  at the center, the center of the edge and the two distinct corners of the BZ, respectively. Graphics (a)–(b) were adapted from [23, p. 25] and are reproduced from [75].

molecules with  $180^\circ$  bond angle, for  $sp^2$  orbitals in a trigonal planar geometry with  $120^\circ$  bond angles, and for  $sp^3$  orbitals in a tetrahedral molecular geometry with  $109.5^\circ$  bond angles [76, pp. 319–321, 77].

Thanks to the versatile binding dynamics of carbon not only an unmatched quantity of carbon compounds exist, but also a large number of carbon allotropes, the most prominent being diamond for  $sp^3$  hybridized carbon and graphite for  $sp^2$  hybridized carbon [78]. Due to the trigonal planar geometry of the  $sp^2$  orbitals in graphite, it consists of covalently bound layers that are stacked and linked by significantly weaker van der Waals interactions [79]. While these individual layers of graphite – graphene – have been studied theoretically for a long time [80–82], they were not isolated intentionally until 2004 [83, 84].

Due to the  $120^\circ$  bond angles of the  $sp^2$  orbitals, graphene forms a two-dimensional hexagonal Bravais lattice (cf. Fig. 2.2 (a)). The rhombic unit cell (gray shaded area in Fig. 2.2 (a)) consists of two carbon atoms that belong to the A and B sublattices, colored in blue and red, respectively, in Fig. 2.2 (a). For the orientation chosen in Fig. 2.2 (a), where the two atoms per unit cell are displaced horizontally, the real-space unit vectors are given by [23, p. 25, 85]

$$\mathbf{a}_1 = \left( \frac{\sqrt{3}}{2}a, \frac{a}{2} \right) \quad \text{and} \quad \mathbf{a}_2 = \left( \frac{\sqrt{3}}{2}a, -\frac{a}{2} \right). \quad (2.1)$$

Here, the lattice constant  $a = |\mathbf{a}_1| = |\mathbf{a}_2| = \sqrt{3}a_{C-C} = 2.46\text{\AA}$  is given by the carbon-carbon bond length  $a_{C-C} = 1.42\text{\AA}$  in graphene [23, p. 25].<sup>1</sup>

<sup>1</sup> In CNTs the carbon-carbon bond length  $a_{C-C} = 1.44\text{\AA}$  is slightly larger than in graphene due to curvature effects [23, p. 38].

The unit vectors  $\mathbf{b}_1$  and  $\mathbf{b}_2$  in reciprocal space are defined by their orthogonality to the real space vectors  $\mathbf{a}_1$  and  $\mathbf{a}_2$ ,

$$\mathbf{a}_i \cdot \mathbf{b}_j = 2\pi\delta_{ij} \quad \text{for } i, j = 1, 2, \quad (2.2)$$

where  $\delta_{ij}$  is the Kronecker delta. Using the expressions in Eq. (2.1), this condition results in the vectors

$$\mathbf{b}_1 = \left( \frac{2\pi}{\sqrt{3}a}, \frac{2\pi}{a} \right) \quad \text{and} \quad \mathbf{b}_2 = \left( \frac{2\pi}{\sqrt{3}a}, -\frac{2\pi}{a} \right), \quad (2.3)$$

corresponding to the reciprocal lattice constant  $4\pi/\sqrt{3}a$  [23, p. 26]. The reciprocal vectors span a Brillouin zone (BZ) of hexagonal shape (gray shaded area in Fig. 2.2 (b)), where the hexagon in reciprocal space is rotated by  $90^\circ$  compared to the real-space hexagonal graphene lattice. Fig. 2.2 (b) also highlights the high-symmetry points  $\Gamma$ ,  $M$ ,  $K$ , and  $K'$  at the center, the center of the edge and the two distinct corners of the BZ, respectively [23, p. 26].

### 2.1.2. Electronic properties and band structure

The electronic properties of graphene are dominated by the unhybridized  $\pi$  electrons of the two A and B carbon atoms per unit cell in Fig. 2.2 (a) [23, p. 26]. A tight-binding approach shows that the quantum-mechanical superposition of the respective  $\pi$  orbitals forms a bonding  $\pi$  band and an antibonding  $\pi^*$  band that constitute the lowest-energy valence and conduction bands in graphene, respectively. The tight-binding energy dispersion relation is given by [23, p. 27]

$$E_{g2D}(\mathbf{k}) = \frac{\varepsilon_{2p} \pm \gamma_0 \cdot w(\mathbf{k})}{1 \pm s \cdot w(\mathbf{k})}, \quad (2.4)$$

where  $\varepsilon_{2p}$  is the energy of an electron in the 2p orbital,  $\gamma_0$  and  $s$  are the nearest-neighbor hopping matrix element and the overlap integral of the two  $\pi$  orbitals, respectively, and the function  $w(\mathbf{k})$  is defined by

$$w(\mathbf{k}) = \sqrt{1 + 4 \cos \frac{\sqrt{3}k_x a}{2} \cos \frac{k_y a}{2} + 4 \cos^2 \frac{k_y a}{2}} \quad \text{for } \mathbf{k} = (k_x, k_y). \quad (2.5)$$

The + and the – sign in Eq. (2.4) correspond to the valence and the conduction band that are shown in red and blue, respectively, in Fig. 2.3 (a), where  $\varepsilon_{2p}$  was set to zero and the parameters  $\gamma_0 = -3.033$  eV and  $s = 0.129$  were fit to first principles calculations [23, p. 27]. The first BZ and the high-symmetry points  $\Gamma$ ,  $M$ ,  $K$ , and  $K'$  are indicated in green. Fig. 2.3 (b) shows the same bands along the edges of the triangle  $\Gamma MK$  together with the four lowest-energy of the six graphene  $\sigma$  bands (black) that were calculated following [23, pp. 29–33]. Since even the lowest-energy sigma bands feature a band gap of  $\sim 6$  eV, the electronic properties of graphene are dominated by the  $\pi$  bands and the  $\sigma$  bands are often neglected [23, p. 26].

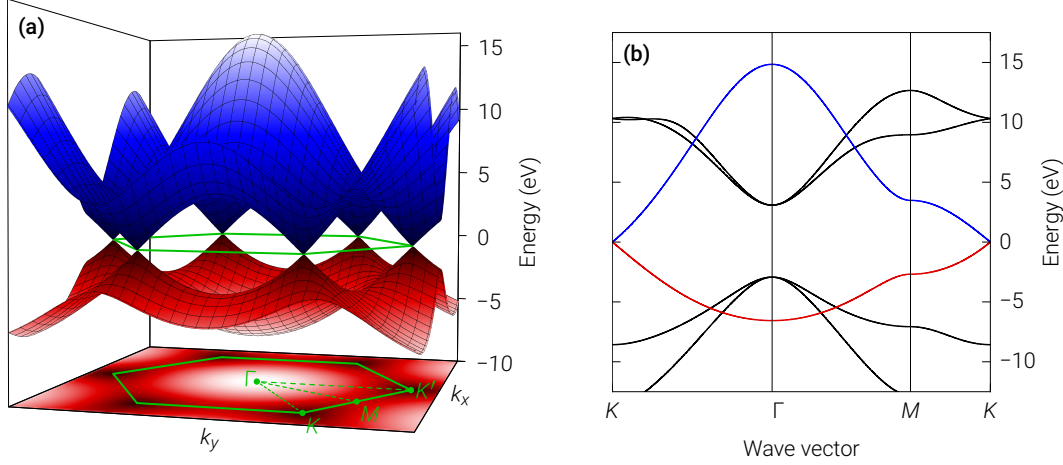


**Figure 2.3.:** Electronic band structure of graphene. **(a)** Dispersion of the graphene valence (red) and conduction band (blue) formed from the unhybridized carbon  $\pi$  orbitals. The hexagonal first BZ featuring the high-symmetry points  $\Gamma$ ,  $M$ ,  $K$ , and  $K'$  is highlighted in green. **(b)** Dispersion of the graphene valence band (red), conduction band (blue), and the four lowest-energy  $\sigma$  bands along the edges of the triangle  $\Gamma MK$ . Graphics (a)–(b) were adapted from [23, pp. 28, 32] and graphic (a) is reproduced from [75].

Note that the accuracy of this tight-binding description decreases with increasing distance to the  $K$  and  $K'$  points in the BZ [86].

At the  $K$  and  $K'$  points the conduction and the valence band of graphene touch in a single point and the energy dispersion relation can be approximated as

$$E_{g2D}(\mathbf{q}) \approx \pm \hbar v_F |\mathbf{q}|, \quad (2.6)$$

where  $v_F = \sqrt{3}|\gamma_0|a/2\hbar \approx 1 \times 10^6$  m/s is the Fermi velocity,  $\mathbf{q}$  is given by  $\mathbf{q} = \mathbf{k} - \mathbf{k}_K$  for wave vectors close to the  $K$  point and by  $\mathbf{q} = \mathbf{k} - \mathbf{k}_{K'}$  for wave vectors close to the  $K'$  point, respectively, and  $|\mathbf{q}| \ll |\mathbf{k}_K|, |\mathbf{k}_{K'}|$  must be fulfilled [82, 87]. Since the effective mass in a crystal is given by the second derivative of the energy dispersion, the linear form of Eq. (2.6) formally describes a massless or an ultrarelativistic particle and correspondingly the charge carrier dynamics in graphene near the  $K$  and  $K'$  points can be formulated in terms of a massless Dirac-like Hamiltonian [87, 88]. At the same time, the density of states (DOS)  $D(E)$ , describing the number of available states in an energy interval  $[E, E + \Delta E]$ , is given by

$$D(E) = \frac{4A_C}{\pi} \cdot \frac{|E|}{v_F^2} \quad (2.7)$$

around the touching points of valence and conduction band, where  $A_C = \frac{1}{4}\sqrt{3}a^2 = \frac{3}{4}\sqrt{3}a_{C-C}^2$  is the area per carbon atom [82, 87]. By consequence, there exists no band gap in graphene, but the DOS is zero around the intersection of valence band and conduction band, rendering graphene a semimetal [87]. Due to the inversion symmetry of the graphene lattice,

the  $K$  and  $K'$  points are generally equivalent in graphene, contrasting materials like monolayer transition metal dichalcogenides (TMDs) that lack inversion symmetry and offer e. g. optical access to their valley degree of freedom [89, 90]. To address the  $K$  and  $K'$  points independently in graphene, inversion symmetry must be explicitly broken, e. g. by introducing defects or edges or by applying lateral electric fields [91–93].

## 2.2. Chirality and crystal structure of single-walled carbon nanotubes

A single-walled CNT can be described as a sheet of graphene rolled into a seamless cylinder (cf. Figs. 2.1 (a)–(c)). The fundamental structure of a single-walled CNT is determined by its diameter that typically ranges between 0.7 nm and  $\sim 10.0$  nm [23, p. 35] and the orientation of the hexagonal graphene lattice with respect to the tube axis. Both characteristics are governed by the *chiral vector*  $\mathbf{C}_h$  that represents the displacement between two carbon atoms in the graphene lattice that come to lie on each other after the imagined rolling process. In the rolled CNT, by consequence, the chiral vector points around the CNT circumference and is orthogonal to the CNT axis [23, p. 37].

Since the chiral vector  $\mathbf{C}_h$  connects two carbon atoms from the same sublattice – otherwise a seamless cylinder could not be formed – it can be expressed as a linear combination of the graphene lattice vectors from Eq. (2.1) as

$$\mathbf{C}_h = n \cdot \mathbf{a}_1 + m \cdot \mathbf{a}_2 \equiv (n, m). \quad (2.8)$$

The pair of integers  $(n, m)$  is also referred to as the *chiral index* or the *chirality* of a CNT. Due to the hexagonal symmetry of the graphene carbon lattice, it is sufficient to consider only combinations of nonnegative integers  $n$  and  $m$  that satisfy  $0 \leq m \leq n$  [23, p. 37].

By definition, the length  $|\mathbf{C}_h|$  of the chiral vector is equal to the circumference of the corresponding CNT and thus the CNT diameter  $d_t$  can be calculated as

$$d_t = \frac{|\mathbf{C}_h|}{\pi} = \frac{a}{\pi} \cdot \sqrt{n^2 + nm + m^2}, \quad (2.9)$$

where the lattice constant  $a = |\mathbf{a}_1| = |\mathbf{a}_2| = \sqrt{3}a_{C-C} = 2.49 \text{ \AA}$  is given by the carbon-carbon bond length  $a_{C-C} = 1.44 \text{ \AA}$  in CNTs [23, p. 38].<sup>2</sup> The *chiral angle*  $\theta$  is defined as the angle between the chiral vector  $\mathbf{C}_h$  and the graphene lattice vector  $\mathbf{a}_1$ . It denotes the tilt angle of the hexagonal graphene lattice with respect to the CNT axis and is restricted to the range  $0^\circ \leq \theta \leq 30^\circ$ , when  $0 \leq m \leq n$ . The value of  $\theta$  is related to the chiral index by [23, p. 39]

$$\cos \theta = \frac{\mathbf{C}_h \cdot \mathbf{a}_1}{|\mathbf{C}_h| \cdot |\mathbf{a}_1|} = \frac{2n + m}{2\sqrt{n^2 + nm + m^2}}. \quad (2.10)$$

---

<sup>2</sup> See footnote 1.

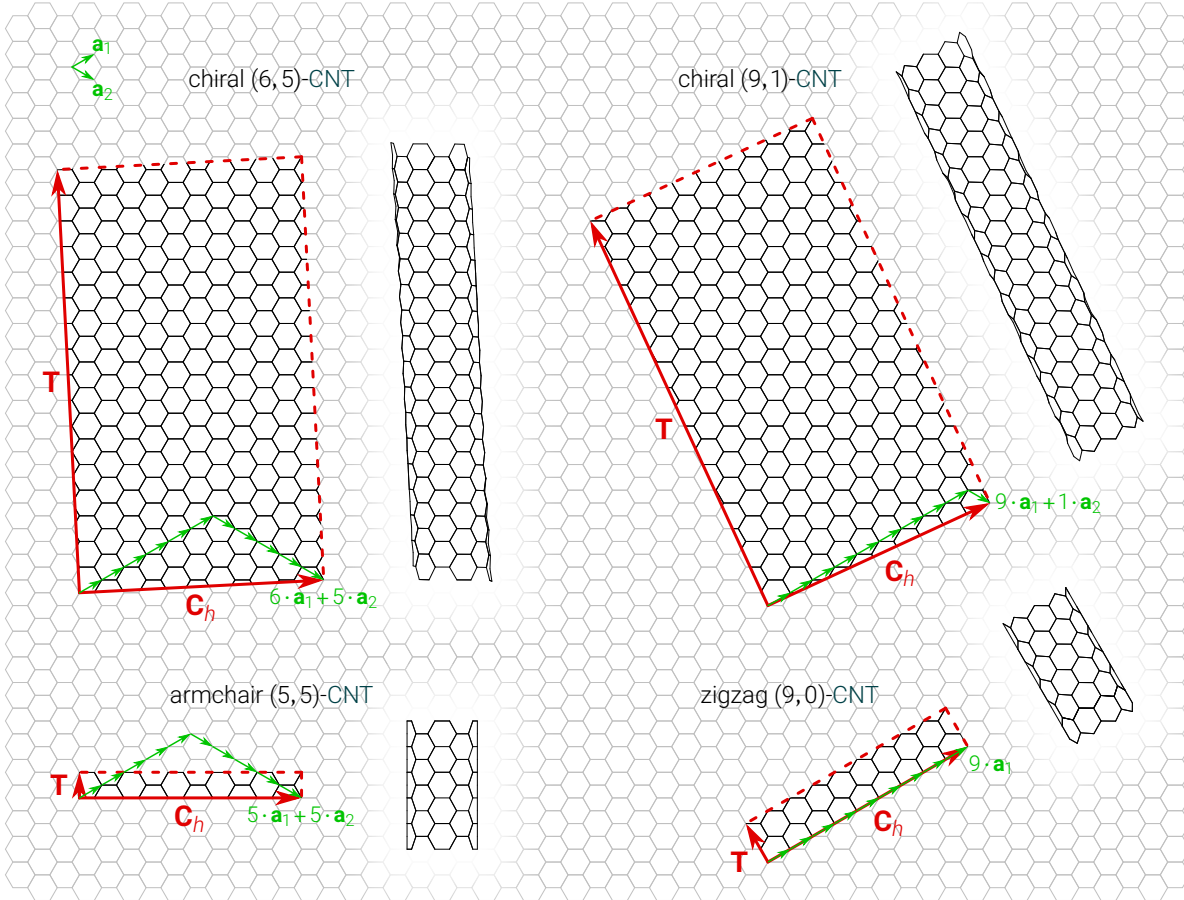


**Figure 2.4.:** Schematic construction of CNTs from a graphene sheet. The chirality of a CNT is defined by the chiral vector  $\mathbf{C}_h$  that is a linear combination with integer coefficients  $n$  and  $m$  of the graphene lattice vectors  $\mathbf{a}_1$  and  $\mathbf{a}_2$  (green arrows). Together with the translation vector  $\mathbf{T}$  the chiral vector  $\mathbf{C}_h$  spans the CNT unit cell (red framed areas) that is rolled along  $\mathbf{C}_h$  to form a seamless cylinder (insets), resulting in a CNT of chirality  $(n, m)$ . The depicted examples are a chiral (6,5)-CNT (top left), a chiral (9,1)-CNT (top right), an armchair (5,5)-CNT (bottom left), and a zigzag (9,0)-CNT (bottom right). The graphic was adapted from [75].

Based on the value of  $\theta$ , single-walled CNTs are often categorized into three classes of geometrical structure [23, pp. 36–37] that are illustrated in Fig. 2.4.

- CNTs with chiral angle  $\theta = 0^\circ$  corresponding to a chiral index of  $(n, 0)$  for some  $n > 0$  are named *zigzag* CNTs. This term stems from the characteristic zigzag edge of the carbon lattice around the CNT circumference (cf. bottom right CNT in Fig. 2.4).
- CNTs with chiral angle  $\theta = 30^\circ$  corresponding to a chiral index of  $(n, n)$  for some  $n > 0$  are named *armchair* CNTs. As for the zigzag CNTs, this term originates from the shape of the carbon lattice around the CNT circumference that resembles the backrest and the armrests of an armchair (cf. bottom left CNT in Fig. 2.4).

- All other CNTs with  $0^\circ < \theta < 30^\circ$  are called *chiral* CNTs. For chiral CNTs the tube axis is tilted with respect to the hexagonal graphene lattice, resulting in a lower crystal symmetry than for zigzag and armchair CNTs. Fig. 2.4 shows the chiral (6, 5)-CNTs and (9, 1)-CNTs that were used for the studies in this work.

Since translational symmetry in CNTs is only given along the tube axis, CNTs feature a one-dimensional crystal lattice with a cylindrical unit cell. The unit vector of this lattice is the translation vector  $\mathbf{T}$  that is perpendicular to the chiral vector  $\mathbf{C}_h$  and whose length is determined by the distance of the first carbon atom through which a line perpendicular to  $\mathbf{C}_h$  passes. Introducing the greatest common divisor  $d_R = \text{gcd}(2n + m, 2m + n)$  the vector  $\mathbf{T}$  can be expressed as a linear combination of the graphene lattice vectors  $\mathbf{a}_1$  and  $\mathbf{a}_2$  as [23, p. 39]

$$\mathbf{T} = \frac{2m + n}{d_R} \cdot \mathbf{a}_1 - \frac{2n + m}{d_R} \cdot \mathbf{a}_2 \equiv (t_1, t_2). \quad (2.11)$$

The length of  $\mathbf{T}$  is given by  $|\mathbf{T}| = \sqrt{3}|\mathbf{C}_h|/d_R$  resulting in the area  $|\mathbf{C}_h \times \mathbf{T}| = \sqrt{3}|\mathbf{C}_h|^2/d_R$  of the unit cell and a number of carbon atoms  $N$  per unit cell of [23, p. 40]

$$N = 2 \cdot \frac{|\mathbf{C}_h \times \mathbf{T}|}{|\mathbf{a}_1 \times \mathbf{a}_2|} = \frac{4(n^2 + nm + m^2)}{d_R}. \quad (2.12)$$

Depending on the common divisors of  $n$  and  $m$ , the value of  $N$  can vary significantly even for similar CNT diameters  $d_t = |\mathbf{C}_h|/\pi$ . For the zigzag (9, 0)-CNT and the armchair (5, 5)-CNT in Fig. 2.4 the translation vectors  $\mathbf{T}$  are given by  $\mathbf{T} = (1, -2)$  and  $\mathbf{T} = (1, -1)$ , corresponding to 36 and 20 carbon atoms per unit cell, respectively. By contrast, for the less symmetric chiral (6, 5) and (9, 1)-CNTs, Eqs. (2.11) and (2.12) yield translation vectors  $\mathbf{T} = (16, -17)$  and  $\mathbf{T} = (11, -19)$ , respectively, as well as the equal number  $N = 364$  of carbon atoms per unit cell. Similarly, the number of electronic energy bands or phonon dispersion branches differs significantly between the CNT chiralities [23, p. 45].

The reciprocal lattice vectors  $\mathbf{K}_1$  and  $\mathbf{K}_2$  of a CNT can be found by formulating an orthogonality criterion analogous to Eq. (2.2) that takes the form

$$\mathbf{C}_h \cdot \mathbf{K}_1 = 2\pi, \quad \mathbf{T} \cdot \mathbf{K}_1 = 0, \quad (2.13a)$$

$$\mathbf{C}_h \cdot \mathbf{K}_2 = 0, \quad \mathbf{T} \cdot \mathbf{K}_2 = 2\pi. \quad (2.13b)$$

Employing Eqs. (2.8), (2.11) and (2.12) the solution for the vectors  $\mathbf{K}_1$  and  $\mathbf{K}_2$  can be written as [23, p. 47]

$$\mathbf{K}_1 = \frac{2}{N} \cdot (-t_2 \cdot \mathbf{b}_1 + t_1 \cdot \mathbf{b}_2) \quad \text{and} \quad \mathbf{K}_2 = \frac{2}{N} \cdot (m \cdot \mathbf{b}_1 - n \cdot \mathbf{b}_2), \quad (2.14)$$

where  $\mathbf{b}_1$  and  $\mathbf{b}_2$  are the reciprocal lattice vectors of graphene from Eq. (2.3). While the definitions of  $\mathbf{K}_1$  and  $\mathbf{K}_2$  are similar, their physical significance is very distinct. Since translational

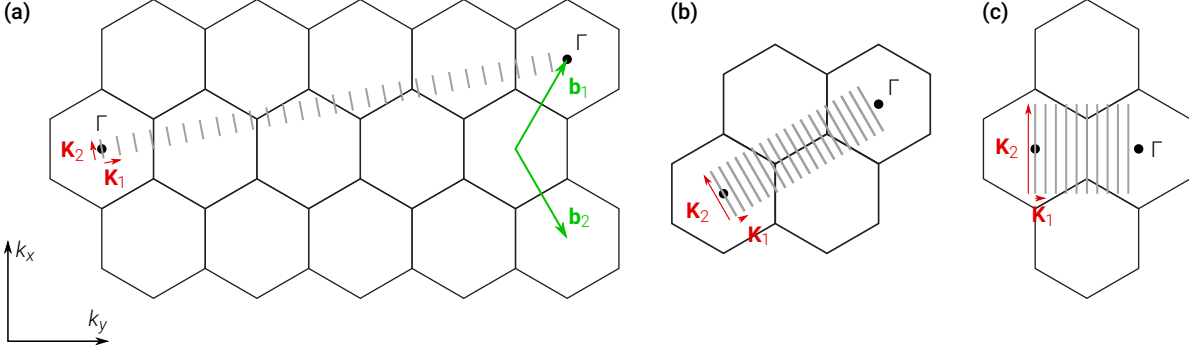


**Figure 2.5.:** First BZs (gray lines) of (a) a chiral (4,2)-CNT, (b) a zigzag (9,0)-CNT, and (c) an armchair (5,5)-CNT spanned by the reciprocal lattice vector  $\mathbf{K}_2$  and the vector  $\mathbf{K}_1$  (red) addressing discrete wave vectors corresponding to the periodic boundary conditions along the CNT circumference. The graphene  $\Gamma$  points and reciprocal unit vectors  $\mathbf{b}_1$  and  $\mathbf{b}_2$  are indicated in black and green, respectively. Graphics (a)–(c) were reproduced from [75].

symmetry in CNTs is only established along the translation vector  $\mathbf{T}$ , only  $\mathbf{K}_2$  is a reciprocal lattice vector, while  $\mathbf{K}_1$  gives rise to discrete wavenumbers in the direction of  $\mathbf{C}_h$  owing to the periodic boundary conditions along the CNT circumference.

Since the real-space lattice vectors  $\mathbf{C}_h$  and  $\mathbf{T}$  are orthogonal – unlike  $\mathbf{a}_1$  and  $\mathbf{a}_2$  in graphene – the length of the reciprocal lattice vector  $\mathbf{K}_2$  can be calculated as [23, p. 47]

$$|\mathbf{K}_2| = \frac{2\pi}{|\mathbf{T}|} = \frac{4\pi}{\sqrt{3}a} \cdot \frac{d_R}{2\sqrt{n^2 + nm + m^2}}. \quad (2.15)$$

Compared to the reciprocal-space unit vectors  $\mathbf{b}_1$  and  $\mathbf{b}_2$  in graphene of length  $4\pi/\sqrt{3}a$  the length of  $\mathbf{K}_2$  differs by the second factor in Eq. (2.15), making it at least  $\frac{1}{2}\sqrt{3}$  times shorter than the  $\mathbf{b}_1$  and  $\mathbf{b}_2$  vectors.<sup>3</sup> In particular for chiral CNTs with small values of  $d_R$  the size of the BZ can be significantly smaller than in graphene.

In circumferential direction, the periodic boundary conditions require a discretization of wave vectors into multiples of  $\mathbf{K}_1$ . Since  $t_1$  and  $t_2$  are integers,  $\frac{N}{2} \cdot \mathbf{K}_1 = -t_2 \cdot \mathbf{b}_1 + t_1 \cdot \mathbf{b}_2$  is a reciprocal lattice vector of graphene and any wave vectors with difference  $\frac{N}{2} \cdot \mathbf{K}_1$  are equivalent. Furthermore, since the numbers  $t_1$  and  $t_2$  are coprime, none of the multiples  $\mu \cdot \mathbf{K}_1$  for  $\mu = 0, \dots, \frac{N}{2} - 1$  is a reciprocal lattice vector of graphene and wave vectors with a difference of  $\mu \cdot \mathbf{K}_1$  for any  $\mu = 0, \dots, \frac{N}{2} - 1$  are distinct [23, p. 47].

By consequence, the first BZ of a CNT is composed of  $\frac{N}{2}$  parallel line segments of length  $|\mathbf{K}_2|$  that are displaced by  $\mathbf{K}_1$ . The first line segment corresponding to  $\mu = 0$  is centered around the  $\Gamma$  point and extends  $\frac{1}{2} \cdot |\mathbf{K}_2|$  in the directions parallel and antiparallel to  $\mathbf{K}_2$ . The other  $\frac{N}{2} - 1$  line segments are shifted by  $\mu \cdot \mathbf{K}_1$ , orthogonal to  $\mathbf{K}_2$ , for  $\mu = 1, \dots, \frac{N}{2} - 1$ .

<sup>3</sup> This follows from  $d_R^2 = \gcd(2n+m, 2m+n)^2 \leq (2n+m)(2m+n) = 2n^2 + 5nm + 2m^2 \leq 3(n^2 + nm + m^2)$ . For armchair CNTs the inequality is strict, i. e.  $|\mathbf{K}_2| = \frac{1}{2}\sqrt{3}|\mathbf{b}_2|$ .

Fig. 2.5 (a) shows the corresponding first BZ (gray lines) for a (4,2)-CNT, one of the smallest chiral CNTs that can be stabilized in nature [94–96]. Due to the relatively small number of  $N = 56$  carbon atoms per unit cell, the first BZ of a (4,2)-CNT consists of 28 parallel line segments compared to a significantly larger number of 182 parallel lines for (6,5)-CNTs and (9,1)-CNTs [23, p. 47]. The black dots in Fig. 2.5 (a) indicate the position of the equivalent  $\Gamma$  points at zero wave vector (left) and at a wave vector of  $\frac{N}{2} \cdot \mathbf{K}_1$  (right). Figs. 2.5 (b) and (c) show the respective first BZs of a (9,0)-CNT and a (6,5)-CNT. Due to the larger value of  $d_R$  for these zigzag and armchair CNTs the length of the line segments constituting the respective first BZs are significantly longer than for the (4,2)-CNT in Fig. 2.5 (a).

### 2.3. Electronic properties and band structure of single-walled carbon nanotubes

The band structure of CNTs can be derived from the band structure of graphene discussed in Section 2.1.2 by a zone-folding approach [23, p. 59] that is presented in the following. Neglecting effects of the CNT curvature, the electronic bands of a CNT are obtained by evaluating the dispersion relation of graphene on the  $\frac{N}{2}$  parallel line segments constituting its first BZ. As for graphene, the electronic structure of CNTs is determined by the  $\pi$  orbitals whose dispersion is given by Eq. (2.4). Using the description of the first BZ of a CNT from Section 2.2, the  $\frac{N}{2}$  one-dimensional dispersion relations are given by [23, p. 60]

$$E_\mu(k) = E_{g2D} \left( k \cdot \frac{\mathbf{K}_2}{|\mathbf{K}_2|} + \mu \cdot \mathbf{K}_1 \right) \quad \text{for } \mu = 0, \dots, \frac{N}{2} - 1 \text{ and } -\frac{\pi}{|\mathbf{T}|} \leq k \leq \frac{\pi}{|\mathbf{T}|}, \quad (2.16)$$

where  $E_{g2D}$  is the dispersion relation of graphene from Eq. (2.4) and  $\mathbf{T}$ ,  $N$ ,  $\mathbf{K}_1$  and  $\mathbf{K}_2$  are given by Eqs. (2.11), (2.12) and (2.14), respectively. The  $\frac{N}{2}$  dispersion relations  $E_\mu(k)$  are usually considered as “folded” to the interval  $[-\pi/|\mathbf{T}|, \pi/|\mathbf{T}|]$  of real numbers for all branches  $\mu = 0, \dots, \frac{N}{2} - 1$  instead of treating them as functions on the  $\frac{N}{2}$  different line segments.

Figs. 2.6 (a)–(c) show the band structures resulting from Eq. (2.16) for a chiral (4,2)-CNT (left panel), a zigzag (9,0)-CNT (central panel), and an armchair (5,5)-CNT (right panel) [23, p. 63]. While the three band diagrams show the same energy range, the respective scales of the wave vector axes vary corresponding to the different sizes of the BZs for the individual CNT chiralities. Since the dispersion relation of graphene given by Eqs. (2.4) and (2.5) is an even function, the dispersion of CNTs is symmetric around zero. Accordingly, the three panels show wave vectors between 0 and  $\pi/|\mathbf{T}|$ , i. e. the positive half of the interval  $[-\pi/|\mathbf{T}|, \pi/|\mathbf{T}|]$ , where the value 0 represents the  $\Gamma$  point that is centered in the line segment corresponding to  $\mu = 0$  in Figs. 2.5 (a)–(c) and the maximum value  $\pi/|\mathbf{T}|$  represents the edge of the first BZ. Using Eq. (2.11) the maximum wave vectors  $\pi/|\mathbf{T}|$  evaluate to  $1/\sqrt{84} = 0.109$

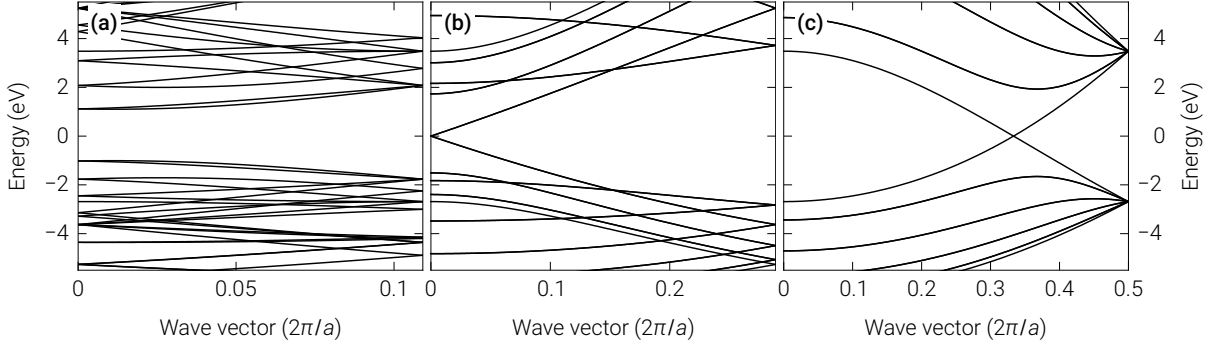


**Figure 2.6.:** Electronic band structures of (a) a chiral (4,2)-CNT, (b) a zigzag (9,0)-CNT, and (c) an armchair (5,5)-CNT. While all three panels show the same energy range, the respective scales of the wave vector axis vary corresponding to the different sizes of the BZs for the individual CNT chiralities. The chiral (4,2)-CNT in (a) features a band gap, while the zigzag (9,0)-CNT and the armchair (5,5)-CNT in (b) and (c), respectively, exhibit band crossings. Graphics (b)–(c) were adapted from [23, p. 63].

for the chiral (4,2)-CNT in Fig. 2.6 (a), to  $1/\sqrt{12} = 0.289$  for the zigzag (9,0)-CNT in Fig. 2.6 (b), and to  $1/2$  for the armchair (5,5)-CNT in Fig. 2.6 (c) in units of  $2\pi/a$ .

The number of branches in Figs. 2.6 (a)–(c) is given by  $\frac{N}{2}$  (cf. Section 2.2), where incidental degeneracies may occur [23, pp. 62–64]. For the chiral (4,2)-CNT in Fig. 2.6 (a) this number  $\frac{N}{2} = 28$  is significantly larger than  $\frac{N}{2} = 18$  and  $\frac{N}{2} = 10$  for the zigzag (9,0)-CNT and the armchair (5,5)-CNT in Figs. 2.6 (b) and (c). At the same time the translation vector  $\mathbf{T}$  scales with  $N$  (cf. Eq. (2.12)) such that a larger number of electronic bands is associated with a narrower first BZ. For the chiral (6,5)-CNTs and (9,1)-CNTs studied in this work, the resulting  $\frac{N}{2} = 182$  (partially degenerate) branches are almost constant over the narrow interval  $[-\pi/|\mathbf{T}|, \pi/|\mathbf{T}|]$  constituting the respective first BZs.

Another striking characteristic in Figs. 2.6 (a)–(c) is the presence or absence of a band crossing at zero energy. While the chiral (4,2)-CNT in Fig. 2.6 (a) features a band gap, the zigzag (9,0)-CNT and the armchair (5,5)-CNT in Figs. 2.6 (b) and (c) exhibit band crossings at wave vectors 0 and  $1/3$  in units of  $2\pi/a$ , respectively [23, p. 64]. As illustrated in Figs. 2.7 (c)–(b), the origin of this difference follows from the dispersion relation of graphene near the  $K$  and  $K'$  points, where the graphene valence and conduction bands can be approximated by two touching cones following Eq. (2.6). If one of the  $\frac{N}{2}$  line segments in Figs. 2.5 (a)–(c) passes through the  $K$  or the  $K'$  point of graphene as in Fig. 2.7 (a), then the corresponding one-dimensional CNT energy bands exhibit a zero energy gap (cf. Fig. 2.7 (b)). By contrast, if none of the line segments passes through either the  $K$  or the  $K'$  point as illustrated in Fig. 2.7 (c), then the CNT features a finite energy gap  $E_{\text{gap}}$  between valence and conduction band (cf. Fig. 2.7 (d)) [23, p. 60].

The condition for a zero-gap energy band is that the distance of the  $K$  or the  $K'$  point of graphene from the line segment corresponding to  $\mu = 0$  in Eq. (2.16), which passes through

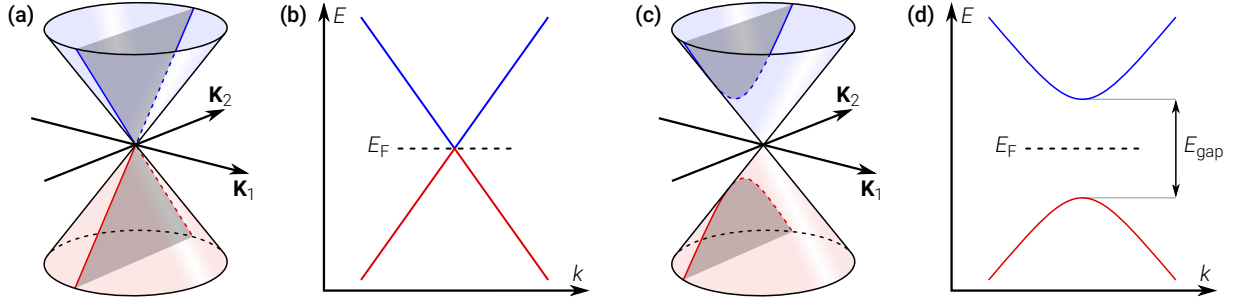


**Figure 2.7.:** Conditions for band crossings and band gaps in the band structure of CNTs. (a) A line segment of the first BZ of a CNT passing through the  $K$  or the  $K'$  point of graphene results in (b) a band crossing of the valence band (red) and the conduction band (blue) at the Fermi energy  $E_F$ . (c) No line segment of the first BZ of a CNT passing through the  $K$  or the  $K'$  point of graphene results in (d) a band gap between the valence band (red) and the conduction band (blue) centered around the Fermi energy  $E_F$ . Graphics (a)–(d) were adapted from [97] and are reproduced from [75].

the  $\Gamma$  point, is an integer multiple of  $|\mathbf{K}_1|$  [23, p. 60]. Due to the symmetry of the first BZ of graphene, for both the  $K$  and the  $K'$  point this requirement results in the prerequisite that  $2n + m$  is a multiple of 3, or equivalently, that<sup>4</sup>

$$n - m \equiv 0 \pmod{3}. \quad (2.17)$$

Other than for graphene, the DOS at the band crossing was shown to be nonzero for CNTs owing to their different dimensionality [23, p. 68]. While graphene is considered a semimetal (cf. Section 2.1.2), CNTs featuring a band crossing therefore show metallic behavior, whereas CNTs with a band gap are semiconducting. From Eq. (2.17) it follows that about one third of all CNTs are metallic, while the remainder is semiconducting [23, p. 61]. In particular, all armchair CNTs are metallic, while zigzag CNTs are only metallic if  $n$  is a multiple of 3.

This work focused on spectroscopic experiments that require a nonzero band gap and accordingly employed semiconducting (6,5)-CNTs and (9,1)-CNTs. The quadratic dispersion of semiconducting CNTs together with their one-dimensional geometry gives rise to a DOS that diverges as  $D(E) \propto 1/\sqrt{E}$  at the band extrema [98], a feature known as Van Hove singularity (VHS) [99]. Due to this strong concentration of the electronic states, optical transitions preferentially occur between the band minima  $c_1, c_2, \dots$  of the conduction bands and the band maxima  $v_1, v_2, \dots$  of the valence bands as illustrated in Fig. 2.8 (c) [23, p. 69]. Here, the band edges  $c_j$  and  $v_i$  are numbered by increasing distance from the Fermi energy  $E_F$  and the corresponding optical transitions are denoted by  $E_{ij}$ .

<sup>4</sup> This condition can be derived by writing the vector from the  $\Gamma$  point to the  $K$  point as  $\frac{3}{2} \cdot \mathbf{b}_1 + \frac{1}{2} \cdot \mathbf{b}_2$ . The distance of the  $K$  point from the line segment passing through the  $\Gamma$  point in units of  $|\mathbf{K}_1|$  can then be calculated as  $(\frac{3}{2} \cdot \mathbf{b}_1 + \frac{1}{2} \cdot \mathbf{b}_2) \cdot \mathbf{K}_1 / |\mathbf{K}_1|^2$  and using  $|\mathbf{K}_1| = 2\pi/|\mathbf{C}_h|$  together with Eqs. (2.3) and (2.9) this evaluates to  $(2n + m)/3$ .

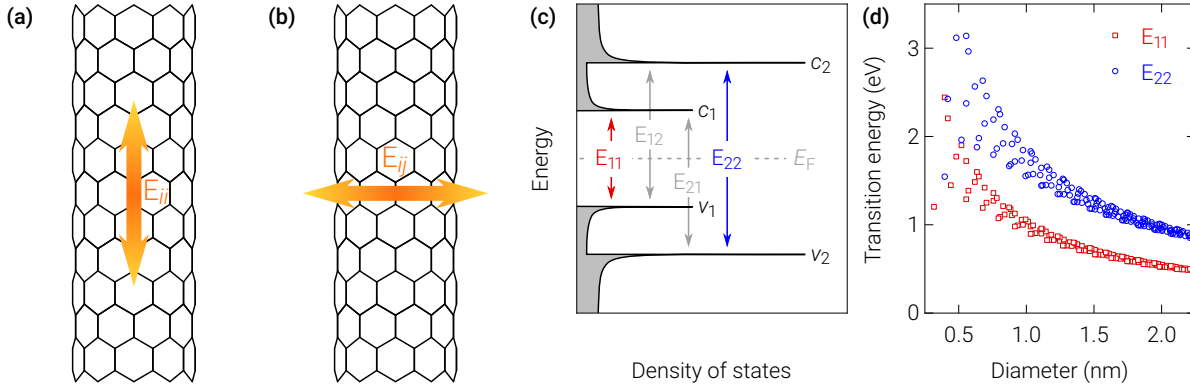


**Figure 2.8.:** Band-to-band transitions of CNTs. **(a)–(b)** Illustration of electric dipole selection rules for optical transitions with light polarization parallel (left) and orthogonal (right) to the CNT axis, respectively. **(c)** Optical transitions between the first two valence band ( $v_1, v_2$ ) and conduction band ( $c_1, c_2$ ) VHSSs, respectively, that are numbered with increasing distance from the Fermi energy  $E_F$ . The transitions  $E_{11}$  (red) and  $E_{22}$  (blue) between valence and conduction band states of equal number are dominant, while the transitions  $E_{12}$  and  $E_{21}$  (gray) are suppressed. **(d)** Kataura plot of the transition energies for  $E_{11}$  and  $E_{22}$  of semiconducting CNTs as a function of the CNT diameter  $d_t$ . The data points follow the empirical formulas from [35]. Graphics (a)–(d) are reproduced from [75].

Optical selection rules for CNTs restrict the possible electric dipole transitions between a conduction band state  $c_j$  and a valence band state  $v_i$  to  $i - j = 0$  for light polarized parallel (cf. Fig. 2.8 (a)) and to  $i - j = \pm 1$  for light polarized orthogonal (cf. Fig. 2.8 (b)) to the CNT axis [100, 101]. While transitions corresponding to  $i - j = \pm 1$  have been observed experimentally [102], the CNT antenna effect and pronounced depolarization effects suppress the interaction between CNTs and light polarized orthogonal to their axis [102, 103] as well as the corresponding optical transitions  $E_{ij}$  with  $i \neq j$  (indicated in gray in Fig. 2.8 (c)). By consequence, the optical transitions  $E_{ii}$  between valence and conduction bands with the same number  $i$ , corresponding to light polarized parallel to the CNT axis, are the predominant electric dipole transitions in CNTs.

Combining the linear approximation of the graphene dispersion relation near the  $K$  and  $K'$  points from Eq. (2.6) with the observation that the closest line segment in Eq. (2.16) passes the  $K$  or  $K'$  point at a distance of  $\frac{1}{3}|\mathbf{K}_1|$  yields an indirectly proportional dependence of the  $E_{11}$  transition energy (red arrows in Fig. 2.8 (c)) on the CNT diameter [23, p. 69, 32],

$$E_{\text{gap}}(d_t) = \frac{2a_{C-C}|\gamma_0|}{d_t}, \quad (2.18)$$

where  $a_{C-C} = 1.44 \text{ \AA}$  is the carbon-carbon bond length in CNTs.<sup>5</sup> Similarly, with the second closest line segment passing the  $K$  or  $K'$  point at a distance of  $\frac{2}{3}|\mathbf{K}_1|$ , the  $E_{22}$  energy (blue

<sup>5</sup> See footnote 1.

arrows in Fig. 2.8 (c) is predicted to be twice as large as the  $E_{11}$  energy. When using a value of  $|\gamma_0| = \sim 2.75$  eV obtained for CNTs [49, 104–107],  $E_{11}$  emission below  $\sim 1000$  nm in the range of silicon photodetectors would require diameters smaller than  $6.4 \text{ \AA}$ . In spectroscopic measurements, the experimental focus therefore lies on the narrowest CNTs.

A plot of the  $E_{11}$  energy as a function of the CNT diameter was first introduced by KATAURA et al. [104]. Due to the curvature of the CNT lattice, however, experimental  $E_{11}$  energies deviate significantly from the scaling formula Eq. (2.18), particularly for small CNT diameters [33, 108]. Since a small  $d_t$  implies a large value of  $|\mathbf{K}_1|$ , deviations from the linear approximation in Eq. (2.6) occur for the narrowest CNTs, a result known as trigonal warping effect [109, 110]. In addition, for pronounced curvatures of the two-dimensional graphene lattice the hexagonal symmetry is broken and the tight-binding derivation of the electronic bands loses its accuracy [111]. This discrepancy was addressed by the introduction of extended tight-binding schemes [112, 113]. Finally, the ratio of  $E_{22}$  to  $E_{11}$  energy has been found to deviate from the theoretical value of 2 [34], which was attributed to many-body electron and hole interactions [114–117].

Based on these findings, a refined Kataura plot in good agreement with experimental data was introduced in [35] that is presented in Fig. 2.8 (d). In particular for small CNT diameters, the spread around the  $1/d_t$  dependency from Eq. (2.18) is significant. A systematic description capturing the deviations was achieved by introducing CNT families. Within each family the number  $2n + m$  is constant, resulting in similar diameters but different chiral angles for the CNTs in the same family [118]. In this framework, the  $E_{11}$  emission energies of the (9, 1)-CNTs and the (6, 5)-CNTs employed in this work are predicted at 912 nm and 976 nm, respectively, and fall inside the silicon window below  $\sim 1000$  nm [33, 35].

## 2.4. Excitonic states in single-walled carbon nanotubes

Photoluminescence (PL) experiments study the light emitted in the radiative recombination of electrons and holes after their optical excitation, typically by a suitable laser. Section 2.3 introduces the single-particle electronic properties of electrons and holes in CNTs by treating these charge carriers as independent particles. While this description is sufficient for many bulk semiconductors, the low dimensionality of CNTs strongly enhances electron-hole interactions [49–51, 115, 119, 120]. An accurate description of PL from CNTs must therefore include the Coulomb attraction between the oppositely charged electrons and holes.

An exciton is a quasiparticle composed of an electron and a hole that are bound by attractive Coulomb interaction, similar to a hydrogen atom [122]. In CNTs, excitons were first observed in two-photon excitation spectroscopy experiments employing optical selection rules that allow for controlled excitation of excitonic p orbital states [50, 119, 120]. These measurements together with other theoretical and experimental studies confirmed that the

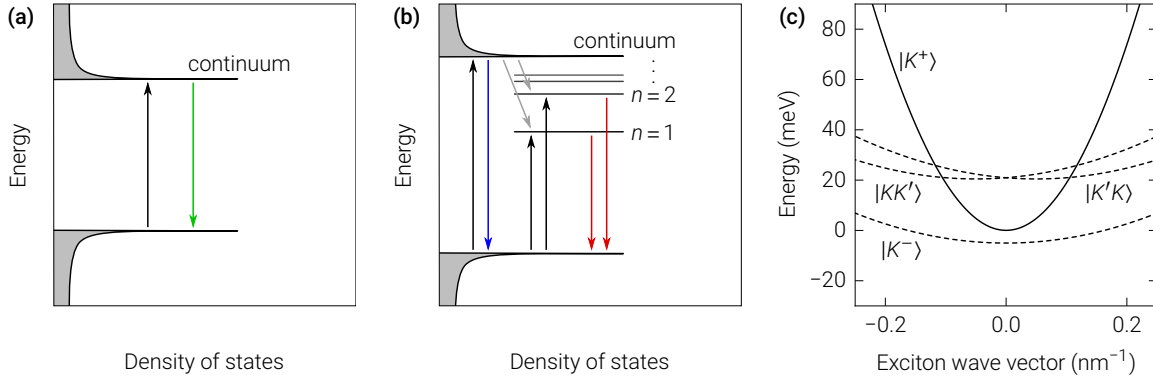


**Figure 2.9.:** Continuum and excitonic states in single-walled CNTs. **(a)** Schematic illustration of optical excitation (black arrow) and PL (green arrow) across the single-particle band gap corresponding to the  $E_{11}$  transition. **(b)** Schematic illustration of optical excitation (black arrows) into different excitonic levels and continuum states, capture of independent charge carriers into excitonic states (gray arrows), PL across the single-particle band gap (blue arrow) and radiative exciton decay (red arrows). **(c)** Energy dispersion of the four singlet exciton states of a (9,4)-CNT comprising one bright (solid line) and three dark states (dashed lines) using the values given in [121]. Graphics (a)–(c) were adapted from [75].

exciton binding energies in CNTs are substantial and reach values of  $\sim 300$  meV for CNTs with diameters of  $\sim 1$  nm [50, 119–121, 123–126].

Figs. 2.9 (a) and (b) illustrate the difference between the two scenarios. In the single-particle picture in Fig. 2.9 (a), electrons are excited from the energetically highest valence band VHS, leaving behind a hole, to the energetically lowest conduction band VHS (black arrow) and decay radiatively in the reverse process (green arrow), corresponding to the  $E_{11}$  transition in CNTs. The introduction of Coulomb interactions modifies the band gap as discussed below and adds additional bound exciton states below the continuum that are characterized by quantum numbers similar to hydrogen orbitals. The population dynamics now include optical excitation (black arrows) from the valence band VHS into the conduction band VHS as well as the different excitonic levels, capture of independent charge carriers into excitonic states (gray arrows), PL across the single-particle band gap (blue arrow) and radiative exciton decay (red arrows). At low temperatures, the exciton ground state ( $n = 1$  in Fig. 2.9 (b)) dominates due to the large exciton binding energy [51].

Since electrons and holes can either occupy the  $K$  or the  $K'$  valley and the spin of both may attain one of two possible directions, a total number of 16 different exciton configurations is possible in the exciton ground state. These 16 configurations decompose into a spin singlet manifold comprising 4 states and a spin triplet manifold comprising the remaining 12 states [127]. While all 16 states are degenerate in the single-particle picture, the introduction of Coulomb interactions partially lifts this degeneracy [121]. The triplet states lie all energetically lower than the singlet states, but cannot be excited by the absorption of a photon or

decay under emission of a photon due to total angular momentum conservation and are therefore called *optically dark* [127, 128].

The four singlet states are superpositions of the spin-up and spin-down configuration [128] that are characterized by the valley in which electron and hole reside. The two intervalley exciton states  $|KK'\rangle$  and  $|K'K\rangle$  both feature nonzero (angular) momentum and are therefore also optically dark [121]. Of the two intravalley exciton states  $K^\pm = \frac{1}{\sqrt{2}}(|KK\rangle \pm |K'K'\rangle)$ , the bonding superposition  $K^+$  is of odd and the antibonding superposition  $K^-$  is of even parity.<sup>6</sup> The energetically lower state  $K^-$  therefore is a dipole-forbidden dark state, while the energetically higher state  $K^+$  is the only optically bright CNT exciton state [129–132]. Fig. 2.9 (c) illustrates the energy dispersion of the four singlet exciton states in a (9, 4)-CNT for zero energy fixed to the energy minimum of the dark  $K^-$  exciton that is located few meV below the minimum of the bright  $K^+$  exciton [121].

Since transitions from the singlet to the triplet manifold are suppressed in the absence of symmetry breaking [130], transitions among the exciton singlet states are most relevant for optical experiments. At low temperatures, the exciton population is expected to accumulate in the lowest-energy, optically dark state  $|K^- \rangle$ , thereby suppressing pronounced PL response [117]. Accordingly, low quantum yields (QYs) of  $\sim 10^{-3}$  were observed in PL experiments [34, 133, 134]. In temperature-dependent PL studies, the maximum QY was observed at intermediate temperatures of 10–40 K, since at lower temperatures most of the exciton population is trapped in the dark  $|K^- \rangle$  state, while at higher temperatures also the dark  $|KK'\rangle$  and  $|K'K\rangle$  states become populated and compromise the optical conversion efficiency [127, 129, 130, 135, 136].

The energy  $E_{\text{exc}}$  of the bright exciton  $|K^+\rangle$  can be expressed as a correction of the single-particle band gap  $E_{\text{gap}}$  using the formula

$$E_{\text{exc}} = E_{\text{gap}} + E_{\text{BGR}} + E_{\text{bind}}, \quad (2.19)$$

where  $E_{\text{bind}}$  is the exciton binding energy of the  $|K^+\rangle$  state and  $E_{\text{BGR}}$  is the band gap renormalization energy that represents a shift of the free-particle band gap due to multi-particle electronic interactions [51, 137]. The two contributions are opposite in sign – while  $E_{\text{bind}}$  is negative,  $E_{\text{BGR}}$  is positive and increases the band gap – and  $E_{\text{BGR}}$  is only slightly larger than  $E_{\text{bind}}$ . By consequence,  $E_{\text{BGR}}$  and  $E_{\text{bind}}$  almost cancel and only lead to a slight increase of  $E_{\text{exc}}$  compared to  $E_{\text{gap}}$  of  $\sim 100$  meV [49, 51, 108, 138].

Similar to Eq. (2.18), several scaling relations have been found that approximate Eq. (2.19), which is difficult to evaluate exactly in many cases. Like the  $E_{11}$  transition energy, the exciton binding energy  $E_{\text{bind}}$  scales as  $1/d_t$  [108, 123, 125, 138, 139]. By contrast, both the splitting

<sup>6</sup> By virtue of the hexagonal crystal symmetry, the parity operator  $\hat{P}$  maps the state  $|KK\rangle$  to  $\alpha|K'K'\rangle$  with some phase factor  $\alpha$ . Using the equality of the velocity operator matrix elements  $\langle KK|\hat{v}|g\rangle = \langle K'K'|\hat{v}|g\rangle$  from [128], where  $|g\rangle$  is the ground state, the identity  $\langle KK|\hat{v}|g\rangle = \langle KK|\hat{P}\hat{P}\hat{v}|g\rangle = \alpha^* \langle K'K'|(-\hat{v})|g\rangle$  can be used to fix the value  $\alpha = -1$ . Similarly,  $\hat{P}|K'K'\rangle = -\hat{P}\hat{P}|KK\rangle = -|KK\rangle$ . These results imply  $\hat{P}K^+ = -K^+$  and  $\hat{P}K^- = K^-$ .

between the bright and dark exciton states  $|K^+\rangle$  and  $|K^-\rangle$  and the splitting between the singlet and the triplet exciton states scale as  $1/d_t^2$  [139, 140].

Apart from the diameter scaling also dependencies of the exciton energy on the dielectric constant  $\epsilon$  of the CNT environment have been reported [68, 141, 142]. In [139, 143] this dielectric screening has been modeled by a  $\epsilon^{-1.4}$  scaling of the exciton binding energy  $E_{\text{bind}}$ . By contrast, in [137] the exciton binding energy  $E_{\text{bind}}$  was modeled to scale as  $\epsilon^{-1.2}$  with a simultaneous scaling of the band gap renormalization  $E_{\text{BGR}}$  as  $\epsilon^{-1}$ . Finally, a shift of the exciton energy by few meV with temperature has been observed [135] and was attributed to a temperature dependence of the band gap energy  $E_{\text{gap}}$  that cannot be expressed by a simple scaling relation [144].

Magnetic fields aligned parallel to the CNT axis result in an Aharonov-Bohm flux [145–147] through the CNT that also causes modifications of the band gap energy  $E_{\text{gap}}$  [103, 148, 149]. More importantly, however, the presence of a magnetic field breaks time-reversal symmetry and thereby enables radiative decay from the exciton state  $|K^-\rangle$  that is parity forbidden at zero magnetic field [121]. By consequence, an increase in QY together with a shift of the exciton energy is expected [128]. Studies of CNT ensembles in magnetic fields accordingly reported both PL brightening [130, 132, 150, 151] and redshifts of the emission energy [132, 150, 151]. On the level of individual CNTs the emergence of a new emission peak energetically slightly below the  $E_{11}$  exciton was observed in agreement with the expected brightening of the dark state  $|K^-\rangle$  [131]. For magnetic fields orthogonal to the CNT axis, no such modifications have been observed [131, 132]. The energy splitting  $\Delta$  between the  $|K^+\rangle$  and the  $|K^-\rangle$  state also depends on the magnetic field and can be expressed by the hyperbolic relation  $\Delta^2 = \Delta_0^2 + \Delta_{\text{AB}}^2$  [121, 131, 132, 150]. Here,  $\Delta_0$  is the zero-field bright-dark splitting and the field-induced splitting  $\Delta_{\text{AB}} = \mu\varphi$  is given by the magnetic coupling constant  $\mu$  and the Aharonov-Bohm flux  $\varphi = \frac{1}{4}\pi d_t^2 B_{\parallel}$ , where  $B_{\parallel} = B \cos\theta$  is the magnetic-field component parallel to the CNT axis.

As first proposed by LAMPERT [152], excitons can capture a third charge carrier – either a second electron or a second hole – and analogously to  $\text{H}^-$  or  $\text{H}_2^+$  form a three-particle bound state called *trion*. The excess charge and the unpaired spin in trions open promising routes to the electronic control of optical properties and spin manipulation techniques [153, 154]. In bulk semiconductors, however, trions are elusive, since their binding energies compared to the neutral exciton state are typically below 1 meV [155, 156]. As has been predicted theoretically, trions are more stable in low-dimensional systems [157]. They are therefore routinely observed in semiconductor quantum dots, but the corresponding trion binding energies of  $\sim 3$ – $10$  meV still require low temperatures to achieve deterministic control [158–162]. In CNTs, by contrast, the trion binding energy is enhanced by strong Coulomb exchange interactions [163]. The diameter-dependent trion binding energy reaches values of  $\sim 130$  meV for CNTs diameters of 1 nm that stabilizes trions even at room temperature, rendering CNTs a particular promising platform for the study of trion physics [163–165].

## 2.5. Second order time-correlation functions

In Section 3.1 a Hanbury Brown-Twiss (HBT) setup comprising two superconducting single-photon detectors (SSPDs) is introduced that acts as an intensity interferometer, measuring correlations in the temporal intensity fluctuations of the light being studied. The signal of such measurements is the shape of the second-order time-correlation function  $g^{(2)}(\tau)$  that is defined by

$$g^{(2)}(\tau) = \frac{\langle I(t)I(t+\tau) \rangle}{\langle I(t) \rangle \langle I(t+\tau) \rangle} = \frac{\langle n_1(t)n_2(t+\tau) \rangle}{\langle n_1(t) \rangle \langle n_2(t+\tau) \rangle} \quad (2.20)$$

where  $\langle \cdot \rangle$  is the average over time  $t$ ,  $I(t)$  is the measured intensity at time  $t$ ,  $n_i(t)$  is the number of photon counts on detector  $i = 1, 2$  at time  $t$ , and  $\tau$  is the time difference between detection events at the two detectors [166]. While the two averages in the denominator evaluate to the time-independent intensity  $I_0$  of the light source, the numerator  $\langle I(t)I(t+\tau) \rangle$  contains information about the dynamics governing the temporal fluctuations of the light intensity. This is the case even though the  $g^{(2)}$  function only correlates intensities but neither electromagnetic field vectors nor phases – as opposed to the first-order correlation function  $g^{(1)}$  that correlates fields instead of intensities –, as was first demonstrated in astronomical observations of Sirius by HANBURY BROWN and TWISS [167] that clearly showed the capability to capture coherence effects. The measured bunching behavior for this classical light source (see Fig. 2.10 (a)) was explained purely by wave mechanical effects [168, 169]. Only later, these results were reinterpreted in the photon picture as the interference of probabilities [170] and cast into the theoretical framework of coherence functions by GLAUBER [166], opening the route towards the application in photon-counting experiments.

In several experiments it was established that the emission from a classical (or chaotic) light source generally features bunching [167, 169], i. e. that given the detection of a photon at some time  $t_0$  the probability to detect another photon at time  $t_0 + \tau$  is increased for short time delays  $\tau$ . In other words, the photons preferentially arrive in packets, or bunches. By consequence, the number of photons in a classical light beam is subject to strong variations, resulting in *super-Poissonian* light statistics, for which the variance of the photon number  $\text{Var}(n)$  is larger than the expectation value  $\langle n \rangle$  [171, pp. 82–87]. The resulting second-order correlation function  $g^{(2)}$  sketched in Fig. 2.10 (a) correspondingly shows a peak around zero delay time with a width given by a timescale  $\tau_0$  that is determined by the dynamics of the light source. Since  $g^{(2)}(\tau)$  approaches unity for large time delays as a signature of uncorrelated behavior, classical or generally bunched light is often identified by the criterion  $g^{(2)}(0) > 1$ .

By contrast, for coherent light like the single mode of a laser, the probability of photon emission is constant and independent of the emission of other photons, resulting in a flat  $g^{(2)}$  function (cf. Fig. 2.10 (b)) with a value of unity [166, 172]. This property of laser light is based on the fact that its photon statistics is given by a Glauber state for which the photon

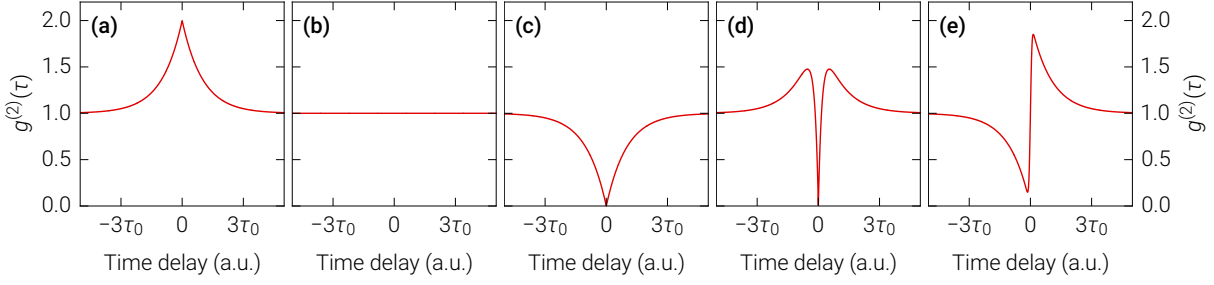


**Figure 2.10.:** Exemplary shapes of the second-order correlation function  $g^{(2)}(\tau)$  for **(a)** bunching with timescale  $\tau_0$ , **(b)** fully coherent light, **(c)** antibunching with timescale  $\tau_0$ , **(d)** bunching with timescale  $\tau_0$  superimposed by antibunching of timescale  $\frac{1}{5}\tau_0$ , and **(e)** conditional emission with timescale  $\tau_0$ .

occupation number follows a Poisson distribution such that the expectation value of the photon number  $\langle n \rangle$  is equal to its variance  $\text{Var}(n)$  and it is therefore referred to a *Poissonian* light [173]. This description is complemented by the experimental finding that the  $g^{(2)}$  function changes from the classical bunching behavior to the Poissonian statistics when the pump of a laser is increased above the lasing threshold, while additional intermediate regimes have also been observed [174]. As for classical light, the condition  $g^{(2)}(0) = 1$  is frequently employed to identify coherent light.

While these two scenarios may be described by classical means, the case of photon antibunching, i. e. the suppression of simultaneous photon emission, is only possible for quantum mechanical emitters. In this scenario, given the observation of a first photon at time  $t_0$ , the probability to detect another photon at time  $t_0 + \tau$  is reduced for short delay times  $\tau$ . The corresponding  $g^{(2)}$  function shows a dip around zero time delay (cf. Fig. 2.10 (c)) with a width given by the timescale  $\tau_0$  that is required to reset the emitter to its initial state [175–177]. The criterion for antibunched light may therefore be formulated as  $g^{(2)}(0) < 1$ . The absence of simultaneous photon emission events can be interpreted as a more equal temporal spacing of photons as is the case for classical light sources or lasers, which is reflected by *sub-Poissonian* light statistics, i. e. the variance of the photon number  $\text{Var}(n)$  is smaller than its expectation value  $\langle n \rangle$  [178]. For many emitters the classical blinking behavior is combined with quantum mechanical antibunching, resulting in intermittent single-photon emission [67, 73]. Fig. 2.10 (d) illustrates the corresponding functional form of  $g^{(2)}(\tau)$  for a blinking timescale 5 times larger than the antibunching timescale.

More complex examples of second-order correlation functions include the case of biexciton-exciton cascades, for which photons are emitted in a defined order [179–182]. In this scenario, the probability to detect a photon is reduced just before, but increased after the emission of the first photon, resulting in an asymmetric shape of  $g^{(2)}(\tau)$  as illustrated in Fig. 2.10 (e). Note that for this result the photons need to be distinguishable, e. g. by means of different wavelengths.

While the condition  $g^{(2)}(0) < 1$  stated above is indicative of antibunching, the perfect single-photon emitter in Fig. 2.10 (c) is characterized by the stronger requirement  $g^{(2)}(0) = 0$ . By consequence, antibunching of light and single-photon emission are not synonymous. For practical purposes, however, the requirement  $g^{(2)}(0) = 0$  is too strict, since experimental imperfections or an uncorrelated background often compromise the single-photon purity. For this reason the threshold value  $g^{(2)}(\tau) = 0.5$  is usually considered to distinguish between the scenario of antibunched light and single-photon emission. To arrive at this value, consider a number of  $N$  ideal, uncorrelated single photon emitters with respective intensities  $I_i(t)$  for  $i = 1, \dots, N$  that are all recorded by the same detector. The  $g^{(2)}$  function for these  $N$  emitters then reads

$$g_N^{(2)}(\tau) = \frac{\langle I(t)I(t+\tau) \rangle}{\langle I(t) \rangle \langle I(t+\tau) \rangle} = \frac{\langle \sum_{i=1}^N \sum_{j=1}^N I_i(t)I_j(t+\tau) \rangle}{\langle \sum_{i=1}^N I_i(t) \rangle \langle \sum_{j=1}^N I_j(t+\tau) \rangle}. \quad (2.21)$$

By assuming an equal time-averaged intensity  $\langle I_i(t) \rangle = I_0$  for all  $i = 1, \dots, N$  the two factors in the denominator can be written as

$$\langle \sum_{i=1}^N I_i(t) \rangle = \sum_{i=1}^N \langle I_i(t) \rangle = N \cdot I_0 \quad \text{and} \quad \langle \sum_{j=1}^N I_j(t+\tau) \rangle = \sum_{j=1}^N \langle I_j(t+\tau) \rangle = N \cdot I_0. \quad (2.22)$$

To similarly calculate the numerator in Eq. (2.21), note that  $\langle I_i(t)I_j(t+\tau) \rangle = I_0^2$  for all  $N^2 - N$  combinations with  $i \neq j$ , since the  $N$  single-photon emitters are uncorrelated by definition, while  $\langle I_i(t)I_i(t+\tau) \rangle = I_0^2 \cdot g^{(2)}(\tau)$  for all  $i = 1, \dots, N$  following Eq. (2.20). Inserting these results into Eq. (2.21) yields

$$g_N^{(2)}(\tau) = \frac{(N^2 - N) \cdot I_0^2 + N \cdot I_0^2 g^{(2)}(\tau)}{N^2 \cdot I_0^2} = \frac{N^2 + N \cdot (g^{(2)}(\tau) - 1)}{N^2} = 1 + \frac{1}{N} \cdot (g^{(2)}(\tau) - 1). \quad (2.23)$$

The assumption that all  $N$  single-photon emitters are ideal implies  $g^{(2)}(0) = 0$ , so  $g_N^{(2)}(0)$  evaluates to

$$g_N^{(2)}(0) = 1 - \frac{1}{N} = 1, \frac{1}{2}, \frac{2}{3}, \frac{3}{4}, \dots \quad \text{for} \quad N = 1, 2, 3, 4, \dots \quad (2.24)$$

By consequence, the condition  $g^{(2)}(0) < 0.5$  is necessary to unambiguously identify an isolated single-photon emitter, since already two equally bright single-photon emitters imply  $g^{(2)}(0) = 0.5$ . This insight also illustrates the difference between single-photon emission and antibunching. The scenario  $0.5 < g^{(2)}(0) < 1$  can be related to an ensemble of multiple single-photon emitters for which simultaneous photon emission is not strictly forbidden but nonetheless suppressed, giving rise to antibunching without single-photon emission.

So far the mode of operation of the HBT setup in Section 3.1 has not been discussed in detail. One important limitation of this setup is its restriction to performing start-stop measurements instead of unconstrained time-correlation experiments. This means that the

electronic correlator time-tagging photon detection events only relates *subsequent* counts on the two channels, while the  $g^{(2)}$  function in Eq. (2.20) calculates correlations between *any* two photons arriving at *any* times. The relation between the measured second-order correlation function of *subsequent* photons  $c^{(2)}(\tau)$  and the desired  $g^{(2)}$  function was found in [183] to equal

$$c^{(2)}(\tau) = g^{(2)}(\tau) \cdot \exp(-\Gamma|\tau|), \quad (2.25)$$

where  $\Gamma$  is the rate of incoming photons. In all experiments reported in this work the timescales of bunching and antibunching were much shorter than  $\Gamma^{-1}$  with typical values for  $\Gamma$  ranging in the order of  $10^4 \text{ s}^{-1}$ . By consequence,  $\exp(-\Gamma|\tau|) \approx 1$  held true on all relevant timescales and the difference between  $c^{(2)}$  and  $g^{(2)}$  could be ignored. The long-time exponential decay of  $c^{(2)}(\tau)$  was noticeable in some data sets, however.



# 3 Experimental methods for confocal microscopy of individual carbon nanotubes

---

Photoluminescence spectroscopy experiments on individual carbon nanotubes were performed with a home-built cryogenic confocal microscope. Isolated emitters were addressed by focusing a titanium-sapphire laser with a low-temperature apochromatic objective to a diffraction-limited spot on the sample that was displaced with nanometer precision using a slip-stick piezo positioning unit and cooled to the temperature of liquid helium. Directional emission of the photoluminescence light in the presence of a solid immersion lens acting as a numerical-aperture-increasing lens was exploited to maximize the signal collected by the objective. Tunable optical long- and shortpass filters were employed to select spectral regions of interest in the carbon nanotube photoluminescence emission. A modular setup based on single-mode fibers allowed for effortless switching between microscope alignment, spectroscopic measurements with a silicon or a indium gallium arsenide detector, or time-resolved photoluminescence decay or photon correlation measurements.

Purified carbon nanotube samples of chiralities (9, 1) and (6, 5) were produced by aqueous two-polymer phase extraction and gel chromatography, respectively. The carbon nanotubes of chirality (9, 1) were coated with either sodium deoxycholate or poly[9,9-dioctylfluorenyl-2,7-diyl] surfactant, while the carbon nanotubes of chirality (6,5) were covalently functionalized by attaching hexyl substituents with a novel chemistry approach based on sodium dithionite. Suitable degrees of dilution for the carbon nanotube suspensions were determined using a scanning electron microscope in order to produce samples with individualized emitters by drop-casting onto solid immersion lenses. The performance of the cryogenic confocal microscope was optimized by analyzing the directional light emission induced by the high refractive index of the solid immersion lenses.

### 3.1. Cryogenic confocal microscope

For all confocal photoluminescence (PL) measurements on individual carbon nanotubes (CNTs), optical excitation was performed with a titanium-sapphire (Ti:sapphire) laser (*Coherent* Mira 900 pumped by a *Coherent* Verdi-G8 laser diode) that was wavelength tunable in the range 690–1000 nm. The laser was either operated in continuous wave (CW) or in pulsed mode with a repetition rate of 76.0 MHz and a pulse duration of  $\sim 200$  fs. The output power was stabilized and regulated by a home-built intensity stabilization setup based on double-passing an acousto-optic modulator, whose detailed description is given in [184].

The intensity-stabilized laser beam was coupled into an optical single-mode fiber and its polarization axis was manipulated by a three-paddle fiber polarization controller. The laser light was guided to the horizontal side arm of the microscope, where it was collimated with a numerical aperture (NA)-matched home-built collimator (green beam in Fig. 3.1) and longer-wavelength Raman photons generated by the light passing through the optical fiber were removed by a shortpass filter (filter edge at 858 nm, 898 nm, or 950 nm). A beam sampler with antireflective coating split the excitation beam into a reflected and a transmitted part, where for an incidence angle of  $45^\circ$  the reflectance ranges between 1–10% depending on the polarization of the incident light. For an s-polarized incident beam, which was set by the help of the polarization paddles for all measurements, the reflected to transmitted intensity ratio attained 10% : 90%. The intensity of the transmitted part was measured by a photodiode and served as reference value for the laser-power stabilization loop.

The reflected light was directed towards the sample and its polarization state was adjusted by passing through a half-wave plate (HWP) to rotate the polarization plane and optionally through a removable quarter-wave plate (QWP) to transform linear into circular polarization. Measurements on individual CNTs were performed under linear excitation and the polarization axis was aligned with the CNT axis by maximizing the PL intensity. Automated two-dimensional scans were recorded with circularly polarized excitation to retain sensitivity for all CNTs irrespective of their orientation.

The CNTs samples were dispersed on the flat side of a hemispherical solid immersion lens (SIL) as detailed in Section 3.2 that acted as a numerical-aperture-increasing lens (NAIL). The SIL was fixed inside a home-built titanium holder and mounted on a slip-stick piezo positioning unit (*attocube systems* ANPxy101 (2 $\times$ ) and ANPz102) that allowed displacement in all three spatial dimensions with sub-micrometer precision. The sample was then placed in the focus of a low-temperature apochromatic objective (*attocube systems* LT-APO/IR/0.81) with an NA of 0.81 and a confocal spot size of  $\sim 1.1 \mu\text{m}$  [75]. A photodiode below the sample was used to monitor the transmitted excitation laser power.

To allow for measurements with a fraction of the randomly oriented dispersed CNTs co-linear with the magnetic field axis, the sample could optionally be rotated by  $90^\circ$  to the so-called Voigt geometry [185], as opposed to the previously described sample mounting

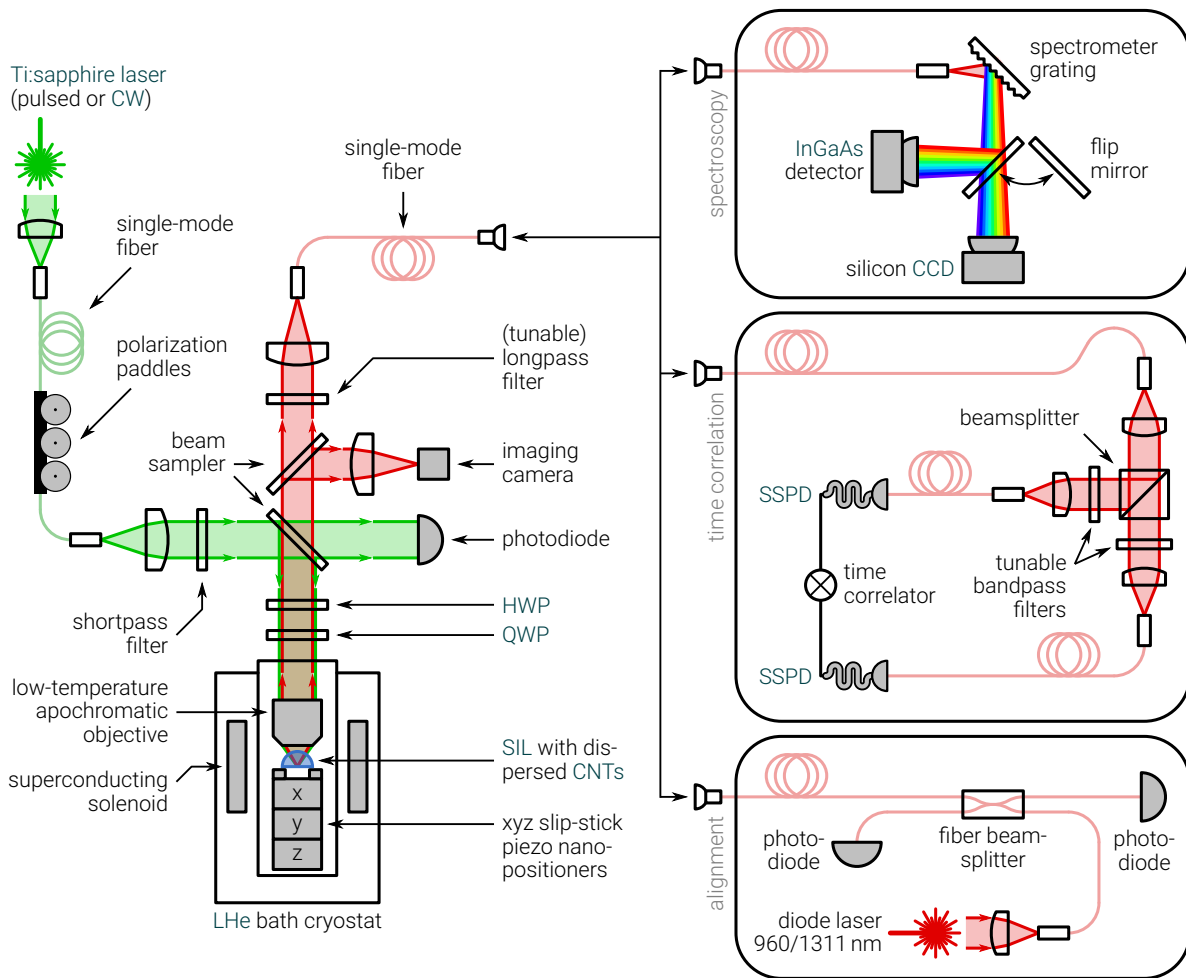


**Figure 3.1.:** Schematic of the cryogenic confocal microscope setup. A single-mode fiber equipped with a three-paddle fiber polarization controller guides the light of a **Ti:sapphire laser**, operated in pulsed or **CW** mode, to the side arm of the microscope. A beam sampler transmits 90 % of the light towards a photodiode serving as reference for the laser-power stabilization loop, while the other 10 % are reflected towards the sample. A variable **HWP** and a removable **QWP** allow for polarization control of the laser light. The sample is deposited on the flat side of a hemispherical **SIL**, mounted beneath the apochromatic objective on an xyz slip-stick piezo positioning unit inside a sealed steel tube filled with helium gas for thermal coupling to the surrounding **LHe** bath, and positioned at the center of the superconducting solenoid magnet. A small fraction of the light collected by the objective from the sample is reflected by another beam sampler in the top arm of the microscope for imaging with a **CCD** camera, while the transmitted light passes a longpass filter before it is coupled into a single-mode fiber. The fiber is either connected to an alignment setup comprising a fiber beamsplitter with two photodiodes and a diode laser of 960 nm or 1311 nm, a spectroscopy or a time-correlation setup. For spectroscopy, the light is dispersed with a spectrometer grating and detected by an **LN-cooled InGaAs** detector or an **LN-cooled silicon CCD**. For time-resolved measurements, a beamsplitter divides the signal into two channels that are both purified with tunable bandpass filters, detected by two **SSPDs**, and time-tagged by an electronic correlator.

in Faraday geometry [186]. For this purpose, an L-shaped titanium adapter was inserted between the slip-stick piezo positioning unit and the sample. In this scenario, the apochromatic objective was replaced by a unit containing a prism that reflected laser beam and PL signal by 90° and, owed to reduced space in the rotated geometry, an aspherical lens (*Geltech* aspheric lens 350570 with NA 0.67) for focusing to the sample. Since the use of a single lens came at the cost of a wavelength-dependent focal length, all measurements that did not require magnetic fields were performed in the aforementioned Faraday geometry, in order to facilitate the experiments.

Sample, objective/lens, and positioning unit were mounted inside a steel tube terminated by a vacuum-sealed anti-reflection-coated window for optical access. The tube was evacuated to a pressure of  $\sim 5 \times 10^{-5}$  mbar and subsequently filled with helium gas at  $\sim 20$  mbar to achieve thermal coupling of the sample to liquid helium (LHe) (4.2 K). The steel tube was then inserted into the LHe bath cryostat and positioned to place the sample in the center of the superconducting solenoid. For temperature-dependent measurements a resistive heater was attached to the sample holder and connected to a power supply with tunable output voltage. For readout, a carbon-composite resistor with nonlinear dependence of the resistance on temperature was thermally coupled to the sample and monitored in a two-point measurement.

Reflected laser light and PL emitted from the sample were collected and collimated by the objective/lens and passed through the QWP, the HWP and the lower beam sampler to the top arm of the microscope (red beam in Fig. 3.1). A second anti-reflection-coated beam sampler reflected part of the light towards a charge-coupled device (CCD) board camera that was used to image the focal spot for alignment purposes or to allow for coarse orientation on the sample. The fraction of the beam transmitted through the second beam sampler passed an optical longpass filter blocking the scattered laser light (filter edge at 860 nm, 900 nm, or 950 nm) and optionally a second, wavelength-tunable long- or bandpass filter (*Semrock* VersaChrome Edge TLP01-995-25x36, TSP01-995-25x36, TLP01-1116-25x36, or TSP01-1116-25x36) removing unwanted fractions of the PL signal. The remaining signal was coupled into an optical single-mode fiber with an NA-matched home-built collimator and guided to the detection devices.

For alignment purposes (lower box in Fig. 3.1), the single-mode fiber from the top arm of the microscope was connected to one port of a fiber beamsplitter with two photodiodes and a diode laser of either 960 nm or 1311 nm wavelength, depending on the desired target wavelength, attached to the three other ports. While blocking the Ti:sapphire laser, the respective diode laser was coupled into the microscope at a fixed power monitored by one of the photodiodes (left in Fig. 3.1) and reflected light was detected by the other photodiode (right in Fig. 3.1). By maximizing the reflected intensity aided by monitoring the focal spot with the CCD board camera, this setup allowed for beam alignment and focal plane adjustment with the slip-stick piezo positioner moving in vertical direction.

Spectroscopic measurements (upper box in Fig. 3.1) were performed by dispersing PL from the sample by a grating monochromator (*Roper Scientific* Acton SP2500). The wavelength-dependent intensity was recorded with either a liquid nitrogen (LN)-cooled silicon CCD (*Roper Scientific* Spec-10:100BR/LN) for signals below  $\sim 1050$  nm or an LN-cooled InGaAs array (*Roper Scientific* OMA V:1024-1.7 LN) for signals above  $\sim 1000$  nm by changing the position of a flip mirror. For broadband spectra, a grating with 150 grooves/mm was used that allowed for a spectral resolution of  $\sim 450$   $\mu\text{eV}$  at 950 nm and of  $\sim 240$   $\mu\text{eV}$  at 1300 nm. For spectrally finer measurements, also two other gratings with 300 grooves/mm and 1200 grooves/mm were available, providing two and eight times higher resolution, respectively.

For time-resolved measurements a Hanbury Brown-Twiss (HBT) setup was used (central box in Fig. 3.1), where the light in the single-mode fiber was again collimated and passed through a beamsplitter with a 50% : 50% splitting ratio. Tunable bandpass filters (*Semrock* VersaChrome Edge TLP01-995-25x36, TSP01-995-25x36, TLP01-1116-25x36, or TSP01-1116-25x36) could be inserted in the pathway of both fractions of the beam and allowed for spectral selection of the different emission features in the PL of CNTs. For the analysis of different wavelength ranges in the two channels, the beamsplitter could also be replaced by a dichroic beamsplitter (*Semrock* BrightLine Di02-R1064-25x36) to increase the photon count by a factor of two each. Both beams were coupled again into single-mode fibers that guided the light to the input-ports of a two-channel superconducting single-photon detector (SSPD) (*Scontel* TCOPRS-CCR-SW-85). Time-correlation measurements were performed by time-tagging the electronic output signals from both SSPDs with an electronic correlator (*PicoQuant* PicoHarp 300). For PL decay measurements under pulsed excitation, the electronic trigger signal of the Ti:sapphire laser and the output signal of only one SSPD were time-tagged, instead.

## 3.2. Sample preparation

The photophysical properties of CNTs are not only determined by their crystal structure (cf. Section 2.3), but also depend strongly on environmental effects that are enhanced by their exceptional surface-to-volume ratio [68, 187, 188]. Accordingly, previous studies have established that experiments based on chemical vapour deposition (CVD)-grown, freely-suspended CNTs that are subject to minimum environmental influences yield particularly undistorted results [67, 189]. These advantages, however, are diminished by chirality purity requirements. For example, applications in CNT-based electronics allow for no more than 0.0001 % contamination by metallic CNTs [190]. Despite recent advances in the tuning of CVD parameters [P8] and the discovery of methods for chirality-deterministic CVD growth of selected CNT chiralities [191–194], these approaches currently cannot provide sufficiently pure CNT samples.

As an alternative approach, a number of methods have been developed that purify CNT samples after their CVD synthesis, including density-gradient ultracentrifugation, chromatography, aqueous two-phase extraction, and selective polymer wrapping [194–199], that are summarized under the phrase *chirality sorting* and allow for purities above 99.9 % [198]. To avoid the formation of CNT bundles in these wet-chemical treatments, however, the CNTs are generally coated with surfactants, accompanied by ultrasonication [200, 201]. By consequence, chirality purified CNTs cannot compete with the clean environmental conditions of CVD-grown, freely suspended CNTs. This brings about the need to either improve the understanding of the interaction between the CNT and the surfactant (see Chapter 4) or to introduce protected states in the CNT that are less susceptible to environmental effects (see Chapter 5).

The studies in this work were based on chirality purified (9, 1)-CNTs coated with sodium deoxycholate (DOC) or poly[9, 9-dioctylfluorenyl-2, 7-diyl] (PFO)<sup>1</sup> and on chirality purified (6, 5)-CNTs functionalized by covalent sidewall chemistry<sup>2</sup> that are introduced in the following.<sup>3</sup> To produce (6, 5)-CNTs with DOC and PFO surfactant wrapping, carbon soot (*Chasm Technologies* SG65i) was dispersed into 2 % DOC via tip sonication in ice bath for 1 h at ~0.9 W/mL followed by centrifugation (*Beckman Coulter* Ja-20 rotor) at 18 krpm for 2 h, collecting the supernatant, and rate zonal centrifugation to isolate the cleanest CNT material [202]. The CNTs were isolated via multistep gradient aqueous two-polymer phase extraction (ATPE) using surfactants (fraction 4B[Mt+MbMt]Mt3BT) [203, 204] followed by forced dialysis using an ultrafiltration cell (*Merck* Millipore Amicon) with a 100 kDa membrane to remove the ATPE polymers and to exchange to 10.0 g/L DOC in H<sub>2</sub>O.

For the exchange of DOC for PFO surfactant, 200 μL of CNTs in 1 % DOC were spun to dry in a 30 kDa centriscin filter (*Merck* Millipore), redispersed with 50 μL of 18 MΩ H<sub>2</sub>O, overlaid with 200 μL ethanol and allowed to sit for 10 min to flocculate before centrifuging 6 min at  $17 \times 10^3$  g to pellet. Next, after 200 μL of ethanol removed, 200 μL of ethanol added to rinse the pellet, it was spun again and, ~200 μL of ethanol removed, 200 μL of ethyl acetate added, the pellet was spun down. After removal of ~200 μL of ethyl acetate and rest for 5 min for evaporation of residual, 200 μL toluene were added and the pellet was spun down. After removal of ~150 μL of toluene, 250 μL of toluene with 200 μL of 2.5 mg/mL PFO in toluene were added and the sample was tip sonicated with a 1/16 inch tip for 5 min at ~1–2 W power without cooling.

To produce the (6, 5)-CNTs-enriched sample, CNTs with sodium dodecyl sulfate (SDS) surfactant dispersed in D<sub>2</sub>O were sorted for high-purity by gel chromatography [205]. To

---

<sup>1</sup> This sample was kindly provided by Jeffrey Fagan from the National Institute of Standards and Technology.

<sup>2</sup> This sample was kindly provided by the group of YuHuang Wang from the University of Maryland.

<sup>3</sup> Parts of this section are based on the publication [P2] available at <https://pubs.acs.org/doi/10.1021/acscentsci.9b00707>. Permission for any further reuse of the excerpted material must be granted by the American Chemical Society.

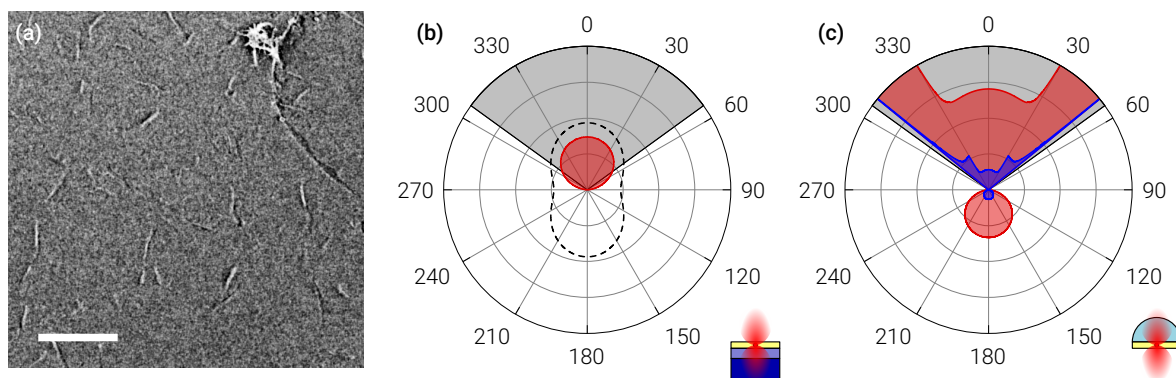


**Figure 3.2.:** (a) Image of isolated surfactant-wrapped CNTs (white lines) dispersed from solution onto a silicon chip with a 100 nm thermal silicon oxide capping layer captured by an SEM with 0.7 kV acceleration voltage. A bundle of aggregated CNTs is located in the top right corner. The scale bar is 4  $\mu\text{m}$ . (b)–(c) Radiation patterns (red curves) of the emitted intensities of a horizontally oriented dipole embedded in a layer of DOC on top of a silicon chip with a 100 nm silicon oxide capping layer (left) and below a hemispherical SIL (right), as illustrated by the insets. No intensity is emitted towards the bottom for the intrinsically transparent silicon substrate as compared to the symmetric radiation pattern of a dipole in vacuum (black dashed line, multiplied by a factor of 5 for clarity). For the SIL substrate, more light is emitted to the top than to the bottom due to near-field effects. The higher integrated intensity originates from field enhancement due to constructive interference of reflected light at the position of the dipole. The dominant emission close to the angle of total internal reflection is illustrated by the blue curve that shows the radiation profile divided by a factor of 5. The gray shaded areas correspond to the NA of the apochromatic objective.

prepare the covalent sidewall functionalization, sodium bicarbonate ( $\text{NaHCO}_3$ ), acetonitrile ( $\text{C}_2\text{H}_3\text{N}$ ) and 1-iodohexane ( $\text{C}_6\text{H}_{13}\text{I}$ ) were added successively to the (6, 5)-CNTs. A reaction between the (6, 5)-CNTs and the 1-iodohexane was then initiated by adding sodium dithionite ( $\text{Na}_2\text{S}_2\text{O}_4$ ), resulting in the formation of hexyl-functionalized carbon nanotubes (hCNTs) that are characterized in Section 5.2.

To obtain samples with dispersed CNTs, a suitable degree of dilution was estimated from the known carbon contents of the CNT suspensions. For all CNT samples a dilution series around this estimation was produced by admixing water with 1 % DOC for all samples with DOC surfactant, or pure water for the sample with PFO surfactant. Of the resulting thinned suspensions 1  $\mu\text{L}$  each was drop-cast onto cleaned n-doped silicon chips with a 100 nm thermal silicon oxide capping layer and analyzed under a scanning electron microscope (SEM) (*Raith e\_Line*). Using a low acceleration voltage of 0.7 kV the dispersed CNTs were visible as white lines on a dark background (cf. Fig. 3.2 (a)) due to charging of the surrounding substrate [206, 207]. Comparing the different distributions of CNTs on the silicon chips, an optimum degree of dilution was chosen that produced results like the sample shown in Fig. 3.2 (a), where all CNTs (white lines) are well-separated from the surrounding CNTs,

except for a single bundle of CNTs in the top right corner. Such bundles were present on all produced samples, but were easily identified in cryogenic PL measurements based on their broad spectral response and excluded from our studies.

The samples for cryogenic PL spectroscopy were then prepared by drop-casting 1  $\mu\text{L}$  of the respective CNT suspension with optimized degree of dilution on the flat side of a hemispherical SIL with 2 mm diameter. The use of a SIL instead of a conventional substrate like a silicon chip improved the operation of the cryogenic confocal microscope in two respects. First, by virtue of its hemispherical geometry the SIL acted as a NAIL [208, 209] and thereby increased the optical resolution that was limited by the Rayleigh criterion  $0.61\lambda/\text{NA}$ , where  $\lambda$  is the wavelength of the light and NA is the numerical aperture of the objective in Fig. 3.1 [210]. At the same time, not only the spatial resolution but also the collected fraction of light was increased by the larger NA. Both effects would be even more pronounced for the alternative Weierstrauss SIL configuration, but due to the absence of chromatic aberrations hemispherical SILs are generally preferred [208].

The second modification arises from the observation that a dipole emitter in the vicinity of a phase boundary emits preferentially into the medium with higher refractive index [211]. The SIL above the sample accordingly modified the dipole emission characteristics and directed the PL from the CNTs towards the objective [211–213]. This effect was particularly pronounced due to the thin layer consisting of CNTs and surfactant that featured a refractive index in between that of vacuum and that of the SIL material, thereby forming a light-channeling waveguide-like structure [214].

Fig. 3.2 (b) illustrates the simulated radiation pattern of a CNT acting as a dipole emitter embedded in a thin layer of DOC surfactant with refractive index  $\sim 1.5$  on top of a silicon chip with a 100 nm silicon oxide capping layer (cf. inset in Fig. 3.2 (b)), the substrate that was used for the SEM imaging in Fig. 3.2 (a). In vacuum, the CNT would emit with the radiation pattern of a dipole (dashed line in Fig. 3.2 (b) shows the average over the azimuth angle) with maximum intensity directed to the top and to the bottom, orthogonal to the CNT axis, and minimum intensity in horizontal direction, due to zero field in the direction parallel to the CNT axis. This shape is modified in the presence of the silicon substrate, where all light emitted downwards is reflected at the interface between silicon oxide and the intransparent silicon such that only the upper lobe of the radiation profile remains. The apochromatic objective with an NA of 0.81 would collect a fraction of 0.68 of the emitted intensity in this configuration.

The radiation pattern for the case of CNTs dispersed on the flat side of a SIL (cf. inset in Fig. 3.2 (c)) is shown in Fig. 3.2 (c) and features significant modifications compared to Fig. 3.2 (b). While only a small fraction of the light is emitted downwards into the region with lowest refractive index [214], most light is directed towards the objective and emitted close to the angle of total internal refraction at the interface between the CNTs embedded in surfactant and the SIL [215]. Since the corresponding critical angle is smaller than the

collection angle of the objective with NA 0.81, all light emitted upwards enters the objective, resulting in a collection efficiency of 0.75.

While the collection efficiencies of 0.68 and 0.75 for the two scenarios are similar, also dissipation effects [215] and light trapped by total internal reflection in the layers with highest refractive index in Fig. 3.2 (b) need to be considered. Using a framework based on decomposition of the dipole radiation into plane waves and the assumption of a fixed dipole radiation power [215–217] a 3.3 times higher intensity for the configuration employing the SIL in Fig. 3.2 (c) is predicted despite the similar light collection efficiencies. This difference can be attributed to field enhancement of the PL emission due to constructive interference of reflected light at the position of the dipole in the geometry of Fig. 3.2 (c).

To maximize both the NA augmentation and the increase in the collected light intensity, SILs fabricated from a quartz glass (*Schott* LASF35) with a high refractive index of 2.022 were chosen [214]. The SILs with dispersed CNTs were mounted on the slip-stick piezo positioning unit introduced in Section 3.1 with their curved side facing the objective. The center of the apex was located under the objective by monitoring the reflection of the focused alignment laser spot off the curved SIL surface. To perform measurements, the SIL was then moved upwards to focus the laser on its flat side. In this configuration, the focal point lies at the center of the sphere and all light rays are perpendicular to the spherical surface. By consequence, no diffraction occurs and the SIL acts as an achromatic optical element by design. To minimize any (chromatic) aberrations, the sample area was restricted to  $\sim 100 \times 100 \mu\text{m}^2$  around the central point of the SIL.



# 4

## Photoluminescence lineshapes of localized excitons in polymer-decorated carbon nanotubes

---

This chapter discusses the influences of environmental effects on the photoluminescence response of localized excitons in cryogenic carbon nanotubes that give rise to a wealth of experimentally observed spectral lineshapes. Earlier studies attributed these variations to a modification of the interactions between excitons and carbon nanotube lattice phonons mediated by mechanical contact to the substrate. This model, however, relies on an implausible value for the exciton-phonon deformation potential coupling. Here, we propose a Holstein-like interaction of the exciton dipole moment with vibrational degrees of freedom in adsorbate molecules as an alternative mechanism responsible for the experimentally observed photoluminescence line shapes. A quantum-mechanical description was developed that captures the dipole-dipole interactions between localized carbon nanotube excitons and dynamical molecular dipoles that are induced by charge displacements in vibrating surfactant molecules. A quadratic damping of the vibronic sidebands with increasing energy difference from the zero phonon line is predicted, providing an explanation for the fading of spectral wings frequently observed experimentally. Density functional theory simulations were performed to calculate the relevant characteristics of molecular vibrations and combined with an estimation of the model parameters from literature values. The comparison with cryogenic spectra of polymer-decorated carbon nanotubes showed an excellent agreement with our model description that is essentially free of fitting parameters. We extended our discussion to also capture the effects of a thermal occupation of vibronic modes at nonzero temperatures. Experiments where the sample temperature and the laser irradiance were varied systematically established an excellent correspondence with the simulated spectra over a broad range of parameters.

## 4.1. Introduction

Due to the exceptionally large binding energy that stabilizes excitons in carbon nanotubes (CNTs) even at room temperature (cf. Section 2.4), photoluminescence (PL) emission from CNTs predominantly originates from these quasiparticles. At elevated temperatures, the excitons may diffuse freely and explore variations in the potential landscape along the CNT axis [52–55, 218–222]. In cryogenic CNTs, by contrast, a thermal energy bath is absent and exciton localization in shallow potential traps of few meV depth is ubiquitous [60–63, 67, 70, 72, 73, 223, pp. 232–244]. Hallmarks of this localization in the PL response of individual CNTs are single-photon emission [63, 67, 72, 73, 224] and the decomposition of thermally broadened spectra at room temperature into multipeak spectra with occasionally asymmetric lineshapes at cryogenic temperatures [61, 135, 225].

The observation of asymmetric spectral lines at low temperatures is incompatible with the simplistic picture of thermally broadened PL from CNTs at room temperature that would narrow symmetrically upon cooldown [61]. The spectral asymmetry has been attributed to the coupling of excitons to a one-dimensional phonon reservoir [226–228]. More complex lineshapes were explained by the confinement of low-energy acoustic phonon modes, resulting in a gap in the phonon dispersion [70, 229, 230]. While a compelling agreement between simulated and experimental CNT spectra can be obtained [70], the required value for the exciton-phonon deformation potential coupling as an important model parameter deviates significantly from theoretical values [227, 228].

With their exceptional surface-to-volume ratio, CNTs couple particularly strongly to their environment [66–68]. In particular, the observation of permanent electric dipole moments of excitons in CNTs [38] revealed an efficient interaction mechanism with microscopic charge fluctuations in the vicinity of the CNT [P6]. This excitonic dipole moment also allows for pronounced coupling mechanisms to phonons in polar materials similar to the Fröhlich interaction [231, 232, 233, pp. 133–135], or for Holstein-like couplings to molecular vibrations [234, 235, 236, pp. 38–43]. Akin to the interaction with a one-dimensional phonon reservoir, both of these effects would result in asymmetric modifications of the exciton lineshape. Based on this finding, we explore dipolar couplings as an alternative explanation for the variations in the spectral lineshapes of cryogenic CNTs in this chapter.

## 4.2. Origins of the spectral lineshape of localized excitons in cryogenic carbon nanotubes

At room temperature, the PL response from CNTs that are significantly longer than an optical spot size is evenly distributed along the CNT axis [60]. This finding indicates that optically generated excitons (cf. Section 2.4) diffusively explore the potential landscape along the

entire CNT length at elevated temperatures. Upon cooldown to cryogenic temperatures, however, the spatially homogeneous PL fragments into emission hot spots [60]. Experimental shifts of the emission peak energy revealed deviations from a temperature-dependent theory of the CNT band gap renormalization (cf. Section 2.4) and established the presence of shallow potential traps with a depth ranging between few and few tens of meV [60, 144]. In the absence of a thermal energy bath, these shallow traps localize the excitons and inhibit their diffusion along the CNT axis.

At the same time, single-photon emission from cryogenic CNTs was observed, confirming the localized nature of the photoexcited states [63, 67, 72, 73, 224]. In addition, spectral variations emerge at lower temperatures that contrast the symmetric, thermally broadened lineshapes at room-temperature [61, 135, 225]. The observed variations include position-dependent emission energies, asymmetric lineshapes and multipeak spectra [223, pp. 233–234]. Also, the cryogenic linewidth was found to vary between broad, asymmetric peaks of more than 10 meV full width at half maximum (FWHM) and narrow symmetric peaks with less than 40  $\mu\text{eV}$  FWHM [61, 67, 70, 72, 135, 227]. This puzzling wealth of spectral profiles has been addressed in a framework of excitons coupling to the one-dimensional phonon reservoir of CNTs [70, 226–230], as sketched in the following.

Asymmetric CNT lineshapes were observed both for the case of unintentional exciton localization [61, 63, 227, 237] and deterministic generation of trapping potentials via covalent functionalization [59, 238]. The model proposed by GALLAND et al. [227] therefore includes localized excitons as a key ingredient and studies their coupling to phonons in a one-dimensional crystal. This description builds upon an extension of the independent boson model from [226] that expresses the exciton absorption spectrum as the imaginary part of the Fourier transform of the linear dipole susceptibility, which has the form

$$\chi(t) = -\Theta(t) \cdot \frac{i|M|^2}{\hbar\epsilon_0} \cdot e^{-i\bar{\Omega}t} \cdot \tilde{\chi}_T(t)\tilde{\chi}_0(t). \quad (4.1)$$

The PL lineshape is then obtained as the mirror image of the absorption spectrum [227]. In Eq. (4.1),  $\Theta(t)$  is the Heaviside step function that reflects the excitation with a  $\delta$ -shaped laser pulse at  $t = 0$ ,  $M$  is the dipolar coupling strength to the laser field,  $\epsilon_0$  is the vacuum permittivity and  $\bar{\Omega}$  is the polaron-shifted exciton transition frequency [226, 227, 239]. The two factors  $\tilde{\chi}_T(t)$  and  $\tilde{\chi}_0(t)$  are the temperature-dependent and the temperature-independent contribution to the linear susceptibility, respectively, that are given by [227]

$$\tilde{\chi}_T(t) = i \exp \left[ \sum_q |\gamma(q)|^2 \left( -n(q) \cdot |e^{-i\omega(q)t} - 1|^2 \right) \right], \quad (4.2a)$$

$$\tilde{\chi}_0(t) = i \exp \left[ \sum_q |\gamma(q)|^2 (e^{-i\omega(q)t} - 1) \right]. \quad (4.2b)$$

Here,  $n(q) = (e^{\hbar\omega(q)/k_B T} - 1)^{-1}$  is the Bose-Einstein phonon occupation number at temperature  $T$ , with  $k_B$  being the Boltzmann constant. The phonon dispersion  $\omega(q)$  is assumed to have the linear form  $\omega(q) = v \cdot q$ , where  $v = 19.9$  km/s is the speed of sound, and  $q$  is the phonon wave vector. Finally,  $\gamma(q) = g(q)/\hbar\omega(q)$  is the dimensionless coupling strength that comprises the exciton-phonon-coupling matrix element  $g(q)$ .

The coupling matrix element can be decomposed as  $g(q) = G(q) \cdot F(q)$ , where  $F(q)$  is the Fourier-transformed exciton form factor [226, 227, 239],

$$F(q) = \int dz |\psi(z)|^2 e^{iq \cdot z}. \quad (4.3)$$

Here,  $\psi(z)$  is the exciton wave function and  $z$  is the coordinate pointing along the CNT axis, such that  $|\psi(z)|^2$  denotes the probability density of the exciton location in the CNT. GALLAND et al. [227] modeled the scenario of exciton localization by assuming a Gaussian probability density,  $\psi(z) = \pi^{-1/4} \sigma^{-1/2} \cdot \exp(-z^2/2\sigma^2)$ , where  $\sigma$  is the exciton confinement length, resulting in the form factor  $F_0$  for confined excitons,

$$F_0(q) = \exp\left(-\frac{q^2 \sigma^2}{4}\right). \quad (4.4)$$

The factor  $G(q)$  is the bulk exciton-phonon-coupling matrix element [226, 239], which is dominated by the deformation-potential coupling for the case of CNTs [227]. In this scenario  $G(q)$  can be written as [226, 227, 239]

$$G(q) = \frac{Dq}{\sqrt{2\rho L \hbar \omega(q)}}, \quad (4.5)$$

where  $D$  is the deformation-potential coupling constant,  $\rho$  is the CNT linear mass density and  $L$  is the CNT length.

Due to the coupling to acoustic phonons, this model predicts asymmetric lower-energy wings for spectral lines at cryogenic temperatures [227]. It is therefore best suited to explain broad, asymmetric PL peaks of CNTs. The spectrum presented in Fig. 4.1 (a) (black data points) features an FWHM of  $\sim 3$  meV and is well reproduced by the model fit (solid red line) obtained for  $T = 4.1$  K,  $D = 13.0$  eV and  $\sigma = 3.2$  nm in good agreement with the values given in [227]. Note that the asymmetric line shape is a characteristic feature of the coupling to a one-dimensional phonon reservoir, while simulated spectra using the same parameters but a higher dimension for the phonon bath result in a markedly different line shape [223, pp. 242–243, 227].

Spectra of cryogenic CNTs frequently also feature other spectral shapes like that presented in Fig. 4.1 (b) (black data points) [70, 229, 230]. While this PL spectrum also exhibits a lower-energy wing, unlike for the spectrum in Fig. 4.1 (a) a pronounced gap separates the wing from the narrow central peak that exhibits an FWHM of only  $\sim 50$   $\mu$ eV. The model presented

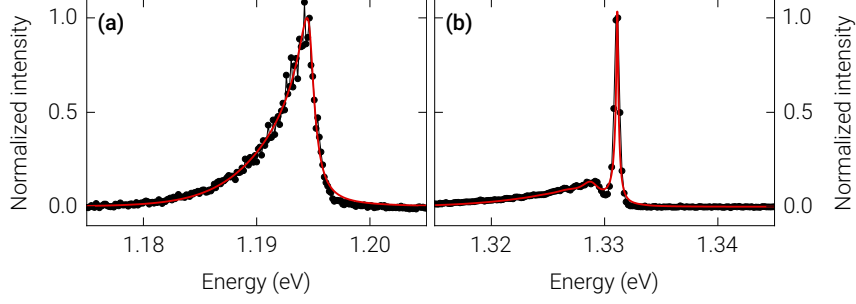


**Figure 4.1:** Fits of extended independent boson models to cryogenic PL spectra of CNTs. **(a)** Asymmetric spectrum with an FWHM of  $\sim 3$  meV (black data points) reproduced by a fit using the form factor  $F_0$  for confined excitons (solid red line) using the parameters  $T = 4.1$  K,  $D = 13.0$  eV, and  $\sigma = 3.2$  nm. **(b)** Spectrum featuring a narrow central peak with an FWHM of  $\sim 50$   $\mu$ eV and a lower-energy wing separated by a pronounced gap (black data points) reproduced by a fit using the form factor  $F_a$  for a barrier of finite length (solid red line) using the parameters  $T = 8.7$  K,  $D = 15.4$  eV,  $\sigma = 2.4$  nm,  $\hbar\omega_c = 1.3$  meV, and  $a = 37$  nm.

above cannot account for such line shapes, however, since the coupling to a reservoir of acoustic phonons always includes arbitrarily small corrections to the exciton energy and therefore does not allow for a gap in the PL spectrum.

VIALLA et al. [70] extended this model by including a suppression of the coupling to the lowest-energy phonons. The reduction of this coupling removes the smallest energy corrections to the exciton emission energy and would therefore result in a spectral gap that matches the shape of the PL spectra observed experimentally. Physically, the reduced coupling can be implemented by assuming an acoustic barrier that prevents the free propagation of low-energy phonons due to mechanical clamping of the CNT to the substrate [70, 223, p. 243]. In the mathematical formulation presented above, this modification gives rise to a different exciton form factor  $F(q)$ . For the case of a symmetric barrier of length  $a$  around the exciton location that suppresses phonons below a threshold frequency  $\omega_c$ , the form factor  $F_a(q)$  evaluates to [70]

$$F_a(q) = F_0(\tilde{\omega}(q)/v) \cdot \left( 1 + \frac{\omega_c^2 \sin^2(a\tilde{\omega}(q)/2v)}{\tilde{\omega}(q)^2} \right)^{-1/2}, \quad (4.6)$$

where  $\tilde{\omega}(q)$  is the complex number  $\tilde{\omega}(q) = \sqrt{\omega(q)^2 - \omega_c^2}$ . The fit of this model in Fig. 4.1 (b) (solid red line) was obtained by using the parameters  $T = 8.7$  K,  $D = 15.4$  eV,  $\sigma = 2.4$  nm,  $\hbar\omega_c = 1.3$  meV, and  $a = 37$  nm and well reproduces the data. Note that the values for  $D$  and  $\sigma$  are similar to the values used for the fit in Fig. 4.1 (a).

While the agreement between model and data in Figs. 4.1 (a)–(b) is compelling, there remains a discrepancy regarding the value of the exciton deformation potential coupling  $D$ . The values used for the fits in Figs. 4.1 (a)–(b) and in [70, 227] lie in the range  $D = 12$ – $16$  eV

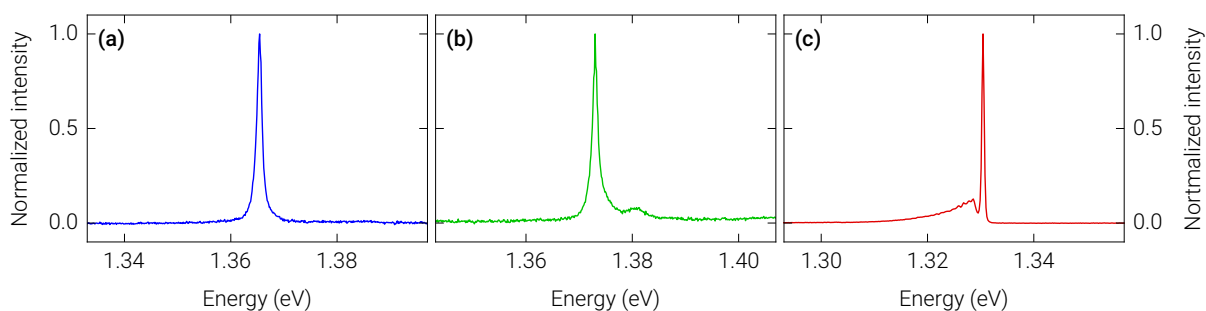


**Figure 4.2.:** Cryogenic spectra of individual CNTs with (a) DOC, (b) DNA, and (c) PFO surfactant wrapping. Graphics (a) and (c) are reproduced from [P1], graphic (b) is reproduced from [241].

that agrees well with reported *electron* deformation potential couplings of  $D = 14\text{ eV}$  in CNTs [240]. For excitons, however, the hole contribution to the deformation potential coupling is expected to cancel the electron contribution, resulting in a significantly smaller coupling constant  $D = \sim 1.5\text{ eV}$  that is mediated via the carbon-carbon bond-length change [223, p. 244, 228]. With this reduced deformation potential coupling, however, the fit quality of the independent-boson model cannot be maintained.

One possible resolution of this discrepancy could be given by a modification of the deformation potential coupling constant for excitons in a localization potential as proposed in [223, p. 244]. Another possible scenario is the dominance of an alternative coupling mechanism, other than the deformation potential coupling to the one-dimensional CNT phonon bath. One candidate for such couplings is promoted by the observation that localized excitons in CNTs exhibit permanent electric dipole moments as large as  $0.7\text{ e}\text{\AA}$  [38]. This exciton dipole moment was shown to provide an efficient interaction mechanism with microscopic charge fluctuations in the CNT environment [P6]. Similarly, dipolar Fröhlich interactions with phonons in polar materials [231, 232, 233, pp. 133–135] or Holstein-like couplings to molecular vibrations [234, 235, 236, pp. 38–43] appear plausible.

Since the CNT lattice only consists of a single atomic species, however, any polar coupling to CNT lattice vibrations is expected to be very small. Efficient dipolar interactions of localized CNT excitons therefore require the presence of external vibrational degrees of freedom. Figs. 4.2 (a)–(c) compare the spectra of three cryogenic CNTs that were prepared to be wrapped by three different surfactants, while all other experimental parameters were kept identical. Fig. 4.2 (a) shows the symmetric PL peak with  $1.1\text{ meV}$  FWHM of a CNT with sodium deoxycholate (DOC) surfactant. The spectrum of a CNT with deoxyribonucleic acid (DNA) surfactant in Fig. 4.2 (b) also features a dominant symmetric peak with  $1.2\text{ meV}$  FWHM, but additionally exhibits a weaker secondary peak. Spectra of other CNTs with DNA wrapping occasionally showed an even higher peak multiplicity with several weak secondary peaks [241]. Finally, the spectrum of a CNT with poly[9,9-dioctylfluorenyl-2,7-diyl]

(PFO) wrapping in Fig. 4.2 (c) features a significantly narrower central peak with  $\sim 450 \mu\text{eV}$  FWHM and a lower-energy wing that is separated from the central peak by an energy gap of  $\Delta E = 1.8 \text{ meV}$ .

The different line shapes in Figs. 4.2 (a)–(c) suggest a significant influence of the CNT environment on their spectral response. This line of reasoning is in contrast to the extended independent boson model discussed above, where only internal degrees of freedom in the form of CNT phonons are considered. While environmental effects should be negligible for pristine samples, this limit is presumably reached only rarely for the case of CNTs. Many studies of CNTs are performed on chirality purified samples that require a wet-chemical treatment [195–199]. By consequence, unintentional surface contamination of CNTs appears plausible as a residue of such preparation steps. Also the observation of narrow and stable lines for highest-purity CNTs that are freely suspended [67, 72] or located on electrostatically calm substrates [P6] is compatible with this picture. In this chapter we therefore investigate possible implications of dipolar couplings between localized excitons in CNTs and their surfactant wrappings.

### 4.3. Quantum-mechanical description of exciton-vibron interactions in carbon nanotubes

This section presents a quantum-mechanical model for the dipolar coupling between localized excitons in CNTs and vibrational degrees of freedom. While the framework is valid also for Fröhlich interactions with polar phonons, the focus lies on Holstein-like couplings to molecular vibrations of CNT surfactants. The total Hamiltonian for the interacting system of a localized exciton in a CNT, molecular vibrations (vibrons) in a surfactant molecule and the photon field can be written as

$$\hat{H} = \hat{H}_{\text{exc}} + \hat{H}_{\text{ph}} + \hat{H}_{\text{vib}} + \hat{H}_{\text{exc-ph}} + \hat{H}_{\text{exc-vib}}, \quad (4.7)$$

where  $\hat{H}_{\text{exc}}$ ,  $\hat{H}_{\text{ph}}$ , and  $\hat{H}_{\text{vib}}$  are the exciton, photon, and vibron contributions to the total energy and  $\hat{H}_{\text{exc-ph}}$  and  $\hat{H}_{\text{exc-vib}}$  describe the exciton-photon and the dipolar exciton-vibron interaction, respectively. The exciton-photon contribution can be written as [242, 243]

$$\hat{H}_{\text{exc}} = \sum_{\mathbf{K}} E_{\mathbf{K}} \cdot \hat{b}_{\mathbf{K}}^{\dagger} \hat{b}_{\mathbf{K}}, \quad (4.8)$$

$$\hat{H}_{\text{ph}} = \sum_{\mathbf{k}} \hbar \omega_{\mathbf{k}} \cdot \left( \hat{a}_{\mathbf{k}}^{\dagger} \hat{a}_{\mathbf{k}} + \frac{1}{2} \right), \quad (4.9)$$

$$\begin{aligned} \hat{H}_{\text{exc-ph}} &= i \sum_{\mathbf{k}, \mathbf{K}} C_{\mathbf{k}} \cdot \left( \hat{a}_{\mathbf{k}} + \hat{a}_{-\mathbf{k}}^{\dagger} \right) \left( \hat{b}_{-\mathbf{K}} - \hat{b}_{\mathbf{K}}^{\dagger} \right) \cdot \delta(\mathbf{k} - \mathbf{K}) = \\ &= i \sum_{\mathbf{k}} C_{\mathbf{k}} \cdot \left( \hat{a}_{\mathbf{k}} + \hat{a}_{-\mathbf{k}}^{\dagger} \right) \left( \hat{b}_{-\mathbf{k}} - \hat{b}_{\mathbf{k}}^{\dagger} \right). \end{aligned} \quad (4.10)$$

Here,  $\hat{b}_{\mathbf{K}}^\dagger$  and  $\hat{b}_{\mathbf{K}}$  are the creation and annihilation operators for an exciton with wave vector  $\mathbf{K}$  and energy  $E_{\mathbf{K}}$ . Similarly,  $\hat{a}_{\mathbf{k}}^\dagger$  and  $\hat{a}_{\mathbf{k}}$  are the creation and annihilation operators for a photon with wave vector  $\mathbf{k}$  and energy  $\hbar\omega_{\mathbf{k}}$ . Finally,  $C_{\mathbf{k}}$  is the exciton-photon coupling constant at wave vector  $\mathbf{k}$ . Note that for simplicity, the possibility to observe excitons in different bands or photons of different polarization has been disregarded in this description.

Due to the concentration of the density of states at the **Van Hove singularities (VHSs)** (cf. **Section 2.3**), the simplifying assumption  $E_{\mathbf{K}} \approx E_{\text{exc}} = \text{const.}$  may be made, where  $E_{\text{exc}}$  is the energy of the  $E_{11}$  excitonic transition. To find the value of  $C_{\mathbf{k}}$ , the discussion is limited to the special case relevant for localized excitons, where either a single exciton or no exciton can be present. This scenario can be formulated by assuming Fermionic creation and annihilation operators  $\hat{b}_{\mathbf{K}}^\dagger = |e\rangle\langle g|$  and  $\hat{b}_{\mathbf{K}} = |g\rangle\langle e|$ , where  $|g\rangle$  denotes the excitonic ground state (no exciton present) and  $|e\rangle$  denotes the excitonic excited state (one exciton present).

Consider the initial state  $|i\rangle = |e, 0\rangle$  comprising one exciton but no photon and the final state  $|f\rangle = |g, 1\rangle$  comprising one photon with appropriate wave vector  $\mathbf{k}$  but no exciton. The coupling constant  $C_{\mathbf{k}}$  can then be expressed by the oscillator strength per sample volume,  $f_{|e\rangle \rightarrow |g\rangle} / V$ , as [244]

$$C_{\mathbf{k}} = \hbar \sqrt{\frac{e^2}{2\varepsilon_0 m_e} \cdot \frac{f_{|e\rangle \rightarrow |g\rangle}}{V}}, \quad (4.11)$$

where  $e$  is the elementary charge,  $\varepsilon_0$  is the vacuum permittivity, and  $m_e$  is the free electron mass. One can use the transition dipole moment  $\langle g|\hat{\mathbf{r}}|e\rangle$  to write  $f_{|e\rangle \rightarrow |g\rangle}$  as

$$f_{|e\rangle \rightarrow |g\rangle} = \frac{2m_e\omega_{\text{exc}}}{3\hbar} \cdot |\langle g|\hat{\mathbf{r}}|e\rangle|^2, \quad (4.12)$$

where  $\hat{\mathbf{r}}$  is the position operator and  $E_{\text{exc}} = \hbar\omega_{\text{exc}}$  is the energy of a photon emitted by the decay of an exciton with energy  $E_{\mathbf{K}} \approx E_{\text{exc}}$  [245]. Using the density of photon states of a given polarization in volume  $V$  [171, pp. 330–332],

$$g(\omega) = \frac{V\omega^2}{2\pi^2 c^3}, \quad (4.13)$$

where  $\omega$  is the angular frequency and  $c$  is the speed of light, the transition rate  $\Gamma_{|i\rangle \rightarrow |f\rangle}$  from initial state  $|i\rangle$  to final state  $|f\rangle$  can be calculated with Fermi's golden rule.

$$\begin{aligned} \Gamma_{|i\rangle \rightarrow |f\rangle} &= \frac{2\pi}{\hbar} |\langle f|\hat{H}_{\text{exc-ph}}|i\rangle|^2 \cdot g(E_{\text{exc}}) = \\ &= \frac{2\pi}{\hbar} \cdot |C_{\mathbf{k}}|^2 \cdot g(\omega_{\text{exc}}) \frac{d\omega}{dE} = \\ &= \frac{2\pi}{\hbar} \cdot \hbar^2 \frac{e^2}{2\varepsilon_0 m_e} \cdot \frac{f_{|e\rangle \rightarrow |g\rangle}}{V} \cdot \frac{V\omega_{\text{exc}}^2}{2\pi^2 \hbar c^3} = \end{aligned}$$

$$\begin{aligned}
 &= \pi \hbar \cdot \frac{e^2}{\epsilon_0 m_e} \cdot \frac{2m_e \omega_{\text{exc}}}{3\hbar} \cdot |\langle g | \hat{\mathbf{r}} | e \rangle|^2 \cdot \frac{\omega_{\text{exc}}^2}{2\pi^2 \hbar c^3} = \\
 &= \frac{e^2 \omega_{\text{exc}}^3}{3\pi \epsilon_0 \hbar c^3} \cdot |\langle g | \hat{\mathbf{r}} | e \rangle|^2
 \end{aligned} \tag{4.14}$$

The result in the last line is just the Einstein  $A$  coefficient [245] that denotes the rate of spontaneous emission from the initial state  $|i\rangle = |e, 0\rangle$ , connecting the value of  $C_{\mathbf{k}}$  to the theory of optical transitions in atoms and molecules.

To find expressions for  $\hat{H}_{\text{vib}}$  and  $\hat{H}_{\text{exc-vib}}$  we follow the discussion of molecular vibrations in [236]. Consider a molecule performing a vibration that is given by the temporal evolution of the displacements  $\Delta x_1, \Delta y_1, \Delta z_1, \dots, \Delta x_N, \Delta y_N, \Delta z_N$  from the rest position of its  $N$  constituting atoms in Cartesian coordinates. When the respective masses of these atoms are denoted by  $m_1, m_2, \dots, m_N$ , the classical kinetic energy  $T_{\text{vib}}$  of this vibration can be calculated as [236, p. 14]

$$T_{\text{vib}} = \frac{1}{2} \sum_{\alpha=1}^N m_{\alpha} \left[ \left( \frac{d\Delta x_{\alpha}}{dt} \right)^2 + \left( \frac{d\Delta y_{\alpha}}{dt} \right)^2 + \left( \frac{d\Delta z_{\alpha}}{dt} \right)^2 \right]. \tag{4.15}$$

By introducing a new set of coordinates  $q_1, q_2, \dots, q_{3N}$  given by

$$\begin{aligned}
 q_1 &= \sqrt{m_1} \Delta x_1, & q_2 &= \sqrt{m_1} \Delta y_1, & q_3 &= \sqrt{m_1} \Delta z_1, \\
 q_4 &= \sqrt{m_2} \Delta x_2, & q_5 &= \sqrt{m_2} \Delta y_2, & q_6 &= \sqrt{m_2} \Delta z_2, & \dots
 \end{aligned} \tag{4.16}$$

the expression for the kinetic energy simplifies to [236, p. 14]

$$T_{\text{vib}} = \frac{1}{2} \sum_{i=1}^{3N} \dot{q}_i^2. \tag{4.17}$$

In this set of coordinates the expression for the potential energy due to the distortion of the molecule from its relaxed geometry is given by [236, p. 15]

$$V_{\text{vib}} = \frac{1}{2} \sum_{i,j=1}^{3N} f_{ij} q_i q_j \quad \text{with} \quad f_{ij} = \left( \frac{\partial^2 V_{\text{vib}}}{\partial q_i \partial q_j} \right)_0. \tag{4.18}$$

While this representation is generally not diagonal, i. e.  $f_{ij} \neq 0$  for  $i \neq j$ , there exists an orthogonal transformation, i. e. an orthogonal matrix  $(l_{ni})_{ni}$  of real numbers and a transformed set of coordinates  $Q_1, Q_2, \dots, Q_N$  given by

$$Q_n = \sum_{i=1}^{3N} l_{ni} q_i \quad \text{for} \quad n = 1, 2, \dots, 3N, \tag{4.19}$$

such that both the kinetic and the potential energy attain diagonal forms that are given by [236, p. 20]

$$T_{\text{vib}} = \frac{1}{2} \sum_{n=1}^{3N} \dot{Q}_n^2 \quad \text{and} \quad V_{\text{vib}} = \frac{1}{2} \sum_{n=1}^{3N} \Omega_n^2 Q_n^2 \quad \text{with} \quad \Omega_n^2 = \left( \frac{\partial^2 V_{\text{vib}}}{\partial Q_n^2} \right)_0. \quad (4.20)$$

The set of coordinates  $Q_1, Q_2, \dots, Q_{3N}$  is called *normal coordinates* [236, pp. 19–20] and will be used exclusively in the following. The result in Eq. (4.20) can be interpreted as an effective decoupling of the molecular vibration into  $3N$  independent classical harmonic oscillators, the *normal modes* of the molecular vibration, corresponding to independent oscillations along the normal coordinates  $Q_1, Q_2, \dots, Q_{3N}$  with respective angular frequencies  $\Omega_1, \Omega_2, \dots, \Omega_{3N}$ . This decoupling translates into the quantum mechanical description, where  $\hat{H}_{\text{vib}}$  can be written as an independent sum of quantum harmonic oscillators,

$$\hat{H}_{\text{vib}} = \sum_{n=1}^{3N} \hbar \Omega_n \cdot \left( \hat{c}_n^\dagger \hat{c}_n + \frac{1}{2} \right). \quad (4.21)$$

Here  $\hat{c}_n^\dagger$  and  $\hat{c}_n$  are the creation and annihilation operators for a vibron in normal mode  $n$  with energy  $\hbar \Omega_n$  corresponding to a molecular vibration along normal coordinate  $Q_n$ .

To derive the dipolar interaction Hamiltonian  $\hat{H}_{\text{exc-vib}}$ , consider the classical electric field at point  $\mathbf{r}$  induced by an exciton at the origin with dipole moment  $\mathbf{p}_{\text{exc}}$  [246, p. 147],

$$\mathbf{F}_{\text{exc}}(\mathbf{r}) = \frac{1}{4\pi\epsilon_0} \cdot \frac{3(\mathbf{p}_{\text{exc}} \cdot \mathbf{e}_r)\mathbf{e}_r - \mathbf{p}_{\text{exc}}}{|\mathbf{r}|^3}, \quad (4.22)$$

where  $\mathbf{e}_r$  is a unit vector pointing towards  $\mathbf{r}$ . Molecular vibrations are generally accompanied by a relative displacement of charges due to the different electron affinities of the constituting atoms [236, pp. 38–43]. By consequence, a vibration along normal coordinate  $Q_n$  induces a dynamic molecular dipole moment

$$\mathbf{p}_n = \frac{\partial}{\partial Q_n} \boldsymbol{\mu}(\mathbf{Q}) \cdot Q_n = \partial_{Q_n} \boldsymbol{\mu}(\mathbf{Q}) \cdot Q_n, \quad (4.23)$$

where  $\boldsymbol{\mu}(\mathbf{Q})$  is the molecular electric dipole moment as a function of the displacement from the relaxed geometry in normal coordinates. Similarly, a superposition of vibrations in different normal modes induces the dipole moment

$$\mathbf{p}_{\text{vib}} = \sum_{n=1}^{3N} \partial_{Q_n} \boldsymbol{\mu}(\mathbf{Q}) \cdot Q_n \quad (4.24)$$

and the potential energy of the molecular dipole  $\mathbf{p}_{\text{vib}}$  in the electric field  $\mathbf{F}_{\text{exc}}(\mathbf{r})$  evaluates to

$$E_{\text{exc-vib}} = -\mathbf{p}_{\text{vib}} \cdot \mathbf{F}_{\text{exc}}(\mathbf{r}) = \sum_{n=1}^{3N} \frac{\partial_{Q_n} \boldsymbol{\mu}}{4\pi\epsilon_0} \cdot \frac{\mathbf{p}_{\text{exc}} - 3(\mathbf{p}_{\text{exc}} \cdot \mathbf{e}_r)\mathbf{e}_r}{|\mathbf{r}|^3} \cdot Q_n. \quad (4.25)$$

By quantization of the normal coordinates  $Q_1, Q_2, \dots, Q_{3N}$  we finally obtain an expression for the dipolar interaction Hamiltonian,

$$\hat{H}_{\text{exc-vib}} = \sum_{\mathbf{K}} \sum_{n=1}^{3N} \frac{\partial_{Q_n} \boldsymbol{\mu}}{4\pi\epsilon_0} \cdot \frac{\mathbf{p}_{\text{exc}} - 3(\mathbf{p}_{\text{exc}} \cdot \mathbf{e}_{\mathbf{r}}) \mathbf{e}_{\mathbf{r}}}{|\mathbf{r}|^3} \cdot \hat{b}_{\mathbf{K}}^\dagger \hat{b}_{\mathbf{K}} \cdot \hat{Q}_n, \quad (4.26)$$

where the introduction of the exciton number operator  $\hat{b}_{\mathbf{K}}^\dagger \hat{b}_{\mathbf{K}}$  indicates that the coupling is only effective in the presence of an exciton. Note that  $\mathbf{p}_{\text{exc}}$ ,  $\mathbf{r}$  and  $\partial_{Q_n} \boldsymbol{\mu}$  are not quantized in this description. We proceed by expressing the normal coordinate operators  $\hat{Q}_n$  in terms of the creation and annihilation operators  $\hat{c}_n^\dagger$  and  $\hat{c}_n$  for a vibron in normal mode  $n$  as

$$\hat{Q}_n = \sqrt{\frac{\hbar}{2\Omega_n}} \cdot (\hat{c}_n^\dagger + \hat{c}_n) \quad \text{for } n = 1, 2, \dots, 3N. \quad (4.27)$$

A factor of  $1/\sqrt{m}$  usually present in the definition of the quantum harmonic oscillator ladder operators was omitted here in accordance with Eq. (4.16). With this definition we arrive at a Holstein-like second quantized form of  $\hat{H}_{\text{exc-vib}}$  [234, 235],

$$\begin{aligned} \hat{H}_{\text{exc-vib}} &= \sum_{\mathbf{K}} \sum_{n=1}^{3N} \sqrt{\frac{\hbar}{2\Omega_n}} \cdot \frac{\partial_{Q_n} \boldsymbol{\mu}}{4\pi\epsilon_0} \cdot \frac{\mathbf{p}_{\text{exc}} - 3(\mathbf{p}_{\text{exc}} \cdot \mathbf{e}_{\mathbf{r}}) \mathbf{e}_{\mathbf{r}}}{|\mathbf{r}|^3} \cdot \hat{b}_{\mathbf{K}}^\dagger \hat{b}_{\mathbf{K}} \cdot (\hat{c}_n^\dagger + \hat{c}_n) \\ &= \sum_{\mathbf{K}} \sum_{n=1}^{3N} D_n \cdot \hat{b}_{\mathbf{K}}^\dagger \hat{b}_{\mathbf{K}} \cdot (\hat{c}_n^\dagger + \hat{c}_n). \end{aligned} \quad (4.28)$$

For the interpretation of PL spectra, the intensity ratio of the vibronic sidebands to the zero phonon line (ZPL), i. e. the spectral line originating from light emitted without coupling to the vibrational degrees of freedom, is of particular interest. The photon emission rate for the ZPL has already been calculated using Fermi's golden rule in Eq. (4.14) and is given by

$$\Gamma_{\text{ZPL}} = \frac{e^2 \omega_{\text{exc}}^3}{3\pi\epsilon_0 \hbar c^3} \cdot |\langle g | \hat{\mathbf{r}} | e \rangle|^2. \quad (4.29)$$

Similarly, consider a second-order process, where an exciton in the CNT first excites a vibron via dipolar coupling and then decays into a photon. The initial state  $|i\rangle = |e, 0_{\text{ph}}, 0_{\text{vib}}\rangle$  for this process comprises one exciton, zero photons and zero vibrons. The system then transfers to the transient state  $|t_n\rangle = |e, 0_{\text{ph}}, 1_n\rangle$  with one exciton, zero photons and one vibron in normal mode  $n$ . Finally, the exciton decays to the final state  $|f_n\rangle = |g, 1_{\mathbf{k}}, 1_n\rangle$  comprising zero excitons, one photon of wave vector  $\mathbf{k}$  and one vibron in normal mode  $n$ .

To calculate the corresponding photon emission rate, we use the generalization of Fermi's golden rule to second-order order transitions [233, pp. 395–398] from an initial state  $|i\rangle$  to a final state  $|f\rangle$ ,

$$\Gamma = \frac{2\pi}{\hbar} \left| \sum_{|t\rangle} \frac{\langle f | \hat{H} | t \rangle \langle t | \hat{H} | i \rangle}{E_i - E_t} \right|^2 g(E_f) \cdot \delta(E_i - E_f), \quad (4.30)$$

where the sum runs over all possible transient states  $|t\rangle$  with corresponding energies  $E_t$  and the delta function  $\delta(E_i - E_f)$  enforces conservation of energy by requiring the same initial and final energies  $E_i$  and  $E_f$ . In the case of a PL spectrum with a vibronic sideband the intermediate state  $|t\rangle$  is fixed, since the different vibronic modes are spectrally resolved and therefore distinguishable. To calculate the transition rate  $\Gamma_{S,n}$  for a Stokes sideband photon [247] after generation of a vibron in mode  $n$ , the summation is therefore omitted.

$$\begin{aligned}
 \Gamma_{S,n} &= \frac{2\pi}{\hbar} \left| \frac{\langle f_n | \hat{H} | t_n \rangle \langle t_n | \hat{H} | i \rangle}{E_i - E_t} \right|^2 g(E_f) \cdot \delta(E_i - E_f) = \\
 &= \frac{2\pi}{\hbar} \left| \frac{\langle g, \mathbf{1}_k, 1_n | \hat{H}_{\text{exc-ph}} | e, 0_{\text{ph}}, 1_n \rangle \langle e, 0_{\text{ph}}, 1_n | \hat{H}_{\text{exc-vib}} | e, 0_{\text{ph}}, 0_{\text{vib}} \rangle}{E_{\text{exc}} - (E_{\text{exc}} + \hbar\Omega_n)} \right|^2 g(\omega_{\mathbf{k}}) \frac{d\omega}{dE} \cdot \\
 &\quad \cdot \delta(E_{\text{exc}} - (\hbar\omega_{\mathbf{k}} + \hbar\Omega_n)) = \\
 &= \frac{2\pi}{\hbar} \left| \frac{C_{\mathbf{k}} \cdot D_n}{\hbar\Omega_n} \right|^2 \frac{V\omega_{\mathbf{k}}^2}{2\pi^2\hbar c^3} \cdot \delta(\hbar\omega_{\mathbf{k}} - (E_{\text{exc}} - \hbar\Omega_n)) = \\
 &= \frac{V\omega_{\mathbf{k}}^2}{\pi\hbar^4\Omega_n^2 c^3} \left| \hbar \sqrt{\frac{e^2}{2\varepsilon_0 m_e} \cdot \frac{2m_e\omega_{\mathbf{k}}}{3V\hbar}} |\langle g | \hat{\mathbf{r}} | e \rangle|^2 \cdot \sqrt{\frac{\hbar}{2\Omega_n}} \cdot \frac{\partial_{Q_n} \boldsymbol{\mu}}{4\pi\varepsilon_0} \cdot \frac{\mathbf{p}_{\text{exc}} - 3(\mathbf{p}_{\text{exc}} \cdot \mathbf{e}_{\mathbf{r}}) \mathbf{e}_{\mathbf{r}}}{|\mathbf{r}|^3}} \right|^2 \cdot \\
 &\quad \cdot \delta(\hbar\omega_{\mathbf{k}} - (E_{\text{exc}} - \hbar\Omega_n)) = \\
 &= \frac{e^2\omega_{\mathbf{k}}^3}{3\pi\varepsilon_0\hbar c^3} \cdot |\langle g | \hat{\mathbf{r}} | e \rangle|^2 \cdot \frac{1}{2\hbar\Omega_n^3} \left| \frac{\partial_{Q_n} \boldsymbol{\mu}}{4\pi\varepsilon_0} \cdot \frac{\mathbf{p}_{\text{exc}} - 3(\mathbf{p}_{\text{exc}} \cdot \mathbf{e}_{\mathbf{r}}) \mathbf{e}_{\mathbf{r}}}{|\mathbf{r}|^3} \right|^2 \delta(\hbar\omega_{\mathbf{k}} - (E_{\text{exc}} - \hbar\Omega_n)) \quad (4.31)
 \end{aligned}$$

As one might expect, the photon energy has to satisfy  $\hbar\omega_{\mathbf{k}} = E_{\text{exc}} - \hbar\Omega_n$  to fulfill the conservation of energy imposed by the delta function. Using the approximation  $\omega_{\mathbf{k}}/\omega_{\text{exc}} \approx 1$  the intensity ratio  $I_{S,n}/I_{\text{ZPL}}$  can be calculated as

$$I_{S,n}/I_{\text{ZPL}} = \Gamma_{S,n}/\Gamma_{\text{ZPL}} \approx \frac{1}{2\hbar\Omega_n^3} \left| \frac{\partial_{Q_n} \boldsymbol{\mu}}{4\pi\varepsilon_0} \cdot \frac{\mathbf{p}_{\text{exc}} - 3(\mathbf{p}_{\text{exc}} \cdot \mathbf{e}_{\mathbf{r}}) \mathbf{e}_{\mathbf{r}}}{|\mathbf{r}|^3} \right|^2. \quad (4.32)$$

Note that in spite of the term  $1/\Omega_n^3$  in Eq. (4.32), generally a dependence  $1/\Omega_n^2$  can be expected for the intensity ratio  $I_{S,n}/I_{\text{ZPL}}$ , since the dynamic molecular dipole moment scales like

$$\mathbf{p}_n = \partial_{Q_n} \boldsymbol{\mu} \cdot Q_n \propto \partial_{Q_n} \boldsymbol{\mu} \cdot \sqrt{\frac{\hbar}{2\Omega_n}}, \quad (4.33)$$

i. e.  $|\partial_{Q_n} \boldsymbol{\mu}|^2$  cancels one factor  $1/\Omega_n$ . By consequence, a quadratic suppression of the vibron sideband for increasing energy difference to the ZPL can be expected.

## 4.4. Spectral signatures of exciton-vibron interactions in polymer-decorated carbon nanotubes

To study effects of polymer wrapping on the spectral lineshape of CNTs, we compared the cryogenic PL of chirality-purified (9,1)-CNTs with either DOC or PFO surfactant. To exclude that spectral differences stem from details of the sample preparation and sorting procedure, we performed surfactant substitution on parts of the DOC-wrapped CNT sample (cf. Section 3.2 for details). Figs. 4.3 (a) and (b) compare the cryogenic PL spectra of the CNTs with DOC and PFO surfactant from Figs. 4.2 (a) and (c) in Section 4.2, respectively. The DOC-wrapped CNT in Fig. 4.3 (a) featured a symmetric emission profile with an FWHM of 1.2 meV obtained from a Lorentzian fit. By contrast, the PL spectrum of the CNT with PFO surfactant in Fig. 4.3 (b) shows a significantly narrower central peak with an FWHM of  $\sim 450 \mu\text{eV}$  and a pronounced lower-energy wing that is separated from the central peak by an energy gap  $\Delta E$  of 1.8 meV. The inset in Fig. 4.3 (b) illustrates that the value of  $\Delta E$  is distributed around 1.7 meV for all observed CNTs with PFO surfactant.

Comparing the FWHM of the central emission peak for CNTs with DOC and PFO surfactant, respectively, reveals a significant difference also at the statistical level. For the sample with DOC-wrapped CNTs, the FWHM scattered between 1 meV and 5 meV (top row in Fig. 4.3 (c)), while PFO-wrapped CNTs from the sample with substituted surfactant consistently exhibited an FWHM below 1 meV (red data in bottom row of Fig. 4.3 (c)). In the latter sample, a small number of CNTs featured emission profiles similar to Fig. 4.3 (a) and were interpreted as emitters where the surfactant exchange was unsuccessful. The FWHM of these CNTs is shown as blue data in the bottom row of Fig. 4.3 (c) and falls between 1 meV and 5 meV consistent with the data for DOC-wrapped CNTs in the top row of Fig. 4.3 (c).

To establish that these contrasting spectral signatures do not originate from different optically active states like in Chapter 5, we also compared the emission energy of the central PL peaks for CNTs with DOC (top row in Fig. 4.3 (d)) and PFO (bottom row in Fig. 4.3 (d)) surfactant, respectively. While the respective means of the PL peak energies of 1.371 eV for DOC and 1.377 eV for PFO are significantly different, we illustrate that both are compatible with the expected  $E_{11}$  exciton energies under moderate amounts of mechanical strain on the CNT lattice and modifications of the dielectric environment.

In a room-temperature absorption measurement of (9,1)-CNTs with DOC surfactant in aqueous solution (data not shown), we identified the  $E_{11}$  peak at 1.354 eV in good agreement with the reported  $E_{11}$  energy of 1.359 eV for (9,1)-CNTs with sodium dodecyl sulfate (SDS) wrapping [33, 35]. Since the latter value was reported both for aqueous solution in [35] and for solution in heavy water in [33], corresponding to refractive indices of 1.333 and 1.328 for the solvent, we assume that the dielectric environment of wrapped CNTs is predominantly governed by the refractive index of the surfactant and less by that of the solvent.

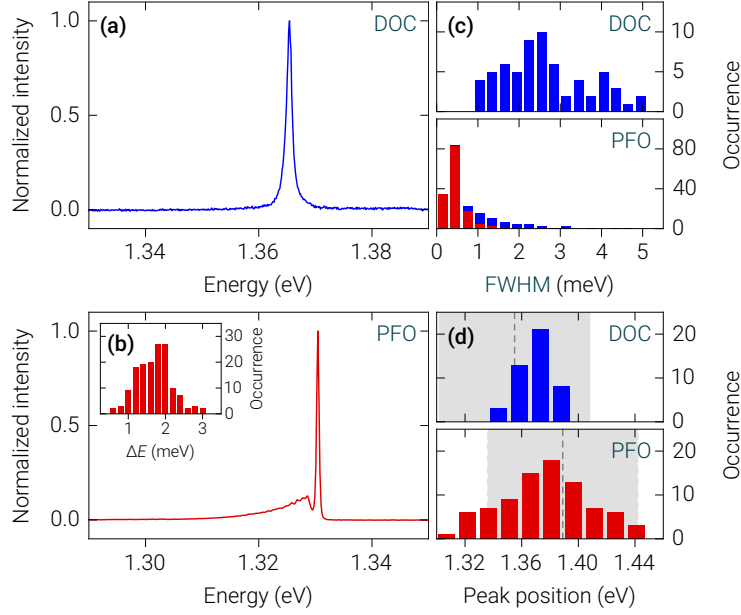


**Figure 4.3.:** Spectral signatures of CNTs with DOC and PFO surfactant. **(a)** Cryogenic PL spectrum of a DOC-wrapped CNT featuring a symmetric emission profile. **(b)** Cryogenic PL spectrum of a PFO-wrapped CNT featuring a narrow central emission peak and a lower-energy wing separated by an energy gap  $\Delta E$ . The inset illustrates that the value of  $\Delta E$  for different CNTs is distributed around 1.7 meV. **(c)** Histograms of FWHMs for the central PL peaks of DOC-wrapped (blue) and PFO-wrapped (red) CNTs, respectively, for the CNTs samples before (top row) and after (bottom row) surfactant substitution of PFO for DOC, respectively. **(d)** Histograms of emission energies for the central PL peaks of DOC-wrapped (blue) and PFO-wrapped (red) CNTs, respectively. The dashed vertical lines show the calculated emission energies at 1.355 eV and 1.389 eV, respectively, while the gray shaded areas highlight the spread of  $E_{11}$  energies consistent with at most 1% mechanical strain. Graphics (a)–(d) are reproduced from [P1].

Using a refractive index of 1.540 for DOC [248], the analytic formula from [139], and the scaling relation from [143], we calculate an exciton binding energy for DOC-wrapped (9, 1)-CNTs of 1.110 eV and obtain a renormalized single-particle band gap of 2.464 eV at room temperature (cf. Section 2.4). Upon cooldown to cryogenic temperatures the band gap is expected to blue-shift by 6.2 meV [144], while a realignment of H<sub>2</sub>O dipoles inside the CNT is predicted to cause a red-shift of about 5 meV [249]. Disregarding any modifications due to a change in dielectric environment or due to mechanical strain, we therefore expect a single-particle band gap of 2.465 eV at cryogenic temperatures and an  $E_{11}$  emission energy of 1.355 eV. Similarly, we assume a refractive index of 1.575 for PFO [250, 251] and obtain an exciton binding energy of 1.076 eV. Together with the previously calculated cryogenic single-particle band gap of 2.465 eV we find a value of 1.389 eV for the  $E_{11}$  emission of cryogenic PFO-wrapped CNTs.

In Fig. 4.3 (d) the observed deviations from these values are at most 35 meV for DOC and 68 meV for PFO surfactant and can be readily explained by the hitherto disregarded influence of mechanical strain and change of dielectric environment due to drop-casting of the aqueous solution of wrapped CNTs onto a substrate. Both the  $E_{11}$  dependency of 53 meV per percent mechanical strain [252, 253] and of about 99 meV per 0.1 refractive index change [143] are large enough to capture the observed spread. For reference, the gray shaded areas in Fig. 4.3 (d) highlight the emission energies accessible through a relatively small mechanical strain of 1 %. We conclude that the central PL peak energies are consistent with the properties of the  $E_{11}$  excitonic state for both surfactants. Weak localization of the  $E_{11}$  exciton was confirmed by the observation of photon antibunching (data not shown).

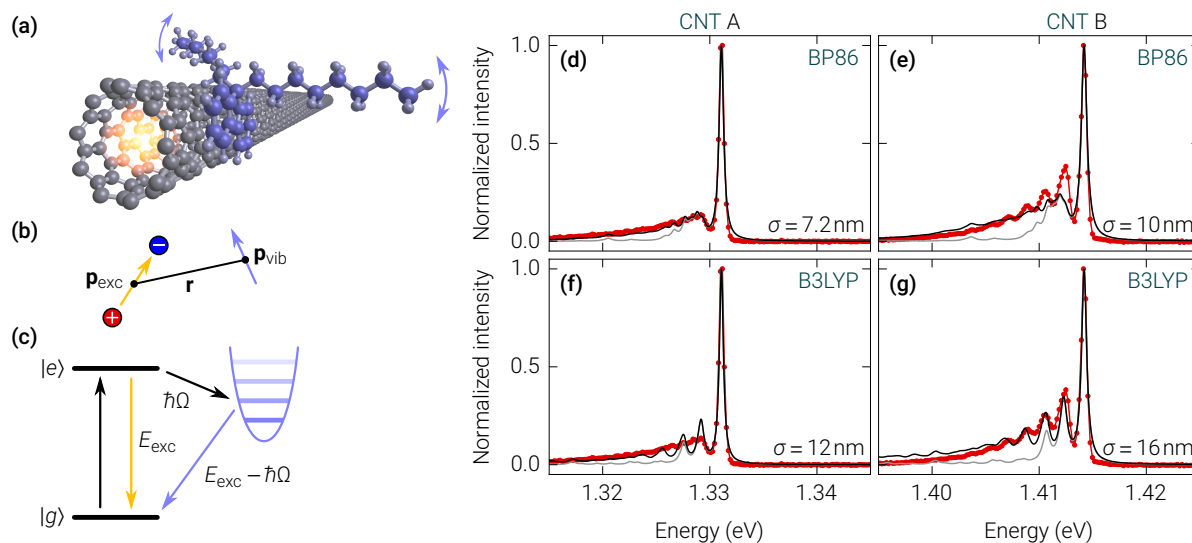
With the PL of the CNTs in Figs. 4.3 (a) and (b), respectively, being attributed to the same excitonic state, we associate the different PL lineshapes with the different surfactants that wrap the corresponding CNTs. This interpretation contrasts the studies discussed in Section 4.2, where phonon modes of the CNT lattice were held responsible for the PL lineshape [70, 227, 229, 230]. Contrary to DOC, surfactant wrapping by PFO is known to form particularly ordered geometries [199, 254–256]. We therefore propose that the symmetric PL peak in Fig. 4.3 (a) originates from inhomogeneous broadening due to coupling to an unordered ensemble of DOC molecules, while the peculiar lower-energy wing in Fig. 4.3 (b) that was observed for all PFO-wrapped CNTs is caused by dipolar interactions with ordered PFO polymers. In the following we focus on the latter case and study the model of exciton-vibron interactions introduced in Section 4.3 for the case of molecular vibrations in PFO.

Fig. 4.4 (a) shows a PFO monomer (blue) close to an exciton (orange) in a (9, 1)-CNT (gray). The relaxed molecular geometry obtained by density functional theory (DFT) respects the presence of van der Waals-like interactions with the CNT that manifest in the bending of the octyl residue protruding to the left. The interaction between the exciton dipole moment  $\mathbf{p}_{\text{exc}}$  and the dynamic molecular dipole  $\mathbf{p}_{\text{vib}}$  that are separated by distance  $\mathbf{r}$  is illustrated in Fig. 4.4 (b). The coupled system of CNT and PFO surfactant, is modeled by the level scheme in Fig. 4.4 (c), where an exciton in the excited state  $|e\rangle$  can decay to the ground state  $|g\rangle$  either directly under emission of a photon with energy  $E_{\text{exc}}$  or in a second order process by generation or absorption of a vibron of energy  $\hbar\Omega$  in the surfactant molecule and emission of a Stokes scattered photon with energy  $E_{\text{exc}} - \hbar\Omega$  or an anti-Stokes scattered photon with energy  $E_{\text{exc}} + \hbar\Omega$ , respectively [247].

Using the results from Section 4.3, the transition rate for the emission of a Stokes (anti-Stokes) photon after generation (absorption) of a vibron of energy  $\hbar\Omega$  can be written as

$$\Gamma \propto \frac{1}{\Omega^2} |\mathbf{p}_{\text{vib}} \cdot \mathbf{F}_{\text{exc}}|^2, \quad (4.34)$$

where  $\mathbf{F}_{\text{exc}}$  is the electric dipole field of the exciton [P6, 38] and  $\mathbf{p}_{\text{vib}}$  is the dynamic molecular dipole moment of the vibron (cf. Section 4.3 for details). The notable  $1/\Omega^2$  dependence in



**Figure 4.4.:** Spectral signatures of exciton-vibron interactions. **(a)** Sketch of an exciton (orange) in a (9,1)-CNT (gray) coupled to a PFO monomer (blue) in relaxed geometry respecting the presence of van der Waals-like interactions. **(b)** Illustration of the interaction between the exciton dipole moment  $\mathbf{p}_{\text{exc}}$  and the dynamic molecular dipole  $\mathbf{p}_{\text{vib}}$ . **(c)** Level-scheme for an excitonic excitation with ground state  $|g\rangle$  and excited state  $|e\rangle$  coupled to a harmonic oscillator of vibrational modes. The exciton energy  $E_{\text{exc}}$  is reduced by  $\hbar\Omega$  upon generation of a vibron with angular frequency  $\Omega$ . **(c)–(g)** Cryogenic PL spectra (red) of two CNTs with weak (left column) and pronounced (right column) oscillations in their lower-energy sidebands, respectively. The simulated spectra include vibron processes up to 1<sup>st</sup> order (gray) and up to 4<sup>th</sup> order (black) and are calculated using the BP86 (top row) and B3LYP (bottom row) functionals, respectively. Graphics (a)–(g) are reproduced from [P1].

this expression provides a simple explanation for the decrease of the lower-energy wing in Fig. 4.3 (b) for increasing energy difference to the central PL peak. While  $F_{\text{exc}}$  can be calculated from quantities reported in literature as illustrated below, the dynamic molecular dipole moment  $\mathbf{p}_{\text{vib}}$  is not readily available and has to be found by other means. To derive this molecular quantity we used DFT simulations employing the BP86 [257–259] or the B3LYP [260, 261] functional.

With both DFT functionals a geometry optimization was performed initially, in order to determine the relaxed molecular geometry of PFO interacting with a CNT (cf. Section A.2 for details). In this geometry, the vibrational normal modes were obtained by diagonalizing the Hessian matrix of the potential energy change with respect to the molecular coordinates. For each normal mode  $n$  of vibration, the dynamic molecular dipole moment  $\partial_{Q_n} \mu$  was calculated from the change in dipole moment between relaxed molecular geometry and a slight displacement along the corresponding normal coordinate.

This general approach was applied to two different scenarios. First, a PFO monomer interacting with a (9,1)-CNT was considered to obtain the vibrational energies and dynamic

molecular dipole moments of the monomer itself. In a second step, also PFO dimers and trimers were investigated to also account for vibrations of the PFO polymer chain, e. g. stretch or breathing modes. In the latter case, we found that the dynamic dipoles are at least one order of magnitude smaller than for the PFO monomer vibrations. We therefore disregard any vibrations of the PFO polymer chain in the following, since their influence on the PL spectra is expected to be negligible.

To determine the distance  $|\mathbf{r}|$  between exciton and molecular dipole, we assume that the exciton is centered around the CNT axis and that the molecular dipole is centered around the PFO center of mass. The distance between these two points can be extracted from the relaxed geometry of a PFO monomer in the vicinity of a CNT that is obtained from the DFT simulations and was found to equal  $|\mathbf{r}| = 6.9 \text{ \AA}$ . By introducing the unit vector  $\mathbf{e}_{\text{exc}}$  pointing into the same direction as  $\mathbf{p}_{\text{exc}}$  the term  $\mathbf{p}_{\text{exc}} - 3(\mathbf{p}_{\text{exc}} \cdot \mathbf{e}_{\mathbf{r}})\mathbf{e}_{\mathbf{r}}$  in Eq. (4.32) can be rewritten as  $|\mathbf{p}_{\text{exc}}|(\mathbf{e}_{\text{exc}} - 3(\mathbf{e}_{\text{exc}} \cdot \mathbf{e}_{\mathbf{r}})\mathbf{e}_{\mathbf{r}})$ , where  $\mathbf{p}_{\text{exc}} = |\mathbf{p}_{\text{exc}}|\mathbf{e}_{\text{exc}}$ . Apart from the value of  $|\mathbf{p}_{\text{exc}}|$  it is therefore necessary to determine the angles between the vectors  $\mathbf{e}_{\text{exc}}$ ,  $\mathbf{e}_{\mathbf{r}}$  and  $\partial_{Q_n}\boldsymbol{\mu}$ . We fix  $\mathbf{e}_{\text{exc}}$  and  $\mathbf{e}_{\mathbf{r}}$  by the assumption that the exciton dipole moment is aligned along the CNT axis and that  $\mathbf{e}_{\mathbf{r}}$  is orthogonal to the CNT axis, since the exciton is expected to couple most strongly to the spatially closest PFO monomer.

The direction of  $\partial_{Q_n}\boldsymbol{\mu}$  is computed by DFT in a coordinate system coupled to the geometric orientation of the molecule. Therefore, the rotation between the PFO monomer and the CNT needs to be considered as an additional parameter. In earlier reports on molecular dynamics simulations of CNTs interacting with PFO it has been found that the backbone of a PFO polymer wraps around CNTs lying flatly on the carbon lattice with a preferred winding angle of about 20–30° [254, 256]. Consistently, we obtained best results for a yaw angle of 25–30° and a small pitch angle of less than 10° of the PFO monomer with respect to the CNT axis.

It remains to find the value of  $|\mathbf{p}_{\text{exc}}|$ . In a first step one can express this quantity through the exciton oscillator strength  $f_{\text{exc}}$  and write [245]

$$|\mathbf{p}_{\text{exc}}| = \frac{3}{2} \frac{\hbar^2 e^2}{E_{\text{exc}} m_e} f_{\text{exc}}, \quad (4.35)$$

where the elementary charge  $e$ , the free electron mass  $m_e$  and the exciton energy  $E_{\text{exc}}$  are known quantities. The exciton oscillator strength can be calculated as the product of the oscillator strength per carbon atom and the number of carbon atoms in the exciton coherence length  $\sigma$  [67, 143], resulting in

$$f_{\text{exc}} = 0.014 \text{ eV}^{-1} \cdot E_{\text{exc}} \pi d_{(9,1)} \sigma / A_C, \quad (4.36)$$

where  $d_{(9,1)} = 0.757 \text{ nm}$  is the diameter of a (9, 1)-CNT [35],  $A_C = \frac{3}{4}\sqrt{3} \cdot a_{\text{C-C}}^2$  is the area per carbon atom, and  $a_{\text{C-C}} = 0.144 \text{ nm}$  is the carbon-carbon bond length [23, p. 38]. Finally,

we assume that the exciton coherence length  $\sigma$  is determined by the CNT dielectric environment, which is dominated by the PFO surfactant. We therefore expect decoherence effects on the length scale of one winding of the PFO polymer backbone. From [254, 256] we estimate a helix pitch of about 50 carbon-carbon bond lengths and therefore expect a value of the order  $\sigma \approx 50 \cdot a_{C-C} = 7.2 \text{ nm}$ .

To obtain a simulated spectrum from these parameters and the vibrational modes found by DFT, a Lorentzian peak with FWHM  $\gamma$  for the ZPL,

$$f(E) = \frac{\gamma/2}{\pi \cdot [(E - E_{\text{exc}})^2 + (\gamma/2)^2]}, \quad (4.37)$$

and vibron replica of the former that are intensity-scaled following Eq. (4.32) are summed for all normal modes. The FWHM  $\gamma$  is extracted from the ZPL in the measured spectra and additionally from the onset of the lower-energy sideband at the spectral gap that separates it from the ZPL. This procedure generally yielded a value  $\gamma_{\text{rep}}$  of the FWHM for the sideband slightly larger than  $\gamma_{\text{ZPL}}$  for the ZPL, which is attributed to a vibronic broadening of the ZPL replica, presumably due to limited vibron lifetimes [262–264].

Figs. 4.4 (d) and (f) show a cryogenic PL spectrum (red data points) of the CNT from Fig. 4.3 (b) (CNT A) together with spectra obtained from DFT simulations employing the BP86 (upper panel) and the B3LYP functional (lower panel), respectively, including vibron processes up to 1<sup>st</sup> order (gray) and up to 4<sup>th</sup> order (black). For both functionals we find that the  $1/\Omega^2$  damping suppresses the lower-energy wing too strongly, whereas the inclusion of higher-order vibron processes restores the damping behavior observed in our data. Note that the only free parameter for the simulated spectra is the exciton coherence length  $\sigma$  that determines the intensity of the lower-energy sideband. The values of  $\sigma = 7.2 \text{ nm}$  for the BP86 functional and  $\sigma = 12 \text{ nm}$  for the B3LYP functional that were found as best fits to the data are in excellent agreement with the estimated coherence length of  $\sigma = 7.2 \text{ nm}$ . Furthermore, the Lorentzian FWHMs  $\gamma_{\text{ZPL}} \approx 500 \mu\text{eV}$  and  $\gamma_{\text{rep}} \approx 700 \mu\text{eV}$  were determined from the experimental spectra.

We also observed that the individual vibronic modes predicted by DFT differ for the BP86 and the B3LYP functional. While the BP86 functional yields a relatively smooth lower-energy wing in Fig. 4.4 (d) in agreement with our data, the B3LYP functional predicts a strongly oscillating sideband that is incompatible with our measurements. The spectrum of another PFO-wrapped CNT (red data points in Figs. 4.4 (e) and (g), CNT B), however, exhibits such pronounced oscillations and is fit remarkably well by the spectrum simulated with the B3LYP functional in Fig. 4.4 (g). As detailed below, the differing results of the two DFT functionals originate from slight variations of the predicted relaxed geometry of PFO interacting with the CNT. This finding suggests that the spectral differences of CNT A and CNT B also originate from different geometric conformations of the PFO surfactant. Note that due to the more pronounced lower-energy sideband of CNT B slightly larger values of  $\sigma = 10 \text{ nm}$  for the

BP86 functional and  $\sigma = 16$  nm for the B3LYP functional were employed. The Lorentzian linewidths were determined as  $\gamma_{\text{ZPL}} \approx 600 \mu\text{eV}$  and  $\gamma_{\text{rep}} \approx 800 \mu\text{eV}$ .

When comparing the spectra obtained with the BP86 functional in Figs. 4.4 (d) and (e) and with the B3LYP functional in Figs. 4.4 (f) and (g), it appears surprising that the individual vibrational modes predicted by DFT are quite different, while at the same time the width of the spectral gap  $\Delta E$  between the ZPL and the vibronic sideband, which is ultimately given by the lowest-energy vibrational mode, are similar and consistent with the experimental data. To resolve this puzzle, we study the robustness of the DFT results for  $\Delta E$ .

We first analyze the origin of the different vibrational modes found by DFT simulations with different functionals. By comparing the results of BP86 and B3LYP we found that the geometry optimization detailed in Section A.2 yields slightly different results. Given the observation that DFT predicts vibrations up to about 400 meV, finding the lowest-energy vibrations around 5 meV amounts to finding almost-degenerate eigenvalues close to zero of the Hessian matrix of the potential energy change with respect to the molecular coordinates. This insight explains the limited reliability of DFT results for low-energy vibrations that are highly sensitive to the precise geometrical input [265].

Yet, the respective lowest-energy vibrational modes only differ by 150  $\mu\text{eV}$  for BP86 and B3LYP. The underlying reason for this can be attributed to the fact that both functionals identify a scissoring motion of the two octyl ligands in the PFO monomer as the lowest-energy vibration. We proceed by showing that the energy of this particular vibrational mode is well-defined and can be obtained even by crude estimates to a remarkable precision.

We model the vibration given by the scissoring motion of the octyl ligands by the simplifying assumption that both the PFO backbone and one of the octyl ligands are fixed due to the van der Waals-like interaction with the CNT as illustrated in Fig. 4.4 (a), while the other octyl ligand performs a rotary motion around the carbon atom it is attached to. The potential energy of this motion can be written as

$$V = \frac{1}{2} H_{\Lambda} \theta^2, \quad (4.38)$$

where  $\theta$  is the deflection angle from the equilibrium position and  $H_{\Lambda}$  is the bending force constant of the bond that connects the octyl ligand with the carbon atom it is attached to. Using a valence force field approximation, a value of  $H_{\Lambda} = 1.086 \text{ m dyn } \text{\AA} / \text{rad}^2$  has been found for  $\text{sp}^3$  hybridized carbon atoms with four other carbon atoms as bond partner [266]. The kinetic energy of the rotary motion of one octyl ligand can be expressed as

$$T = \frac{1}{2} I \dot{\theta}^2, \quad (4.39)$$

where  $I$  is the moment of inertia of the ligand with respect to the carbon atom it is bound to. To calculate the moment of inertia, we assume that the octyl ligand has a zigzag shape

with the tetrahedral angle as kink angle and that at each kink one carbon and two hydrogen atoms contribute to the moment of inertia with the same perpendicular distance. Then,

$$I = \sum_{n=1}^8 (m_C + 2m_H) \left( n \cdot a_{CC} \sin \frac{\tau}{2} \right)^2 + m_H (9 \cdot a_{CC} \sin \frac{\tau}{2})^2 = 7.72 \times 10^{-44} \text{ kg m}^2, \quad (4.40)$$

where  $m_C = 1.993 \times 10^{-26} \text{ kg}$  and  $m_H = 1.674 \times 10^{-27} \text{ kg}$  are the masses of  $^{12}\text{C}$  and  $^1\text{H}$ , where  $a_{C-C} = 154 \text{ pm}$  is the alkane carbon-carbon bond length, slightly different from the graphene carbon-carbon bond length, and where  $\tau = 109.47^\circ$  is the tetrahedral angle. The expressions for  $V$  and  $T$  describe a harmonic oscillator with angular frequency

$$\omega = \sqrt{\frac{H_\Lambda}{I}} = 3.751 \times 10^{12} \text{ s}^{-1}, \quad (4.41)$$

which amounts to a quantum mechanical energy of  $\hbar\omega = 2.469 \text{ meV}$ .

In spite of the crudeness of our estimate, this value is close to the mean value of  $1.7 \text{ meV}$  in the histogram in Fig. 4.3 (b). We attribute this result to the simplicity of the scissoring motion making a more complex analysis obsolete. Given the assumption that the scissoring motion of PFO is its lowest-energy vibrational mode, which appears plausible in the light of its simple geometrical nature, we can therefore conclude that its energy in DFT simulations is not expected to depend strongly on the detailed geometrical structure resulting from the different DFT functionals. This finding explains the very similar gap energy  $\Delta E$  for the spectra obtained from BP86 and B3LYP.

By contrast, already the third vibrational mode – following the two possible scissoring motions in orthogonal directions – has a strong torsional component both for the BP86 and the B3LYP functional, suggesting a much stronger influence of the precise relaxed geometry. This finding agrees well with the observation that the first two respective vibrational modes are similar in energy ( $1.746 \text{ meV}$  and  $2.258 \text{ meV}$  for BP86 and  $1.893 \text{ meV}$  and  $2.233 \text{ meV}$  for B3LYP), while the subsequent modes are more volatile in view of the specifics of the chosen DFT method (cf. Figs. 4.4 (d)–(g)).

In conclusion we found an excellent agreement between the cryogenic spectra of PFO-wrapped CNTs and simulated spectra based on the vibrational modes of a PFO monomer obtained from DFT and a model describing the exciton-vibron interaction that is essentially free of fit parameters. The only variable parameter  $\sigma$  is estimated accurately from the geometric structure of PFO documented in literature [254, 256]. The comparison of simulated spectra based on the BP86 and the B3LYP functional suggests that spectral variations of the lower-energy sideband in Figs. 4.4 (d)–(g) can be explained by different geometric conformations of the PFO surfactant. By contrast the gap energy  $\Delta E$  was identified to be determined by two scissoring modes of the PFO monomer that are expected to be largely independent of details of the geometric structure and explain the consistent value of  $\Delta E$  even for a substantial variety of different PL spectra.

## 4.5. Temperature dependence of exciton-vibron interactions in polymer-decorated carbon nanotubes

Complementary to the cryogenic spectra presented in Section 4.4 we also performed temperature-dependent measurements to illuminate the increasing intensity of Stokes and anti-Stokes [247] sidebands at higher temperatures. This section introduces the necessary modifications to the quantum-mechanical description in Section 4.3 that is limited to zero temperature, in order to also cover finite temperatures. While the Hamiltonian in Eq. (4.7) is temperature independent, the initial state  $|i\rangle = |e, 0_{\text{ph}}, 0_{\text{vib}}\rangle$  in the derivation of the transition rate  $\Gamma_{S,n}$  for a Stokes sideband photon in Eq. (4.31) can be generalized to include a temperature dependence. Due to thermal excitation, we may assume that initially a number of  $s$  vibrons is present in mode  $n$  such that the initial state reads  $|i_n^{(s)}\rangle = |e, 0_{\text{ph}}, s_n\rangle$ . To calculate the transition rate  $\Gamma_{S,n}^{(s)}$  for a Stokes sideband photon in the presence of  $s$  vibrons in mode  $n$ , the transient state  $|t_n\rangle$  and the final state  $|f_n\rangle$  are adapted accordingly as  $|t_n^{(s+1)}\rangle = |e, 0_{\text{ph}}, (s+1)_n\rangle$  and  $|f_n^{(s+1)}\rangle = |g, 1_{\text{ph}}, (s+1)_n\rangle$ . Using the properties of the creation and annihilation operators  $\hat{c}_n^\dagger$  and  $\hat{c}_n$ , the matrix elements in Eq. (4.31) are then modified to

$$\langle t_n^{(s+1)} | \hat{H}_{\text{exc-vib}} | i_n^{(s)} \rangle = \sqrt{s+1} \cdot \langle t_n^{(1)} | \hat{H}_{\text{exc-vib}} | i_n^{(0)} \rangle = \sqrt{s+1} \cdot \langle t_n | \hat{H}_{\text{exc-vib}} | i \rangle \quad (4.42)$$

and

$$\langle f_n^{(s+1)} | \hat{H}_{\text{exc-ph}} | t_n^{(s+1)} \rangle = \langle f_n^{(0)} | \hat{H}_{\text{exc-ph}} | t_n^{(0)} \rangle = \langle f_n | \hat{H}_{\text{exc-ph}} | t_n \rangle. \quad (4.43)$$

The Stokes transition rate  $\Gamma_{S,n}^{(s)}$  for  $s$  initial vibrons in mode  $n$  is obtained by following the calculation in Eq. (4.31) using the modified matrix elements that results in

$$\Gamma_{S,n}^{(s)} = (s+1) \cdot \Gamma_{S,n}. \quad (4.44)$$

At a given temperature  $T$  the probability  $p_n(s)$  to find  $s$  vibrons in vibrational mode  $n$  is given by the Boltzmann distribution [267] and can be written as

$$p_n(s) = [1 - \exp(-\beta\hbar\Omega_n)] \cdot \exp(-s\beta\hbar\Omega_n), \quad (4.45)$$

where  $\beta = 1/k_B T$  is the thermodynamic beta,  $k_B$  is the Boltzmann constant, and  $\Omega_n$  is the angular frequency of the vibration in normal mode  $n$ . The transition rate  $\Gamma_{S,n}^{(\cdot)\beta}$  for a Stokes sideband photon in the presence of a thermal occupation of vibrons in mode  $n$  can be calculated as the expectation value of the transition rates  $\Gamma_{S,n}^{(s)}$ :

$$\begin{aligned}
 \Gamma_{S,n}^{\langle \cdot \rangle \beta} &= E[\Gamma_{S,n}^{(s)}] = \sum_{s=0}^{\infty} p_n(s) \Gamma_{S,n}^{(s)} = \\
 &= [1 - \exp(-\beta \hbar \Omega_n)] \cdot \Gamma_{S,n} \cdot \sum_{s=0}^{\infty} (s+1) \exp(-s\beta \hbar \Omega_n) = \\
 &= [1 - \exp(-\beta \hbar \Omega_n)] \cdot \Gamma_{S,n} \cdot \frac{1}{[1 - \exp(-\beta \hbar \Omega_n)]^2} = \\
 &= \frac{\Gamma_{S,n}}{1 - \exp(-\beta \hbar \Omega_n)} \tag{4.46}
 \end{aligned}$$

In the presence of thermally excited vibrons, also an anti-Stokes sideband is expected. To formulate this scenario, consider an initial state  $|i_n^{(s)}\rangle = |e, 0_{\text{ph}}, s_n\rangle$  with a number of  $s$  vibrons in mode  $n$  together with the corresponding transient and final states  $|t_n^{(s-1)}\rangle = |e, 0_{\text{ph}}, (s-1)_n\rangle$  and  $|f_n^{(s-1)}\rangle = |g, 1_{\text{ph}}, (s-1)_n\rangle$ . Like for the Stokes sideband the matrix elements in Eq. (4.31) are modified to

$$\langle t_n^{(s-1)} | \hat{H}_{\text{exc-vib}} | i_n^{(s)} \rangle = \sqrt{s} \cdot \langle t_n^{(0)} | \hat{H}_{\text{exc-vib}} | i_n^{(1)} \rangle = \sqrt{s} \cdot \langle t_n^{(1)} | \hat{H}_{\text{exc-vib}} | i_n^{(0)} \rangle = \sqrt{s} \cdot \langle t_n | \hat{H}_{\text{exc-vib}} | i \rangle \tag{4.47}$$

and

$$\langle f_n^{(s)} | \hat{H}_{\text{exc-ph}} | t_n^{(s)} \rangle = \langle f_n^{(0)} | \hat{H}_{\text{exc-ph}} | t_n^{(0)} \rangle = \langle f_n | \hat{H}_{\text{exc-ph}} | t_n \rangle. \tag{4.48}$$

Following the calculation in Eq. (4.31), the anti-Stokes transition rate  $\Gamma_{AS,n}^{(s)}$  for  $s$  initial vibrons in mode  $n$  is found to equal

$$\Gamma_{AS,n}^{(s)} = s \cdot \Gamma_{S,n}. \tag{4.49}$$

The transition rate  $\Gamma_{AS,n}^{\langle \cdot \rangle \beta}$  for an anti-Stokes sideband photon in the presence of a thermal occupation of vibrons in mode  $n$  is obtained as the expectation value of the transition rates  $\Gamma_{AS,n}^{(s)}$ :

$$\begin{aligned}
 \Gamma_{AS,n}^{\langle \cdot \rangle \beta} &= E[\Gamma_{AS,n}^{(s)}] = \sum_{s=0}^{\infty} p_n(s) \Gamma_{AS,n}^{(s)} = \\
 &= [1 - \exp(-\beta \hbar \Omega_n)] \cdot \Gamma_{S,n} \cdot \sum_{s=0}^{\infty} s \cdot \exp(-s\beta \hbar \Omega_n) = \\
 &= [1 - \exp(-\beta \hbar \Omega_n)] \cdot \Gamma_{S,n} \cdot \frac{\exp(-\beta \hbar \Omega_n)}{[1 - \exp(-\beta \hbar \Omega_n)]^2} = \\
 &= \frac{\Gamma_{S,n} \cdot \exp(-\beta \hbar \Omega_n)}{1 - \exp(-\beta \hbar \Omega_n)}
 \end{aligned}$$

The temperature dependence of the ZPL linewidth  $\gamma_{\text{ZPL}}$  in Eq. (4.37) has been extensively studied in semiconductor quantum dots and was found to follow the functional form

$$\gamma_{\text{ZPL}}(T) = \gamma_0 + \alpha_{\text{ac}} \cdot T + \frac{\alpha_{\text{op}}}{\exp(\beta E_{\text{op}}) - 1}, \quad (4.50)$$

where  $\alpha_{\text{ac}}$  and  $\alpha_{\text{op}}$  are the coupling constants to acoustic and optical phonons in the CNT lattice, respectively, and  $E_{\text{op}}$  is the energy of the lowest-energy optical CNT phonon [268–271]. The value of  $\alpha_{\text{ac}}$  was calculated in [228] for CNTs and the expression  $\alpha_{\text{ac}} = 2\pi\alpha k_B$  was found, where  $k_B$  is the Boltzmann constant and

$$\alpha = \frac{g_2^2 \sqrt{\rho_G} (1 + \nu)^2}{\pi^2 \hbar d_{(9,1)} Y_G^{3/2}} \cdot \cos^2 3\theta_{(9,1)}. \quad (4.51)$$

Here,  $d_{(9,1)} = 0.757 \text{ nm}$  is the diameter and  $\theta_{(9,1)} = 5.21^\circ$  is the chiral angle of a (9, 1)-CNT [35]. The off-diagonal electron-phonon coupling constant  $g_2 = 1.5 \text{ eV}$ , the graphene mass density  $\rho_G = 7.6 \times 10^{-7} \text{ kg/m}^2$ , the Poisson ratio  $\nu = 0.2$  and the graphene 2D Young modulus  $Y_G = 340 \text{ N/m}$  are all given in [228] and allow to compute the result

$$\alpha_{\text{ac}} = 7.37 \times 10^{-6} \text{ eV/K}. \quad (4.52)$$

The most prominent optical phonon in CNTs is the unique **radial breathing mode (RBM)** [23, pp. 172–173] that features an energy of 37.2 eV in (9, 1)-CNTs in the absence of environmental effects [272]. Accordingly, we assume  $E_{\text{op}} = 37.2 \text{ eV}$  in Eq. (4.51). Note, however, that for (6, 5)-CNTs, whose RBM energy also lies at 37.2 eV [35, 272], three optical phonon modes energetically below the RBM at about 3.1 meV, 9.2 meV, and 26 meV have been reported [273]. For (9, 1)-CNTs we are not aware of a comparable study of all low-energy phonons. The existence of similar optical phonon modes energetically below the RBM in (9, 1)-CNTs would either imply a smaller value for  $E_{\text{op}}$  or the contribution of multiple terms  $\alpha_{\text{op}}/(\exp(\beta E_{\text{op}}) - 1)$  to Eq. (4.51). As illustrated below, however, a good agreement with the data is obtained even when such modifications are disregarded. The two remaining parameters  $\gamma_0$  and  $\alpha_{\text{op}}$  in Eq. (4.51) have not been reported for CNTs to the best of our knowledge and are therefore treated as free fit parameters.

Also the broadening of the ZPL replica,  $\Delta\gamma = \gamma_{\text{rep}} - \gamma_{\text{ZPL}}$ , is a temperature-dependent quantity. The evolution with increasing temperature was modeled by a linear relation

$$\Delta\gamma = \delta_0 + \alpha_\delta \cdot T \quad (4.53)$$

that was found to provide a satisfactory description for the linewidths of molecular vibrations and phonon couplings in CNTs or semiconductor quantum dots [263, 268, 274–276].

Figs. 4.5 (a)–(d) show spectra of the CNT discussed in Figs. 4.3 (b), 4.4 (d), and (f) at temperatures of 4 K, 10 K, 30 K, and 105 K (red data points). The simulated spectra (solid black lines)

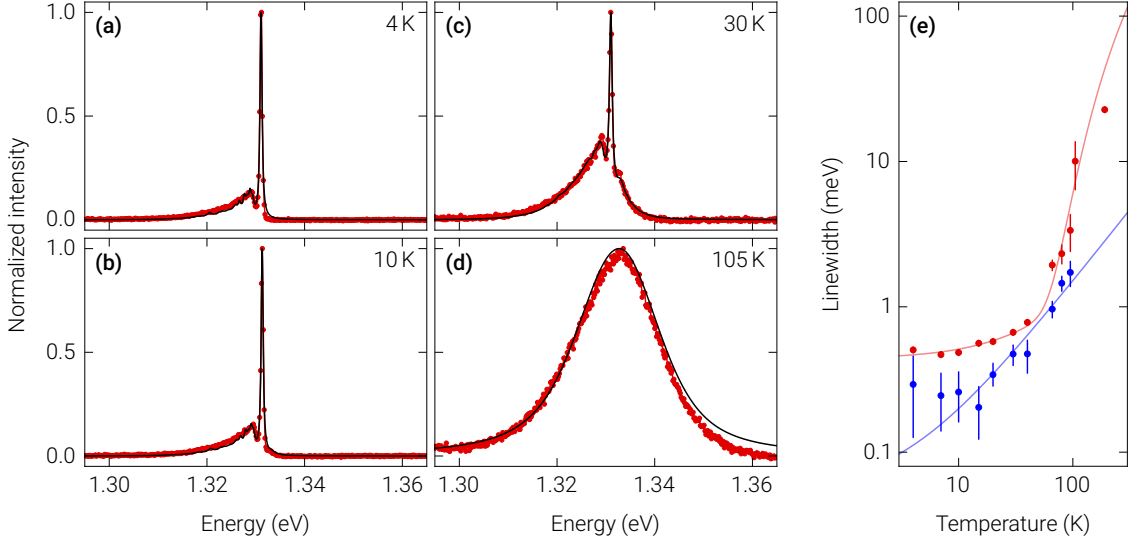


**Figure 4.5.:** Temperature dependence of PL spectra of PFO-wrapped CNTs. (a)–(d) PL spectra at different temperatures of the PFO-wrapped CNT from Figs. 4.3 (b), 4.4 (d), and (f) (red data points) with simulated spectra including 4<sup>th</sup> order vibron processes (solid black lines) that were calculated using the BP86 functional. Measured heater temperatures are noted in in the respective top right corners. (e) ZPL linewidth  $\gamma_{ZPL}$  (red data points) and ZPL linewidth broadening  $\Delta\gamma$  (blue data points) obtained from fits of the ZPL and the vibronic sideband or their merger at different sample temperatures. Error bars are occasionally covered by the symbol size. The solid red line models the temperature dependence of  $\gamma_{ZPL}$  according to Eq. (4.50), while the solid blue line shows a linear fit to the temperature dependence of  $\Delta\gamma$ . Graphics (a)–(e) are reproduced from [P1].

obtained with the BP86 functional include vibron processes up to 4<sup>th</sup> order and capture both the increasing intensity of the Stokes and the anti-Stokes sideband up to 30 K and the merging of the ZPL with the sidebands at even higher temperatures. Note that the readout values of the temperature sensor (cf. Section 3.1) and  $\sigma = 7.2$  nm from Fig. 4.4 (d) were used in the simulation such that only the quantities  $\gamma_0$ ,  $\alpha_{op}$ ,  $\delta_0$ , and  $\alpha_\delta$ , modeling the broadening of the ZPL and the vibronic replica, are free model parameters.

For sample temperatures up to  $\sim 40$  K the linewidths  $\gamma_{ZPL}$  and  $\gamma_{rep}$  were directly obtained from the PL spectra. At higher temperatures they were indirectly accessible, since both values influence the width of the broad PL peak originating from the merging of the ZPL and the vibronic sidebands. The red and blue data points in Fig. 4.5 (e) show the best fits for  $\gamma_{ZPL}$  and  $\Delta\gamma$ , respectively, and their uncertainties that were obtained with this procedure. The solid red line in Fig. 4.5 (e) shows the best fit of Eq. (4.50) to the optimum values of  $\gamma_{ZPL}$ , excluding the data point at 190 K, for which the temperature readout was considered unreliable due to the large temperature gradient between the sample and the liquid helium bath. The corresponding best fit parameters were determined as  $\gamma_0 = 438 \mu\text{eV}$  and  $\alpha_{op} = 360 \text{ meV}$ . The relatively large value of  $\alpha_{op}$  compared to  $\alpha_{ac}T$  is consistent with values reported for

semiconductor quantum dots [270, 277], where the ratio  $\alpha_{\text{op}}/\alpha_{\text{ac}}T$  has been found to range within the same order of magnitude.

The solid blue line in Fig. 4.5 (e) shows the best fit of Eq. (4.53) to the values obtained for  $\Delta\gamma$ . The corresponding best fit parameters were identified as  $\delta_0 = 53\mu\text{eV}$  and  $\alpha_\delta = 15\mu\text{eV/K}$ . Note that data points for  $\Delta\gamma$  are missing for higher temperatures, since this parameter is difficult to estimate for fully merged ZPL and vibron sidebands. In this region, the extrapolation of Eq. (4.53) with the determined values of  $\delta_0$  and  $\alpha_\delta$  was used to simulate the spectra.

## 4.6. Effect of excitation power on spectral characteristics of polymer-decorated carbon nanotubes

The study of GALLAND et al. [227] not only analyzed the effects of varying temperature on the spectral lineshape of individual CNTs but also compared them to the effects of increasing excitation laser power. The observed changes in lineshape in their work are consistent with a local heating of the sample that gives rise to an increased effective temperature of the CNT phonon bath. Figs. 4.6 (a)–(f) similarly compare the effects of an increase in temperature (top row) and in excitation laser power (bottom row) on the spectral response of the CNT from Figs. 4.5 (a)–(d). To analyze also spectral features of weak intensity a logarithmic scale was chosen. The experimental parameters in the three respective columns were selected to yield similar intensities of the Stokes sideband.

Figs. 4.6 (a)–(c) show three spectra (red data points) recorded at a fixed excitation laser power of  $2\mu\text{W}$  for sample temperatures of 4 K, 10 K, and 20 K, respectively. In the three panels a gradual increase of the Stokes sideband is evident together with the emergence of an anti-Stokes sideband that is absent in Fig. 4.6 (a), but clearly visible in Fig. 4.6 (c). The simulated spectra (solid black lines) including 4<sup>th</sup> order vibron processes were calculated using the BP86 functional and reflect this behavior. Note that instead of the Lorentz peak in Eq. (4.37) a Voigt profile was used here to best reproduce the base of the ZPL.

The spectra in Figs. 4.6 (d)–(f) (red data points) were measured at a fixed temperature of 4 K and excitation laser powers of  $2\mu\text{W}$ ,  $80\mu\text{W}$ , and  $240\mu\text{W}$  and feature a similar increase of the Stokes sideband as in Figs. 4.6 (a)–(c). The emergence of the anti-Stokes sideband, however, is much less pronounced than in Figs. 4.6 (a)–(c). Note that the ZPL peak position has shifted by  $\sim 4\text{ meV}$  between the two series of measurements. The solid black and dotted black lines in Figs. 4.6 (d)–(f) show simulated spectra that were optimized to fit the Stokes and anti-Stokes sideband, respectively. While in Fig. 4.6 (d) the two fits are practically identical (effective temperature of 4.2 K, each), they show a significant difference in Fig. 4.6 (e). For the latter spectrum the solid black line (effective temperature of 12.0 K) is in good agreement with the Stokes sideband, except for an underestimation of the wing intensity far from the ZPL that can be attributed to the omission of even higher order vibronic processes. For the anti-

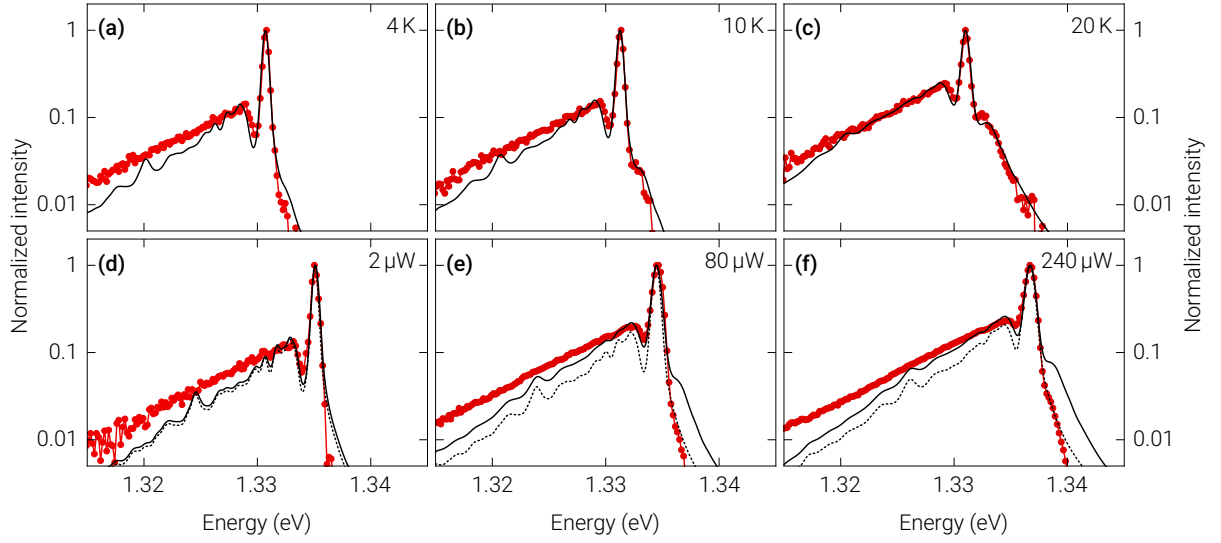


**Figure 4.6.:** Comparison of PL spectra of the PFO-wrapped CNT from Figs. 4.5 (a)–(d) (red data points) recorded at (a)–(c) different sample temperatures denoted in the respective top right corners with fixed excitation laser power of  $2 \mu\text{W}$  and at (d)–(f) fixed sample temperature of 4 K with different excitation laser powers denoted in the respective top right corners. The black lines show simulated spectra including 4<sup>th</sup> order vibron processes that were calculated using the BP86 functional. Solid and dotted lines in the bottom panels indicate fitting to the Stokes and anti-Stokes vibronic sidebands, respectively. Note that instead of the Lorentz peak in Eq. (4.37) a Voigt profile was used to best reproduce the base of the ZPL.

Stokes sideband, however, a prominent wing with a secondary peak is predicted that is absent in the data. The black dotted line (effective temperature of 4.2 K), by contrast, follows the anti-Stokes sideband well, but underestimates the entire Stokes sideband. Note that on the chosen logarithmic scale this deviation appears smaller than on a linear scale. The same trend is observed in Fig. 4.6 (f), although the difference is smaller (effective temperatures of 16.0 K and 4.2 K, respectively).

The unequal evolution of the Stokes and anti-Stokes sidebands indicates that the influence of the excitation power cannot be solely attributed to a local heating of the sample that would result in spectra similar to Figs. 4.6 (a)–(c). Another common effect of an increase in the excitation power is the induced spectral jitter of the emission peak energy [P6, 278]. We illustrate how a combination of local sample heating and power-induced spectral wandering on short timescales conclusively explain the spectral shapes in Figs. 4.6 (d)–(f).

Figs. 4.7 (a)–(c) illustrate how jitter acting on timescales below the temporal resolution of the spectrometer modifies the recorded spectral shape. The spectrum in Fig. 4.7 (a) that is identical to the black dashed line from Fig. 4.6 (e) is taken as a model for the spectral response of a PFO-wrapped CNT in the absence of spectral wandering. Jittering on short timescales is implemented by the assumption that the entire spectrum including vibronic

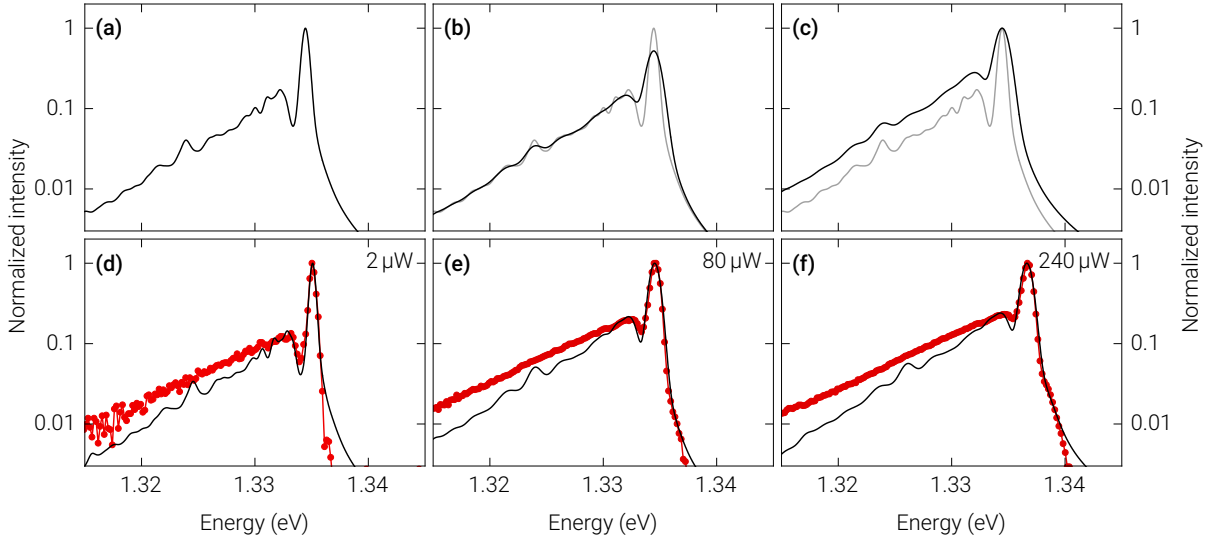


**Figure 4.7.:** Effects of spectral jitter on the PL shape of PFO-wrapped CNTs. (a) Simulated spectrum from Fig. 4.6 (e). (b) Spectrum from (a) unaltered (gray) and smoothed by convolution with a Gaussian peak featuring an FWHM of  $500\ \mu\text{eV}$  (black). (c) Spectrum from (a) unaltered (gray) and smoothed as in (b), then normalized to the ZPL maximum (black). (d)–(f) PL spectra from Figs. 4.6 (d)–(f) (red data points) fit by simulated spectra including 4<sup>th</sup> order vibron processes calculated using the BP86 functional that were additionally smoothed by convolution with a Gaussian (solid black lines).

sidebands statistically wanders around a central position and that the spectrometer time-averages these shifted spectra. For the assumption of purely random jitter, this behavior is simulated by convoluting the spectrum from Fig. 4.7 (a) with a Gaussian function. The spectrum obtained for a Gaussian featuring an FWHM of  $500\ \mu\text{eV}$  is shown as solid black line in Fig. 4.7 (b) together with the spectrum from Fig. 4.7 (a) in gray. The Gaussian smoothing washes out the spectral features of the Stokes sideband but also reduces the maximum intensity of the ZPL. For the comparison of spectra with different intensities, all spectra in this chapter are normalized to the peak intensity of the ZPL. The result of this step is shown as solid black line in Fig. 4.7 (c) together with the spectrum from Fig. 4.7 (a) in gray. Comparing the two curves illustrates that the Gaussian smoothing results in an apparent increase of the Stokes sideband, while the rest of the spectrum is largely unaltered.

Figs. 4.7 (d)–(f) show simulated spectra including 4<sup>th</sup> order vibron processes calculated using the BP86 functional that were additionally smoothed by convolution with a Gaussian (solid black lines) to fit the spectra from Figs. 4.6 (d)–(f) (red data points). The corresponding effective temperatures and Gaussian FWHMs are 4.2 K, 4.2 K, and 6.2 K and  $9\ \mu\text{eV}$ ,  $414\ \mu\text{eV}$ , and  $407\ \mu\text{eV}$ , respectively. For all three panels the agreement between fit and data is significantly better than in Figs. 4.6 (d)–(f). In particular, in Fig. 4.7 (e) the anti-Stokes sideband is almost absent in agreement with the low effective temperature of 4.2 K. The weakly de-

veloped anti-Stokes sideband in Fig. 4.6 (f), by comparison, can be attributed to a slightly higher effective temperature of 6.2 K that is owed to the even higher excitation laser power. The spectrum in Fig. 4.6 (f) therefore illustrates that both local heating of the sample and laser-induced jitter must be taken into account to correctly interpret the PL dependency on the excitation laser power.

## 4.7. Conclusion

In this chapter, we presented an elaborate analysis of environmental effects on the spectral response of localized excitons in cryogenic CNTs. At low temperatures the diffusive excitons in CNTs localize in shallow potential traps or at defect sites and exhibit PL with a wealth of individual lineshapes. Earlier studies attributed these variations to different coupling mechanisms of localized excitons to the CNT phonon modes [70, 227, 229, 230]. While the agreement between these models and the data is compelling, a discrepancy remains regarding the value of the exciton-phonon deformation potential coupling that is in disagreement with theoretical results [228]. The observation of permanent electric dipole moments in CNTs [38] provides another coupling mechanism that may account for the lineshapes observed in PL spectra. We developed a model based on dipolar couplings to vibrational degrees of freedom in surfactant molecules as the origin of different spectral responses. This mechanism is conceptually similar to exciton-ligand couplings in colloidal quantum dots [279], but was previously unreported for the case of CNTs.

A quantum-mechanical description was developed that captures the dipole-dipole interaction between the exciton and dynamical molecular dipole moments that are induced by charge displacements in a vibrating molecule. A coupling term was derived that resembles the form of a Holstein interaction. The intensity of Stokes and anti-Stokes sideband photons were found to exhibit a quadratic damping with increasing energy difference from the ZPL that explains the fading of spectral wings frequently observed in experiments. The model parameters were estimated from literature values, while the characteristics of the involved molecular vibrations were simulated with DFT for the case of a PFO surfactant. Comparison with cryogenic spectra of PFO-wrapped CNTs revealed that our model is in excellent agreement with the data, while it is also essentially free of fit parameters. Details of the chosen DFT method were found to give rise to modifications of the predicted spectral response that were attributed to differences in the calculated relaxed molecular geometry and related to similar variations in the experimental spectra. The spectral gap between ZPL and vibronic sidebands observed for PFO-wrapped CNTs was identified as a robust quantity across different DFT approaches.

The quantum-mechanical description was extended to capture the dependence of the Stokes and anti-Stokes sidebands on the sample temperature. The broadening of the ZPL

with temperature was modeled by a description established for semiconductor quantum dots, using parameters that were reported for CNTs where available. The comparison with experimental spectra showed an excellent agreement and resulted in fit values of the remaining parameters that are consistent with reports for semiconductor quantum dots. In a similar experiment we varied the excitation laser power and observed an increase of the Stokes sideband, while the anti-Stokes sideband did not emerge accordingly. This discrepancy was resolved by taking into account laser-induced spectral jitter that results in an asymmetric enhancement of the blue and red PL sidebands.



# 5

## Excitonic properties of quantum defects in covalently functionalized carbon nanotubes

---

This chapter presents studies of the photophysical properties of chirality-purified carbon nanotubes that were covalently functionalized by the attachment of hexyl substituents. In the functionalized carbon nanotube samples two new peaks in the photoluminescence response were observed with energies below the diffusive exciton emission. These spectral features were attributed to neutral excitons and negatively charged trions localized at the generated defect sites. The novel photoluminescence emission exhibited signatures of nonclassical light statistics coupled with an exceptional brightness, rendering the localized trion state the brightest trion reported in carbon nanotubes to date. Cryogenic photoluminescence spectroscopy of individual hexyl-functionalized carbon nanotubes revealed pronounced diversity on the level of single emitters, both in terms of spectral position of the emission features and in terms of time-resolved photoluminescence decay. Magneto-photoluminescence experiments established that in contrast to diffusive excitons in carbon nanotubes optically dark states are not responsible for these variations in the optical response of the localized states. Furthermore, photon correlation measurements divided the hexyl-functionalized carbon nanotubes into two classes of emitters with strong and weak crosscorrelations between the exciton and trion emission. By numerical analysis of rate models, the two cases were found to be captured by models comprising either a single defect site or multiple interacting defect sites that exchange population with an optically dark shelving state. In the latter scenario, the interaction mechanism was attributed to Coulomb repulsion that is effective due to the expected proximity of neighboring defect sites given their progressive generation on the same carbon nanotube via lattice destabilization in the course of the chemical functionalization. Building on this result, the observed variations in the optical response were interpreted in this framework of different defect configurations.

## 5.1. Introduction

Future applications of carbon nanotubes (CNTs) in photonics-based quantum technologies require detailed control of their photophysical properties to accomplish bright and temporally stable emission of nonclassical light. While the photoemission from diffusive excitons in CNTs is characterized by a low quantum yield (QY) due to the presence of an energetically lower dark state (cf. Section 2.4) and exciton quenching [55, 280], the localization of excitons promotes bright photoluminescence (PL) featuring nonclassical photon statistics [60, 63, 67, 73]. The incorporation of intentional defects into the  $sp^2$  carbon lattice of CNTs constitutes a route towards deterministic exciton localization opening the path to tailored CNT based quantum light emitters. Covalent functionalization has been established as a versatile tool for the generation of such defects that provides ample freedom in the design of the desired emission characteristics.

Earlier reports focused on the incorporation of oxygen defects into the CNT lattice [56, 281] that boost the QY [57, 238] and allow for room-temperature single-photon emission [64], but suffer from PL intensity and energy fluctuations and laser-induced bleaching [238]. More recently,  $sp^3$  defects in the  $sp^2$  CNT lattice have attracted growing attention. Functionalization with aryl groups via diazonium chemistry [58] has been established as a platform for broadband tunable emitters covering the whole telecom range [59, 71] and featuring room-temperature single-photon emission of exceptional purity [47].

However, the mentioned reaction pathways are limited in the choice of the chemical residue [48], restricting the freedom to engineer the quantum defect properties. Building on these insights, we based our studies on CNTs that are functionalized using a novel flexible chemistry approach driven by sodium dithionite ( $Na_2S_2O_4$ ) [48]. In this chapter, we report the excitonic properties and the non-classical light emission statistics of CNTs with  $sp^3$  defects created by this method. The investigated CNT samples were kindly provided by the group of YuHuang Wang from the University of Maryland.

## 5.2. Preparation and characterization of hexyl-functionalized carbon nanotubes

This section sketches the preparation and characterization of (6,5)-CNTs that were functionalized by covalently attaching hexyl groups to produce  $sp^3$  defects in the CNT  $sp^2$  carbon lattice.<sup>1</sup> The resulting hybrid system of CNT and hexyl group is referred to hereafter as hexyl-functionalized carbon nanotube (hCNT).

---

<sup>1</sup> Parts of this section are based on the publication [P2] available at <https://pubs.acs.org/doi/10.1021/acscentsci.9b00707>. Permission for any further reuse of the excerpted material must be granted by the American Chemical Society.

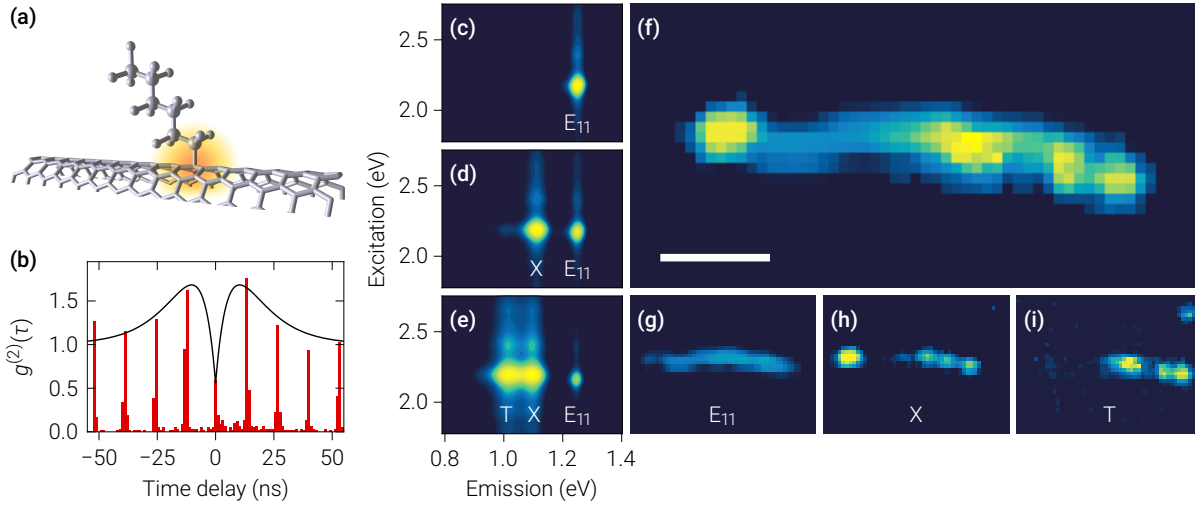


**Figure 5.1.:** Characterization of hCNT samples. **(a)** Schematic of a (6,5)-CNT (bottom) functionalized by an attached hexyl chain (top) with an exciton trapped in the corresponding defect state (orange). **(b)** Second-order correlation function  $g^{(2)}(\tau)$  for the trion emission of an isolated hCNT at 4.2 K under pulsed excitation at 850 nm with  $50 \mu\text{W}$  laser power. **(c)–(e)** Room-temperature ensemble PLE maps of pristine (6,5)-CNTs (top) and hexyl-functionalized (6,5)-CNTs in the hole-doped (middle) and the electron-doped regime (bottom). **(f)** Spectrally integrated PL intensity emitted along a  $\sim 7 \mu\text{m}$  long hCNT, recorded by hyperspectral imaging under off-resonant excitation at 730 nm with  $2.9 \mu\text{W}$  laser power at room-temperature. Scale bar is  $2 \mu\text{m}$ . **(g)–(i)** Individual spatial PL intensity maps of the hCNT in **(f)** at the spectral maxima of  $E_{11}$  (1.25 eV, left), X (1.13 eV, middle) and T (1.01 eV, right) recorded under the same experimental conditions as in **(f)**. The measurements in **(c)–(e)** were performed by the group of YuHuang Wang from the University of Maryland. The measurements in **(f)–(i)** were performed by the group of Stephen Doorn from the Los Alamos National Laboratory. Graphics **(b)–(i)** are reproduced from [P2].

The chemical synthesis of hCNTs introduced in the following was performed by the group of YuHuang Wang from the University of Maryland and is reproduced from [48], where the procedure is described in more detail. Initially, CNTs with sodium dodecyl sulfate (SDS) surfactant dispersed in  $\text{D}_2\text{O}$  were sorted for high-purity (6,5)-CNTs by gel chromatography [205]. Successively, sodium bicarbonate ( $\text{NaHCO}_3$ ), acetonitrile ( $\text{C}_2\text{H}_3\text{N}$ ) and 1-iodohexane ( $\text{C}_6\text{H}_{13}\text{I}$ ) were added to the (6,5)-CNTs. The reaction between the (6,5)-CNTs and the 1-iodohexane was then initiated by adding sodium dithionite ( $\text{Na}_2\text{S}_2\text{O}_4$ ), resulting in the formation of hCNTs schematically shown in Fig. 5.1 (a). Based on the same chemistry, quantum defects in CNTs generated by attaching a different residue may be obtained by substituting 1-iodohexane by virtually any hydrocarbon precursor containing iodine [48].

The room-temperature photoluminescence excitation (PLE) maps in Figs. 5.1 (c)–(e) illustrate the changing PL response of (6,5)-CNTs in the course of this reaction.<sup>2</sup> In the map

<sup>2</sup> This data was recorded by the group of YuHuang Wang from the University of Maryland.

in Fig. 5.1 (c) that was recorded before the addition of sodium dithionite only a single PL peak at 1.25 eV (992 nm) is present, in good agreement with literature values for the  $E_{11}$  emission [33, 35]. Sodium dithionite was then admixed, starting the formation of hCNTs and giving rise to two new emission features X at 1.13 eV (1095 nm) and T at 1.01 eV (1226 nm), as shown in Fig. 5.1 (e).

The route towards understanding the nature of these two new emitting states lies within the observation that sodium dithionite not only initiates the formation of hCNTs but also acts as a reducing agent that introduces excess electrons into the CNTs [P2]. By tuning the system to a hole-doped regime instead, e. g. by lowering pH, the intensity of T emission was reduced significantly compared to the intensity of X emission, as indicated in Fig. 5.1 (d). This observation indicates that X and T are different charge configurations of the newly created defect sites in hCNTs.

The origin of emission in the X spectral band was already investigated in an earlier study of CNTs functionalized with the same chemistry as discussed above [48]. That work combined recording of PL in the course of the chemical reaction with simultaneous Raman scattering and X-ray photoelectron spectroscopy (XPS) measurements. It was found that the rise of PL in the X spectral band is accompanied by an increase of the disorder-induced Raman D band ( $\sim 1300\text{ cm}^{-1}$ ) that is a direct measure of covalent generation of defects in the CNT  $sp^2$  lattice [282–284]. Similarly, XPS revealed the simultaneous appearance of a  $sp^3$  carbon 1s peak as a shoulder of the  $sp^2$  carbon 1s peak [48]. In conjunction, this proves that the X emission originates from  $sp^3$  defects introduced by functionalizing the CNTs with hexyl.

PL in the T spectral band, however, was not discussed in [48], since the functionalizing substituent employed in that work featured practically no T emission, as detailed below. Nonetheless, systematic studies of PL intensities of X and T as a function of pH in [P2] revealed that X and T can be attributed to an electrically neutral and a negatively charged regime, respectively. This result suggests that X corresponds to electrically neutral excitons localized at the generated  $sp^3$  defects, while T corresponds to similarly localized negative trions comprising two electrons and one hole.

Room-temperature hyperspectral maps of dispersed hCNTs were recorded to gain deeper insight into the nature of the X and T emission.<sup>3</sup> Fig. 5.1 (f) shows the spectrally integrated PL intensity emitted along a  $\sim 7\text{ }\mu\text{m}$  long hCNT. In the individual hyperspectral maps for  $E_{11}$ , X and T in Figs. 5.1 (g)–(i) the spatial intensity variations in Fig. 5.1 (f) decompose into homogeneous  $E_{11}$  emission (cf. Fig. 5.1 (g)) and hot spots of PL in the X and T spectral band (cf. Figs. 5.1 (h) and (i)) that are spatially correlated. Unlike the uniform  $E_{11}$  emission, PL in the X and T spectral bands therefore must originate from the same localized emitting sites. These findings provide strong evidence that also PL in the T spectral band originates from the same  $sp^3$  defects in the CNT lattice as the X emission.

---

<sup>3</sup> This data was recorded by the group of Stephen Doorn from the Los Alamos National Laboratory.

To further establish the localized nature of T emission, we performed cryogenic photon correlation measurements in the corresponding spectral band. Fig. 5.1 (b) shows normalized T photon coincidence counts for an individual hCNT at 4.2 K under pulsed laser excitation at 850 nm with 50  $\mu$ W (red histogram). The fit of the second-order correlation function  $g^{(2)}(\tau)$  to the data (black line) reveals pronounced bunching and a strong antibunching dip at zero time delay corresponding to a single-photon purity of  $\eta = 0.89$  [P2]. This hallmark of quantum light statistics for PL in the T spectral band is yet another proof of localization of the photoexcited states, which constitutes a prerequisite for the suppression of simultaneous photon emission. For PL in the X spectral band we obtained similar results (data not shown). In conjunction, the above findings prove that X and T emission originate from neutral excitons and negatively charged trions, respectively, both trapped at the  $sp^3$  defects generated by the covalent attachment of hexyl residues to the  $sp^2$  lattice of (6, 5)-CNTs.

After the nature of the X and T emission features has been established, a short outlook shall highlight the versatility of the presented functionalization approach. Quantitative ensemble PL measurements showed that the T emission from hCNTs is exceptionally bright, more than three times brighter than  $E_{11}$  [48]. This finding is in contrast to free trions in unfunctionalized CNTs (cf. Section 2.4) that can only be observed for high excitation powers [164] or strong doping [285] with intensities significantly below that of  $E_{11}$ . Already in earlier studies, localized trions were found to exceed the brightness of free trions, but even the strongest previously reported trion PL was more than seven times weaker than in hCNTs [286], rendering the T emission from hCNTs the brightest reported trion to date [48].

Furthermore, systematic studies of (6, 5)-CNTs functionalized with different fluorinated residues identified a route towards deterministic tunability of X and T emission energies. The experiments in [48, P2] found that both  $E_X$  and  $E_T$  redshift linearly with increasing Taft constant  $\sigma^*$  [287–289], which measures the influence of a substituent through polar effects [290, 291]. Since  $\sigma^*$  is a function of electronegativity [291], the substitution of fluorine for hydrogen in the hexyl residue varies  $\sigma^*$  over a broad range of values, allowing  $E_X$  and  $E_T$  to range from 133 meV to 190 meV [48] and from 253 meV to 277 meV [P2], respectively.

At the same time, for deep trapping of T corresponding to a large Taft constant  $\sigma^*$ , the PL intensity of T becomes weak due to the pronounced electron-withdrawing nature of highly fluorinated residues, depleting the trap of excess negative charges that are required for the formation of trions [P2]. Since the earlier study in [48] employed perfluorinated hexyl residues to functionalize (6, 5)-CNTs, T emission was almost absent and the Raman and XPS experiments mentioned above focused on the properties of X only.

In conclusion, the presented methods pave the way to a flexible chemistry for the covalent functionalization of CNTs that creates materials hosting both trapped neutral excitons and trapped negative trions with exceptionally bright PL. The microscopic nature of the corresponding defect states and the pronounced quantum characteristics of light emitted from individual hCNTs are discussed in the following sections.

### 5.3. Multiplicity of defect states in cryogenic hexyl-functionalized carbon nanotubes

In Section 5.2 the properties of hCNTs were mainly discussed in terms of ensemble characterizations at room temperature. This section focuses on studies of isolated hCNTs at cryogenic temperatures and aims to highlight variations in their physical properties at the single-tube level.<sup>4,5</sup>

For these measurements, we dispersed hCNTs prepared as introduced in Section 5.2 from an aqueous suspension onto the flat side of a hemispherical solid immersion lens (SIL) with an average spatial density of less than one hCNT per focal spot area of  $\sim 1 \mu\text{m}$  diameter (cf. Section 3.2). The sample was then cooled to cryogenic temperatures and placed into the focus of the confocal microscope as detailed in Section 3.1 to record PL of individual hCNTs.

The room-temperature ensemble PLE map of the investigated hCNT batch in Fig. 5.2 (a) shows three broad emission maxima of PL in the  $E_{11}$ , X, and T spectral bands at 1.25 eV, 1.13 eV, and 1.01 eV, respectively, with  $\sim 50$  meV full width at half maximum (FWHM) line-width.<sup>6</sup> By contrast, these features decomposed into much narrower peaks of variable emission energy and intensity at the individual level at 4.2 K (Fig. 5.2 (b)). The variety of PL spectra included examples with a single dominating peak (topmost spectrum in Fig. 5.2 (b)), two peaks with comparable intensity (second spectrum from top in Fig. 5.2 (b)) or multipeak spectra (third spectrum from top in Fig. 5.2 (b)).

A statistical analysis of the recorded peak positions for all observed hCNTs in the histogram in Fig. 5.2 (c) (gray) revealed an accumulation in three emission bands that closely resembled the room-temperature ensemble spectrum (blue line) obtained from the line cut (white dashed line) in the PLE scan in Fig. 5.2 (a). The microscopic origin of these spectral variations contributing to the  $\sim 50$  meV broadening at room temperature was further investigated by the experiments described in the following.

Time-resolved PL decay measurements were performed by exciting individual hCNTs with the Ti:sapphire laser in pulsed mode, selecting the spectral bands corresponding to  $E_{11}$ , X, and T emission by suitable combinations of optical long and short pass filters, and time correlating laser trigger signals and PL events detected by a superconducting single-photon detector (SSPD) (cf. Section 3.1). As for the PL spectra in Fig. 5.2 (b), we found differing characteristics for the PL decay of single hCNTs.

---

<sup>4</sup> Parts of this section are based on the publication [P2] available at <https://pubs.acs.org/doi/10.1021/acscentsci.9b00707>. Permission for any further reuse of the excerpted material must be granted by the American Chemical Society.

<sup>5</sup> Parts of this section are based on the publication [P3] available at <https://pubs.acs.org/doi/10.1021/acs.nanolett.9b02553>. Permission for any further reuse of the excerpted material must be granted by the American Chemical Society.

<sup>6</sup> This data was recorded by the group of YuHuang Wang from the University of Maryland.

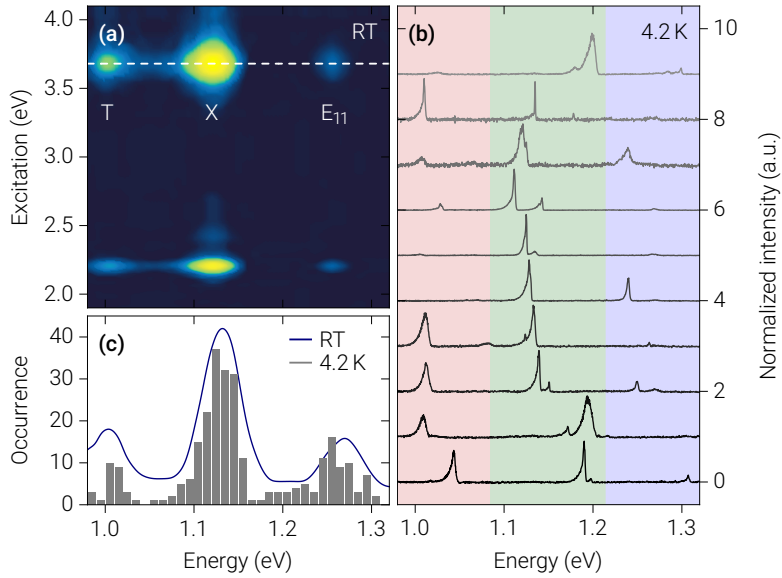


**Figure 5.2.:** Room-temperature and cryogenic hCNT spectra. **(a)** Room-temperature ensemble PLE map of hCNTs in the electron-doped regime showing  $E_{11}$ , X, and T emission with peak energies at 1.25 eV, 1.13 eV, and 1.01 eV, respectively. **(b)** Selection of normalized PL spectra of individual hCNTs at 4.2 K, offset vertically for clarity. The spectral bands of  $E_{11}$ , X, and T emission are shaded in blue, green, and red, respectively. **(c)** Histogram of emission peak energies of all recorded cryogenic hCNT PL spectra (gray) compared with the room-temperature ensemble spectrum (dark blue) obtained from the line-cut indicated by the dashed line in (a). The graphics (a)–(c) are reproduced from [P3].

Figs. 5.3 (a)–(c) show representative PL decay measurements in the  $E_{11}$ , X, and T spectral band (blue, green, and red, respectively) of an individual hCNT. Biexponential fits to the data revealed the presence of a dominating decay component with a corresponding lifetime  $\tau_1$  for each of the three emission features, while the amplitude of the second decay component was found to equal zero within the fit error bounds. This second decay component was therefore neglected, resulting in the monoexponential fits shown in Figs. 5.3 (a)–(c) (solid lines) with lifetimes  $\tau_1 = 50$  eV, 410 eV, and 390 eV for  $E_{11}$ , X, and T, respectively. Note that particularly for  $E_{11}$  in Fig. 5.3 (a) a small part of the PL decay of relative magnitude  $\sim 10^{-3}$  is not captured by the monoexponential fit. However, also a biexponential fit is not able to fully reproduce this fraction of the data. Instead, it could be attributed to the instrument response function (IRF) (gray) that flattens at similar time delays.

Analogous PL decay measurements for another hCNT are presented in Figs. 5.3 (d)–(f). Unlike the PL decay in Figs. 5.3 (a)–(c), both decay components of biexponential fits to the data (solid lines) were pronounced with short to long lifetime component ratios of 89% : 11% for  $E_{11}$ , 55% : 45% for X, and 67% : 33% for T. The corresponding short and long lifetimes were determined as  $\tau_1 = 70$  eV, 230 eV, and 120 eV and  $\tau_2 = 200$  eV, 590 eV, and 450 eV for  $E_{11}$ , X, and T, respectively. Note that the different excitation laser powers of 20  $\mu$ W and 1  $\mu$ W

## 5. PROPERTIES OF QUANTUM DEFECTS IN FUNCTIONALIZED CARBON NANOTUBES

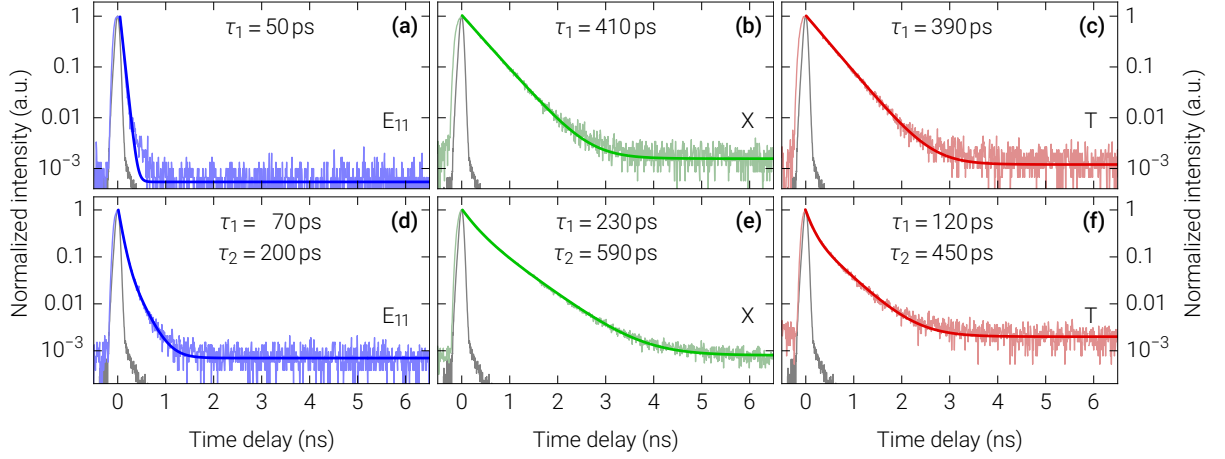


**Figure 5.3.:** Time-resolved PL decay measurements of individual hCNTs at 4.2 K. **(a)–(c)** PL decay for the  $E_{11}$  (blue, left), X (green, middle), and T (red, right) emission of an hCNT characterized by monoexponential fits (solid lines) within error bars with corresponding lifetimes  $\tau_1$ . The hCNT was excited off-resonantly at 850 nm with 20  $\mu$ W laser power. The IRF is shown in gray. **(d)–(f)** PL decay for the  $E_{11}$  (blue, left), X (green, middle), and T (red, right) emission of an hCNT characterized by biexponential fits (solid lines) with corresponding lifetimes  $\tau_1$  and  $\tau_2$ . The hCNT was excited off-resonantly at 842 nm with 1  $\mu$ W laser power. The IRF is shown in gray. The graphics (d)–(f) are reproduced from [P3].

in Figs. 5.3 (a)–(c) and in Figs. 5.3 (d)–(f), respectively, cannot account for the different decay dynamics, since care was taken to excite the hCNTs in the linear-response regime.

To allow for an overview of the variations in the PL decay dynamics, Figs. 5.4 (a)–(c) present the fraction of the total PL decay intensity associated with the shorter lifetime  $\tau_1$  (closed circles) and the longer lifetime  $\tau_2$  (open circles) in the  $E_{11}$  (left), the X (middle), and the T (right) spectral band for all analyzed hCNTs. Note that for emitters with monoexponential decay characteristics the longer lifetime  $\tau_2$  was omitted, explaining the different number of closed and open symbols in Figs. 5.4 (a)–(c).

The significantly prolonged PL lifetimes for X and T as compared to  $E_{11}$  are consistent with previous reports identifying this characteristic as a hallmark of exciton localization at covalent  $sp^3$  defects in CNTs [292]. By contrast, the observation of both monoexponential and biexponential PL decay requires closer inspection. Already in earlier studies, pristine CNTs have been observed to occasionally exhibit either monoexponential [225, 293] or biexponential [63, 294, 295] PL decay behavior. Both limits were captured within the same framework in [296] by assuming the existence of a dark state and, in the case of monoexponential decay, the presence of an extrinsic nonradiative decay channel due to coupling to the environment or exciton trapping at defects.

While a dark state slightly below the  $E_{11}$  energy in CNTs is well-established (cf. [36, 139] and Section 2.4) and the  $E_{11}$  lifetimes measured here coincide with earlier reports on pristine

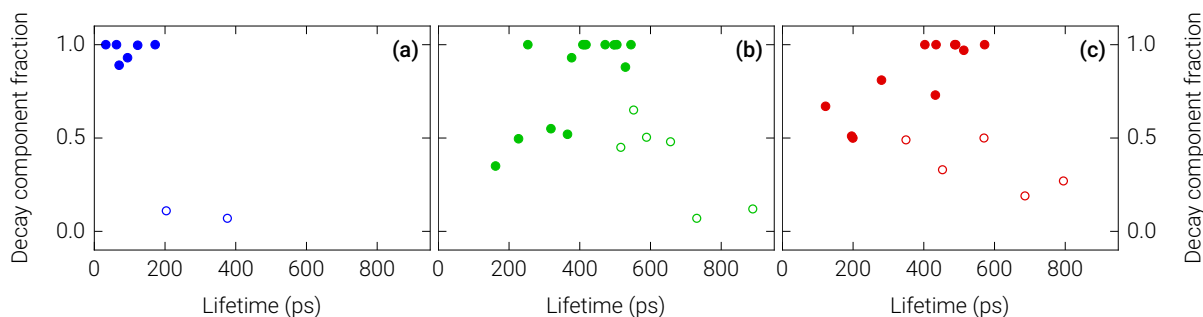


**Figure 5.4.:** Fraction of the total PL decay of hCNTs associated with the shorter lifetime  $\tau_1$  (closed circles) and the longer lifetime  $\tau_2$  (open circles) in (a) the  $E_{11}$ , (b) the X, and (c) the T spectral band. Note that for a number of hCNTs the fraction associated with  $\tau_2$  was zero within error bounds, explaining the different number of closed and open symbols. The graphics (a)–(c) are reproduced from [P3].

CNTs at cryogenic temperatures [225], dark states in the energetic vicinity of X and T appear implausible in view of the exceptional brightness of these states. Assuming a similar dark state mechanism for X and T characterized by predominantly nonradiative decay would imply brighter PL from  $E_{11}$  than from X and T owing to the shorter  $E_{11}$  lifetimes, which is not in agreement with experimental findings. Furthermore, based on the bright PL emission, X and T QYs were estimated to exceed the value expected for a complete conversion of the bright  $E_{11}$  population to the trapped states [P2]. This finding indicates an efficient radiative relaxation mechanism for X and T that is incompatible with the presence of a dark state governing the PL decay dynamics.

To test this reasoning we placed the sample in the center of a superconducting solenoid and probed the presence of dark states in the energetic vicinity of X and T using magnetophotoluminescence (MPL) spectroscopy on individual hCNTs. To illustrate the effects of a magnetic field on the  $E_{11}$  dark state, Fig. 5.5 (d) shows the PL response of an individual (6,5)-CNT from an unfunctionalized control sample for magnetic fields between 0 T and 8 T.

The  $E_{11}$  spectral shape evolved in agreement with the effects of an increasing Aharonov-Bohm flux [145–147] colinear with the CNT axis. Below the  $E_{11}$  emission peak at 1.296 eV a second PL peak at 1.291 eV emerged that was previously identified as the parity-forbidden lowest-energy singlet exciton state, being optically inactive at zero magnetic field but gaining increasing optical intensity with growing magnetic flux (cf. [128] and Section 2.4). Fig. 5.5 (a) presents the corresponding spectra for magnetic fields of 0 T, 4 T, and 8 T. Lorentzian fits to the bright and dark exciton peaks were performed for all magnetic fields (solid gray lines) with their respective sums (solid dark blue lines) reproducing the data. The areas under the individual Lorentzian fits revealed that the dark exciton exceeds the intensity of the bright exciton for magnetic fields above  $\sim 4$  T.

From the peak centers of the two respective Lorentzian functions also the bright-dark splitting  $\Delta$  was obtained for all magnetic fields. In a plot of  $\Delta^2$  as a function of squared mag-

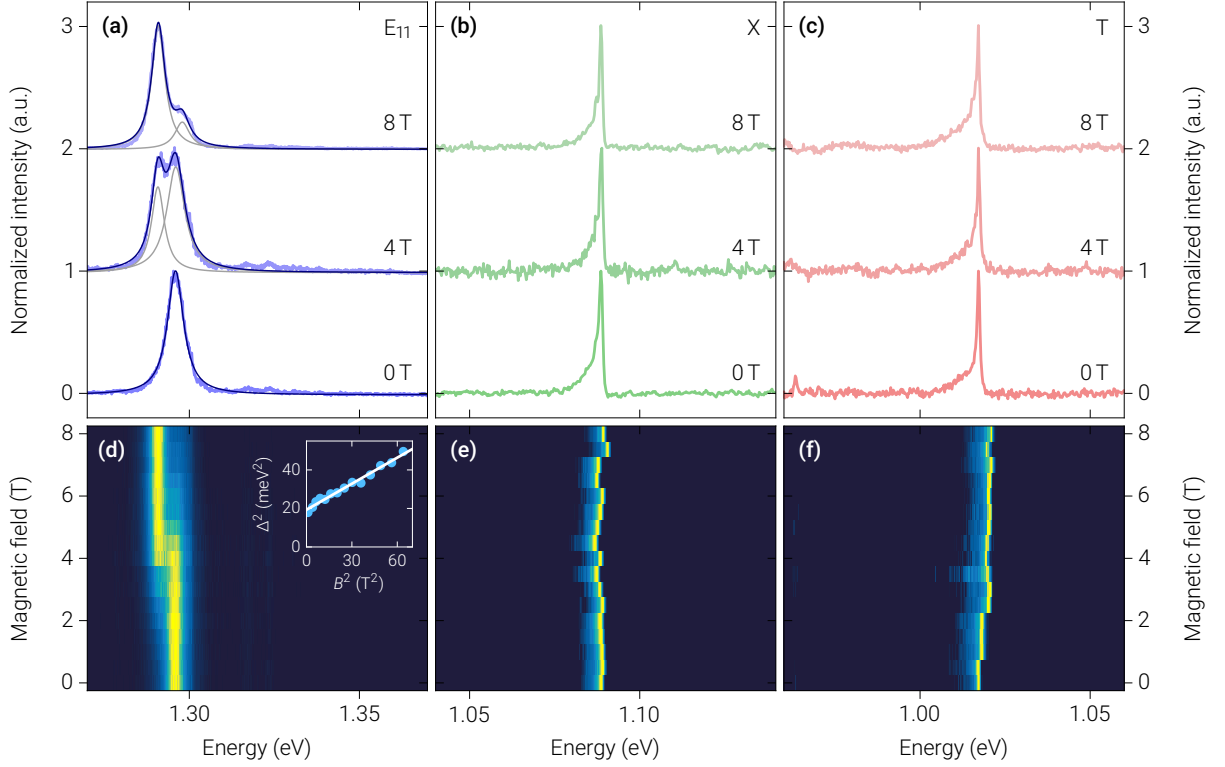


**Figure 5.5.:** MPL spectroscopy of pristine and covalently functionalized CNTs. **(a)–(c)** Normalized PL spectra of E<sub>11</sub> emission from a pristine (6,5)-CNT (blue, left panel), as well as X (green, central panel) and T (red, right panel) emission from hCNTs at zero magnetic field (bottom row), 4 T (middle row), and 8 T (top row). The solid gray lines in (a) show Lorentzian fits to the bright and dark exciton peaks with their sum plotted as solid dark blue line. **(d)–(f)** Evolution of the PL response in the E<sub>11</sub> (left panel), X (central panel), and T (right panel) spectral bands of the respective CNTs in (a)–(c). The inset in (d) illustrates the magnetic-field dependency of the singlet E<sub>11</sub> bright-dark splitting  $\Delta$ . The graphics (a)–(f) are reproduced from [P2].

netic field  $B^2$  (inset in Fig. 5.5 (d)) the fit values (blue data points) were well reproduced by the hyperbolic relation  $\Delta^2 = \Delta_0^2 + \Delta_{AB}^2$  (solid white line) [150]. Here,  $\Delta_0$  is the zero-field bright-dark splitting and the field-induced splitting  $\Delta_{AB} = \mu\phi$  is given by the Aharonov-Bohm flux  $\phi = \frac{1}{4}\pi d_{(6,5)}^2 B_{\parallel}$  (cf. [150]) with  $d_{(6,5)} = 0.757$  nm being the diameter of a (6,5)-CNT [35] and  $B_{\parallel} = B \cos\theta$  being the magnetic-field component parallel to the CNT axis. By determining the angle  $\theta$  between the CNT axis and magnetic field through the CNT PL antenna effect [297] to 45°, the magnetic coupling constant and the zero-field bright-dark splitting were found to equal  $\mu = 1.8$  meV/T · nm<sup>2</sup> and  $\Delta_0 = 4.5$  meV, respectively, similar to values previously reported in literature [131, 132]. In conjunction, these findings prove the presence of a E<sub>11</sub> dark state in unfunctionalized (6,5)-CNTs (cf. Section 2.4).

By contrast, neither the X (Figs. 5.5 (b) and (e)) nor the T emission peaks (Figs. 5.5 (c) and (f)) of individual hCNTs showed any significant change subject to magnetic fields up

to 8 T. Both emission features remained solitary peaks throughout the entire magnetic field sweep and also no splittings or systematic energy shifts were observed within the experimental limits given by the spectral resolution limit of our spectrometer ( $\sim 300 \mu\text{eV}$ ) and random temporal fluctuations of the emission energy ( $\sim 2 \text{ meV}$ ). In agreement with the exceptional brightness of the hCNT defect PL, this finding supports the interpretation that X and T are the respective lowest-energy states of the neutral and negatively charged trap, increasing the QY of the radiative relaxation pathway. The absence of a prominent dark-state contribution to X and T emission, however, calls for a different mechanism explaining the frequent occurrence of two pronounced decay components in Figs. 5.4 (b) and (c).

The lack of a systematic shift in the PL energy for T in Figs. 5.5 (c) and (f) is remarkable given the observation that an unpaired spin of the excess electron contained in the trion state should couple to the magnetic field (cf. Section 2.4), causing a Zeeman splitting of the emission energy [298, 299]. This puzzle is resolved by considering the intervalley nature of trions in CNTs. Due to the weak spin-orbit coupling in CNTs [300] the exchange interaction favors the intervalley configuration of the two electrons (both electrons in opposite valleys) over the intravalley configuration (both electrons in the same valley). In the recombination process, the electron with unpaired spin is thus effectively a spectator of an exciton residing in the opposite valley.

By consequence the total spin projections along the magnetic field axis are the same for the initial state (trion) and the final state (excess electron), resulting in the same energy difference for the optical transition irrespective of the orientation of the unpaired spin. This scenario is conceptually similar to optical transitions in monolayer transition metal dichalcogenide (TMD) crystals, in which the splitting induced by magnetic fields is entirely due to the valley Zeeman effect, while the spin Zeeman contribution is zero [301, 302]. By contrast, the valley Zeeman effect in CNTs is expected to be very small due to the electron-hole symmetry inherited from graphene [303].

With pronounced couplings of X and T to a dark state being excluded, a straightforward explanation for the presence of two different PL lifetimes lies within the scenario of simultaneously observing two distinct emitters in the focal spot of the confocal microscope. While the occurrence of two hCNTs in close proximity was disfavored by choosing a low spatial concentration of CNTs on the substrate, other studies have established that the chemistry for covalent functionalization of CNTs promotes the generation of proximal defects within the same CNT via defect-assisted local destabilization of the carbon lattice [48, 304]. As opposed to earlier reports discussing also divalent functionalization, i. e. binding of residues to more than one CNT carbon atom [305], the more deterministic sodium dithionite chemistry used for this work is expected to preferentially give rise to monovalent defects in close proximity. The validity of the hypothesis that biexponential PL decay for X and T may be explained by the presence of more than one defect site per focal spot is investigated further by means of PL time correlation measurements in Section 5.4.

## 5.4. Photon correlation spectroscopy of defect states in cryogenic hexyl-functionalized carbon nanotubes

The MPL spectroscopy measurements presented in Section 5.3 suggested the absence of dark states in the energetic vicinity of X and T in hCNTs and motivated the hypothesis that biexponential PL decay for X and T as in Figs. 5.3 (e) and (f) are caused by two proximal covalent defects in the focal spot of the confocal microscope. In order to test this hypothesis, we performed photon correlation spectroscopy of E<sub>11</sub>, X, and T emission from individual cryogenic hCNTs and employed characteristic features in the correlation data as guidelines for the formulation of a model capturing the population dynamics among the E<sub>11</sub>, X, and T states.<sup>7</sup> To this end, hCNTs were excited with the Ti:sapphire laser in continuous wave (CW) mode, spectral bands in the PL corresponding to E<sub>11</sub>, X, and T were selected by suitable combinations of optical long and short pass filters, and PL was detected and time-correlated with two SSPDs in a Hanbury Brown-Twiss (HBT) configuration (cf. Section 3.1). For autocorrelation measurements, both SSPDs were set to detect PL in the same spectral band of either E<sub>11</sub>, X, or T, whereas for crosscorrelation measurements different spectral bands were selected for the two single-photon counting channels. This configuration allowed for the measurement of photon coincidence counts in both autocorrelation and crosscorrelation, as introduced in Section 2.5.

For reference, we first performed E<sub>11</sub> autocorrelation measurements on single hCNTs at 4 K that are presented in Figs. 5.6 (a)–(c). To examine the different degrees of photon antibunching and bunching, we considered a model of a bright exciton state that exchanges population with a reservoir of dark excitons [67, 73, 306].<sup>8</sup> In this framework, the  $g^{(2)}$  function is given by the expression in Eq. (B.15) in Section B.1,

$$g^{(2)}(\tau) = \left(1 - \eta \cdot e^{-\frac{|\tau|}{\tau_0}}\right) \left(1 + \frac{\tau_d}{\tau_s} e^{-\left(\frac{1}{\tau_s} + \frac{1}{\tau_d}\right)|\tau|}\right), \quad (5.1)$$

where also a derivation from a three-level system is presented. In Eq. (5.1),  $\tau_0$  is an effective timescale that determines the duration at which single-photon emission prevails,  $\kappa_s = 1/\tau_s$  and  $\kappa_d = 1/\tau_d$  are the shelving and deshelling rates for transitions from the bright state to the dark state and vice versa, and  $\eta$  is the degree of photon antibunching correlation (cf. Section B.1 for details).

<sup>7</sup> Parts of this section are based on the publication [P3] available at <https://pubs.acs.org/doi/10.1021/acs.nanolett.9b02553>. Permission for any further reuse of the excerpted material must be granted by the American Chemical Society.

<sup>8</sup> Note that the notion of a *dark state* in this model is different from the dark state employed in [296] that was ruled out for X and T in Section 5.3. While here the dark state is a shelving state without a decay channel that would compromise the QY, the dark state in [296] is solely characterized by nonradiative decay. For details refer to Figs. B.1 (a) and (b) in Section B.1.

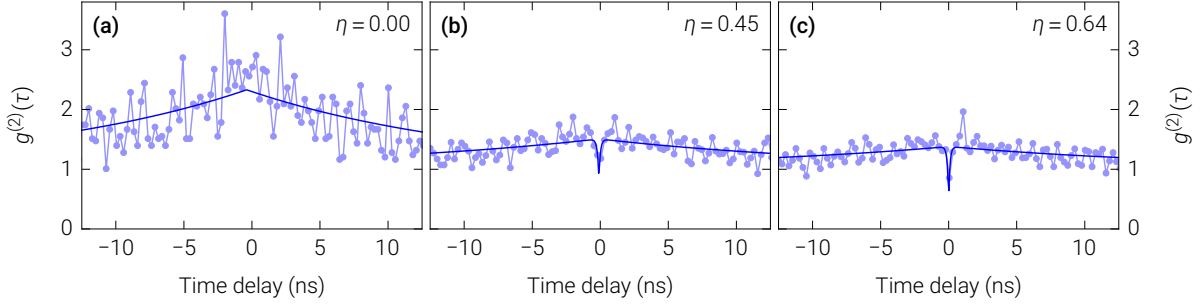


**Figure 5.6.:** Normalized photon coincidence counts  $g^{(2)}(\tau)$  for the  $E_{11}$  autocorrelation of different hCNTs featuring (a) bunching only with no antibunching, (b) weak bunching with weak antibunching, and (c) weak bunching with moderate antibunching. The hCNTs were excited off-resonantly at 840 nm, 852 nm, and 838 nm with  $10\ \mu\text{W}$ ,  $20\ \mu\text{W}$ , and  $25\ \mu\text{W}$  laser power, respectively. Fits to the data (solid blue lines) and degrees of autocorrelation  $\eta$  were obtained from the model  $g^{(2)}$  function from Eq. (5.1). The graphics (a)–(c) are reproduced from [P3].

As a measure for the degree of bunching due to PL intermittency we define  $g_{\text{max}}^{(2)} = 1 + \tau_d / \tau_s$  as the maximum value of the second factor in Eq. (5.1) at  $\tau = 0$ . When  $\kappa_s > \kappa_d$ , bunching is predominant in the sense that the emitter spends more time in the dark state than in the bright state, and this scenario is captured by  $g_{\text{max}}^{(2)} > 2$ . By contrast, for  $g_{\text{max}}^{(2)} < 2$  the emitter spends more time in the bright state than in the dark state. While in the absence of bunching the condition  $g^{(2)}(0) < 0.5$  is considered an evidence for single photon emission (cf. [63, 67] and Section 2.5), this requirement is not applicable in the presence of blinking due to the multiplication with the second term in Eq. (5.1). Instead, the degree of correlation  $\eta$  can be obtained from the  $g^{(2)}$  function by calculating  $\eta = 1 - g^{(2)}(0) / g_{\text{max}}^{(2)}$ , and the condition  $\eta > 0.5$  is indicative of single photon emission.

The model  $g^{(2)}$  function from Eq. (5.1) was employed to obtain fits<sup>9</sup> (solid blue lines) to the data presented in Figs. 5.6 (a)–(c) and to derive the degree of autocorrelation  $\eta$ . As evident from the different shapes of the fit functions and the values of  $\eta$  noted in the respective panels, we occasionally observed bunching with no antibunching (left panel,  $\eta = 0.00$ ), weak bunching with weak antibunching (central panel,  $\eta = 0.45$ ), and weak bunching with moderate antibunching (right panel,  $\eta = 0.64$ ). While the varying strength of bunching just as the differing fraction of biexponential decay in Fig. 5.4 (a) may be ascribed to extrinsic effects [74], the incidental observation of  $E_{11}$  antibunching [63] in conjunction with PL energy redshifts of few meV [60] are indicative of weak  $E_{11}$  exciton localization.

Figs. 5.7 (a)–(d) show normalized photon coincidence counts for X (green, upper panels) and T (red, lower panels) autocorrelation, respectively, for two different hCNTs denoted hCNT A (left column) and hCNT B (right column) in the following. The autocorrelation data

<sup>9</sup> Note that there is a fundamental difference between the measured photon coincidence counts and the  $g^{(2)}$  function for high photon count rates. Here, the count rates were low enough to neglect this difference and the two terms will sometimes be used synonymously in this section. For details refer to Section 2.5.

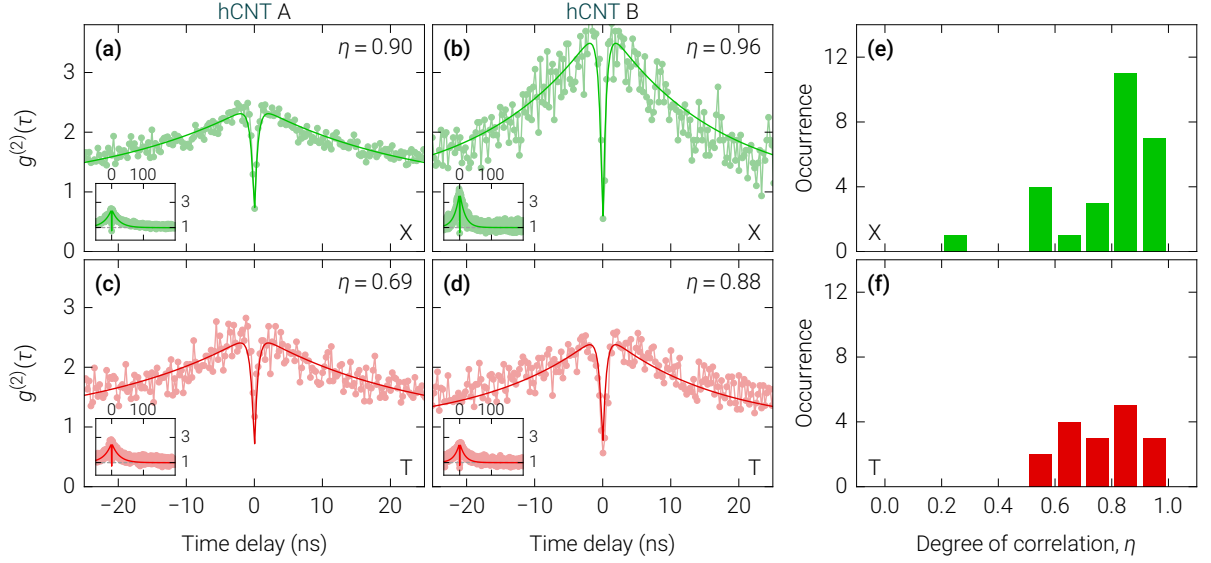


**Figure 5.7.:** Autocorrelation data of individual hCNTs. (a)–(d) Normalized photon coincidence counts  $g^{(2)}(\tau)$  for the autocorrelation of X (green, upper panels) and T (red, lower panels) for two different hCNTs A and B, excited resonantly via their respective  $E_{11}$  states at 975 nm and 960 nm with 1  $\mu$ W and 3  $\mu$ W laser power. The insets illustrate that  $g^{(2)}(\tau)$  approaches unity on long time scales. Fits to the data (solid lines) were obtained with the  $DS_1$  model (left column) and the  $DS_2$  model (right column), respectively. The values for the degree of autocorrelation  $\eta$  were determined using Eq. (5.1). (e)–(f) Distribution of the degrees of correlation  $\eta$  obtained from Eq. (5.1) for autocorrelations of X (green, upper panel) and T (red, lower panel), respectively. The graphics (a)–(f) are reproduced from [P3].

for both spectral features exhibited antibunching ( $g^{(2)}(\tau) < 1$ ) on timescales shorter than  $\sim 1$  ns and bunching ( $g^{(2)}(\tau) > 1$ ) on timescales longer than  $\sim 1$  ns, respectively, characteristic for intermittent single-photon emission [67, 73, 307, 308]. For sufficiently large delay times, photon emission from both states was uncorrelated, as illustrated by the insets in Figs. 5.7 (a)–(d) with  $g^{(2)}(\tau)$  approaching unity on long time scales. These signatures identify the X and T states in both hCNTs as single photon emitters subject to PL intermittency.

The model  $g^{(2)}$  function in Eq. (5.1) was employed to fit the autocorrelation data of all investigated hCNTs. For the hCNTs A and B the resulting best fit functions (solid lines in Figs. B.2 (a)–(d) in Section B.1) yielded degrees of autocorrelation  $\eta$  of 0.90 and 0.96 for X, and 0.69 and 0.88 for T, respectively. At the statistical level, the histograms in Figs. 5.7 (e) and (f) show that  $\eta > 0.5$  was observed for all hCNTs, except for one single hCNT with  $\eta = 0.3$  in X autocorrelation. This finding identifies the X and T states in cryogenic hCNTs as strongly correlated single-photon emitters. In a similar manner, the shelving and deshelling timescales  $\tau_s$  and  $\tau_d$  were analyzed and exhibited ranges of 10–900 ns (with medians of 37 ns and 53 ns for  $\tau_s$  and  $\tau_d$ ) for X emission, and 10–100 ns (with similar medians of 37 ns and 47 ns for  $\tau_s$  and  $\tau_d$ ) for T emission.

In order to relate the PL intermittency of the X and T states to the corresponding distributions of exciton population, we first considered a model where the two states are their mutual dark reservoirs, subsequently termed **ME** model. In this scenario, trapping and release of an additional charge at the defect site would switch the hCNT PL between the charged and neutral exciton emission and render X and T the respective dark states of each other, conceptually similar to earlier correlation studies on spectral wandering [73, 308] and charge hopping in semiconductor quantum dots [181, 309, 310]. According to this microscopic picture, both X and T emission would naturally be subject to blinking and thus exhibit bunching in autocorrelation measurements as in Figs. 5.7 (a)–(d) without the need to introduce a separate dark reservoir. The blinking time scale would correspondingly reflect the defect charging dynamics, with the PL photons providing snapshots of the defect charge configuration within the subnanosecond timescale of radiative decay.

The level scheme in Fig. B.3 in Section B.2 was constructed as a description for this scenario of mutually exclusive emission from X and T and the corresponding rate equation was solved numerically to obtain  $g^{(2)}$  fit functions to the autocorrelation data in Figs. 5.7 (a)–(d). The resulting best fits in Figs. B.4 (a)–(f) in Section B.2, however, are unable to reproduce the data, since the bunching behavior is only correctly reproduced for either X (Figs. B.4 (a) and (b)) or T (Figs. B.4 (d) and (e)), but not for both at the same time. This result can be understood by the observation that the autocorrelation data of both X and T assume values greater than 2 in the vicinity of zero time delay, implying  $g_{\max}^{(2)} > 2$  for both X and T. Turning back to the definition  $g_{\max}^{(2)} = 1 + \kappa_s/\kappa_d$ , however, it is evident that this outcome is impossible within the **ME** model, where blinking is explained by the mutual exclusiveness of emission from X and T, rendering the ratios of shelving and deshelling rate  $\kappa_s/\kappa_d$  from the perspective of X and T the inverse of each other. Consequently,  $g_{\max}^{(2)} > 2$  for X automatically implies  $g_{\max}^{(2)} < 2$  for T and vice versa (cf. Section B.2 for details).

More strikingly, the **ME** model is unable to capture the characteristics of X and T cross-correlation measurements. While the crosscorrelation data of hCNTs A (Fig. 5.8 (a)) and B (Fig. 5.8 (c)) featured a combination of antibunching on timescales shorter than  $\sim 1$  ns and bunching on timescales longer than  $\sim 1$  ns, respectively, just like the autocorrelation data, the **ME** model yields a too broad antibunching dip on the time scale of blinking and no bunching at all (solid gray lines in Figs. 5.8 (a), (c), B.4 (c), and (f)). This result is in agreement with earlier studies of charge-fluctuating quantum emitters [181, 307–310] and proves that the assumption of mutually exclusive emission from X and T cannot account for the bunching in the crosscorrelation data.

By contrast, the pronounced bunching in Fig. 5.8 (a) rather indicates that both X and T blink independent of the defect charge configuration. Unlike for the **ME** model, this observation suggests a blinking mechanism distinct from the defect states. To capture this scenario, we considered a model based on the level scheme presented in Fig. 5.8 (d), in the following named **DS<sub>1</sub>** model, where in addition to the ground state  $|0\rangle$ , the free exciton continuum

## 5. PROPERTIES OF QUANTUM DEFECTS IN FUNCTIONALIZED CARBON NANOTUBES

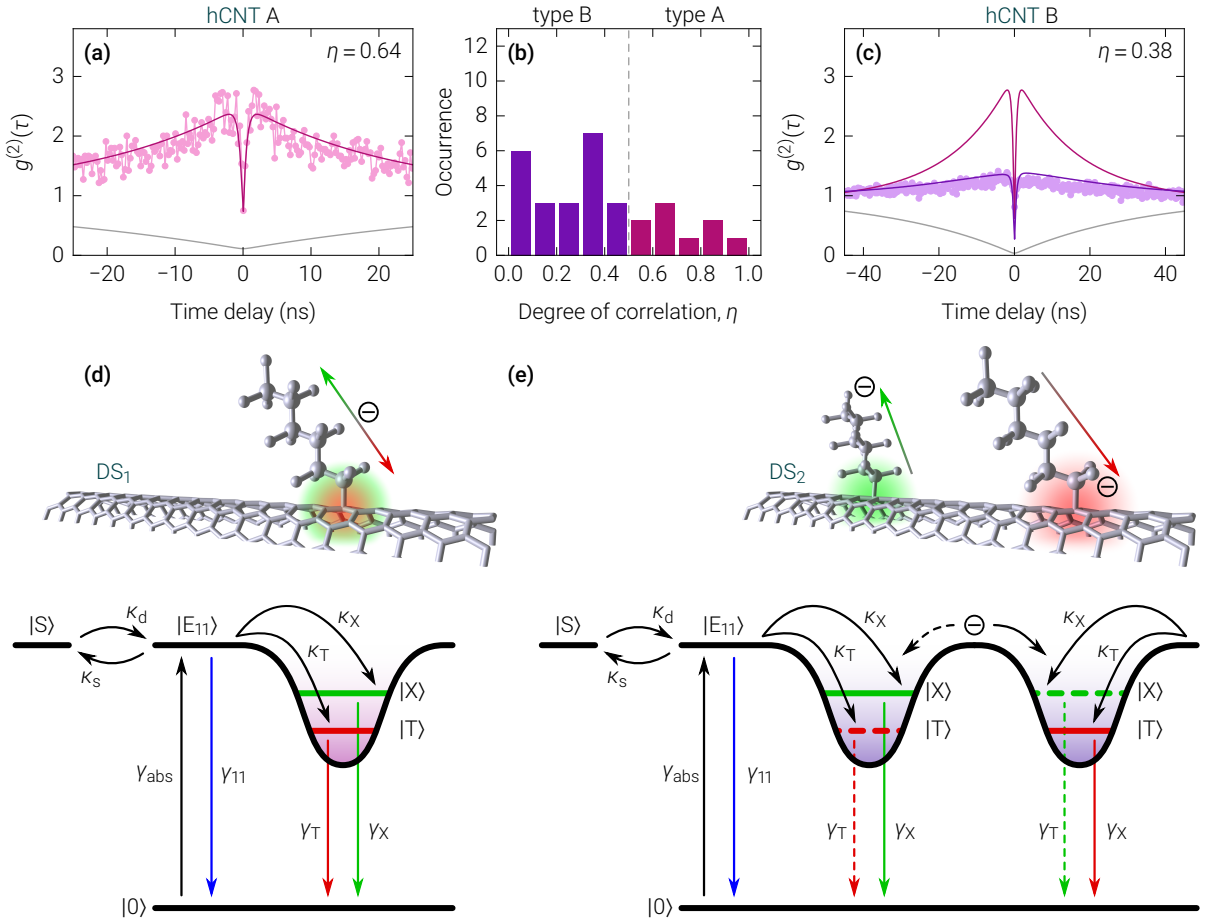


**Figure 5.8.:** Crosscorrelation data of individual hCNTs. (a) and (c) Normalized photon coincidence counts  $g^{(2)}(\tau)$  for the crosscorrelation of X and T emission from hCNTs A (left) and B (right) from Figs. 5.7 (a)–(d), excited resonantly via their respective  $E_{11}$  states at 975 nm and 960 nm with 1  $\mu$ W and 3  $\mu$ W laser power. Fits to the data (solid lines) illustrate the predictions for the  $g^{(2)}$  function given by the ME model (gray), the  $DS_1$  model (pink) and the  $DS_2$  model (violet) discussed in the main text. (b) Histogram of the degree of antibunching in the crosscorrelation of X and T. The dashed line at  $\eta = 0.5$  separates the CNTs with low (type B, violet) and high degrees of correlation (type A, pink). (d)–(e) Schematic of defect PL from a single and a double trap state, respectively, corresponding to type A and B hCNTs. The respective level schemes comprise the ground state  $|0\rangle$ , the free exciton continuum  $|E_{11}\rangle$ , the defect localized states  $|X\rangle$  and  $|T\rangle$ , and a shelving state  $|S\rangle$ . Transitions between these states are indicated by arrows with the model-relevant rates. The graphics (a)–(e) are reproduced from [P3].

$|E_{11}\rangle$ , and a single defect site comprising the states  $|X\rangle$  and  $|T\rangle$  an additional shelving state  $|S\rangle$  is included that acts as a dark reservoir constituting the origin of PL intermittency.<sup>10</sup> While in our PL experiments the exciton population was excited either resonantly or nonresonantly, higher energy states were eliminated in Fig. 5.8 (d) for simplicity by introducing an effective

<sup>10</sup> See footnote 8.

absorption rate  $\gamma_{\text{abs}}$  for the generation of  $E_{11}$  excitons that feature a radiative decay rate  $\gamma_{11}$ . This photoexcited bright exciton population can either interconvert with the dark reservoir at shelving and deshelving rates  $\kappa_s$  and  $\kappa_d$  or give rise to PL from X and T states at radiative decay rates  $\gamma_X$  and  $\gamma_T$  upon capture at rates  $\kappa_X$  and  $\kappa_T$  by a neutral or charged defect site, respectively.

As for the ME model, the corresponding rate equation was solved numerically to obtain  $g^{(2)}$  fit functions (cf. Section B.3). The respective best fits for hCNT A are shown as solid green and red lines for the autocorrelation data of X and T in Figs. 5.7 (a) and (c) and as solid pink line for the crosscorrelation data of X and T in Fig. 5.8 (a). It should be emphasized that all fit parameters were fixed by the fits to autocorrelation data, leaving no free parameters for the crosscorrelation data in Fig. 5.8 (a) (cf. Section B.3 for details). The overall good agreement between data and model therefore supports the assumption of an additional shelving state |S) as the origin of PL intermittency in X and T auto and crosscorrelation.

For hCNT B, however, the  $DS_1$  model is not able to produce an equally good agreement with the data. While the X and T autocorrelation measurements for hCNT B (Figs. 5.7 (b) and (d)) yielded results similar to the corresponding data for hCNT A (Figs. 5.7 (a) and (c)), the respective crosscorrelation results in Figs. 5.8 (a) and (c) were strikingly different. Whereas for hCNT A both bunching ( $g_{\text{max}}^{(2)} > 2$ ) and antibunching ( $\eta = 0.64$ ) were pronounced (cf. Fig. 5.8 (a)), both characteristics were weakly developed ( $g_{\text{max}}^{(2)} < 2$ ,  $\eta = 0.38$ ) for hCNT B (cf. Fig. 5.8 (c)). In consequence, we found a poor agreement between the hCNT B crosscorrelation data and the  $g^{(2)}$  fit function predicted by the  $DS_1$  model that overestimated both the degree of bunching and antibunching (solid pink line in Fig. 5.8 (c)), when fixing all fit parameters through the X and T autocorrelation data.

The contrasting behavior between hCNTs A and B was found to be a universal property of photon crosscorrelation measurements on individual hCNTs. While the degree of antibunching in X or T autocorrelation was generally found to exceed the threshold for single-photon emission,  $\eta > 0.5$  (Figs. 5.7 (e) and (f)), the corresponding value for X and T crosscorrelation showed a distribution between 0 and 1 with a majority of emitters falling into the regime  $\eta < 0.5$ . Depending on the value of  $\eta$  in X and T crosscorrelation, all investigated hCNTs were categorized as either type A (of which hCNT A is a representative), where  $\eta > 0.5$ , or type B (of which hCNT B is a representative), where  $\eta < 0.5$ . Regarding the PL intermittency, we similarly observed strong photon bunching for all X and T autocorrelation measurements, whereas for the crosscorrelation case bunching was generally strong only for hCNTs of type A and weak for type B.

Among the different characteristics between hCNTs of type A and type B the varying degree of bunching is particularly directive. Since the value  $g_{\text{max}}^{(2)}$  may be interpreted as the ratio of time intervals an emitter spends in a bright or dark configuration, respectively, the weak bunching in X and T crosscorrelation for type B hCNTs is particularly puzzling. Strong bunching in both X and T autocorrelation would imply that for both X and T emission

the emitter spends more time in the dark configuration than in the bright configuration. The *same* emission, however, when recorded in a crosscorrelation measurement would exhibit only weak bunching implying that the *joint* emission from X and T is bright for a greater fraction of time than dark. Not surprisingly, modifications to the  $DS_1$  model like the incorporation of additional shelving states as for the MSS model discussed in Section B.4 are unable to resolve this discrepancy.

Turning back to the observation that multiple covalent defects on the same CNT preferentially form in close proximity [48, 304], we consider another microscopic description. Two hexyl defects in sufficient proximity, both within the focal spot of the confocal microscope, would give rise to PL emission from their respective X and T states subject to time correlations governed by interactions between the neighboring sites. This scenario is depicted schematically in Fig. 5.8 (e), where the interaction between two defects is given by anticorrelation of their respective charge states due to repulsive Coulomb interaction between excess electrons residing on covalent hexyl chains [P2]. In the level scheme of Fig. 5.8 (e), this situation is represented by an electron hopping between the two defect sites.

Analogously to the  $DS_1$  model, a rate equation was formulated and solved numerically to obtain  $g^{(2)}$  fit functions (cf. Section B.5). Other than for the  $DS_1$  model, best fits for this model, in the following termed  $DS_2$  model, were found by using both autocorrelation and crosscorrelation data. For the autocorrelation data this procedure resulted in the  $g^{(2)}$  functions shown as solid lines in Figs. 5.7 (b) and (d). The corresponding  $g^{(2)}$  fit for the crosscorrelation is shown as solid violet line in Fig. 5.8 (c) and reproduces the data significantly better than the fit based on the  $DS_1$  model (solid pink line in Fig. 5.8 (c)). We therefore conclude that the  $DS_2$  model represents an adequate description of hCNTs of type B.

We proceed to give an intuitive interpretation of the fits in Figs. 5.7 (b), (d), and 5.8 (c) that pair strong autocorrelation with weak crosscorrelation. While pronounced antibunching in PL autocorrelation, indicative of single-photon emission from two different emitters, appears implausible at first glance, this feature is preserved by the suppression of equal charge states for the two defects in the  $DS_2$  model. Under this prerequisite, PL in the X and T spectral bands, respectively, originates predominantly from only one of the two defect sites at a given time. In other words, an autocorrelation measurement would detect photons from the two traps in random alteration, effectively summing the  $g^{(2)}$  functions of two blinking single photon emitters, resulting in both dominant bunching and antibunching.

For crosscorrelation measurements, by contrast, the two photon detection channels in the X and T spectral bands, respectively, would typically record photons from different defect sites and a change in charge configuration would swap the mapping between the traps and the detectors. In this scenario, both the degree of bunching and antibunching are compromised, since the photon emission events being correlated originate predominantly from two different defect sites with temporally independent emission statistics. A residual correlation is still present in the data due to events where after the detection of a first photon

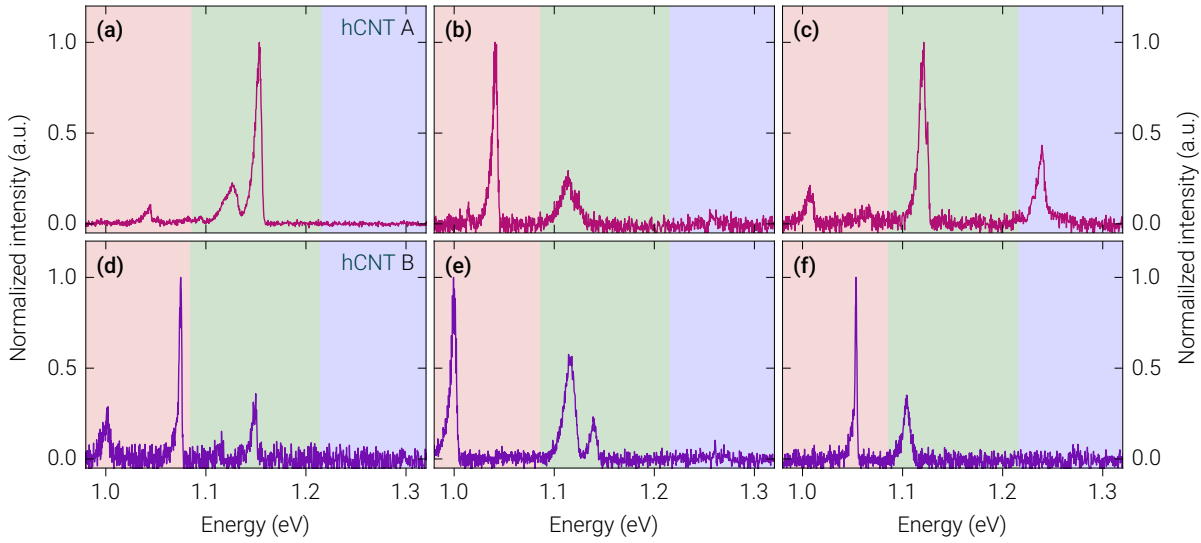


**Figure 5.9.:** Spectra of individual hCNTs with varying degree of crosscorrelation. (a)–(c) Cryogenic spectra of three hCNTs with strong crosscorrelations. The spectrum in (a) corresponds to hCNT A from Figs. 5.7 (a), (c), and 5.8 (a). (d)–(f) Cryogenic spectra of three hCNTs with weak crosscorrelations. The spectrum in (d) corresponds to hCNT B from Figs. 5.7 (b), (d), and 5.8 (c). The spectral regions of  $E_{11}$ , X and T emission are shaded in blue, green and red, respectively. The graphics (a)–(f) are reproduced from [P3].

the traps change their charge configuration and a second photon in the other spectral band from the same trap is recorded. Interestingly, our analysis of the fit quality showed that the suppression of strong crosscorrelation based on this mechanism requires the two emissive sites to differ in their respective charging and discharging rates.

In conclusion, we found that PL from both the X and T states exhibits strong signatures of single-photon emission and that the variety of results for the crosscorrelation measurements can be interpreted by the presence of a single or multiple defect sites within one focal spot that are subject to varying degrees of interaction. We also review other experimental results within the context of this finding. Figs. 5.9 (a)–(f) present spectra of hCNTs with strong crosscorrelations (pink, upper panels) and weak crosscorrelations (violet, lower panels), respectively. The blue, green and red shaded areas indicate the spectral bands of emission from  $E_{11}$ , X, and T, respectively. Note that the PL intensities within the different spectral bands were not corrected for the spectrally varying quantum efficiency of the InGaAs detector. The spectra in Figs. 5.9 (a) and (d) correspond to the hCNTs A and B discussed in Figs. 5.7 (a)–(d), 5.8 (a), and (c), respectively.

Based on the finding that strong X and T crosscorrelations correspond to a single defect site, generally one PL peak per X or T spectral band would be expected in Figs. 5.9 (a)–(c). While this is the case for Figs. 5.9 (b) and (c), the spectrum of hCNT A in Fig. 5.9 (a) features a double-peak in the spectral band of X. Since the pronounced antibunching in Fig. 5.7 (a)

excludes the possibility of two different emitters, this spectral signature likely originates from a temporally switching single-defect configuration as previously reported for cryogenic nanotubes with exciton-localizing unintentional defects [63] and defect-functionalized CNTs [59].

For hCNTs with weak crosscorrelation in Figs. 5.9 (d)–(f), by contrast, potentially unequal emission energies of neighboring defect sites caused by local variations of mechanical strain or dielectric screening would give rise to multiple PL peaks per X or T spectral band. Indeed, in the spectrum of hCNT B in Fig. 5.9 (d) two peaks are visible in each of the X and T spectral bands. The spectra in Figs. 5.9 (e) and (f), however, feature a pronounced double peak only for X but not for T and for none of the two states, respectively. These latter cases are therefore either characterized by incidentally equal emission energies of the two neighboring defects or time intervals during acquisition of the spectra in Figs. 5.9 (e) and (f), where PL from one defect site was switched off.

This selection of spectra highlights the rich variety of features that may arise due to the time-averaging manner of the corresponding experiments. While the time-correlation measurements discussed above clearly separated all hCNTs into two groups, a categorization based on spectral signatures appears difficult in view of hCNTs with similar spectra like in Figs. 5.9 (a) and (e) but clearly distinct degrees of X and T crosscorrelation. We conclude that the interpretation of time-averaged PL spectra is limited and inferior to time-resolved correlation spectroscopy.

To reveal possible correlations of the degree of correlation,  $\eta$ , and the degree of bunching,  $g_{\max}^{(2)}$ , between the different auto and crosscorrelation measurements, we present scatter plots for the values of  $\eta$  in Figs. 5.10 (a)–(c) and for the values of  $g_{\max}^{(2)}$  in Figs. 5.10 (d)–(f). We first consider the degree of correlation,  $\eta$ , which in the framework of the DS<sub>1</sub> and DS<sub>2</sub> models is determined by the intensity ratio of the PL signal and an uncorrelated background signal within the X and T spectral bands (cf. Sections B.3 and B.5 for details). Since these spectral bands are disjoint, we expect no correlation between the value of  $\eta$  for the autocorrelation of X and T. Indeed, the corresponding values scatter in the entire top right quadrant of Fig. 5.10 (a), where  $\eta > 0.5$  holds for the autocorrelation of both X and T. While the finding  $\eta > 0.5$  shows that both X and T are single photon emitters, there is no indication that a high degree of correlation for X also implies a high degree of correlation for T or vice versa. In that case, the data points would follow a diagonal line in Fig. 5.10 (a).

In a comparison of  $\eta$  between the autocorrelation of X or T and the crosscorrelation of X and T, for emitters captured by the DS<sub>1</sub> model a positive correlation for the autocorrelation and the crosscorrelation values of  $\eta$  is expected, as the emission background from the autocorrelation contributes “half” to the emission background in the crosscorrelation. If *all* emitters were properly described by the DS<sub>1</sub> model, the data points in Figs. 5.10 (b) and (c) would therefore follow diagonal lines indicative of this positive correlation. By contrast, no such correlation was observed in Figs. 5.10 (b) and (c). Instead, we find emitters with  $\eta > 0.5$

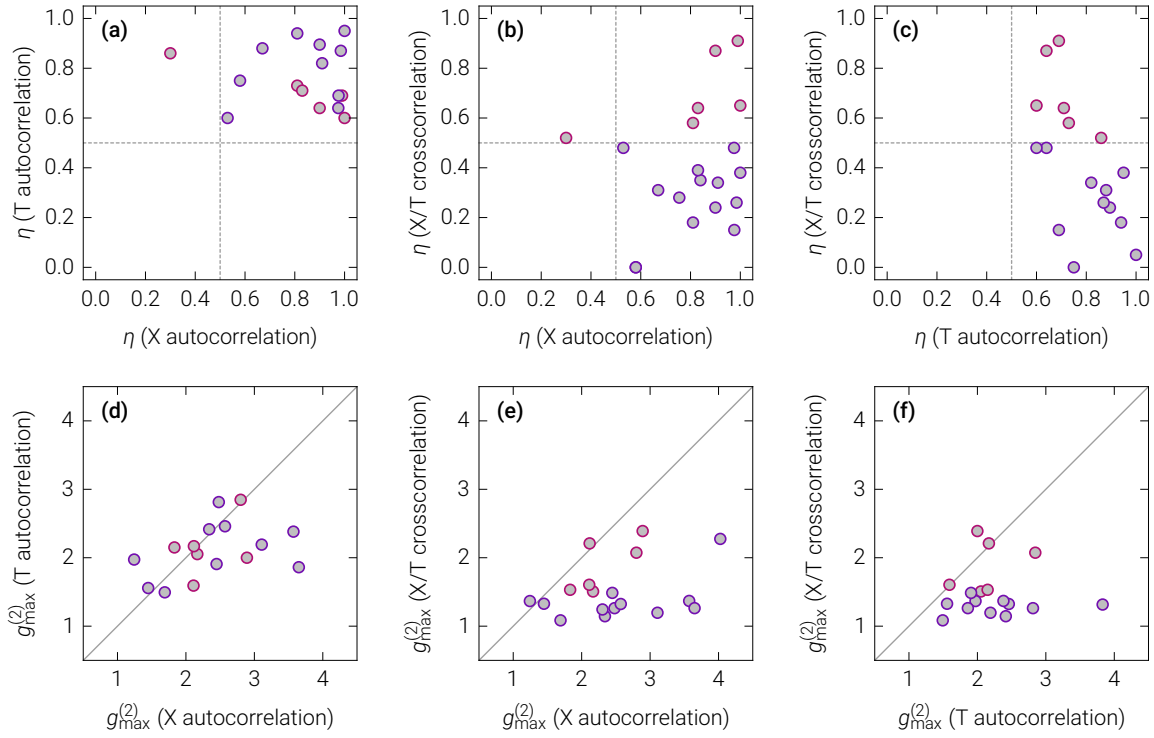


**Figure 5.10.:** Comparison of auto and crosscorrelation characteristics. **(a)–(c)** Scatter plots of the degree of correlation,  $\eta$ , obtained for autocorrelation of X and T (left panel), autocorrelation of X and crosscorrelation of X and T (central panel), and autocorrelation of T and crosscorrelation of X and T (right panel). Dashed lines indicate the threshold value  $\eta = 0.5$  for single photon emission. **(d)–(f)** Scatter plots of the bunching amplitude,  $g_{\max}^{(2)}$ , obtained for autocorrelation of X and T (left panel), autocorrelation of X and crosscorrelation of X and T (central panel), and autocorrelation of T and crosscorrelation of X and T (right panel). Solid lines indicate equal values of  $g_{\max}^{(2)}$ . Violet data points correspond to  $\eta < 0.5$  in the crosscorrelation of X and T, while pink data points correspond to  $\eta > 0.5$  in the crosscorrelation of X and T. The graphics (a)–(f) are reproduced from [P3].

(pink data points) and  $\eta < 0.5$  (violet data points) in the crosscorrelation of X and T for any value  $\eta$  in the autocorrelation of X or T. This finding constitutes another proof that the  $DS_1$  model is not applicable to data featuring  $\eta < 0.5$  in the crosscorrelation of X and T.

The introduction of the  $DS_2$  model resolves this inconsistency. In the case where  $\eta < 0.5$  in the crosscorrelation of X and T (violet data points in Figs. 5.10 (b) and (c)), the degree of correlation is not only governed by the presence of an additional background signal, but also by the charging dynamics of the two defect sites. Therefore, no correlation between the autocorrelation and the crosscorrelation measurements is expected due to the different mechanisms determining the value of  $\eta$ . For the remaining emitters with strong crosscorrelation (pink data points in Figs. 5.10 (b) and (c)), the weak positive correlation between the auto and crosscorrelation values of  $\eta$  is still anticipated, but was not identified, possibly

due to a too small number of observed emitters that fall into the category  $\eta > 0.5$  for the crosscorrelation of X and T.

Similar comparisons were performed for the values of  $g_{\max}^{(2)}$ , measuring the amplitude of bunching, between the different auto and crosscorrelation measurements. Both in the DS<sub>1</sub> and the DS<sub>2</sub> model, the bunching mechanism for X and T is attributed to the same shelving state |S>. We therefore expect equal values for  $g_{\max}^{(2)}$  in the autocorrelation of X and T irrespective of the value of  $\eta$  in crosscorrelation, which is confirmed by both the pink and the violet data points in Fig. 5.10 (d) following the solid gray line that indicates equal time scales.

For the comparison of  $g_{\max}^{(2)}$  between the autocorrelation of X or T and the crosscorrelation of X and T in Figs. 5.10 (b) and (c) we distinguish between strong crosscorrelation,  $\eta > 0.5$  (pink data points), and weak crosscorrelation,  $\eta < 0.5$  (violet data points). For the case  $\eta > 0.5$ , just like for the comparison between X and T autocorrelation, the DS<sub>1</sub> model predicts equal values for  $g_{\max}^{(2)}$  due to population shelving in the same state |S>, which is confirmed by the pink data points in Figs. 5.10 (b) and (c) following the solid gray line.

For  $\eta < 0.5$  in the crosscorrelation of X and T, however, we observe smaller values for  $g_{\max}^{(2)}$  for the crosscorrelation of X and T than for the autocorrelation of X or T (violet data points in Figs. 5.10 (b) and (c)). This finding is consistent with the blinking dynamics expected for emitters that are captured by the DS<sub>2</sub> model. Due to the suppression of equal charge states of the two defect sites, in autocorrelation measurements only one of the two defect sites emits in the monitored spectral band at a time and therefore the population transfer between a single trap and the shelving state governs the blinking dynamics. In crosscorrelation measurements, however, emission from both defect sites is recorded at the same time and therefore the emitter is considered in the off state only when the exciton population of both traps transfers to the shelving state. Since the transitions between trap and shelving state are independent for both defect sites, this scenario effectively results in a less pronounced blinking behavior.

We also investigated potential dependencies of the degrees of correlation and bunching on the excitation laser power. For quantum-dot like emitters it has been reported previously that spectral diffusion [P6, 278], intensity fluctuations [311, 312] and the purity of single-photon emission [313] may all depend on the excitation laser power. To test for such dependencies, we plot the degree of correlation,  $\eta$ , and the shelving and deshelving rates,  $\kappa_s$  and  $\kappa_d$ , as a function of the excitation laser power in Figs. 5.11 (a)–(f).<sup>11</sup>

Figs. 5.11 (a)–(c) show the degree of antibunching  $\eta$  as a function of the excitation laser power for X autocorrelation (Fig. 5.11 (a)), T autocorrelation (Fig. 5.11 (b)) and the crosscor-

---

<sup>11</sup> Note that for most auto and crosscorrelation measurements excitation was performed resonantly with the E<sub>11</sub> transition such that the excitation laser energy was not systematically varied. Fig. B.2 (f) in Section B.1, however, shows the dependence of the blinking timescale on the detuning of the excitation laser from the E<sub>11</sub> energy that was recorded for the X and T autocorrelation.

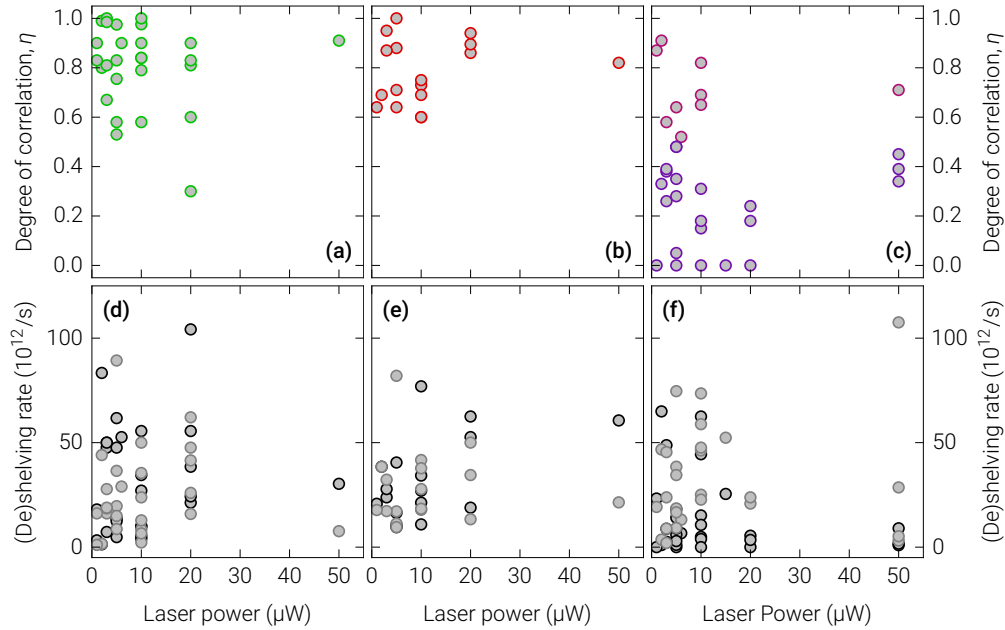


**Figure 5.11.:** Dependence of auto and crosscorrelation characteristics on excitation laser power. (a)–(c) Degree of correlation,  $\eta$ , as a function of excitation laser power for X autocorrelation (left panel), T autocorrelation (central panel) and X and T crosscorrelation (right panel). In (c), violet and pink data correspond to  $\eta < 0.5$  and  $\eta > 0.5$ , respectively. (d)–(f) Shelving and deshelling rates,  $\kappa_{s,\text{eff}}$  (black symbols) and  $\kappa_{d,\text{eff}}$  (gray symbols), obtained from fits with Eq. (5.1) as a function of the excitation laser power for X autocorrelation (left panel), T autocorrelation (central panel) and X and T crosscorrelation (right panel). The graphics (a)–(f) are reproduced from [P3].

relation of X and T (Fig. 5.11 (c)), respectively. In the latter plot, violet and pink data points correspond to  $\eta < 0.5$  and  $\eta > 0.5$  in the crosscorrelation of X and T, respectively. In all three cases no obvious dependence of the degrees of correlation  $\eta$  on the excitation power was found, supporting our interpretation of X and T states as quantum-dot-like emitters in linear response.

Figs. 5.11 (d)–(f) show the effective shelving rate  $\kappa_{s,\text{eff}}$  (black data points) and the effective deshelling rate  $\kappa_{d,\text{eff}}$  (gray data points) obtained from fits with Eq. (5.1) as a function of the excitation laser power for X autocorrelation (Fig. 5.11 (d)), T autocorrelation (Fig. 5.11 (e)) and the crosscorrelation of X and T (Fig. 5.11 (f)).<sup>12</sup> Also this set of data shows no obvious dependence on the excitation power. While the absence of excitation power dependency is plausible for the degree of antibunching  $\eta$ , the fits found in the framework of the  $\text{DS}_1$  model in Figs. B.6 (a)–(c) and the  $\text{DS}_2$  model in Figs. B.10 (a)–(c) changed their shape significantly when varying  $\gamma_{\text{abs}}$ ,  $\gamma_{\text{abs}}^L$ , and  $\gamma_{\text{abs}}^R$  while keeping the rates  $\kappa_s$ ,  $\kappa_s^L$ , and  $\kappa_s^R$  constant at the same

<sup>12</sup> Note that the rates  $\kappa_{s,\text{eff}}$  and  $\kappa_{d,\text{eff}}$  obtained from fits with Eq. (5.1) are generally not equal to the rates  $\kappa_s$  and  $\kappa_d$  in Eq. (B.27) or Eq. (B.39) and are therefore considered as *effective rates* here. Nonetheless,  $\kappa_{s,\text{eff}}$  and  $\kappa_{d,\text{eff}}$  are convenient quantities to detect trends in the blinking dynamics.

time. Hence, an increase of excitation laser power that would increase  $\gamma_{\text{abs}}$ ,  $\gamma_{\text{abs}}^L$ , and  $\gamma_{\text{abs}}^R$  but leave the shelving and deshelving rates unaltered would seem to contradict the absence of such dependencies in Figs. 5.11 (d)–(f).

This discrepancy is resolved by also considering Fig. B.2 (f) in Section B.1, where a dependence of the blinking time on the detuning of the excitation laser energy from the energy of  $E_{11}$  was observed. This finding indicates that relaxation from higher energy states after non-resonant excitation or capture of diffusive exciton population at the defect sites act as a time-limiting factor, thereby governing the effective rate  $\gamma_{\text{abs}}$ . In other words, while a change of  $\gamma_{\text{abs}}$  is expected to alter the values of  $\kappa_{\text{s,eff}}$  and  $\kappa_{\text{d,eff}}$ , a change in excitation laser power does not necessarily imply a change of the rate  $\gamma_{\text{abs}}$ . Based on this interpretation, a change of  $\gamma_{\text{abs}}$  would only be observed for very low excitation powers for which time-correlation experiments are unfeasible due to insufficient signal.

In summary we find that within the limits given by our experimental setup, no dependence of the degree of correlation or the blinking dynamics on the excitation laser power was observed. This finding proves that the microscopic origin of the PL intermittency in hCNTs is different from that in self-assembled quantum dots, where substantial power dependencies have been reported [307, 309]. Also, a decrease in photon-antibunching purity, as observed for other CNT-based emitters [313], could not be reproduced. These findings illustrate the stability of our results over a broad range of the detected photon flux.

## 5.5. Conclusion

In this chapter we reviewed the photophysical properties of (6, 5)-CNTs that were covalently functionalized with a novel chemistry approach based on sodium dithionite. The introduction of  $sp^3$  defects in the  $sp^2$  carbon lattice of the CNTs gives rise to two new emission features X and T at 1.13 eV and 1.01 eV, respectively, in addition to the pristine  $E_{11}$  emission at 1.25 eV. A combination of experimental methods established X and T as neutral excitons and negatively charged trions, respectively, trapped at the same sites of covalent functionalization [48, P2]. The two defect states were also identified as sources of single-photon emission in agreement with their localized nature [P2]. The brightness of T emission was found to be exceptional, rendering the T emission from hCNTs the brightest reported trion emission in CNTs to date [48]. Furthermore, flexible tunability of the X and T emission energies through modification of the functionalizing substituent was demonstrated [48, P2].

In our experiments, we observed substantial spectral variation of the PL from hCNTs at the individual level. Time-resolved measurements revealed the occurrence of hCNTs with both mono and biexponential PL decay characteristics in the X and T spectral bands with consistently longer PL lifetimes than for  $E_{11}$ . While biexponential decay in pristine CNTs is commonly attributed to the presence nonradiative decay channels, high QYs of X and T dis-

favor this scenario for the hCNT defect emission. MPL experiments, while clearly showing a brightening of the  $E_{11}$  dark state with increasing Aharonov-Bohm flux, additionally excluded the possibility of nonradiative PL decay. Instead, the generation of multiple proximal defects within one CNT assisted by local destabilization of the carbon lattice was identified as a possible source of biexponential PL decay characteristics.

Photon correlation measurements of X and T emission revealed pronounced photon bunching and antibunching in X and T autocorrelation for all observed hCNTs. By contrast, crosscorrelation measurements of X and T separated all hCNTs into two classes of strong (type A) and weak (type B) crosscorrelation, respectively. The numerical analysis of different rate models and fits of the corresponding  $g^{(2)}$  functions to the normalized coincidence counts narrowed down the choice of potential level schemes modeling the exciton population dynamics between the considered electronic states. Consistent results were obtained by attributing hCNTs of type A to a model comprising a single defect site coupled to a shelving state and by extending this model for hCNTs of type B to include multiple interacting defect sites. The analysis of correlations in the degrees of bunching and antibunching between the different detection channels was found to support this interpretation, which is also in agreement with the observation of both mono and biexponential PL decay characteristics. Contrasting other quantum-dot-like emitters, no dependencies of these properties on the excitation laser power were observed, proving the robustness of our results over a broad range of PL intensities. In addition, the variations in the spectral response of individual hCNTs were found to be of little significance in the identification of single or multiple trap states.

Our results provide valuable input for the future design of covalently functionalized CNTs as sources of nonclassical light. We identified pronounced interaction mechanisms of proximal defect sites that substantially modify the dynamics of localized excitons. To achieve detailed control over the excitonic states in CNT-based single-photon emitters, we suggest further research to identify routes towards the deterministic generation of solitary defects in the CNT lattice. Mastering this technique would allow for substantial improvements in the generation of luminescing quantum defects in the CNT lattice with tailored photophysical properties.



# 6

## Summary and outlook

---

The tunability of their photoluminescence (PL) emission wavelength renders semiconducting carbon nanotubes (CNTs) interesting candidates for applications in optoelectronics and photonics [36]. Due to their exceptionally large binding energy the charge carriers in semiconducting CNTs form bound electron-hole pairs – excitons – that dominate the photo-physical properties of CNTs [49–51]. The excitons are frequently confined in local potential traps, e. g. at intentional defect sites in covalently functionalized CNTs or in shallow potential minima at low temperatures [48, 57, 58, 60, 62]. This localization is accompanied by exciton dipole moments as large as  $\sim 1 e\text{\AA}$  [38] and exciton population dynamics that are governed by their quantum-mechanical nature [63]. The latter property qualifies localized excitons in CNTs for quantum information processing applications [47, 64, 65]. At the same time, couplings of the localized excitons to the environment give rise to variations in emission energy [60, 61], spectral wandering [P6], and intensity fluctuations [69] that provide insights into their fundamental physical properties [P6, 38, 59, 60, 70, 71]. In addition, a thorough understanding of the relevant interaction mechanisms is beneficial for the further development of CNT-based nonclassical devices [65].

In this thesis, the interaction mechanisms of localized CNT excitons were studied for two different classes of samples. In both scenarios, chirality purified CNTs were used in order to eliminate spectral variations originating from different CNT crystal structures. In the first part of this work we focused on (9, 1)-CNTs that were wrapped with poly[9,9-dioctylfluorenyl-2,7-diyl] (PFO) surfactants. This sample featured weakly localized excitons in shallow potential traps originating from variations in the dielectric CNT environment that is dominated by the surfactant. The second study investigated covalently functionalized (6,5)-CNTs that hosted strongly localized neutral excitons and negatively charged trions. Both CNT materials were drop-cast from aqueous solution onto the flat side of a hemispherical solid immersion lens (SIL) and placed in the focus of a home-built confocal microscope. The resulting sparse distribution of CNTs allowed to address individual emitters, on which spectrally resolved and time-resolved PL studies were performed.

In Chapter 4, the peculiar asymmetric PL lineshape of PFO-wrapped (9, 1)-CNTs was compared with earlier studies attributing the spectral response to variations of the deformation-potential coupling of localized excitons and acoustic CNT phonon modes [70, 227, 229, 230]. While the agreement between these models and the data is compelling, the required value for the deformation-potential coupling strength is in disagreement with theoretical estimates [228]. We proposed a dipolar interaction mechanism between the exciton dipole moment and molecular vibrations of PFO as an alternative explanation for the observed lineshapes. A quantum-mechanical description of this coupling was developed that resembles the form of a Holstein interaction. This mechanism is conceptually similar to exciton-ligand couplings in colloidal quantum dots [279], but was previously unreported for the case of CNTs. The relevant properties of the molecular vibrations in PFO were simulated with density functional theory (DFT), while the exciton dipole moment was estimated from literature values. The resulting model is essentially free of fit parameters and yielded simulated spectra in excellent agreement with the data. Furthermore, the correspondence between simulation and experiment was robust over a broad range of sample temperatures and excitation laser irradiances.

In Chapter 5, we studied (6, 5)-CNTs that were covalently functionalized to introduce  $sp^3$  defects into the  $sp^2$  CNT carbon lattice. This functionalization gives rise to two new emission features that correspond to localized neutral excitons and negatively charged trions trapped at the defect sites. In our experiments we observed substantial variations in spectral shape and PL decay characteristics at the level of individual CNTs. Magneto-photoluminescence (MPL) experiments established that in contrast to diffusive CNT excitons, these differences cannot be attributed to parity-dark states. In addition, photon correlation measurements of the defect states revealed pronounced photon bunching and antibunching for all studied emitters, but varying degrees of exciton-trion crosscorrelation that grouped the functionalized CNTs into two categories. The numerical analysis of different rate models narrowed down the choice of potential level schemes describing the corresponding exciton population dynamics. Consistent results were obtained by attributing emitters with strong crosscorrelations to CNTs with a single defect site and emitters with weak crosscorrelations to multiple interacting defect sites on the same CNT, respectively. The interaction mechanism was attributed to Coulomb repulsion between proximal defect sites that are generated progressively on the same CNT via lattice destabilization in the course of the chemical functionalization.

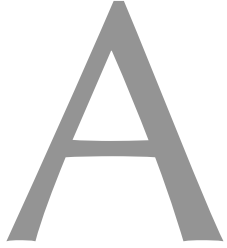
Both studies identified dipolar and electrostatic couplings as important interaction mechanisms of localized excitons in CNTs with their environment. This finding is in agreement with earlier results on CNT excitons confined in a localization potential [P6, 38]. The combination of our studies on two different classes of samples provides guidelines for the future design of CNT-based quantum light emitters. To obtain narrow PL lineshapes, an electrostatically calm substrate is required, as suggested elsewhere [P6]. For chirality purification,

however, CNTs are routinely wrapped in surfactant molecules [200, 201]. Our results show that apart from the emission energy [241] these surfactants also strongly modify the PL lineshape. While for aqueous processing of CNT samples the use of surfactants appears indispensable, the surfactant molecules can be engineered to minimize influences on the spectral shape. For polymer surfactants the results of Chapter 4 suggest to seek for stiff monomers that support no low-energy vibrations, since the influence of polymer backbone vibrations was found to be of inferior importance. The absence of low-energy vibrations would suppress the intensity of vibronic spectral sidebands due to the pronounced damping of higher-energy modes.

At the same time, covalent functionalization of CNTs paves the way to protected, strongly bound excitonic states that support quantum characteristics even at room temperature [47, 64]. However, the generation of proximal defect sites in the course of the chemical functionalization strongly modifies the exciton population dynamics. Therefore, we suggest further research to identify routes towards the deterministic generation of solitary defects in the CNT lattice. Mastering this technique would constitute an important step in the creation of CNT lattice defects with reproducible properties. Together with narrow PL emission lines engineered by the choice of suitable surfactants, these advances would allow for substantial improvements in the future generation of luminescing quantum defects in the CNT lattice with tailored photophysical properties.

The prospective routine generation of CNT-based emitters with reproducible quantum properties is envisioned to allow for the fabrication of superior nonclassical devices. Through the coupling to photonic resonators, a sizable Purcell enhancement of PL brightness and single-photon purity together with a pinning of the emission wavelength to the cavity mode has been demonstrated [65, 224, 314–317]. These advances bring the characteristics of PL from CNTs close to the regime of photon indistinguishability, which, however, has yet to be demonstrated [65]. With the expected further improvements in this field of research, the integration of CNTs into larger photonic circuits is within reach [315] that would allow for complex applications like quantum repeaters, quantum simulators, or quantum teleportation [318]. These developments demonstrate that CNTs are at the forefront of the envisioned success of carbon-based technologies.





# Aspects of density functional theory simulations

---

## A.1. Fundamentals of density functional theory

This section provides an overview of the working principles of **density functional theory (DFT)** and introduces nomenclature and descriptions of the different parameters used for the simulations performed in this work. The discussion follows the excellent perspective by BECKE [319] unless stated otherwise.

In the following discussion we generally assume the Born-Oppenheimer approximation [320] that states that in a system of atomic nuclei and electrons the spatial positions of the nuclei are frozen and constitute the external potential  $V_{\text{ext}}$  governing the evolution of the electrons. In this scenario the Hamiltonian reads

$$\hat{H} = -\frac{\hbar^2}{2m_e} \sum_i \nabla_{\mathbf{r}_i}^2 + \sum_i V_{\text{ext}}(\mathbf{r}_i) + \frac{1}{2} \sum_{j \neq i} \sum_i \frac{e^2}{4\pi\epsilon_0 |\mathbf{r}_j - \mathbf{r}_i|}, \quad (\text{A.1})$$

where  $i$  and  $j$  run from 1 to the total number  $N$  of electrons,  $m_e$  is the electron mass,  $e$  is the elementary charge,  $\epsilon_0$  is the vacuum permittivity and  $\mathbf{r}_i$  is the coordinate vector of electron  $i$ . The typical task of **DFT** simulations is to derive key quantities like the ground state energy or the molecular dipole moment of this system after finding the correct electron distribution in the presence of  $V_{\text{ext}}$ .

Such quantities may naturally be derived from the multi-particle electron wave function  $\Psi$  that is accessible through (approximate) solution of the corresponding Schrödinger equation, e. g. in the framework of the Hartree-Fock method [321–324]. From a computational perspective, however, this approach is undesirable due to the nonlocal exchange operator in the Hamiltonian that impedes an efficient numerical treatment [319, p. 2]. A computationally more feasible approach was proposed by HOHENBERG and KOHN [325] and KOHN and SHAM [326] by considering the total electron density  $\rho$  instead of the multi-particle electron wave function  $\Psi$  as discussed in the following.

While the total electron density  $\rho$  can be readily computed from  $\Psi$ , which in turn is determined by  $V_{\text{ext}}$ , it was proven in [325, 327] that this line of argument can be inverted and that for any given functional form of  $\rho$  there exists a unique external potential  $V_{\text{ext}}$  for which the corresponding ground state has the total electron density  $\rho$ . This means that the three functionals  $V_{\text{ext}}$ ,  $\Psi$  and  $\rho$  are equivalent in the sense that any of the three determines the other two and therefore that any of the three can serve as the starting point to derive secondary quantities like the ground state energy or the molecular dipole moment. The basic concept of DFT lies within the approach to find  $\rho$  instead of  $\Psi$ .

Exploiting the finding that the multi-particle electron wave function  $\Psi$  is a functional of the total electron density  $\rho$  it is furthermore possible to express the kinetic energy  $T$  and the Coulomb interaction energy  $U$ , defined by

$$T = -\frac{\hbar^2}{2m_e} \int d^3\mathbf{r} \Psi^\dagger(\mathbf{r}) \nabla^2 \Psi(\mathbf{r}) \quad \text{and} \quad U = \frac{1}{2} \int d^3\mathbf{r} d^3\mathbf{r}' \frac{e^2}{4\pi\epsilon_0 |\mathbf{r} - \mathbf{r}'|} \Psi^\dagger(\mathbf{r}) \Psi^\dagger(\mathbf{r}') \Psi(\mathbf{r}') \Psi(\mathbf{r}), \quad (\text{A.2})$$

as functionals of  $\rho$  and to define the functional  $F[\rho] = T[\rho] + U[\rho]$ . Most notably,  $F$  is a universal functional of  $\rho$ , i. e. its definition is independent of  $V_{\text{ext}}$ , such that the total energy of the electron density  $\rho$  in the presence of an external potential  $V_{\text{ext}}$  can be expressed as

$$E[\rho] = \int d^3\mathbf{r} V_{\text{ext}}(\mathbf{r}) \rho(\mathbf{r}) + F[\rho]. \quad (\text{A.3})$$

This energy functional also fulfills the variational principle [325] stating that  $E[\rho]$  attains its minimum for the total electron density  $\rho$  that corresponds to the external potential  $V_{\text{ext}}$ .

For any given external potential  $V_{\text{ext}}$  the corresponding total electron density  $\rho$  can therefore be determined by requiring that the functional derivative  $\delta E[\rho]/\delta\rho$  be zero. In spite of the proven existence of  $E$  as a functional of  $\rho$ , however, expressions for  $T$  and  $U$  and therefore for  $E$  are only known in terms of  $\Psi$  but not in terms of  $\rho$  such that it is not possible to write down a closed expression for  $\delta E[\rho]/\delta\rho$  [319, p. 3].

To proceed, consider the ansatz that  $\rho$  can be written as the density of a Slater determinant of orthonormal orbitals  $\psi_i$  [326],

$$\rho = 2 \sum_{i=1}^{N/2} |\psi_i|^2, \quad (\text{A.4})$$

where for simplicity an even number  $N$  of electrons has been assumed that occupy each orbital  $\psi_i$  in pairs of opposite spin, giving rise to the factor of 2 on the right hand side in Eq. (A.4) [319, p. 3]. Note that there is no direct connection between the orbitals  $\psi_i$  and the multi-particle electron wave function  $\Psi$ .

In practical calculations the  $\psi_i$  are typically taken from a basis set of atomic orbitals in a linear combination of atomic orbitals (LCAO) approach, turning the considered differential equations into algebraic equations. While exponentially decaying Slater-type orbitals [328]

are a natural choice motivated by the solutions of the Schrödinger equation for the hydrogen atom, the calculation of the related integrals is computationally difficult. As an alternative, Gaussian-type orbitals have been proposed [329], for which explicit formulas for integrals and gradients are known [330]. Commonly, the valence atomic orbital that is mainly contributing to chemical bonding is represented by more than one basis function. The resulting split-valence basis sets are named double, triple or quadruple-zeta bases, following the common use of  $\zeta$  as exponent in Slater-type orbital basis functions [331].

Using the representation of  $\rho$  in Eq. (A.4) the total kinetic energy  $T_S$  of the Slater determinant and the classical Coulomb self energy  $C$ ,

$$T_S[\rho] = -\frac{\hbar^2}{2m_e} \sum_{i=1}^{N/2} 2 \int d^3\mathbf{r} \psi_i^\dagger(\mathbf{r}) \nabla^2 \psi_i(\mathbf{r}) \quad \text{and} \quad C[\rho] = \frac{1}{2} \int d^3\mathbf{r} d^3\mathbf{r}' \frac{e^2}{4\pi\epsilon_0|\mathbf{r}-\mathbf{r}'|} \rho(\mathbf{r})\rho(\mathbf{r}') \quad (\text{A.5})$$

can be introduced as an approximation to the kinetic energy  $T$  and the Coulomb interaction energy  $U$  [319, p. 3]. Defining the *exchange-correlation* energy,

$$E_{XC}[\rho] = T[\rho] + U[\rho] - T_S[\rho] - C[\rho], \quad (\text{A.6})$$

we arrive at the representation of the total energy from [319, p. 3],

$$F[\rho] = T_S[\rho] + C[\rho] + E_{XC}[\rho]. \quad (\text{A.7})$$

Using the definition in Eq. (A.4), the requirement  $\delta E[\rho]/\delta\rho = 0$  can be reformulated as  $\delta E[\rho]/\delta\psi_i = 0$  for all  $i$ . Given the definitions of  $T_S$  and  $C$ , their functional derivatives with respect to  $\psi_i$  can be explicitly calculated, leading to the Kohn-Sham orbital equation [326],

$$-\frac{\hbar^2}{2m_e} \nabla^2 \psi_i + V_{KS} \psi_i = \epsilon_i \psi_i, \quad (\text{A.8})$$

where  $\epsilon_i$  is the orbital energy of the  $i^{\text{th}}$  Kohn-Sham orbital and the effective Kohn-Sham potential is defined by [319, p. 3, 326]

$$V_{KS}(\mathbf{r}) = V_{\text{ext}}(\mathbf{r}) + \int d^3\mathbf{r}' \frac{e^2}{4\pi\epsilon_0|\mathbf{r}-\mathbf{r}'|} \rho(\mathbf{r}') + \frac{\delta E_{XC}[\rho]}{\delta\rho}(\mathbf{r}). \quad (\text{A.9})$$

Eq. (A.8) has the form of a Schrödinger equation of *independent* particles subject to the effective potential  $V_{KS}$ , a posteriori justifying the choice to write  $\rho$  as the density of a Slater determinant in Eq. (A.4). Hence, DFT is an *independent-particle theory*, as opposed to e. g. the Hartree-Fock method. Note, however, that  $V_{KS}$  is dependent on  $\rho$  such that Eq. (A.8) needs to be solved in a *self-consistent field* (SCF) approach in an iterative manner, starting from an initial assumed total electron density  $\rho_0$  [326].

The crucial part in this description is the functional  $E_{XC}$  that captures all correlation and exchange contributions in  $F$  that are not contained in  $T_S$  and  $C$ . Although one can expect that the relative magnitude of  $E_{XC}$  is small compared to  $T_S$  and  $C$ , precise DFT simulations rely on good approximations for the functional  $E_{XC}$ , since “[w]e are assured of its existence, but no explicit expression is known” [319, p. 4]. We will therefore briefly discuss different approaches to find suitable expressions for  $E_{XC}$ .

**Local density approximation.** A straightforward approach to express  $E_{XC}$  was given in [325, 326] in terms of the **local density approximation (LDA)**, where the spatial exchange-correlation energy density  $e_{XC}^{\text{UEG}}$  of the uniform electron gas is used to write  $E_{XC}$  as [319, p. 4]

$$E_{XC}^{\text{LDA}} = \int d^3\mathbf{r} e_{XC}^{\text{UEG}}(\rho(\mathbf{r})). \quad (\text{A.10})$$

The LDA is evidently best-suited for a slowly varying total electron density  $\rho$ .

**Lowest-order gradient correction.** Using the adiabatic connection method,  $E_{XC}$  can be split into an exchange part  $E_X$  and a correlation part  $E_C$  as  $E_{XC} = E_X + E_C$ , where  $|E_X|$  can be shown to dominate  $|E_C|$  [319, p. 5]. The LDA expression for  $E_X$  [319, p. 6],

$$E_X^{\text{LDA}} = -\frac{3}{2} \left( \frac{3}{4\pi} \right)^{1/3} \frac{e^2}{4\pi\epsilon_0} \int d^3\mathbf{r} \rho(\mathbf{r})^{4/3}, \quad (\text{A.11})$$

is therefore an obvious candidate for improvement. In the framework of the **lowest-order gradient correction (LGC)**,  $E_X^{\text{LDA}}$  is replaced by a functional including the gradient of  $\rho$  [332, 333],

$$E_X^{\text{LGC}} = E_X^{\text{LDA}} - \beta \frac{e^2}{4\pi\epsilon_0} \int d^3\mathbf{r} \frac{(\nabla\rho(\mathbf{r}))^2}{\rho(\mathbf{r})^{4/3}}, \quad (\text{A.12})$$

where  $\beta = 0.003\text{--}0.004$  is a numerical parameter [319, p. 6].

**Generalized gradient approximation.** To account for divergence issues in the LGC, more general approaches of the form

$$E_X^{\text{GGA}} = \frac{e^2}{4\pi\epsilon_0} \int d^3\mathbf{r} \rho(\mathbf{r})^{4/3} f_X(s), \quad (\text{A.13})$$

where  $f_X$  is an even function of the reduced density gradient  $s = |\nabla\rho|/\rho^{4/3}$  with  $f_X(0) = 1$ , have been investigated. Such functionals are termed **generalized gradient approximation (GGA)**, since they can be viewed as an expansion in  $s^2$  beyond the LGC [319, p. 7].

The BP86 functional used in this work falls into this class with the exchange energy  $E_X$  given by  $f_X(s) = \beta s / (1 + 6\beta \sinh^{-1} s)$  with  $\beta = 0.0042$  [258], a choice capturing the long-range  $-1/r$  dependency of the Coulomb potential [319, p. 7]. The correlation energy  $E_C$  is similarly given by a GGA expression [257, 259].

**Meta-GGA functionals.** Functionals that in addition to the density gradient  $\nabla\rho$  also comprise the kinetic energy density

$$\tau = -\frac{\hbar^2}{m_e} \sum_{i=1}^{N/2} |\nabla\psi_i|^2 \quad (\text{A.14})$$

are known as meta-GGA functionals [319, p. 8]. In the framework of DFT these functionals require additional attention, since  $\tau$  is not known as a functional of  $\rho$ . This limitation may be circumvented by applying differentiation with respect to orbitals instead of functional derivatives [334, 335]. Therefore, meta-GGA functionals are not formulated purely within DFT, as they require input other than the total electron density  $\rho$ .

**Hybrid functionals.** All types of functionals discussed so far depend on the *local* value of  $\rho$ ,  $\nabla\rho$  or  $\tau$  and by consequence are not well suited to capture delocalization effects that are important in many systems [319, p. 9]. One approach to account for this defect is the inclusion of the *exact* Hartree-Fock exchange energy [319, p. 2]

$$E_X^{\text{exact}} = -\frac{e^2}{4\pi\epsilon_0} \int d\mathbf{r}_1 \int d\mathbf{r}_2 \frac{|\sum_{i=1}^{N/2} \psi_i^\dagger(\mathbf{r}_1)\psi_i(\mathbf{r}_2)|^2}{|\mathbf{r}_1 - \mathbf{r}_2|}. \quad (\text{A.15})$$

Functionals of this form are named hybrid functionals, as they combine the GGA exchange energy with the Hartree-Fock exchange energy [319, p. 10]. As for the meta-GGA functionals,  $E_X^{\text{exact}}$  needs to be calculated by differentiation with respect to orbitals, meaning that it is *not* part of the exchange energy in the Kohn-Sham formulation [319, p. 10].

The B3LYP functional [261] employed in this work falls into this class by combining the B3 hybrid exchange functional [260] with the LYP correlation functional [336].

**Hyper-GGA functionals.** In systems with strong nonlocal effects the partial incorporation of exact exchange as performed in hybrid functionals may be insufficient [319, p. 10]. The use of purely exact exchange is able to lift this limitation, but requires the introduction of entirely new correlation functionals that are also nonlocal [319, p. 10]. The resulting functionals are termed exact-exchange based functionals or hyper-GGA functionals and generally have a rather high computational cost.

A limitation that is common to all mentioned local density DFT functionals lies within their failure to reproduce the long-range London  $-C_6/r^6$  interaction [337–339], inhibiting the accurate description of van der Waals forces and similar interactions [319, p. 12]. Different strategies have been pursued to add a dispersion term with  $-C_6/r^6$  long-range behavior to the existing DFT functionals. An overview over these strategies is given in [319, p. 13].

## A.2. Details of density functional theory simulations

This section discusses computational details of the DFT approach used to calculate the frequencies  $\Omega_n$  and the electric dipole moments  $\partial_{Q_n}\mu$  of the vibrational normal modes in the system of poly[9,9-dioctylfluorenyl-2,7-diyl] (PFO) interacting with a (9,1)-carbon nanotube (CNT), as discussed in Section 4.3. All calculations reported here were performed with the general-purpose quantum chemistry program package ORCA [340].

Starting point for any DFT simulation was one or more PFO monomers in approximately relaxed geometry that was obtained from a chemical database. These were placed close to a (9,1)-CNT designed with the nanotube builder in the molecule editor and visualizer Avogadro [341]. The result was used as an approximate starting point for all subsequent DFT calculations.

As the next step, a geometry optimization at the DFT level was performed. In this procedure the energy of the electronic system is calculated together with its gradient with respect to the nuclear coordinates. The latter are then updated e. g. using the BFGS algorithm [342–345] until an energetic minimum is reached. To avoid unnecessary and computationally expensive optimization of the CNT structure, all atoms comprising the CNT lattice were assigned to a separate fragment which was excluded from geometry optimization. Also, atoms estimated to contribute only weakly to the interaction between CNT and PFO were removed from the CNT lattice to account for the polynomial scaling of the runtime with input size of DFT algorithms.

The selection of the specific DFT method was guided by the observation that due to the  $\Omega_n^{-2}$  proportionality in the intensity ratio in Eq. (4.32) in Section 4.3 the low-energy vibrations of PFO are of highest interest. Given the limited reliability of DFT results for low-energy vibrations [265], two different DFT approaches were selected to test the robustness of our results. To this end one GGA and one hybrid DFT functional (cf. Section A.1) were chosen.

Based on the comprehensive benchmark in [346] the well-performing and robust BP86 functional [257–259] was selected from the GGA functionals. From the hybrid functionals we chose B3LYP with 20 % Hartree-Fock exchange [260, 261, 336] because of its frequent use [347] and in spite of a rather mediocre result in the aforementioned benchmark [346]. This choice was founded on the expectation that these two functionals with different working mechanisms and levels of precision can provide a reasonable estimate for the accuracy of our DFT results for low-energy vibrations. For both functionals we selected the Ahlrichs' type triple-zeta def2-TZVP basis set of atomic orbitals [348]. Note that it was established in [346] that there is practically no benefit in using more complex quadruple-zeta basis sets for the type of calculations performed in this work.

For more efficient calculations we employed the resolution of the identity (RI) approximation [349–352] for the BP86 functional that approximates products of Gaussian-type

basis functions with the help of an auxiliary basis set, thereby reducing computational cost [353]. For the B3LYP functional RI was combined with the chain of spheres exchange (COSX) approach that reduces the number of evaluations needed to compute the exchange energy by constructing a number of shells around each basis function and disregarding pairwise overlaps for any basis function that drops below a predetermined threshold outside a given shell [354]. In conjunction, RI and COSX are known as the RIJCOSX approximation [354–356]. For both functionals the def2/J RI auxiliary basis set was used [357].

As discussed in Section A.1 the ability of local density DFT functionals to reproduce the long-range London  $-C_6/r^6$  interaction is limited. In order to include a proper description of the van der Waals-like interaction between PFO and CNT, we explicitly included dispersion correction with the Becke-Johnson damping scheme (D3BJ) [358, 359].

The selected computational parameters in ORCA for the BP86 functional were Tight SCF convergence and the Grid4 and FinalGrid6 numerical integration grids. For the B3LYP functional we used slightly stronger constraints with VeryTight SCF convergence and integration grids Grid5, GridX6 and FinalGrid6 to compensate for the uncertainties introduced by the additional RIJCOSX approximation.

After finding the relaxed molecular geometry with the BP86 or the B3LYP functional using the sketched DFT approach, in a next step the associated molecular vibrations were analyzed. Generally, the vibrational normal modes of a molecule in relaxed geometry can be computed through diagonalization of the Hessian matrix of the potential energy change with respect to the molecular coordinates that is readily available in ORCA through the Freq and NumFreq keywords.

This approach, however, would also calculate vibrations of the CNT lattice that are tabulated in literature and therefore not desired for this work. A seemingly easy solution to this issue lies within removing all CNT lattice atoms for the sake of any vibrational frequency calculations. Yet, this method fails entirely, since the previously calculated geometry is no relaxed geometry without the presence of the CNT, whereas the computation of vibrational frequencies strongly relies on starting from an energetic minimum.

Therefore, a different approach needs to be pursued. With the Partial\_Hess keyword ORCA offers the possibility to freeze a number of atoms in a NumFreq calculation and to derive the vibrational frequencies associated only to the remaining atoms. This functionality is employed to freeze any CNT lattice atoms and to thereby disregard any vibrations of the CNT lattice.

The well-known formula stating that there exist  $3N - 6$  molecular vibrations in a system of  $N$  atoms [236, pp. 22–27] translates to this scenario as follows. Since no vibrations of the CNT lattice are being calculated, the CNT can be viewed as a single particle without internal structure. Together with the  $N$  atoms in the molecule, consequently there is a total number of  $N + 1$  particles in the system, giving rise to  $3(N + 1) - 6 = 3N - 3$  vibrational modes. Due to the interaction between CNT and the molecule there exist 3 vibrational modes more than for

the isolated molecule. For  $N = 71$  in the case of a PFO monomer, this results in 210 distinct vibrational modes to consider.

Unfortunately, due to a limitation of ORCA, in conjunction with the `Partial_Hess` keyword only the vibrational normal modes and the corresponding frequencies but not the infrared activities are being returned. To work around this problem, a helper tool was programmed in Python that introduces small displacements of the molecular coordinates from the relaxed geometry along the previously calculated normal modes of vibration. For each coordinate displacement, another run of ORCA was then initiated to calculate the energy and the molecular dipole moment of the given configuration.

By combining these calculations, both the frequencies and the dynamic molecular dipole moments of all normal modes can be obtained. While the frequencies found by this method can be used to cross check with the frequencies from the `Partial_Hess` calculation, the dynamical molecular dipole moments allow to compute the infrared activities as detailed in Section A.3.

### A.3. Conversion between molecular dipole moments and integrated molar absorptivity

Any results of DFT simulations are properties of individual molecules, whereas many experimentally accessible quantities are measured on a large number of molecules. In this work, we most notably employ the dynamic molecular dipole moment associated with a molecular vibration in a given normal mode that corresponds to the wavelength-dependent extinction coefficient in macroscopic samples. The latter is often expressed by means of the integrated molar absorptivity in  $\text{km/mol}$ , a quantity computed by many quantum chemistry software packages, including ORCA. In this section we discuss the conversion between these two molecular and macroscopic quantities that requires some deeper insights into the physics of molecular vibrations. The discussion in this section follows [236, pp. 162–166], unless stated otherwise.

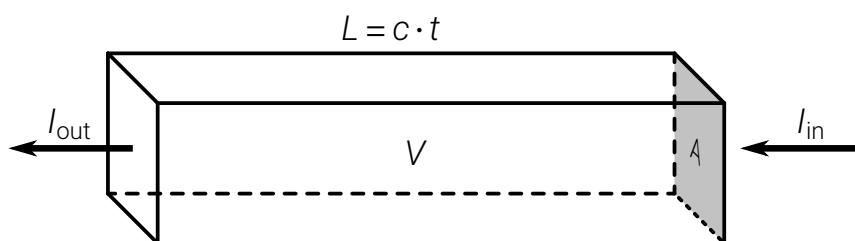


**Figure A.1.:** A beam of light with incoming spectral irradiance  $I_{\text{in}}$  enters a cuboidal volume  $V = A \cdot L$  orthogonally through a face with area  $A$  and is attenuated to the outgoing spectral irradiance  $I_{\text{out}}$  after length  $L = c \cdot t$ .

To formulate the attenuation of light due to interaction with a chemical species, consider a cuboidal volume  $V = A \cdot L$  as shown in Fig. A.1 and a beam of light entering the volume orthogonally through a face of area  $A$ . The light travels along the length  $L = c \cdot t$  of the volume in time  $t$ , where  $c$  is the speed of light. When expressing the total energy  $E$  in volume  $V$  through the spectral energy density  $\varepsilon(\omega)$  as a function of the angular frequency  $\omega = 2\pi\nu$ , the conservation of energy can be expressed as follows.

$$\begin{aligned}
0 &= \frac{dE}{dt} = \frac{d}{dt} \int d\omega \varepsilon(\omega) = \int d\omega \frac{d}{dt} \varepsilon(\omega) = \\
&= \int d\omega I_{\text{in}}(\omega) \cdot A - \int d\omega I_{\text{out}}(\omega) \cdot A + \int d\omega \frac{\partial}{\partial t} \varepsilon(\omega) = \\
&= \int d\omega [I(L_0, \omega) - I(L_0 + L, \omega)] \cdot A + \int d\omega \frac{\partial}{\partial t} \varepsilon(\omega) \tag{A.16}
\end{aligned}$$

Here,  $I_{\text{in}}(\omega) = I(L_0, \omega)$  and  $I_{\text{out}}(\omega) = I(L_0 + L, \omega)$  are the spectral irradiances of the light beams entering and leaving the volume  $V$  at positions  $L_0$  and  $L + L_0$ , respectively. Using the transition rate  $\Gamma_{i \rightarrow j}$  from a quantum state  $|i\rangle$  of the molecule to a quantum state  $|j\rangle$ , the term  $\partial_t \varepsilon(\omega)$  can be written as

$$\frac{\partial}{\partial t} \varepsilon(\omega) = \sum_{|i\rangle, |j\rangle} N_i \Gamma_{i \rightarrow j} \cdot \hbar \omega_{ij} \cdot \delta(\omega - |\omega_{ij}|), \tag{A.17}$$

where  $|i\rangle$  and  $|j\rangle$  run over all possible quantum states,  $N_i$  is the number of molecules in quantum state  $|i\rangle$  in volume  $V$ ,  $\hbar \omega_{ij}$  is the energy difference for a transition from state  $|i\rangle$  to state  $|j\rangle$ , in particular  $\omega_{ij} = -\omega_{ji}$ , and  $\delta$  is the Dirac delta function. Note that both sides of this equation have unit  $\text{J/s}^{-1}/\text{s} = \text{J}$ , since the delta function has unit  $1/\text{s}^{-1}$ .

We proceed by transforming the expression for  $\partial_t \varepsilon(\omega)$  in Eq. (A.17). In a first step we separate positive and negative  $\omega_{ij}$ .

$$\begin{aligned}
\frac{\partial}{\partial t} \varepsilon(\omega) &= \sum_{|i\rangle, |j\rangle} N_i \Gamma_{i \rightarrow j} \cdot \hbar \omega_{ij} \cdot \delta(\omega - |\omega_{ij}|) \\
&= \sum_{|i\rangle, |j\rangle} N_i \Gamma_{i \rightarrow j} \cdot \hbar \omega_{ij} \cdot \delta(\omega - \omega_{ij}) + && \text{(terms with } \omega_{ij} > 0) \\
&\quad + \sum_{|i\rangle, |j\rangle} N_i \Gamma_{i \rightarrow j} \cdot \hbar \omega_{ij} \cdot \delta(\omega + \omega_{ij}) && \text{(terms with } \omega_{ij} < 0) \\
&= \sum_{|j\rangle} \sum_{E_i > E_j} N_i \Gamma_{i \rightarrow j} \cdot \hbar \omega_{ij} \cdot \delta(\omega - \omega_{ij}) + \\
&\quad - \sum_{|i\rangle} \sum_{E_j > E_i} N_i \Gamma_{i \rightarrow j} \cdot \hbar \omega_{ji} \cdot \delta(\omega - \omega_{ji}) \tag{A.18}
\end{aligned}$$

Here, the sums of the form  $\sum_{E_k > E_l}$  run over all states  $|k\rangle$  with an energy  $E_k$  larger than the energy  $E_l$  of state  $|l\rangle$ . For a single possible transition between states  $|i\rangle$  and  $|j\rangle$  the transition rate  $\Gamma_{i \rightarrow j}$  can be expressed by Fermi's golden rule as

$$\Gamma_{i \rightarrow j} = \frac{2\pi}{\hbar} \cdot |\langle i | \hat{H} | j \rangle|^2, \quad (\text{A.19})$$

which is symmetric in  $i$  and  $j$ . Therefore, a swap of variables  $i$  and  $j$  allows to combine the two sums Eq. (A.18) and leads to the result [236, p. 163]

$$\frac{\partial}{\partial t} \varepsilon(\omega) = \sum_{|j\rangle} \sum_{E_i > E_j} (N_i - N_j) \Gamma_{i \rightarrow j} \cdot \hbar \omega_{ij} \cdot \delta(\omega - \omega_{ij}). \quad (\text{A.20})$$

By introducing the total number of particles  $N$  in volume  $V$  and the canonical partition sum  $Z$ , assuming thermal equilibrium, this can be further rewritten as

$$\begin{aligned} \frac{\partial}{\partial t} \varepsilon(\omega) &= \sum_{|j\rangle} \sum_{E_i > E_j} \frac{N}{Z} \left( e^{-\beta E_i} - e^{-\beta E_j} \right) \Gamma_{i \rightarrow j} \cdot \hbar \omega_{ij} \cdot \delta(\omega - \omega_{ij}) \\ &= \sum_{|j\rangle} \sum_{E_i > E_j} \frac{N}{Z} e^{-\beta E_j} \left( e^{-\beta \hbar \omega_{ij}} - 1 \right) \Gamma_{i \rightarrow j} \cdot \hbar \omega_{ij} \cdot \delta(\omega - \omega_{ij}), \end{aligned} \quad (\text{A.21})$$

where  $\beta$  is the thermodynamic beta. Eq. (A.21) shows that  $\partial_t \varepsilon(\omega)$  is a temperature-dependent quantity in general. For most practical purposes, however,  $\hbar \omega_{ij}$  is much larger than the thermal energy and the term  $\exp(-\beta \hbar \omega_{ij})$  can be neglected [236, p. 165]. This is particularly the case for the desired conversion rule between dynamic molecular dipole moment and integrated molar absorptivity, for which zero temperature is assumed.

Exploiting the delta function in Eq. (A.21),  $\omega$  can be substituted for  $\omega_{ij}$  and  $\Gamma_{i \rightarrow j}$  can be written as the product of the Einstein B coefficient  $B_{ij}^\omega$  [245] and the spatio-spectral energy density  $\rho(\omega) = \varepsilon(\omega)/V$ ,

$$\frac{\partial}{\partial t} \varepsilon(\omega) = - \sum_{|j\rangle} \sum_{E_i > E_j} \frac{N}{Z} e^{-\beta E_j} \cdot B_{ij}^\omega \rho(\omega) \cdot \hbar \omega \cdot \delta(\omega - \omega_{ij}). \quad (\text{A.22})$$

When considering an infinitesimal length  $dL$  instead of the finite length  $L$ , the difference of spectral irradiances in Eq. (A.16) can be formulated as a differential,

$$\int d\omega [I(L_0, \omega) - I(L_0 + dL, \omega)] \cdot A = - \int d\omega \frac{\partial}{\partial L} I(L, \omega) \Big|_{L=L_0} \cdot dL \cdot A. \quad (\text{A.23})$$

By employing the fact that  $I(L, \omega) = c \cdot \rho(\omega)$  [236, p. 163] we can finally combine Eq. (A.22) and Eq. (A.23) to derive a differential equation for  $I(L, \omega)$ ,

$$\int d\omega \frac{\partial}{\partial L} I(L, \omega) \Big|_{L=L_0} = - \int d\omega \sum_{|j\rangle} \sum_{E_i > E_j} \frac{n}{Z} e^{-\beta E_j} \cdot B_{ij}^\omega \cdot I(L, \omega) \cdot \frac{\hbar \omega}{c} \cdot \delta(\omega - \omega_{ij}), \quad (\text{A.24})$$

where the spatial density  $n = N/V$  of molecules has been used. By introducing the molar concentration  $C = n/N_A$ , where  $N_A = 6.022 \times 10^{23} \text{ mol}^{-1}$  is the Avogadro constant, Eq. (A.24) can be written in the form of the Beer-Lambert law to base  $e$  [360, pp. 16–22, 361, 362],

$$\left. \frac{\partial}{\partial L} I(L, \omega) \right|_{L=L_0} = -\varepsilon(\omega) \cdot C \cdot I(L, \omega). \quad (\text{A.25})$$

Here,  $\varepsilon(\omega)$  is the *molar attenuation coefficient* or absorptivity at angular frequency  $\omega$  that has unit  $\text{m}^2/\text{mol}$  and can be expressed as

$$\varepsilon(\omega) = \sum_{|j\rangle} \sum_{E_i > E_j} \frac{n}{Z} e^{-\beta E_j} \cdot \frac{B_{ij}^\omega}{C} \cdot \frac{\hbar\omega}{c} \cdot \delta(\omega - \omega_{ij}) = \sum_{|j\rangle} \sum_{E_i > E_j} \frac{N_A}{Z} e^{-\beta E_j} \cdot B_{ij}^\omega \cdot \frac{\hbar\omega}{c} \cdot \delta(\omega - \omega_{ij}). \quad (\text{A.26})$$

In many cases, however, it is more appropriate to consider the weight of a spectral line centered at  $\omega_0$  with full width  $\delta\omega$  that is given by the *integrated molar absorptivity*,

$$\Psi_\omega = \int_{\omega_0 - \delta\omega/2}^{\omega_0 + \delta\omega/2} d\omega \varepsilon(\omega) = \int_{\omega_0 - \delta\omega/2}^{\omega_0 + \delta\omega/2} d\omega \sum_{|j\rangle} \sum_{E_i > E_j} \frac{N_A}{Z} e^{-\beta E_j} \cdot B_{ij}^\omega \cdot \frac{\hbar\omega}{c} \cdot \delta(\omega - \omega_{ij}). \quad (\text{A.27})$$

To perform integration over the delta function, for every state  $|j\rangle$  we define the interval of energies  $I_j = [E_j + \hbar\omega_0 - \hbar\delta\omega/2, E_j + \hbar\omega_0 + \hbar\delta\omega/2]$  to obtain

$$\Psi_\omega = \sum_{|j\rangle} \sum_{E_i \in I_j} \frac{N_A}{Z} e^{-\beta E_j} \cdot B_{ij}^\omega \cdot \frac{\hbar\omega_0}{c}. \quad (\text{A.28})$$

As a spectral line is typically composed of a number of related transitions [236, pp. 163–166], the summation over  $E_i$  can be carried out by defining an effective Einstein B coefficient  $B_{\delta\omega, j}^\omega(\omega_0)$  such that  $B_{\delta\omega, j}^\omega(\omega_0)\rho(\omega_0)$  is the summed transition probability from *any* state with  $E_i \in I_j$  to the final state  $|j\rangle$ . This leads to the result

$$\Psi_\omega = \sum_{|j\rangle} \frac{N_A}{Z} e^{-\beta E_j} B_{\delta\omega, j}^\omega(\omega_0) \cdot \frac{\hbar\omega_0}{c} = N_A \cdot \left\langle B_{\delta\omega, j}^\omega(\omega_0) \right\rangle_\beta \cdot \frac{\hbar\omega_0}{c}, \quad (\text{A.29})$$

where  $\langle \cdot \rangle_\beta$  is the canonical ensemble average.

In a similar way as the Einstein B coefficient  $B_{ij}^\omega$  [245], the integrated molar absorptivity is dependent on the domain that is used to measure frequencies, as indicated by the index  $\omega$ . For spectroscopic purposes, wavenumbers  $\tilde{\nu}$  are frequently used instead of angular frequencies  $\omega$ . Using the relation  $\tilde{\nu} = \omega/2\pi c$  the integrated molar absorptivity  $\Psi_{\tilde{\nu}}$  in the wavenumber domain can be calculated as

$$\Psi_{\tilde{\nu}} = \Psi_\omega \cdot \frac{d\tilde{\nu}}{d\omega} = \frac{1}{2\pi c} \cdot \Psi_\omega. \quad (\text{A.30})$$

While  $\Psi_\omega$  has unit  $\text{m}^2/\text{mol}\cdot\text{s}$ , the unit of  $\Psi_{\bar{\nu}}$  is  $\text{m}/\text{mol}$ . For numerical values in a practical range, the latter can also be given in  $\text{km}/\text{mol}$ .

For the purpose of a conversion rule between dynamic molecular dipole moment and integrated molar absorptivity, we again assume zero temperature such that Eq. (A.29) simplifies to

$$\Psi_\omega = N_A \cdot B_{\delta\omega,g}^\omega(\omega_0) \cdot \frac{\hbar\omega_0}{c}, \quad (\text{A.31})$$

where  $|g\rangle$  is the ground state of the considered molecule. Also, in quantum chemistry simulations the resulting spectral lines are not limited by resolution and therefore well separated, except for perfectly degenerate cases, so the summed transition probability  $B_{\delta\omega,g}^\omega(\omega_0)$  reduces to the Einstein B coefficient  $B_{eg}^\omega$  of a specific single transition from an excited state  $|e\rangle$  to the ground state  $|g\rangle$  that corresponds to the energy difference  $\hbar\omega_0$ . Note that unlike the discussion in [236, pp. 165–166], the summation over degenerate higher excitations of the harmonic oscillators corresponding to molecular vibrations in the respective normal modes  $n$  is explicitly disregarded here, as those are discussed separately in Section 4.5.

The Einstein B coefficient  $B_{eg}^\omega$  can be expressed through the transition dipole moment  $\mu_{eg}$  as

$$B_{eg}^\omega = \frac{1}{4\pi\epsilon_0} \cdot \frac{4\pi^2}{3\hbar^2} \cdot |\mu_{eg}|^2 = \frac{\pi}{3\epsilon_0\hbar^2} \cdot |\mu_{eg}|^2, \quad (\text{A.32})$$

where  $\epsilon_0$  is the vacuum permittivity [245]. As in Section 4.3 we consider the excited state  $|e\rangle = |1_n\rangle$  with one vibron in normal mode  $n$  and the ground state  $|g\rangle = |0_{\text{vib}}\rangle$  comprising zero vibrons and write the transition dipole moment as

$$\mu_{eg} = \partial_{Q_n}\mu \cdot \langle g|\hat{Q}_n|e\rangle = \partial_{Q_n}\mu \cdot \langle 0_{\text{vib}}|\hat{Q}_n|1_n\rangle = \partial_{Q_n}\mu \cdot \sqrt{\frac{\hbar}{2\Omega_n}} \quad (\text{A.33})$$

with  $Q_n$  being the normal coordinate for a molecular vibration in mode  $n$  with angular frequency  $\Omega_n$ . For the Einstein B coefficient we thus obtain

$$B_{eg}^\omega = \frac{\pi}{3\epsilon_0\hbar^2} \cdot |\partial_{Q_n}\mu|^2 \cdot \frac{\hbar}{2\Omega_n} = \frac{\pi}{6\epsilon_0\hbar\Omega_n} \cdot |\partial_{Q_n}\mu|^2 \quad (\text{A.34})$$

and by inserting into Eq. (A.31) and employing that  $\omega_0 = \Omega_n$  by definition we finally find the result

$$\Psi_\omega = N_A \cdot \frac{\pi}{6c\epsilon_0} |\partial_{Q_n}\mu|^2. \quad (\text{A.35})$$

For the wavenumber domain we use the conversion formula Eq. (A.30) to derive

$$\Psi_{\bar{\nu}} = N_A \cdot \frac{1}{12c^2\epsilon_0} |\partial_{Q_n}\mu|^2. \quad (\text{A.36})$$

Since the output of frequency and dynamic molecular dipole calculations in ORCA returns the value of  $\Psi_{\tilde{\nu}}$  in km/mol, in the output file named T\*\*2, a formula for  $\mu_{eg}$  as a function of  $\Psi_{\tilde{\nu}}$  is of particular interest. By solving Eq. (A.36) for  $\partial_{Q_n}\boldsymbol{\mu}$  and inserting into Eq. (A.33) we find

$$|\mu_{eg}| = \sqrt{\frac{12c^2\varepsilon_0 \cdot \Psi_{\tilde{\nu}}}{N_A}} \cdot \sqrt{\frac{\hbar}{2\Omega_n}} = \hbar c \cdot \sqrt{\frac{6\varepsilon_0}{N_A}} \cdot \sqrt{\frac{\Psi_{\tilde{\nu}}}{\hbar\Omega_n}}. \quad (\text{A.37})$$

When  $\mu_{eg}$  is given in Debye,  $\Psi_{\tilde{\nu}}$  is given in km/mol and  $\hbar\Omega_n$  is given in meV, then Eq. (A.37) yields the following conversion formula for the numerical values.

$$\{|\mu_{eg}|\}_D = 0.2224 \cdot \sqrt{\frac{\{\Psi_{\tilde{\nu}}\}_{\text{km/mol}}}{\{\hbar\Omega_n\}_{\text{meV}}}} \quad (\text{A.38})$$



# B

## Photon emission statistics of carbon nanotube defect sites in the framework of rate models

---

To connect the level schemes shown in Figs. 5.8 (d) and (e) with the fits to the normalized coincidence counts  $g^{(2)}(\tau)$  presented in Figs. 5.7 (a)–(d), 5.8 (a), and (c), a formalism is required to convert the schematic considerations into mathematical models that allow for (numerical) solution and fitting to the data. A common approach lies within the assumption that the dynamics between different states in a level scheme satisfy the Markov property [363], meaning that the system is memoryless in the sense that the probability for a transition from one state to another is only dependent on the current state of the system but not on the history of events that preceded the current configuration. In this scenario, for the case of a level scheme with a finite number of discrete states, the Chapman–Kolmogorov equation formulating the transition probabilities of a Markov process simplifies to the master equation

$$\frac{dp_n(t)}{dt} = \sum_{m=1}^M [W_{mn}p_m(t) - W_{nm}p_n(t)], \quad (\text{B.1})$$

where  $p_n(t)$  is the probability to find the system in state  $n$  at time  $t$ ,  $W_{mn}$  is the (constant) transition probability per unit time from state  $m$  to state  $n$ , and summation is performed over all accessible states  $m = 1, \dots, M$  [364, pp. 96–97].

For a physical system, the transition rate  $\Gamma_{mn}$  between two states  $m$  and  $n$  is connected to the transition probability by  $\Gamma_{mn} = N \cdot W_{mn}$ , where  $N$  is the total number of occupations. By the additional assumption  $N = 1$ , effectively excluding exciton–exciton interactions for the case of **hexyl-functionalized carbon nanotubes (hCNTs)**, thereby limiting the analysis to the weak-excitation regime,  $\Gamma_{mn}$  may be substituted for  $W_{mn}$  in Eq. (B.1), turning the master equation into the rate equation

$$\frac{dp_n(t)}{dt} = \sum_{m=1}^M [\Gamma_{mn}p_m(t) - \Gamma_{nm}p_n(t)]. \quad (\text{B.2})$$

Note that both Eq. (B.1) and Eq. (B.2) are gain-loss equations, where the positive terms

represent gain of state  $n$  due to transitions from other states  $m$  and the negative terms account for losses from state  $n$  into other states [364, p. 97].

By interpreting the summation over  $m$  as a matrix multiplication, Eq. (B.2) may be written as a system of first-order ordinary differential equations (ODEs),

$$\frac{d}{dt} \mathbf{p}(t) = \mathbf{A} \cdot \mathbf{p}(t), \quad (\text{B.3})$$

where  $\mathbf{p}(t) = (p_1(t), \dots, p_M(t))^T$  is the column vector of all occupation probabilities and the square matrix  $\mathbf{A}$  is given by

$$A_{ij} = \Gamma_{ji} - \sum_{m=1}^M \Gamma_{im} \cdot \delta_{ij}, \quad (\text{B.4})$$

where  $i, j = 1, \dots, M$  and  $\delta_{ij}$  is the Kronecker delta.

This chapter approaches different level schemes that are used to interpret the exciton dynamics in hCNTs through the mathematical description as a system of first-order ODEs like in Eq. (B.3).<sup>1</sup> Apart from the DS<sub>1</sub> and DS<sub>2</sub> models presented in Figs. 5.8 (d) and (e), also other models and their failures are examined, in order to allow for a more intuitive interpretation on how the different constituents act in the considered level schemes and as a result influence the shape of the corresponding  $g^{(2)}$  function.

## B.1. Blinking single-photon source with one emissive state

To illustrate the working mechanism of intermittent single photon emission from hCNTs and to derive the key figures  $\eta$  and  $g_{\max}^{(2)}$  measuring the prevalence of antibunching and bunching, respectively, we employed the three-level system in Fig. B.1 (b) comprising the ground state  $|0\rangle$ , a bright state  $|B\rangle$  and a dark shelving state  $|S\rangle$ . Note that this kind of shelving state is sometimes ambiguously referred to as simply a *dark state*, which, however, is fundamentally different from the type of dark state that is ruled out for X and T in Section 5.3. This latter kind of dark state was employed in [296] to capture both mono and biexponential photoluminescence (PL) decay characteristics by the level scheme that is replicated from [296] in Fig. B.1 (a).

In both level schemes in Fig. B.1 the exciton population may interconvert between the bright state  $|B\rangle$  and the dark state  $|D\rangle$  or the shelving state  $|S\rangle$  with rates  $\gamma_{\uparrow}$  and  $\gamma_{\downarrow}$  or  $\kappa_s$  and  $\kappa_d$ , respectively. However, the two models differ strikingly regarding their decay characteristics from the states  $|D\rangle$  and  $|S\rangle$ , respectively. In the model from [296] in Fig. B.1 (a) direct decay from the dark state  $|D\rangle$  to the ground state  $|0\rangle$  occurs with rate  $\Gamma_D$ , while in the

---

<sup>1</sup> Parts of this chapter are based on the publication [P3] available at <https://pubs.acs.org/doi/10.1021/acs.nanolett.9b02553>. Permission for any further reuse of the excerpted material must be granted by the American Chemical Society.

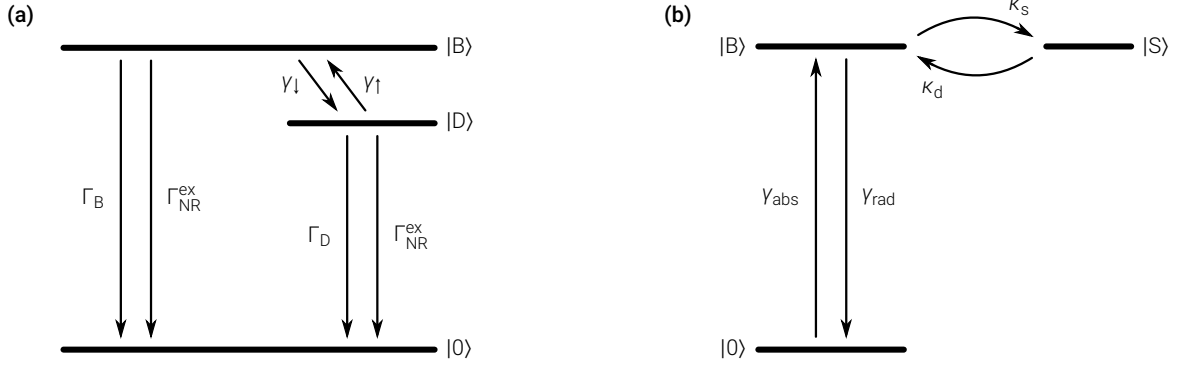


**Figure B.1.:** (a) Level system employed in [296] to capture mono and biexponential PL decay characteristics in one model comprising the ground state  $|0\rangle$ , a bright state  $|B\rangle$ , and a dark state  $|D\rangle$  with corresponding transition rates subject to an extrinsic nonradiative decay channel with varying rate  $\Gamma_{NR}^{ex}$ . (b) Three-level system comprising the ground state  $|0\rangle$ , a bright state  $|B\rangle$ , and a shelving state  $|S\rangle$  with corresponding transition rates. The two-level subsystems comprising the states  $|0\rangle$  and  $|B\rangle$ , and comprising the states  $|B\rangle$  and  $|S\rangle$  are used to model photon antibunching due to single-photon emission and bunching arising from PL intermittency (blinking), respectively. The graphic (a) is a replica of the level scheme discussed in [296], the graphic (b) is reproduced from [P3].

three-level system in Fig. B.1 (b) no direct decay from the shelving state  $|S\rangle$  to the ground state  $|0\rangle$  is possible. By consequence, the decay channel in Fig. B.1 (a) from  $|B\rangle$  via  $|D\rangle$  to  $|0\rangle$  compromises the quantum yield (QY) of the system, while the QY in Fig. B.1 (b) is equal to 1 by design. Instead, the decay time from  $|B\rangle$  to  $|0\rangle$  may be prolonged by transient shelving to state  $|S\rangle$ . The loss of QY in Fig. B.1 (a) is particularly pronounced for the case where  $|D\rangle$  is energetically lower than  $|B\rangle$ , which is generally assumed for carbon nanotubes (CNTs) as discussed in Section 2.4, such that  $\gamma_{\downarrow}$  is much larger than  $\gamma_{\uparrow}$ . In addition to this mechanism, nonradiative decay with variable rate  $\Gamma_{NR}^{ex}$  caused by extrinsic effects is considered in the model of [296]. By consequence, the exceptional PL brightness of X and T discussed in Section 5.3 excludes pronounced nonradiative decay channels for these states and invalidates the model from [296] shown in Fig. B.1 (a), but does not conflict with the level scheme in Fig. B.1 (b) as an explanation for intermittent single photon emission from hCNTs.

To analyze the characteristic properties of this level scheme, we followed the approach in Eq. (B.3) and formulated the master equation governing the population dynamics in terms of the system of first-order ODEs

$$\frac{d}{dt} \begin{pmatrix} p_{|0\rangle}(t) \\ p_{|B\rangle}(t) \\ p_{|S\rangle}(t) \end{pmatrix} = \begin{pmatrix} -\gamma_{abs} & \gamma_{rad} & 0 \\ \gamma_{abs} & -\gamma_{rad} - \kappa_s & \kappa_d \\ 0 & \kappa_s & -\kappa_d \end{pmatrix} \begin{pmatrix} p_{|0\rangle}(t) \\ p_{|B\rangle}(t) \\ p_{|S\rangle}(t) \end{pmatrix}, \quad (\text{B.5})$$

where  $p_{|0\rangle}(t)$ ,  $p_{|B\rangle}(t)$ , and  $p_{|S\rangle}(t)$  are the probabilities to find the system in state  $|0\rangle$ ,  $|B\rangle$ , or  $|S\rangle$ , respectively, and  $\gamma_{abs}$ ,  $\gamma_{rad}$ ,  $\kappa_s$ , and  $\kappa_d$  are the transition rates indicated in Fig. B.1 (b).

A general analytic solution of Eq. (B.5) was found to lead to lengthy expressions that impede an intuitive interpretation of the dynamics in the level scheme of Fig. B.1 (b). For many realistic scenarios, however, additional assumptions can be used to simplify the theoretical description. Typically, the dynamics between the bright state  $|B\rangle$  and the shelving state  $|S\rangle$  is slower than both excitation and relaxation, such that  $\gamma_{\text{abs}}, \gamma_{\text{rad}} \gg \kappa_s, \kappa_d$ . In this case, higher order terms of the form  $\kappa/\gamma$  can be omitted, where  $\kappa$  stands for either  $\kappa_s$  or  $\kappa_d$  and  $\gamma$  stands for either  $\gamma_{\text{abs}}$  and  $\gamma_{\text{rad}}$ .

Based on this simplification, a product form for the second-order correlation function  $g^{(2)}$  can be derived, Eq. (B.15), where the two factors describe the contributions of PL intermittency (blinking) and single-photon emission, respectively. In particular, this result shows that in the simple framework of the three-level system in Fig. B.1 (b) single-photon emission is solely determined by the dynamics within the two-level subsystem comprising the states  $|0\rangle$  and  $|B\rangle$ , while the blinking behavior originates from the two-level subsystem comprising the states  $|B\rangle$  and  $|S\rangle$ .

For brevity, the lengthy derivation of a general solution to Eq. (B.5) is skipped here and instead the contributions from both two-level subsystems in Fig. B.1 (b) are considered separately. This ansatz implicitly assumes a perfect decoupling of the dynamics in both two-level subsystems that is only accurate in the case  $\gamma_{\text{abs}} \gg \gamma_{\text{rad}}$ . Corrections that arise when  $\gamma_{\text{abs}} \gg \gamma_{\text{rad}}$  does not hold, are discussed after the derivation of Eq. (B.15).

For both two-level subsystems master equations of the form given by Eq. (B.3) allow to solve for the vector  $\mathbf{p}$  of occupation probabilities. To arrive at expressions for the second-order correlation function  $g^{(2)}$ , we employed the representation

$$g^{(2)}(\tau) = \frac{\langle I(t)I(t+\tau) \rangle}{\langle I(t) \rangle \langle I(t+\tau) \rangle} = \frac{\langle I_0 p(t) \cdot I_0 p(t+\tau) \rangle}{\langle I_0 p(t) \rangle \langle I_0 p(t+\tau) \rangle} = \frac{\langle p(t)p(t+\tau) \rangle}{\langle p(t) \rangle \langle p(t+\tau) \rangle}, \quad (\text{B.6})$$

where  $\langle \cdot \rangle$  is the average over time  $t$ ,  $I(t)$  is the measured intensity at time  $t$ ,  $I_0$  is the time-averaged emission intensity and  $p(t)$  is the probability to detect a photon at time  $t$  [166].

First, consider the two-level subsystem comprising the states  $|B\rangle$  and  $|S\rangle$  (top part in Fig. B.1 (b)) that describes shelving from a bright state  $|B\rangle$  into a dark state  $|S\rangle$  with rate  $\kappa_s$  and deshelving with rate  $\kappa_d$ . The dynamics in this two-level system are formulated by the master equation

$$\frac{d}{dt} \begin{pmatrix} p_{|B\rangle}(t) \\ p_{|S\rangle}(t) \end{pmatrix} = \begin{pmatrix} -\kappa_s & \kappa_d \\ \kappa_s & -\kappa_d \end{pmatrix} \begin{pmatrix} p_{|B\rangle}(t) \\ p_{|S\rangle}(t) \end{pmatrix}, \quad (\text{B.7})$$

yielding solutions for  $p_{|B\rangle}(t)$  and  $p_{|S\rangle}(t)$  that allow for the computation of  $g^{(2)}(\tau)$  using Eq. (B.6). In the steady state limit, both  $\langle p(t) \rangle$  and  $\langle p(t+\tau) \rangle$  in Eq. (B.6) are given by the time-independent probability  $p_{|B\rangle}(\infty)$  to find the system in the bright state  $|B\rangle$ , since there is no photon emission from the shelving state  $|S\rangle$ . For the numerator in Eq. (B.6) we find

$$\begin{aligned}\langle p(t)p(t+\tau) \rangle &= \langle p_{|B\rangle}(t) \cdot p_{|B\rangle \rightarrow |B\rangle}(t+\tau|t) \rangle = \langle p_{|B\rangle}(t) \cdot p_{|B\rangle \rightarrow |B\rangle}(\tau) \rangle \\ &= p_{|B\rangle}(\infty) \cdot p_{|B\rangle \rightarrow |B\rangle}(\tau),\end{aligned}\quad (\text{B.8})$$

where  $p_{|B\rangle \rightarrow |B\rangle}(t+\tau|t)$  is the probability to find the system in state  $|B\rangle$  both at time  $t$  and  $t+\tau$ , and  $p_{|B\rangle \rightarrow |B\rangle}(\tau)$  is the probability for returning from state  $|B\rangle$  to state  $|B\rangle$  after time difference  $\tau$ . Solving Eq. (B.7) yields

$$p_{|B\rangle}(\infty) = \kappa_d / (\kappa_s + \kappa_d) \quad (\text{B.9a})$$

$$p_{|B\rangle \rightarrow |B\rangle}(\tau) = \kappa_d / (\kappa_s + \kappa_d) + \kappa_s / (\kappa_s + \kappa_d) \cdot \exp[-(\kappa_s + \kappa_d)|\tau|] \quad (\text{B.9b})$$

and with the inverse rates  $\tau_s = 1/\kappa_s$  and  $\tau_d = 1/\kappa_d$  we obtain the result of SANTORI et al. [306] for blinking self-assembled quantum dots,

$$g^{(2)}(\tau) = 1 + \frac{\kappa_s}{\kappa_d} e^{-(\kappa_s + \kappa_d)|\tau|} = 1 + \frac{\tau_d}{\tau_s} e^{-\left(\frac{1}{\tau_s} + \frac{1}{\tau_d}\right)|\tau|}. \quad (\text{B.10})$$

For the case of single photon emission consider the two-level subsystem comprising the states  $|0\rangle$  and  $|B\rangle$  (left part in Fig. B.1 (b)) that is described by the master equation

$$\frac{d}{dt} \begin{pmatrix} p_{|0\rangle}(t) \\ p_{|B\rangle}(t) \end{pmatrix} = \begin{pmatrix} -\gamma_{\text{abs}} & \gamma_{\text{rad}} \\ \gamma_{\text{abs}} & -\gamma_{\text{rad}} \end{pmatrix} \begin{pmatrix} p_{|0\rangle}(t) \\ p_{|B\rangle}(t) \end{pmatrix}. \quad (\text{B.11})$$

The condition of single photon emission is imposed by introducing the additional requirement that immediately after emission of a photon the system is projected into the ground state  $|0\rangle$ . While  $\langle p(t) \rangle$  and  $\langle p(t+\tau) \rangle$  in Eq. (B.6) are given by the time-independent probability  $p_{|B\rangle}(\infty)$  as before, for the numerator in Eq. (B.6) we now find

$$\begin{aligned}\langle p(t)p(t+\tau) \rangle &= \langle p_{|B\rangle}(t) \cdot p_{|0\rangle \rightarrow |B\rangle}(t+\tau|t) \rangle = \langle p_{|B\rangle}(t) \cdot p_{|0\rangle \rightarrow |B\rangle}(\tau) \rangle \\ &= p_{|B\rangle}(\infty) \cdot p_{|0\rangle \rightarrow |B\rangle}(\tau),\end{aligned}\quad (\text{B.12})$$

where  $p_{|0\rangle \rightarrow |B\rangle}(t+\tau|t)$  is the probability to find the system in state  $|0\rangle$  at time  $t$  and in state  $|B\rangle$  at time  $t+\tau$  and  $p_{|0\rangle \rightarrow |B\rangle}(\tau)$  is the probability for a transition from  $|0\rangle$  to  $|B\rangle$  after time difference  $\tau$ . Solving the system of first-order ODEs Eq. (B.11) yields

$$p_{|B\rangle}(\infty) = \gamma_{\text{abs}} / (\gamma_{\text{abs}} + \gamma_{\text{rad}}) \quad (\text{B.13a})$$

$$p_{|0\rangle \rightarrow |B\rangle}(\tau) = \gamma_{\text{abs}} / (\gamma_{\text{abs}} + \gamma_{\text{rad}}) \cdot (1 - \exp[-(\gamma_{\text{abs}} + \gamma_{\text{rad}})|\tau|]) \quad (\text{B.13b})$$

and with the abbreviation  $\tau_0 = 1/(\gamma_{\text{abs}} + \gamma_{\text{rad}})$  we obtain the result of HOFMANN et al. [67] for single-photon emission from CNTs,

$$g^{(2)}(\tau) = 1 - e^{-(\gamma_{\text{abs}} + \gamma_{\text{rad}})|\tau|} = 1 - e^{-|\tau|/\tau_0}. \quad (\text{B.14})$$

To formulate a model that captures both bunching due to PL intermittency and antibunching due to single-photon emission, we finally consider the  $g^{(2)}$  function that is given by the product of Eq. (B.14) and Eq. (B.10). Moreover, in order to describe imperfect antibunching given by  $g^{(2)}(0) > 0$ , the term  $\exp(-|\tau|/\tau_0)$  is multiplied with an additional factor  $\eta \leq 1$ , resulting in the expression given by WALDEN-NEWMAN et al. [73] for single-photon emission from spectrally diffusing CNTs,

$$g^{(2)}(\tau) = \left(1 - \eta \cdot e^{-\frac{|\tau|}{\tau_0}}\right) \left(1 + \frac{\tau_d}{\tau_s} e^{-\left(\frac{1}{\tau_s} + \frac{1}{\tau_d}\right)|\tau|}\right). \quad (\text{B.15})$$

The derivation of Eq. (B.15) no longer yields the correct result when the implicit assumption from above,  $\gamma_{\text{abs}} \gg \gamma_{\text{rad}}$ , is relaxed, since the formal decoupling of both two-level subsystems in Fig. B.1 (b) is lost. The general solution of Eq. (B.5) shows, however, that Eq. (B.15) still holds to lowest order in  $\kappa/\gamma$ , when  $\tau_s = (\gamma_{\text{abs}} + \gamma_{\text{rad}})/(\gamma_{\text{abs}} \cdot \kappa_s)$  is used instead of  $\tau_s = 1/\kappa_s$ . This modification can be interpreted as the introduction of an effective shelving time that takes into account that the shelving state  $|S\rangle$  is not directly accessible from the ground state  $|0\rangle$  by weighting  $1/\kappa_s$  with the occupation probability  $\gamma_{\text{abs}}/(\gamma_{\text{abs}} + \gamma_{\text{rad}})$  of the excited state  $|B\rangle$ .

We employed the three-level system in Fig. B.1 (b) to model the normalized coincidence counts  $g^{(2)}(\tau)$  of hCNTs A and B from Section 5.4 by finding fits of Eq. (B.15) the data. The resulting best fits for hCNT A (Figs. B.2 (a) and (c)) and hCNT B (Figs. B.2 (b) and (d)) were used to determine the degree of correlation  $\eta$  (noted in the top right respective corners of Figs. B.2 (a)–(d)), the time constant  $\tau_0$ , the shelving time  $\tau_s$  and the deshelving time  $\tau_d$ .

Applying this procedure to all hCNTs of our study, we found that  $\tau_0 \ll \tau_s, \tau_d$  holds for all examined emitters (data not shown), verifying the previous assumption  $\gamma_{\text{abs}}, \gamma_{\text{rad}} \gg \kappa_s, \kappa_d$ . Furthermore, in a plot of deshelving time  $\tau_d$  against shelving time  $\tau_s$  (Fig. B.2 (e)) for X and T (green and red data points, respectively) the data scattered around the solid gray line of equal time scales and mostly fell within the gray shaded area corresponding to values between 1/2 and 2 for  $\tau_s/\tau_d$ .

The individual timescales  $\tau_s$  for shelving and  $\tau_d$  for deshelving can therefore be replaced by a single blinking time  $\tau_{\text{blink}}$  that represents the characteristic timescale after which the emitter transitions from its bright to its dark configuration or vice versa. Complementary to the laser excitation power dependency presented in Figs. 5.11 (a)–(f) we investigated the dependence of  $\tau_{\text{blink}}$  on the detuning between  $E_{11}$  and the excitation laser energy. Fig. B.2 (f) shows the results for X and T autocorrelations (green and red data points, respectively) together with the center-of-mass for three groups of data points around 0 meV, 70 meV, and 190 meV detuning (black diamonds). We observed an increase of the blinking time with increasing laser detuning and discuss in the following how this finding can be explained by a variation of the rate  $\gamma_{\text{abs}}$ .

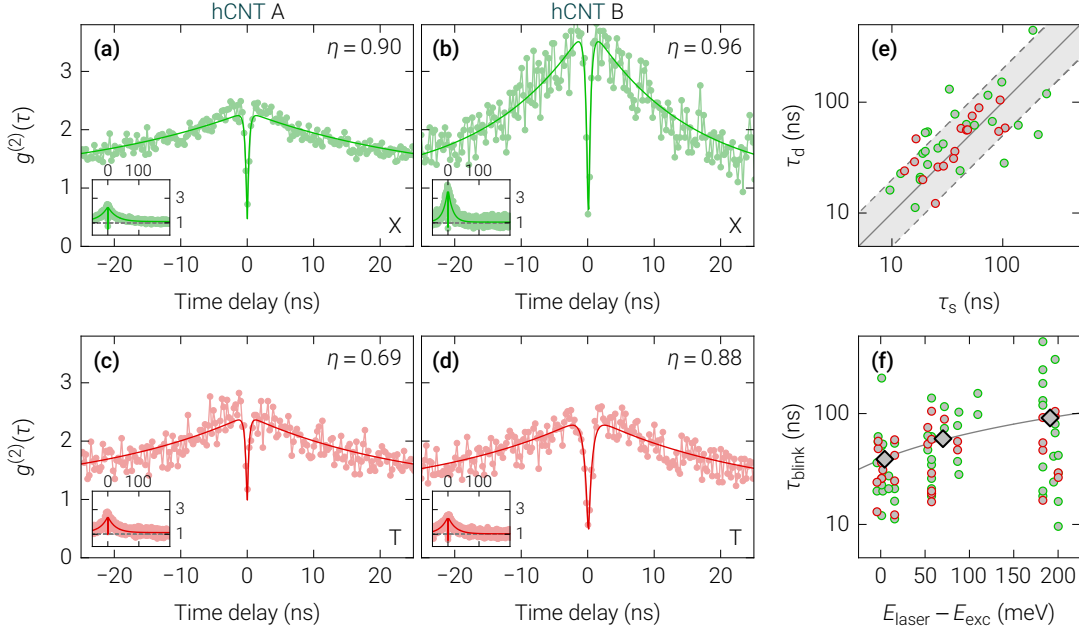


**Figure B.2.:** (a)–(d) Normalized photon coincidence counts  $g^{(2)}(\tau)$  for the autocorrelation of X (light green) and T (light red) for hCNTs A and B (left and right column, respectively) reproduced from Figs. 5.7 (a)–(d). Fits to  $g^{(2)}(\tau)$  (solid lines) were obtained with Eq. (B.15). The insets illustrate that  $g^{(2)}(\tau)$  approaches unity on long timescales. (e) Shelving and deshelving time scales  $\tau_s$  and  $\tau_d$  for X and T (green and red data points, respectively) scatter around the solid gray line of equal time scales. (f) Blinking time scales of X and T (green and red data points, respectively) as a function of the energy difference between the  $E_{11}$  exciton energy  $E_{\text{exc}}$  and excitation laser energy  $E_{\text{laser}}$ . Black diamonds show the center-of-mass for three groups of data points around 0 meV, 70 meV, and 190 meV detuning, respectively. The solid gray line shows a linear fit of the blinking time scale as a function of laser detuning. The graphics (a)–(f) are reproduced from [P3].

Since  $\gamma_{\text{abs}}$  was introduced in Section 5.4 as an effective rate capturing the actual excitation path via relaxation from a higher energy state, this rate is expected to decrease with increasing detuning due to a less efficient relaxation mechanism with growing energy mismatch. We quantified this decrease by finding a confidence interval for  $\gamma_{\text{abs}}$  by employing an affine invariant Markov chain Monte Carlo ensemble sampler [365, 366] for fits of Eq. (B.15) to normalized photon coincidence counts featuring different blinking times  $\tau_{\text{blink}}$ . Indeed, we observed a decrease of  $\gamma_{\text{abs}}$  by a factor of 1.5 when assuming the range 39–91 ns for  $\tau_{\text{blink}}$  given by the three center-of-mass points introduced in Fig. B.2 (f).

Interestingly, we found no dependence of the blinking time on the laser excitation power (cf. Figs. 5.11 (d)–(f)). This finding proves that the microscopic origin of the PL intermittency is different in hCNTs than in self-assembled quantum dots, where substantial power dependencies have been observed [307, 309], and may indicate that relaxation from higher energy states in hCNTs is a time-limiting factor that determines the value of the effective rate  $\gamma_{\text{abs}}$ .

## B.2. Blinking single-photon source with two competing emissive states

The scenario discussed in Section 5.4, where T is the negatively charged counterpart of X, and emission from X and T is mutually exclusive, is formulated in terms of the level scheme in Fig. B.3. The system is assumed to exhibit switching between a neutral state (left hand side) and a negatively charged state (right hand side) with rates  $\kappa_{XT}$  and  $\kappa_{TX}$ , respectively. In the neutral state, emission from the trap state is attributed to X, while in the negatively charged state, emission from the trap state is attributed to T. In addition, the ground state  $|0\rangle$  and the exciton continuum state  $|E_{11}\rangle$  are split into two respective states  $|0\rangle_X, |0\rangle_T$  and  $|E_{11}\rangle_X, |E_{11}\rangle_T$  of different charge, in order to support a “memory” of the current trap charge state, even if the trap is not occupied. For brevity, this model of mutual exclusive emission is called ME model in the following.

For numerical analysis, we formulated the master equation describing the dynamics of the level-scheme in Fig. B.3 in terms of the system of first-order ODEs

$$\frac{d}{dt} \mathbf{p}_{\text{ME}}(t) = \mathbf{A}_{\text{ME}} \cdot \mathbf{p}_{\text{ME}}(t), \quad (\text{B.16})$$

where  $\mathbf{p}_{\text{ME}}(t)$  is given by

$$\mathbf{p}_{\text{ME}}(t) = \begin{pmatrix} p_{|0\rangle_X}(t) \\ p_{|0\rangle_T}(t) \\ p_{|E_{11}\rangle_X}(t) \\ p_{|E_{11}\rangle_T}(t) \\ p_{|X\rangle}(t) \\ p_{|T\rangle}(t) \end{pmatrix}, \quad (\text{B.17})$$

$p_{|\psi\rangle}(t)$  is the probability to find the system in state  $|\psi\rangle$  at time  $t$  as in Eqs. (B.5), (B.7) and (B.11) in Section B.1, and  $\mathbf{A}_{\text{ME}}$  is given by

$$\mathbf{A}_{\text{ME}} = \begin{pmatrix} -\gamma_{\text{abs}} - \kappa_{XT} & \kappa_{TX} & \gamma_{11} & 0 & \gamma_X & 0 \\ \kappa_{XT} & -\gamma_{\text{abs}} - \kappa_{TX} & 0 & \gamma_{11} & 0 & \gamma_T \\ \gamma_{\text{abs}} & 0 & -\gamma_{11} - \kappa_{XT} - \kappa_X & \kappa_{TX} & 0 & 0 \\ 0 & \gamma_{\text{abs}} & \kappa_{XT} & -\gamma_{11} - \kappa_{TX} - \kappa_T & 0 & 0 \\ 0 & 0 & \kappa_X & 0 & -\gamma_X & 0 \\ 0 & 0 & 0 & \kappa_T & 0 & -\gamma_T \end{pmatrix}. \quad (\text{B.18})$$

Note that in this rate equation the transition between the neutral and charged trap states is excluded if the trap is occupied, since the rates  $\kappa_{TX}$  and  $\kappa_{XT}$  do not appear in the lower right ( $2 \times 2$ ) matrix subblock of  $\mathbf{A}_{\text{ME}}$ . This choice is motivated by the observation that the trap state changes its energy upon charging and discharging, thereby suppressing this transition

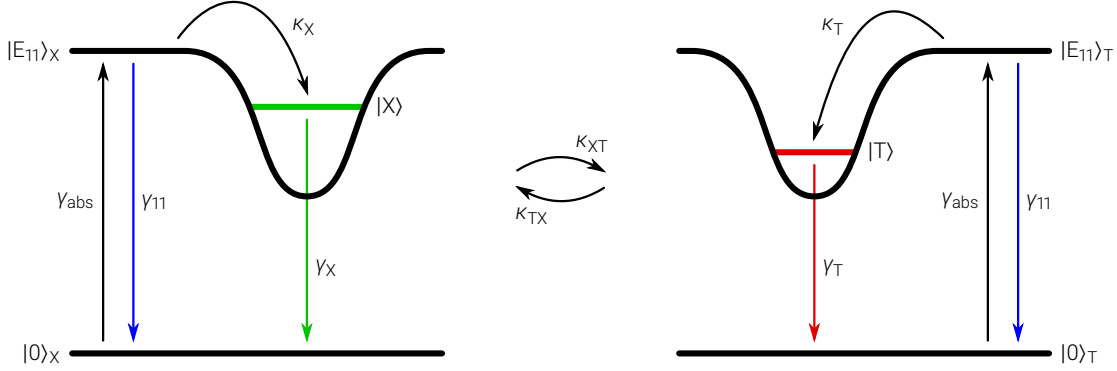


**Figure B.3.:** Level scheme used to model mutually exclusive emission from X and T. The left hand side corresponds to a neutral state of the defect site with (neutral) ground state  $|0\rangle_X$ , (neutral) exciton continuum  $|E_{11}\rangle_X$  and neutral trap state  $|X\rangle$ . The right hand side corresponds to a negatively charged state of the defect site with (charged) ground state  $|0\rangle_T$ , (charged) exciton continuum  $|E_{11}\rangle_T$  and charged trap state  $|T\rangle$ . The graphic is reproduced from [P3].

in the absence of a thermal energy bath. Depending on the details of the charging and discharging mechanisms, there are other suitable choices respecting this energy difference, e. g. by only including the transition from X to T but not from T to X or by introducing unequal rates preferring the transition from X to T and suppressing the transition from T to X. These scenarios have been investigated, but no significant differences to the results discussed below have been found.

Inserting  $p_{|X\rangle}(t)$  and  $p_{|T\rangle}(t)$  into Eq. (B.6), the normalized coincidence counts  $g_{XX}^{(2)}(\tau)$ ,  $g_{TT}^{(2)}(\tau)$  and  $g_{XT}^{(2)}(\tau)$  for the autocorrelations of X and T as well as the crosscorrelation of X and T, respectively, take the form

$$g_{XX}^{(2)}(\tau) = \frac{\langle p_{|X\rangle}(t) p_{|X\rangle}(t+\tau) \rangle}{\langle p_{|X\rangle}(t) \rangle \langle p_{|X\rangle}(t+\tau) \rangle}, \quad (\text{B.19a})$$

$$g_{TT}^{(2)}(\tau) = \frac{\langle p_{|T\rangle}(t) p_{|T\rangle}(t+\tau) \rangle}{\langle p_{|T\rangle}(t) \rangle \langle p_{|T\rangle}(t+\tau) \rangle}, \quad (\text{B.19b})$$

$$g_{XT}^{(2)}(\tau) = \frac{\langle p_{|X\rangle}(t) p_{|T\rangle}(t+\tau) \rangle}{\langle p_{|X\rangle}(t) \rangle \langle p_{|T\rangle}(t+\tau) \rangle}. \quad (\text{B.19c})$$

As before,  $\langle p_{|\psi\rangle}(t) \rangle = p_{|\psi\rangle}(\infty)$  and  $\langle p_{|\psi\rangle}(t+\tau) \rangle = p_{|\psi\rangle}(\infty)$  hold true for any state  $|\psi\rangle$  in the steady state limit and single photon emission is implemented by the assumption that the system is projected into the ground state after a photon was emitted. Furthermore, the numerators in Eq. (B.19) are given by

$$\begin{aligned} \langle p_{|\psi\rangle}(t) p_{|\phi\rangle}(t+\tau) \rangle &= \langle p_{|\psi\rangle}(t) p_{|0(\psi)\rangle \rightarrow |\phi\rangle}(t+\tau|t) \rangle = \langle p_{|\psi\rangle}(t) \cdot p_{|0(\psi)\rangle \rightarrow |\phi\rangle}(\tau) \rangle \\ &= p_{|\psi\rangle}(\infty) \cdot p_{|0(\psi)\rangle \rightarrow |\phi\rangle}(\tau), \end{aligned} \quad (\text{B.20})$$

where  $|0(\psi)\rangle$  is the ground state that the system is projected into after the emission of a photon from state  $|\psi\rangle$ ,  $p_{|\chi\rangle\rightarrow|\phi\rangle}(t+\tau|t)$  is the probability to find the system in state  $|\chi\rangle$  at time  $t$  and in state  $|\phi\rangle$  at time  $t+\tau$ , and  $p_{|\chi\rangle\rightarrow|\phi\rangle}(\tau)$  is the probability for a transition from  $|\chi\rangle$  to  $|\phi\rangle$  after time difference  $\tau$ . Combining these results with Eq. (B.19) finally yields

$$g_{\text{XX}}^{(2)}(\tau) = \frac{p_{|0\rangle_{\text{X}}\rightarrow|X\rangle}(\tau)}{p_{|X\rangle}(\infty)}, \quad g_{\text{TT}}^{(2)}(\tau) = \frac{p_{|0\rangle_{\text{T}}\rightarrow|T\rangle}(\tau)}{p_{|T\rangle}(\infty)}, \quad g_{\text{XT}}^{(2)}(\tau) = \frac{p_{|0\rangle_{\text{X}}\rightarrow|T\rangle}(\tau)}{p_{|T\rangle}(\infty)}. \quad (\text{B.21})$$

To calculate the probabilities of the form  $p_{|\psi\rangle}(\infty)$  and  $p_{|\chi\rangle\rightarrow|\phi\rangle}(\tau)$  we expressed solutions of Eq. (B.16) as  $\mathbf{p}_{\text{ME}}(t) = \exp(t \cdot \mathbf{A}_{\text{ME}}) \cdot \mathbf{p}_{\text{ME}}(0)$  using the matrix exponential  $\exp(\mathbf{A})$ . By choosing a suitable initial condition  $\mathbf{p}_{\text{ME}}(0)$  of the form  $(0, \dots, 0, 1, 0, \dots, 0)$  this allowed for direct numerical calculation of  $p_{|\chi\rangle\rightarrow|\phi\rangle}(\tau)$ , while  $p_{|\psi\rangle}(\infty)$  could be found from  $\lim_{t \rightarrow \infty} \exp(t \cdot \mathbf{A}_{\text{ME}})$ .

Any rate model that is solved by this approach yields perfect antibunching, since single-photon emission from a given state  $|\psi\rangle$  is introduced by the assumption that after the emission of a photon the system is instantaneously projected into the ground state such that  $p_{|\psi\rangle\rightarrow|0\rangle}(0) = 0$  by definition and therefore  $g^{(2)}(0) = 0$  by generalization of Eq. (B.21). For experimental data, however, this is often not the case, mainly due to finite bin width of time-correlation steps or due to a stray background signal.

To include the possibility of imperfect antibunching in our models, we considered an additional uncorrelated background signal, as discussed in the following. Starting from the second-order correlation function

$$g^{(2)}(\tau) = \frac{\langle I_1(t) I_2(t+\tau) \rangle}{\langle I_1(t) \rangle \langle I_2(t+\tau) \rangle}, \quad (\text{B.22})$$

where  $I_1(t)$  and  $I_2(t)$  are the time-dependent emission intensities in two (possibly identical) spectral bands 1 and 2, each intensity  $I_i(t)$  may be decomposed into a time-dependent contribution  $I_{|i\rangle}(t)$  from an emitter state  $|i\rangle$  and a time-independent background intensity  $I_i^B$  by writing  $I_i(t) = I_{|i\rangle}(t) + I_i^B$ . Eq. (B.22) can then be transformed as

$$\begin{aligned} g^{(2)}(\tau) &= \frac{\langle (I_{|1\rangle}(t) + I_1^B)(I_{|2\rangle}(t+\tau) + I_2^B) \rangle}{\langle I_{|1\rangle}(t) + I_1^B \rangle \langle I_{|2\rangle}(t+\tau) + I_2^B \rangle} \\ &= \frac{\langle I_{|1\rangle}(t) I_{|2\rangle}(t+\tau) \rangle + \langle I_{|1\rangle}(t) \rangle I_2^B + I_1^B \langle I_{|2\rangle}(t+\tau) \rangle + I_1^B I_2^B}{(\langle I_{|1\rangle}(t) \rangle + I_1^B)(\langle I_{|2\rangle}(t+\tau) \rangle + I_2^B)} \\ &= \frac{\langle I_{|1\rangle}(t) I_{|2\rangle}(t+\tau) \rangle + I_{|1\rangle}^0 I_2^B + I_1^B I_{|2\rangle}^0 + I_1^B I_2^B}{(I_{|1\rangle}^0 + I_1^B)(I_{|2\rangle}^0 + I_2^B)}, \end{aligned} \quad (\text{B.23})$$

where  $I_{|1\rangle}^0$  and  $I_{|2\rangle}^0$  are the time-averages of the time-dependent intensities  $I_{|1\rangle}(t)$  and  $I_{|2\rangle}(t)$ , respectively. By introducing the “pure” second-order correlation function of the emitter

without background signal,

$$g_{\text{pure}}^{(2)}(\tau) = \frac{\langle I_{|1\rangle}(t)I_{|2\rangle}(t+\tau) \rangle}{\langle I_{|1\rangle}(t) \rangle \langle I_{|2\rangle}(t+\tau) \rangle} = \frac{\langle I_{|1\rangle}(t)I_{|2\rangle}(t+\tau) \rangle}{I_{|1\rangle}^0 I_{|2\rangle}^0}, \quad (\text{B.24})$$

Eq. (B.23) can be rewritten as

$$g^{(2)}(\tau) = \frac{I_{|1\rangle}^0 I_{|2\rangle}^0}{(I_{|1\rangle}^0 + I_1^B)(I_{|2\rangle}^0 + I_2^B)} \cdot g_{\text{pure}}^{(2)}(\tau) + \frac{I_{|1\rangle}^0 I_2^B + I_1^B I_{|2\rangle}^0 + I_1^B I_2^B}{(I_{|1\rangle}^0 + I_1^B)(I_{|2\rangle}^0 + I_2^B)}. \quad (\text{B.25})$$

Defining the background intensity ratios  $\zeta_1 = I_{|1\rangle}^0 / I_1^B$  and  $\zeta_2 = I_{|2\rangle}^0 / I_2^B$  finally yields

$$g^{(2)}(\tau) = \frac{1}{(1 + 1/\zeta_1)(1 + 1/\zeta_2)} \cdot g_{\text{pure}}^{(2)}(\tau) + \frac{1 + \zeta_1 + \zeta_2}{(1 + \zeta_1)(1 + \zeta_2)}. \quad (\text{B.26})$$

We illustrate the limits of the ME model by showing its failure to reproduce the data of hCNT A from Section 5.4. In Figs. B.4 (a)–(f), the solid lines show plots of  $g^{(2)}(\tau)$  obtained by substituting  $g_{\text{XX}}^{(2)}(\tau)$ ,  $g_{\text{TT}}^{(2)}(\tau)$  and  $g_{\text{XT}}^{(2)}(\tau)$  from Eq. (B.21) for  $g_{\text{pure}}^{(2)}(\tau)$  in Eq. (B.26) and introducing two background intensity ratios  $\zeta_X$  and  $\zeta_T$  for the spectral bands of X and T, respectively. In Figs. B.4 (a)–(c) a fitting procedure was used to find the best fit of  $g^{(2)}(\tau)$  to the autocorrelation data of X (light green), thereby fixing all parameters in Eqs. (B.16) and (B.26) except  $\gamma_T$ ,  $\kappa_T$  and  $\zeta_T$ . By varying only these three remaining parameters, however, the resulting functional dependencies of  $g_{\text{TT}}^{(2)}(\tau)$  and  $g_{\text{XT}}^{(2)}(\tau)$  were unable to reproduce the autocorrelation data of T (light red) and the crosscorrelation data of X and T (orchid) as shown for an exemplary set of rates #1 in Figs. B.4 (b) and (c). In a complementary way, in Figs. B.4 (d)–(f), a fitting procedure was used to find the best fit of  $g^{(2)}(\tau)$  to the autocorrelation data of T (light red). As before, a variation of the still undetermined parameters  $\gamma_X$ ,  $\kappa_X$  and  $\zeta_X$  could not reproduce the autocorrelation data of X (light green) and the crosscorrelation data of X and T (orchid) as shown for a set of rates #2 in Figs. B.4 (c) and (d).

From a closer inspection of the level scheme in Fig. B.3 we determined the origin of the failure to reproduce the data in Figs. B.4 (a)–(f), proving that the ME model is conceptually unable to explain our measurements. For the autocorrelation of X and T we observed a contrasting behavior for the functional form of  $g^{(2)}(\tau)$  in Figs. B.4 (a), (b), (d), and (e): if  $g^{(2)}(\tau)$  well reproduces the bunching behavior for the autocorrelation of X, it falls short to do so for the autocorrelation of T (gray curve too flat in Fig. B.4 (b)) and vice versa (gray curve too flat in Fig. B.4 (d)). In particular we found that the autocorrelation data of both X and T assume values greater than 2 in the vicinity of zero time delay, whereas  $g_{\text{max}}^{(2)} > 2$  is only possible for the autocorrelation of either X or T in the framework of the ME model. Turning back to the definition  $g_{\text{max}}^{(2)} = 1 + \kappa_s / \kappa_d$  this observation is readily understood: since blinking in the ME model is explained by the mutual exclusiveness of emission from X and T, the

## B. PHOTON EMISSION STATISTICS IN THE FRAMEWORK OF RATE MODELS

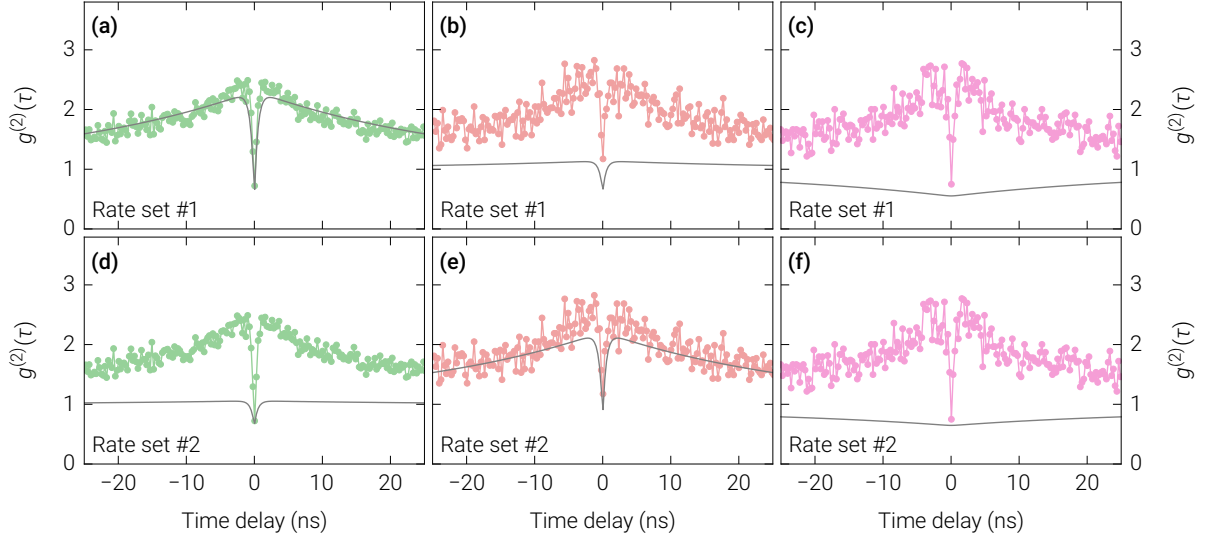


**Figure B.4.:** Normalized coincidence counts  $g^{(2)}(\tau)$  for the autocorrelation of X (light green) and T (light red) as well as the crosscorrelation of X and T (orchid) for hCNT A reproduced from Figs. 5.7 (a), (c), and 5.8 (a). Solid lines show plots of  $g^{(2)}(\tau)$  predicted by the ME model for (a)–(c) a set of rates in Fig. B.3 optimized to reproduce the autocorrelation of X (top row, rate set #1) and (d)–(f) a set of rates in Fig. B.3 optimized to reproduce the autocorrelation of T (bottom row, rate set #2). The corresponding rates have values  $\gamma_{11} = 1.0 \times 10^{11} \text{ s}^{-1}$ ,  $\kappa_X = 2.0 \times 10^7 \text{ s}^{-1}$ ,  $\kappa_T = 2.3 \times 10^{13} \text{ s}^{-1}$ ,  $\gamma_X = 2.0 \times 10^9 \text{ s}^{-1}$ ,  $\gamma_T = 2.0 \times 10^9 \text{ s}^{-1}$ ,  $\kappa_{XT} = 2.3 \times 10^7 \text{ s}^{-1}$ ,  $\kappa_{TX} = 9.1 \times 10^6 \text{ s}^{-1}$ ,  $\zeta_X = 2.2$ , and  $\zeta_T = 1.6$  for rate set #1 as well as  $\gamma_{11} = 1.0 \times 10^{11} \text{ s}^{-1}$ ,  $\kappa_X = 4.5 \times 10^{13} \text{ s}^{-1}$ ,  $\kappa_T = 7.7 \times 10^6 \text{ s}^{-1}$ ,  $\gamma_X = 2.0 \times 10^9 \text{ s}^{-1}$ ,  $\gamma_T = 2.0 \times 10^9 \text{ s}^{-1}$ ,  $\kappa_{XT} = 4.7 \times 10^6 \text{ s}^{-1}$ ,  $\kappa_{TX} = 2.9 \times 10^7 \text{ s}^{-1}$ ,  $\zeta_X = 1.5$ , and  $\zeta_T = 0.8$  for rate set #2. The dependence on  $\gamma_{\text{abs}}$  was weak and  $\gamma_{\text{abs}} = 1.0 \times 10^8 \text{ s}^{-1}$  was chosen for both cases. The graphics (a)–(f) are reproduced from [P3].

ratios of shelving and deshelving rate  $\kappa_s/\kappa_d$  from the perspective of X and T are the inverse of each other. Consequently,  $g_{\text{max}}^{(2)} > 2$  for X implies  $g_{\text{max}}^{(2)} < 2$  for T and vice versa.

For the crosscorrelation of X and T, the ME model fails to explain the occurrence of bunching combined with antibunching on a shorter timescale, but instead shows a too broad antibunching dip and no bunching (Figs. B.4 (c) and (f)). This feature is intuitively understood by the observation that bunching in crosscorrelation is caused by PL intermittency of both X and T, which cannot be accounted for by the assumption of mutually exclusive emission, where a mere switching between X and T instead of a global blinking behavior is to be expected. This finding is in agreement with earlier reports on competing emission from two different emissive states [181, 308–310].

In summary, the ME model is unable to reproduce our measurement results for the crosscorrelation of X and T. In addition, for all emitters with strong bunching in the autocorrelation of X and T, indicated by  $g_{\text{max}}^{(2)} > 2$ , the ME model also fails to capture the autocorrelation data. We conclude that the ME model is conceptually inapt to explain our observations.

### B.3. Emission from a single defect site in the presence of a shelving state

As an alternative to the ME model we introduce the model discussed in Section 5.4, where an additional shelving state  $|S\rangle$  constitutes the origin of PL intermittency. We begin with the scenario illustrated in Fig. B.5 where only a single defect site is present, for brevity termed  $DS_1$  model, to fit the data with pronounced bunching and antibunching in the crosscorrelation of X and T. Formulating the master equation of the level scheme in Fig. B.5 as a system of first-order ODEs as in Eq. (B.3) results in

$$\frac{d}{dt} \begin{pmatrix} p_{|0\rangle}(t) \\ p_{|E_{11}\rangle}(t) \\ p_{|S\rangle}(t) \\ p_{|X\rangle}(t) \\ p_{|T\rangle}(t) \end{pmatrix} = \underbrace{\begin{pmatrix} -\gamma_{\text{abs}} & \gamma_{11} & 0 & \gamma_X & \gamma_T \\ \gamma_{\text{abs}} & -\gamma_{11} - \kappa_S - \kappa_X - \kappa_T & \kappa_d & 0 & 0 \\ 0 & \kappa_S & -\kappa_d & 0 & 0 \\ 0 & \kappa_X & 0 & -\gamma_X & 0 \\ 0 & \kappa_T & 0 & 0 & -\gamma_T \end{pmatrix}}_{\mathbf{A}_{DS_1}} \underbrace{\begin{pmatrix} p_{|0\rangle}(t) \\ p_{|E_{11}\rangle}(t) \\ p_{|S\rangle}(t) \\ p_{|X\rangle}(t) \\ p_{|T\rangle}(t) \end{pmatrix}}_{\mathbf{p}_{DS_1}(t)}. \quad (\text{B.27})$$

As before we used solutions of Eq. (B.27) of the form  $\mathbf{p}_{DS_1}(t) = \exp(t \cdot \mathbf{A}_{DS_1}) \cdot \mathbf{p}_{DS_1}(0)$  to find numerical expressions for the normalized coincidence counts for the autocorrelations of X and T as well as the crosscorrelation of X and T, respectively,

$$g_{XX}^{(2)}(\tau) = \frac{p_{|0\rangle \rightarrow |X\rangle}(\tau)}{p_{|X\rangle}(\infty)}, \quad g_{TT}^{(2)}(\tau) = \frac{p_{|0\rangle \rightarrow |T\rangle}(\tau)}{p_{|T\rangle}(\infty)}, \quad g_{XT}^{(2)}(\tau) = \frac{p_{|0\rangle \rightarrow |T\rangle}(\tau)}{p_{|T\rangle}(\infty)} \quad (\text{B.28})$$

derived by calculations similar to Eqs. (B.19) to (B.21). To account for imperfect antibunching, we followed Eqs. (B.23) to (B.26) to express the  $g^{(2)}$  function as

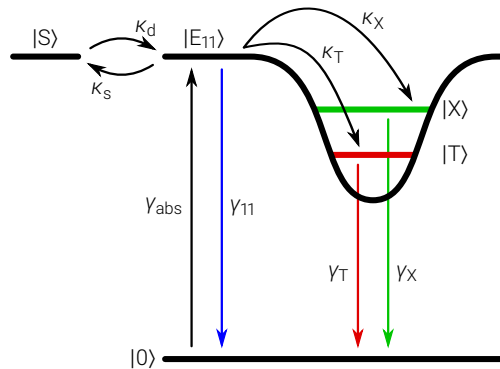


**Figure B.5.:** Level scheme used to model a single defect site in the presence of a shelving state. The exciton continuum  $|E_{11}\rangle$ , the localized states  $|X\rangle$  and  $|T\rangle$ , and the shelving state  $|S\rangle$  are populated from the ground state  $|0\rangle$  with the indicated rates. The graphic is reproduced from [P3].

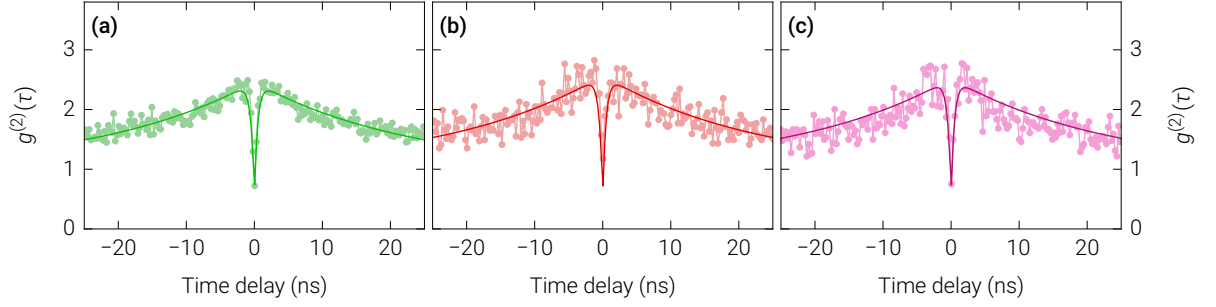


**Figure B.6.:** Normalized coincidence counts  $g^{(2)}(\tau)$  for (a) the autocorrelation of X (light green), (b) the autocorrelation of T (light red), and (c) the crosscorrelation of X and T (orchid) for hCNT A from Section 5.4. Fits to  $g^{(2)}(\tau)$  were obtained with the DS<sub>1</sub> model (solid lines) and resulted in  $\gamma_{11} = 4.2 \times 10^{10} \text{ s}^{-1}$ ,  $\kappa_X = 4.0 \times 10^{10} \text{ s}^{-1}$ ,  $\kappa_T = 1.5 \times 10^{11} \text{ s}^{-1}$ ,  $\gamma_X = 2.0 \times 10^9 \text{ s}^{-1}$ ,  $\gamma_T = 2.0 \times 10^9 \text{ s}^{-1}$ ,  $\kappa_d = 1.0 \times 10^7 \text{ s}^{-1}$ ,  $\zeta_X = 1.9$ , and  $\zeta_T = 2.1$ . The fits were found to depend only on the effective transition rate from  $|0\rangle$  to  $|D\rangle$ , leaving freedom for the individual values of  $\gamma_{\text{abs}}$  and  $\kappa_s$ . Choosing  $\gamma_{\text{abs}} = 1.0 \times 10^8 \text{ s}^{-1}$  resulted in the best-fit value  $\kappa_s = 1.4 \times 10^{11} \text{ s}^{-1}$ . The graphics (a)–(c) are reproduced from [P3].

$$g^{(2)}(\tau) = \frac{1}{(1 + 1/\zeta_1)(1 + 1/\zeta_2)} \cdot g_{\text{pure}}^{(2)}(\tau) + \frac{1 + \zeta_1 + \zeta_2}{(1 + \zeta_1)(1 + \zeta_2)}, \quad (\text{B.29})$$

where  $\zeta_1 = I_{|1\rangle}^0 / I_1^B$  and  $\zeta_2 = I_{|2\rangle}^0 / I_2^B$  are the background intensity ratios in two (possibly identical) spectral bands 1 and 2.

We obtained fits to the data of hCNT A from Section 5.4 by substituting  $g_{XX}^{(2)}(\tau)$ ,  $g_{TT}^{(2)}(\tau)$  and  $g_{XT}^{(2)}(\tau)$  for  $g_{\text{pure}}^{(2)}(\tau)$  in Eq. (B.29) and introducing two background intensity ratios  $\zeta_X$  and  $\zeta_T$  for the spectral bands of X and T. This choice allowed to fix all model rates,  $\zeta_X$ , and  $\zeta_T$  by fitting to the autocorrelation data of X and T and to subsequently test the model by comparing the crosscorrelation data with the resulting functional dependency of  $g_{XT}^{(2)}(\tau)$ . As a representative for hCNTs with pronounced bunching and antibunching in the crosscorrelation of X and T, the autocorrelation of X (light green) and T (light red) as well as the crosscorrelation of X and T (orchid) of hCNT A from Section 5.4 are plotted in Figs. B.6 (a)–(c). The solid lines show the predictions for  $g^{(2)}(\tau)$  according to the DS<sub>1</sub> model using the fitting method described above. We emphasize the good agreement between model fit and data obtained without additional parameters for the crosscorrelation of X and T in Fig. B.6 (c).

## B.4. Emission from a single defect site in the presence of multiple shelving states

Fig. 5.8 (c) in Section 5.4 shows that the DS<sub>1</sub> model is unable to explain the low degree of bunching for hCNTs with weak crosscorrelation, of which hCNT B is a representative. A natural approach to resolve this mismatch between model and data therefore is the consid-

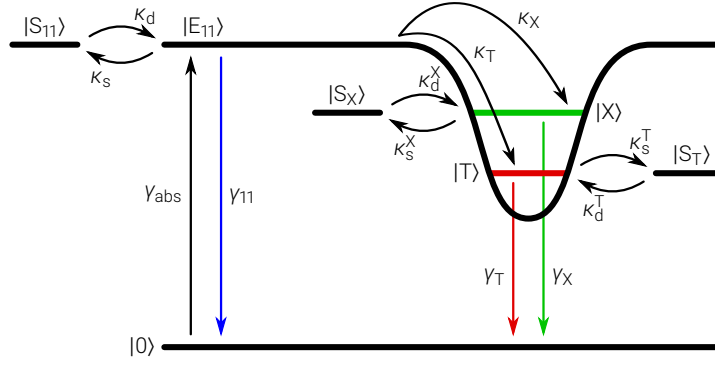


**Figure B.7.:** Level scheme used to model a single defect site in the presence of multiple shelving states. The exciton continuum  $|E_{11}\rangle$  and the localized states  $|X\rangle$  and  $|T\rangle$  exchange population with the shelving states  $|S_{11}\rangle$ ,  $|S_X\rangle$ , and  $|S_T\rangle$  and the ground state  $|0\rangle$  with the indicated rates.

eration of a more complex blinking dynamics. Fig. B.7 shows a level scheme where instead of a single shelving state  $|S\rangle$  three individual shelving states  $|S_{11}\rangle$ ,  $|S_X\rangle$ , and  $|S_T\rangle$  are considered that exchange population with the states  $|E_{11}\rangle$ ,  $|X\rangle$ , and  $|T\rangle$ , respectively. In this section we investigate whether the more complex shelving dynamics arising from this model, termed **MSS** model in the following, is able to explain the blinking characteristics that differ between the autocorrelation and the crosscorrelation measurements for hCNTs of type B.

As in Eq. (B.3), the dynamics in the level scheme of Fig. B.7 were formulated in terms of the system of first-order ODEs

$$\frac{d}{dt} \mathbf{p}_{\text{MSS}}(t) = \mathbf{A}_{\text{MSS}} \cdot \mathbf{p}_{\text{MSS}}(t), \quad (\text{B.30})$$

where the vector of occupation probabilities  $\mathbf{p}_{\text{MSS}}(t)$  is given by

$$\mathbf{p}_{\text{MSS}}(t) = \begin{pmatrix} p_{|0\rangle}(t) \\ p_{|E_{11}\rangle}(t) \\ p_{|S_{11}\rangle}(t) \\ p_{|X\rangle}(t) \\ p_{|T\rangle}(t) \\ p_{|S_X\rangle}(t) \\ p_{|S_T\rangle}(t) \end{pmatrix}, \quad (\text{B.31})$$

$p_{|\psi\rangle}(t)$  is the probability to find the system in state  $|\psi\rangle$  at time  $t$  as in Sections B.2 and B.3 and the square matrix  $\mathbf{A}_{\text{MSS}}$  is given by

## B. PHOTON EMISSION STATISTICS IN THE FRAMEWORK OF RATE MODELS

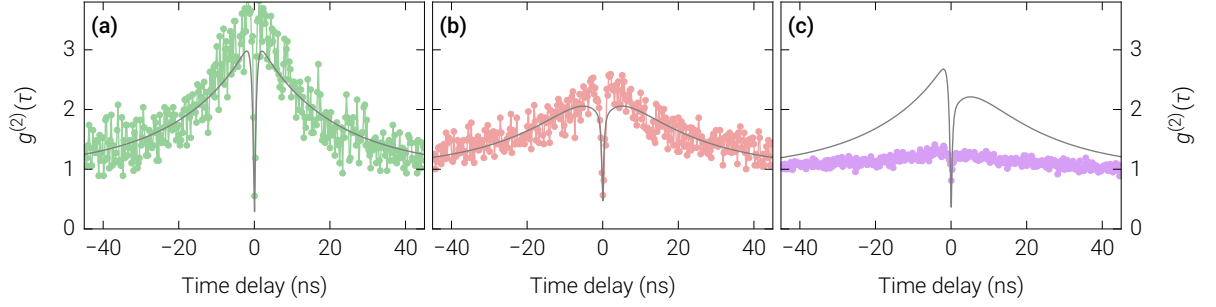


**Figure B.8.:** Normalized coincidence counts  $g^{(2)}(\tau)$  for (a) the autocorrelation of X (light green), (b) the autocorrelation of T (light red), and (c) the crosscorrelation of X and T (lavender) for hCNT B from Section 5.4. Fits to  $g^{(2)}(\tau)$  were obtained with the MSS model (solid lines) and resulted in fit parameters with values  $\gamma_{11} = 1.7 \times 10^{11} \text{ s}^{-1}$ ,  $\kappa_X = 1.3 \times 10^{11} \text{ s}^{-1}$ ,  $\kappa_T = 1.4 \times 10^{11} \text{ s}^{-1}$ ,  $\gamma_X = 2.0 \times 10^9 \text{ s}^{-1}$ ,  $\gamma_T = 2.0 \times 10^9 \text{ s}^{-1}$ ,  $\kappa_s = 3.0 \times 10^{11} \text{ s}^{-1}$ ,  $\kappa_d = 1.6 \times 10^7 \text{ s}^{-1}$ ,  $\kappa_s^X = 3.2 \times 10^6 \text{ s}^{-1}$ ,  $\kappa_d^X = 1.0 \times 10^{15} \text{ s}^{-1}$ ,  $\kappa_s^T = 9.0 \times 10^8 \text{ s}^{-1}$ ,  $\kappa_d^T = 3.4 \times 10^8 \text{ s}^{-1}$ ,  $\zeta_X = 2.2 \times 10^3$ , and  $\zeta_T = 6.0$ . The fits were found to depend only weakly on  $\gamma_{\text{abs}}$  and a value of  $\gamma_{\text{abs}} = 1.0 \times 10^8 \text{ s}^{-1}$  was chosen.

$$\mathbf{A}_{\text{MSS}} = \begin{pmatrix} -\gamma_{\text{abs}} & \gamma_{11} & 0 & \gamma_X & \gamma_T & 0 & 0 \\ \gamma_{\text{abs}} & -\gamma_{11} - \kappa_s - \kappa_X - \kappa_T & \kappa_d & 0 & 0 & 0 & 0 \\ 0 & \kappa_s & -\kappa_d & 0 & 0 & 0 & 0 \\ 0 & \kappa_X & 0 & -\gamma_X - \kappa_s^X & 0 & \kappa_d^X & 0 \\ 0 & \kappa_T & 0 & 0 & -\gamma_T - \kappa_s^T & 0 & \kappa_d^T \\ 0 & 0 & 0 & \kappa_s^X & 0 & -\kappa_d^X & 0 \\ 0 & 0 & 0 & 0 & \kappa_s^T & 0 & -\kappa_d^T \end{pmatrix}. \quad (\text{B.32})$$

Analogous to Section B.3, solutions of Eq. (B.30) of the form  $\mathbf{p}_{\text{MSS}}(t) = \exp(t \cdot \mathbf{A}_{\text{MSS}}) \cdot \mathbf{p}_{\text{MSS}}(0)$  were used to express the normalized coincidence counts for the autocorrelations of X and T as well as the crosscorrelation of X and T, respectively, as

$$g_{\text{XX}}^{(2)}(\tau) = \frac{p_{|0\rangle \rightarrow |X\rangle}(\tau)}{p_{|X\rangle}(\infty)}, \quad g_{\text{TT}}^{(2)}(\tau) = \frac{p_{|0\rangle \rightarrow |T\rangle}(\tau)}{p_{|T\rangle}(\infty)}, \quad g_{\text{XT}}^{(2)}(\tau) = \frac{p_{|0\rangle \rightarrow |T\rangle}(\tau)}{p_{|T\rangle}(\infty)}. \quad (\text{B.33})$$

To account for imperfect antibunching, following Eqs. (B.23) to (B.26) the results for  $g_{\text{XX}}^{(2)}(\tau)$ ,  $g_{\text{TT}}^{(2)}(\tau)$  and  $g_{\text{XT}}^{(2)}(\tau)$  were substituted for  $g_{\text{pure}}^{(2)}(\tau)$  in

$$g^{(2)}(\tau) = \frac{1}{(1 + 1/\zeta_1)(1 + 1/\zeta_2)} \cdot g_{\text{pure}}^{(2)}(\tau) + \frac{1 + \zeta_1 + \zeta_2}{(1 + \zeta_1)(1 + \zeta_2)}, \quad (\text{B.34})$$

and for  $\zeta_1 = I_{|1\rangle}^0 / I_1^B$  and  $\zeta_2 = I_{|2\rangle}^0 / I_2^B$  the respective background intensity ratios  $\zeta_X$  and  $\zeta_T$  for the spectral bands of X and T were inserted.

Figs. B.8 (a)–(c) show fits of Eq. (B.34) (solid grey lines) to the normalized coincidence counts of hCNT B from Section 5.4 for the autocorrelation of X (light green), the autocorrelation of T (light red), and the crosscorrelation of X and T (lavender). As in Section B.3, all

rates in the model as well as  $\zeta_X$  and  $\zeta_T$  were fixed by fitting to the autocorrelation data of X and T and the MSS model was then tested by comparing the crosscorrelation data of X and T with the resulting functional dependency of  $g_{XT}^{(2)}(\tau)$ .

While the quality of the fits to the autocorrelation data in Figs. B.8 (a) and (b) is comparable to that obtained with the DS<sub>2</sub> model in Figs. 5.7 (b) and (d), the prediction for  $g_{XT}^{(2)}(\tau)$  in the framework of the MSS model is unable to reproduce the crosscorrelation data for hCNT B in Fig. B.8 (c). Not only is the degree of bunching overestimated as is the case for the DS<sub>1</sub> model in Fig. 5.8 (c), but also the symmetry for reversal of the time delay axis is broken. While the measured photon coincidence counts were symmetric in Fig. B.8 (c), the bunching characteristics of the model prediction resembles that of the unequal X and T autocorrelation for negative and positive time delays, respectively.

This result is understood by observing that for the crosscorrelation measurements a positive time delay corresponds to the emission of a photon first in the X and then in the T spectral band, while for negative time delay the order of the emission events is reversed. In the first case, the system is projected into the ground state after the emission of a photon from  $|X\rangle$  and the exciton population must transfer from the ground state to  $|T\rangle$  for a second photon to be emitted in the T spectral band. Population trapping into one of the shelving states is therefore particularly relevant for the  $|S_T\rangle$  state that is directly accessible from  $|T\rangle$  and the blinking dynamics is governed by the corresponding rates  $\kappa_s^T$  and  $\kappa_d^T$ .

Similarly, for negative time delays the exciton population must transfer from the ground state to  $|X\rangle$  and the shelving state  $|S_X\rangle$  with the corresponding rates  $\kappa_s^X$  and  $\kappa_d^X$  determines the blinking dynamics. The introduction of independent rates  $\kappa_s^X$ ,  $\kappa_s^T$ ,  $\kappa_d^X$ , and  $\kappa_d^T$  therefore unsurprisingly produces asymmetric bunching with respect to the reversal of delay time. Conversely, the strictly symmetric crosscorrelation data for all investigated hCNTs of both type A and B provide a strong indication for the absence of multiple shelving states in the exciton dynamics of hCNTs. Apart from the bunching in crosscorrelation being too pronounced also in the framework of the MSS model, this finding strongly disfavors any models that implement additional shelving mechanisms and in particular invalidates the MSS model.

## B.5. Emission from two correlated defect sites in the presence of a shelving state

To explain the data with weak bunching and antibunching in the crosscorrelation of X and T, we extended the DS<sub>1</sub> model by the introduction of a second defect site. In order to preserve pronounced antibunching in the autocorrelation of X and T, we further assumed that the two defect sites are favored to be in opposite charge states. For brevity, this model is termed the DS<sub>2</sub> model in the following.

## B. PHOTON EMISSION STATISTICS IN THE FRAMEWORK OF RATE MODELS

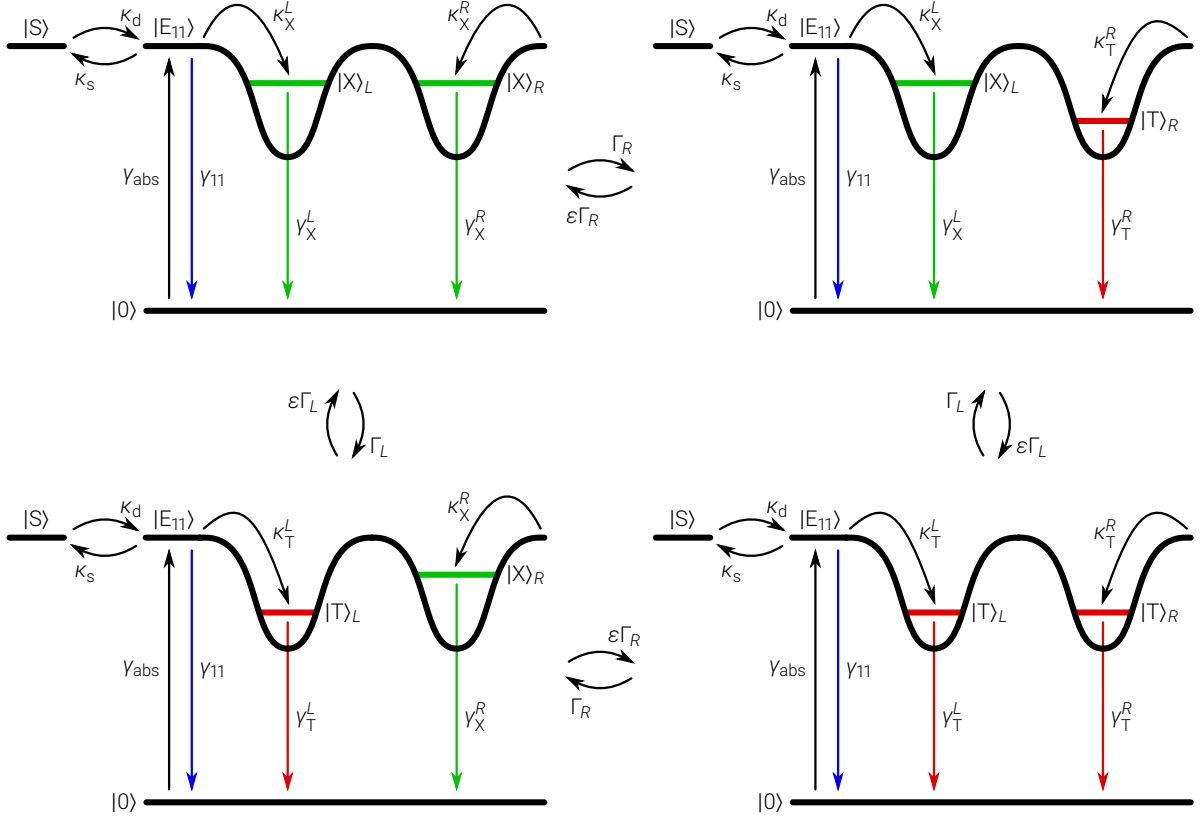


**Figure B.9.:** Simplified sketch of the level scheme used to model a double defect site in the presence of a shelving state. The charge states of the left and the right defect site change with rates  $\Gamma_L$  and  $\Gamma_R$ , respectively, and transitions into equal charge states of both traps are suppressed by a factor  $\epsilon < 1$ . For each charge configuration we consider the ground state  $|0\rangle$ , the exciton continuum  $|E_{11}\rangle$ , the localized states of the left ( $|X\rangle_L$  or  $|T\rangle_L$ ) and the right ( $|X\rangle_R$  or  $|T\rangle_R$ ) defect site and the shelving state  $|S\rangle$  with their corresponding transition rates. The graphic is reproduced from [P3].

While the level scheme in Fig. 5.8 (e) in Section 5.4 illustrates this behavior schematically, a theoretical description of the  $DS_2$  model requires a “memory” of the charge state of both defect sites, even if they are not occupied. A suitable level scheme including this feature is sketched in Fig. B.9, where a left and a right defect site,  $L$  and  $R$ , are considered. The two traps change their charge state with rates  $\Gamma_L$  and  $\Gamma_R$ , respectively, while a transition resulting in two equal charge states is suppressed by a factor  $\epsilon < 1$ . For fixed charges, the dynamics of the two defect sites are equivalent to the dynamics in Fig. B.5. Excitation and decay of  $E_{11}$  occur with rates  $\gamma_{\text{abs}}^i$  and  $\gamma_{11}^i$ , where  $i$  is either  $L$  (left trap) or  $R$  (right trap). The trap states are populated with rates  $\kappa_X^i$  or  $\kappa_T^i$  and decay with rates  $\gamma_X^i$  or  $\gamma_T^i$  depending on their current charge state. The shelving state  $|S\rangle$  is populated with rate  $\kappa_s^i$  and depopulated with rate  $\kappa_d^i$ .

Note that although there are different rates  $\kappa_s^L$  and  $\kappa_d^L$  for the left and  $\kappa_s^R$  and  $\kappa_d^R$  for the right defect site in the  $DS_2$  model, this choice does not conflict with the observed asymmetry

in the crosscorrelation fit of the MSS model in Fig. B.8 (c). The crucial difference between both scenarios is that in the MSS model there are different shelving states for X and T, while for the DS<sub>2</sub> model the two defect sites interact with the shelving state with different rates, but for both defect sites the rates for X and T are identical. By consequence, no strong asymmetry for  $g^{(2)}$  in crosscorrelation is expected for the DS<sub>2</sub> model.

The numerical solution of the rate model corresponding to the level scheme in Fig. B.9 can be obtained by solving the system of first-order ODEs from Eq. (B.3), conceptually identical to the solutions found for the ME, the DS<sub>1</sub>, and the MSS model. However, there are 64 possible states to be considered making a more structured approach necessary. First, a master equation for the left defect site as a function of its charge state, succinctly denoted as  $\chi_L = 0$  or  $\chi_L = -$ , is formulated as

$$\frac{d}{dt} \begin{pmatrix} p_{|0\rangle_L}(t) \\ p_{|E_{11}\rangle_L}(t) \\ p_{|S\rangle_L}(t) \\ p_{|\Lambda(\chi_L)\rangle_L}(t) \end{pmatrix} = \underbrace{\begin{pmatrix} -\gamma_{\text{abs}}^L & \gamma_{11}^L & 0 & \gamma_{\Lambda(\chi_L)}^L \\ \gamma_{\text{abs}}^L & -\gamma_{11}^L - \kappa_s^L - \kappa_{\Lambda(\chi_L)}^L & \kappa_d^L & 0 \\ 0 & \kappa_s^L & -\kappa_d^L & 0 \\ 0 & \kappa_{\Lambda(\chi_L)}^L & 0 & -\gamma_{\Lambda(\chi_L)}^L \end{pmatrix}}_{\mathbf{L}(\chi_L)} \underbrace{\begin{pmatrix} p_{|0\rangle_L}(t) \\ p_{|E_{11}\rangle_L}(t) \\ p_{|S\rangle_L}(t) \\ p_{|\Lambda(\chi_L)\rangle_L}(t) \end{pmatrix}}_{\boldsymbol{\ell}(\chi_L, t)}, \quad (\text{B.35})$$

where  $|\Lambda(\chi_L)\rangle_L$  is the current configuration of the left localized state depending its charge state  $\chi_L$ , i. e.  $|\Lambda(0)\rangle_L = |X\rangle_L$  and  $|\Lambda(-)\rangle_L = |T\rangle_L$ . Next, a master equation for both defect sites as a function of the charge states  $\chi_R$  and  $\chi_L$  of the right and the left defect site, respectively, is written as

$$\frac{d}{dt} \mathbf{r}(\chi_R, \chi_L, t) = \mathbf{R}(\chi_R, \chi_L) \cdot \mathbf{r}(\chi_R, \chi_L, t). \quad (\text{B.36})$$

Here, the  $16 \times 1$  vector  $\mathbf{r}(\chi_R, \chi_L, t)$  of occupation probabilities reads

$$\mathbf{r}(\chi_R, \chi_L, t) = \begin{pmatrix} p_{|0\rangle_R}(t) \cdot \boldsymbol{\ell}(\chi_L, t) \\ p_{|E_{11}\rangle_R}(t) \cdot \boldsymbol{\ell}(\chi_L, t) \\ p_{|S\rangle_R}(t) \cdot \boldsymbol{\ell}(\chi_L, t) \\ p_{|\Lambda(\chi_R)\rangle_R}(t) \cdot \boldsymbol{\ell}(\chi_L, t) \end{pmatrix} \quad (\text{B.37})$$

and the  $16 \times 16$  square matrix  $\mathbf{R}(\chi_R, \chi_L)$  has the form

$$\mathbf{R}(\chi_R, \chi_L) = \begin{pmatrix} \mathbf{L}(\chi_L) - \gamma_{\text{abs}}^R \mathbf{I}_4 & \gamma_{11}^R \mathbf{I}_4 & \mathbf{0}_4 & \gamma_{\Lambda(\chi_R)}^R \mathbf{I}_4 \\ \gamma_{\text{abs}}^R \mathbf{I}_4 & \mathbf{L}(\chi_L) - (\gamma_{11}^R + \kappa_s^R + \kappa_{\Lambda(\chi_R)}^R) \mathbf{I}_4 & \kappa_d^R \mathbf{I}_4 & \mathbf{0}_4 \\ \mathbf{0}_4 & \kappa_s^R \mathbf{I}_4 & \mathbf{L}(\chi_L) - \kappa_d^R \mathbf{I}_4 & \mathbf{0}_4 \\ \mathbf{0}_4 & \kappa_{\Lambda(\chi_R)}^R \mathbf{I}_4 & \mathbf{0}_4 & \mathbf{L}(\chi_L) - \gamma_{\Lambda(\chi_R)}^R \mathbf{I}_4 \end{pmatrix}, \quad (\text{B.38})$$

where  $\mathbf{I}_4$  is a  $4 \times 4$  identity matrix,  $\mathbf{0}_4$  is a  $4 \times 4$  zero matrix and  $|\Lambda(\chi_R)\rangle_R$  is the current configuration of the right localized state depending on its charge state  $\chi_R$ , i. e.  $|\Lambda(0)\rangle_R = |X\rangle_R$  and  $|\Lambda(-)\rangle_R = |T\rangle_R$ .

Finally, the system of first-order ODEs for  $\mathbf{r}(\chi_R, \chi_L, t)$  is combined with the charging and discharging dynamics of the two defect sites. As discussed in Section B.2, there is only a weak dependence of  $g^{(2)}(\tau)$  on the choice of rates modeling the charging and discharging dynamics for the case of an occupied trap state. In order not to further increase complexity, the simplest approach is chosen here, where the corresponding rates are independent of the occupation of the defect site. This yields the master equation

$$\frac{d}{dt} \mathbf{p}_{\text{DS}_2}(t) = \mathbf{A}_{\text{DS}_2} \cdot \mathbf{p}_{\text{DS}_2}(t), \quad (\text{B.39})$$

where the  $64 \times 1$  vector  $\mathbf{p}_{\text{DS}_2}(t)$  of occupation probabilities is given by

$$\mathbf{p}_{\text{DS}_2}(t) = \begin{pmatrix} \mathbf{r}(0, 0, t) \\ \mathbf{r}(-, 0, t) \\ \mathbf{r}(0, -, t) \\ \mathbf{r}(-, -, t) \end{pmatrix}, \quad (\text{B.40})$$

and the  $64 \times 64$  square matrix  $\mathbf{A}_{\text{DS}_2}$  has the form

$$\mathbf{A}_{\text{DS}_2} = \begin{pmatrix} \mathbf{R}(0, 0) - (\Gamma_R + \Gamma_L)\mathbf{I}_{16} & \varepsilon\Gamma_R\mathbf{I}_{16} & \varepsilon\Gamma_L\mathbf{I}_{16} & \mathbf{0}_{16} \\ \Gamma_R\mathbf{I}_{16} & \mathbf{R}(-, 0) - \varepsilon(\Gamma_R + \Gamma_L)\mathbf{I}_{16} & \mathbf{0}_{16} & \Gamma_L\mathbf{I}_{16} \\ \Gamma_L\mathbf{I}_{16} & \mathbf{0}_{16} & \mathbf{R}(0, -) - \varepsilon(\Gamma_R + \Gamma_L)\mathbf{I}_{16} & \Gamma_R\mathbf{I}_{16} \\ \mathbf{0}_{16} & \varepsilon\Gamma_L\mathbf{I}_{16} & \varepsilon\Gamma_R\mathbf{I}_{16} & \mathbf{R}(-, -) - (\Gamma_R + \Gamma_L)\mathbf{I}_{16} \end{pmatrix}. \quad (\text{B.41})$$

Analogous to  $\mathbf{I}_4$  and  $\mathbf{0}_4$  from above,  $\mathbf{I}_{16}$  is a  $16 \times 16$  identity matrix and  $\mathbf{0}_{16}$  is a  $16 \times 16$  zero matrix.

In order to calculate the  $g^{(2)}$  function from the vector  $\mathbf{p}_{\text{DS}_2}(t)$  of occupation probabilities using the expression derived in Eq. (B.6),

$$g^{(2)}(\tau) = \frac{\langle I(t)I(t+\tau) \rangle}{\langle I(t) \rangle \langle I(t+\tau) \rangle} = \frac{\langle p(t)p(t+\tau) \rangle}{\langle p(t) \rangle \langle p(t+\tau) \rangle}, \quad (\text{B.42})$$

it is now important to observe that there are different states in the system that contribute to the emission in the X and T spectral bands. In a measurement of the normalized coincidence counts  $g^{(2)}(\tau)$ , time correlations between start and stop events of *all* photons detected in the corresponding spectral bands are performed as discussed in Section 2.5 and therefore the respective signals are added up. The probabilities in Eq. (B.42) may thus be found by summing the occupation probabilities of all relevant states to obtain

$$\langle p(t) \rangle = \sum_{|i\rangle} p_{|i\rangle}(\infty) \quad \text{and} \quad \langle p(t+\tau) \rangle = \sum_{|f\rangle} p_{|f\rangle}(\infty), \quad (\text{B.43})$$

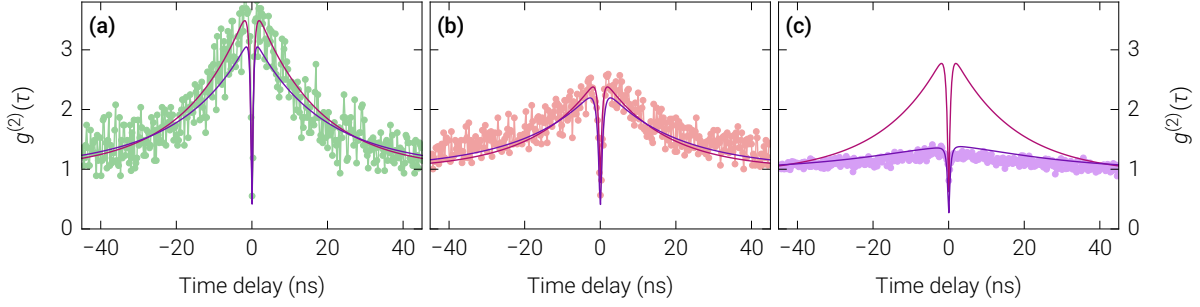


**Figure B.10.:** Normalized coincidence counts  $g^{(2)}(\tau)$  for (a) autocorrelation of X (light green), (b) autocorrelation of T (light red), and (c) crosscorrelation of X and T (lavender) for hCNT B from Section 5.4. Fits to  $g^{(2)}(\tau)$  were obtained with the  $DS_1$  model (solid pink lines) and the  $DS_2$  model (solid violet lines). The fit parameters for the  $DS_1$  model are  $\gamma_{\text{abs}} = 1.0 \times 10^8 \text{ s}^{-1}$ ,  $\gamma_{11} = 4.9 \times 10^{10} \text{ s}^{-1}$ ,  $\kappa_X = 5.4 \times 10^{11} \text{ s}^{-1}$ ,  $\kappa_T = 2.9 \times 10^9 \text{ s}^{-1}$ ,  $\gamma_X = 2.0 \times 10^9 \text{ s}^{-1}$ ,  $\gamma_T = 2.0 \times 10^9 \text{ s}^{-1}$ ,  $\kappa_s = 7.8 \times 10^{11} \text{ s}^{-1}$ ,  $\kappa_d = 2.9 \times 10^9 \text{ s}^{-1}$ ,  $\zeta_X = 5.8$ , and  $\zeta_T = 1.7$ . The fit parameters for the  $DS_2$  model are  $\gamma_{\text{abs}}^L = 3.6 \times 10^9 \text{ s}^{-1}$ ,  $\gamma_{\text{abs}}^R = 3.7 \times 10^9 \text{ s}^{-1}$ ,  $\gamma_{11}^L = 1.3 \times 10^{10} \text{ s}^{-1}$ ,  $\gamma_{11}^R = 1.0 \times 10^{10} \text{ s}^{-1}$ ,  $\kappa_X^L = 3.6 \times 10^7 \text{ s}^{-1}$ ,  $\kappa_X^R = 1.0 \times 10^8 \text{ s}^{-1}$ ,  $\kappa_T^L = 6.1 \times 10^6 \text{ s}^{-1}$ ,  $\kappa_T^R = 8.4 \times 10^6 \text{ s}^{-1}$ ,  $\gamma_X^L = 9.9 \times 10^9 \text{ s}^{-1}$ ,  $\gamma_X^R = 3.8 \times 10^9 \text{ s}^{-1}$ ,  $\gamma_T^L = 1.2 \times 10^9 \text{ s}^{-1}$ ,  $\gamma_T^R = 1.0 \times 10^9 \text{ s}^{-1}$ ,  $\kappa_s^L = 3.3 \times 10^8 \text{ s}^{-1}$ ,  $\kappa_s^R = 1.0 \times 10^8 \text{ s}^{-1}$ ,  $\kappa_d^L = 5.4 \times 10^6 \text{ s}^{-1}$ ,  $\kappa_d^R = 1.8 \times 10^7 \text{ s}^{-1}$ ,  $\Gamma_L = 1.3 \times 10^7 \text{ s}^{-1}$ ,  $\Gamma_R = 2.9 \times 10^9 \text{ s}^{-1}$ ,  $\varepsilon = 0.22$ ,  $\zeta_X = 8.9$ , and  $\zeta_T = 4.9$ . As in Figs. B.6 (a)–(c), the values of  $\gamma_{\text{abs}}$  and  $\kappa_s$ ,  $\gamma_{\text{abs}}^L$  and  $\kappa_s^L$  as well as  $\gamma_{\text{abs}}^R$  and  $\kappa_s^R$  are interdependent and the same fit quality can be achieved with different values for these rates. The graphics (a)–(c) are reproduced from [P3].

where the sums run over all initial states  $|i\rangle$  and final states  $|f\rangle$  that contribute to the emission in the respective spectral bands. In a similar way, the numerator in Eq. (B.42) can be written as

$$\langle p(t)p(t+\tau) \rangle = \sum_{|i\rangle} \sum_{|f\rangle} \sum_{|0(i)\rangle} p_{|i\rangle}(\infty) \cdot p_{|0(i)\rangle \rightarrow |f\rangle}(\tau), \quad (\text{B.44})$$

where the third sum runs over all possible ground states  $|0(i)\rangle$  that the system is projected into after emission from the state  $|i\rangle$ . This summation is necessary, since  $|0(i)\rangle$  is not necessarily unique. For example, if both traps are in state  $|X\rangle$ , then after emission of a photon in the spectral band of X it is undetermined whether the left or the right defect site has been projected into the corresponding ground state.

We used solutions of Eq. (B.39) of the form  $\mathbf{p}_{DS_2}(t) = \exp(t \cdot \mathbf{A}_{DS_2}) \cdot \mathbf{p}_{DS_2}(0)$  to compute Eqs. (B.43) and (B.44) and inserted the results into Eq. (B.42) to obtain the respective  $g^{(2)}$  functions  $g_{XX}^{(2)}(\tau)$ ,  $g_{TT}^{(2)}(\tau)$ , and  $g_{XT}^{(2)}(\tau)$  for the autocorrelations of X and T as well as the crosscorrelation of X and T. To account for imperfect antibunching, we followed the calculations in Eqs. (B.23) to (B.26) in order to substitute the simulated  $g^{(2)}$  functions  $g_{XX}^{(2)}(\tau)$ ,  $g_{TT}^{(2)}(\tau)$  and  $g_{XT}^{(2)}(\tau)$  for  $g_{\text{pure}}^{(2)}(\tau)$  in

$$g^{(2)}(\tau) = \frac{1}{(1 + 1/\zeta_1)(1 + 1/\zeta_2)} \cdot g_{\text{pure}}^{(2)}(\tau) + \frac{1 + \zeta_1 + \zeta_2}{(1 + \zeta_1)(1 + \zeta_2)}, \quad (\text{B.45})$$

and introduced two background intensity ratios  $\zeta_X$  and  $\zeta_T$  for the spectral bands of X and T for  $\zeta_1 = I_{|1\rangle}^0 / I_1^B$  and  $\zeta_2 = I_{|2\rangle}^0 / I_2^B$ .

In Figs. B.10 (a)–(c) we compare the fits obtained with the  $DS_1$  and the  $DS_2$  model for the correlation data of hCNT B discussed in Section 5.4 as a representative for the class of hCNTs with weak bunching and antibunching in the crosscorrelation of X and T. For the autocorrelation measurements of X and T we found a comparable fit quality for the  $DS_1$  model (solid pink lines) and the  $DS_2$  model (solid violet lines) in Figs. B.10 (a) and (b). For the crosscorrelation of X and T (Fig. B.10 (c)), however, the  $DS_1$  model overestimates both bunching and antibunching (solid pink line), whereas the  $DS_2$  model reproduces the data reasonably well (solid violet line).

## List of Abbreviations

Term	Description	Page List
ATPE	Aqueous two-polymer phase extraction	32
B3LYP	A hybrid DFT functional [261] combining the B3 [260] with the LYP [336] functional	52, 54–56, 101–103
BP86	A generalized gradient approximation DFT functional based on [257–259]	52, 54–56, 60–63, 100, 102, 103
BZ	Brillouin zone	7–9, 13–16
CCD	Charge-coupled device	29–31
CNT	Carbon nanotube	1–3, 6, 7, 10–21, 28, 29, 31–35, 38–43, 47, 49–56, 59–65, 68–71, 74–77, 82, 84, 86, 90, 91, 93–95, 102, 103, 113, 115, 116, 134
COSX	Chain of spheres exchange	103, 135
CVD	Chemical vapour deposition	31, 32
CW	Continuous wave	28, 29, 78
D3BJ	Becke-Johnson damping scheme for dispersion correction [358, 359]	103
DFT	Density functional theory	3, 51–56, 64, 94, 97–104, 133
DNA	Deoxyribonucleic acid	42
DOC	Sodium deoxycholate	32–34, 42, 49–51
DOS	Density of states	9, 16
DS <sub>1</sub>	Model of emission from a single defect in the presence of a shelving state as discussed in Section B.3	80–84, 86–89, 112, 123, 124, 127, 129, 131, 132, 134
DS <sub>2</sub>	Model of emission from two proximal defects in the presence of a shelving state as discussed in Section B.5	80, 82, 84, 86–89, 112, 127–129, 131, 132

LIST OF ABBREVIATIONS

---

Term	Description	Page List
FWHM	Full width at half maximum	39–43, 49, 50, 54, 63, 72
GGA	Generalized gradient approximation	100–102, 133
HBT	Hanbury Brown and Twiss experiment [167–169]	22, 24, 31, 78
hCNT	Hexyl-functionalized carbon nanotube	33, 68–86, 90, 91, 111–113, 116, 117, 121, 122, 124–127, 131, 132
HWP	Half-wave plate	28–30
InGaAs	Indium gallium arsenide detector	29, 31, 85
IRF	Instrument response function	73, 74
LHe	Liquid helium	29, 30
LN	Liquid nitrogen	29, 31
LCAO	Linear combination of atomic orbitals	98
LDA	Local density approximation	100
LGC	Lowest-order gradient correction	100
ME	Model of mutually exclusive emission from a single defect as discussed in Section B.2	81–83, 118, 121–123, 129
MPL	Magneto-photoluminescence	75, 76, 78, 91, 94
MSS	Extension of the $DS_1$ model including multiple shelving states as discussed in Section B.4	84, 125–127, 129
NA	Numerical aperture	28, 30, 33–35
NAIL	Numerical-aperture-increasing lens	28, 34
ODE	Ordinary differential equation	112, 113, 115, 118, 123, 125, 129, 130
PFO	Poly[9,9-dioctylfluorenyl-2,7-diyl]	32, 33, 42, 49–56, 60, 62–64, 93, 94, 102–104
PL	Photoluminescence	1–3, 18–21, 28, 30, 31, 34, 35, 38–42, 47–52, 54, 56, 60, 62–65, 68–86, 90, 91, 93–95, 112–114, 116, 117, 134
PLE	Photoluminescence excitation	69, 72, 73
QWP	Quarter-wave plate	28–30
QY	Quantum yield	20, 21, 68, 75, 77, 78, 90, 113
RBM	Radial breathing mode	59

---

---

<b>Term</b>	<b>Description</b>	<b>Page List</b>
RI	Resolution of the identity	102, 103, 135
RIJCOSX	Combination of the split-RI-J [367] and the COSX [354] approximation	103
SCF	Self-consistent field	99, 103
SDS	Sodium dodecyl sulfate	32, 49, 69
SEM	Scanning electron microscope	33, 34
SIL	Solid immersion lens	28, 29, 33–35, 72, 93
SSPD	Superconducting single-photon detector	22, 29, 31, 72, 78
Ti:sapphire	Titanium-sapphire laser	28–31, 72, 78
TMD	Transition metal dichalcogenide	10, 77
VHS	Van Hove singularity	16, 17, 19, 44
XPS	X-ray photoelectron spectroscopy	70, 71
ZPL	Zero phonon line	47, 48, 54, 55, 59–64

---



## References

- [1] ROSS, I. M.: *The foundation of the silicon age*. Bell Labs Tech. J. **2**, 4 (1997). DOI: [10.1002/bltj.2080](https://doi.org/10.1002/bltj.2080).
- [2] MOORE, G. E.: *Cramming more components onto integrated circuits*. Electronics **38**, 8 (1965).
- [3] SIFFERT, P. and KRIMMEL, E. (eds.): *Silicon: Evolution and Future of a Technology*. Springer-Verlag, Berlin, Heidelberg 2004. DOI: [10.1007/978-3-662-09897-4](https://doi.org/10.1007/978-3-662-09897-4).
- [4] BETTELHEIM, F. A., BROWN, W. H., CAMPBELL, M. K., and FARRELL, S. O.: *Introduction to General, Organic and Biochemistry*. 9<sup>th</sup> ed. Brooks/Cole, Cengage Learning, Belmont 2009.
- [5] FORREST, S. R. and THOMPSON, M. E.: *Introduction: Organic Electronics and Optoelectronics*. Chem. Rev. **107**, 4 (2007). DOI: [10.1021/cr0501590](https://doi.org/10.1021/cr0501590).
- [6] TANG, C. W.: *Two-layer organic photovoltaic cell*. Appl. Phys. Lett. **48**, 2 (1986). DOI: [10.1063/1.96937](https://doi.org/10.1063/1.96937).
- [7] SHAW, J. M. and SEIDLER, P. F.: *Organic electronics: Introduction*. IBM J. Res. Dev. **45**, 1 (2001). DOI: [10.1147/rd.451.0003](https://doi.org/10.1147/rd.451.0003).
- [8] FLANDROIS, S. and SIMON, B.: *Carbon materials for lithium-ion rechargeable batteries*. Carbon **37**, 2 (1999). DOI: [10.1016/S0008-6223\(98\)00290-5](https://doi.org/10.1016/S0008-6223(98)00290-5).
- [9] LANDI, B. J., GANTER, M. J., CRESS, C. D., DILEO, R. A., and RAFFAELLE, R. P.: *Carbon nanotubes for lithium ion batteries*. Energy Environ. Sci. **2**, 6 (2009). DOI: [10.1039/B904116H](https://doi.org/10.1039/B904116H).
- [10] ZHANG, L. L. and ZHAO, X. S.: *Carbon-based materials as supercapacitor electrodes*. Chem. Soc. Rev. **38**, 9 (2009). DOI: [10.1039/B813846J](https://doi.org/10.1039/B813846J).
- [11] GRUNER, G.: *Carbon nanotube transistors for biosensing applications*. Anal. Bioanal. Chem. **384**, 2 (2006). DOI: [10.1007/s00216-005-3400-4](https://doi.org/10.1007/s00216-005-3400-4).
- [12] YAMADA, T., HAYAMIZU, Y., YAMAMOTO, Y., YOMOGIDA, Y., IZADI-NAJAFABADI, A., FUTABA, D. N., and HATA, K.: *A stretchable carbon nanotube strain sensor for human-motion detection*. Nat. Nanotechnol. **6**, 5 (2011). DOI: [10.1038/nnano.2011.36](https://doi.org/10.1038/nnano.2011.36).

- [13] GHOSH, S., SOOD, A. K., and KUMAR, N.: *Carbon Nanotube Flow Sensors*. Science **299**, 5609 (2003). DOI: 10.1126/science.1079080.
- [14] DI, J., ZHANG, X., YONG, Z., ZHANG, Y., LI, D., LI, R., and LI, Q.: *Carbon-Nanotube Fibers for Wearable Devices and Smart Textiles*. Adv. Mater. **28**, 47 (2016). DOI: 10.1002/adma.201601186.
- [15] ZHANG, X. A., YU, S., XU, B., LI, M., PENG, Z., WANG, Y., DENG, S., WU, X., WU, Z., OUYANG, M., and WANG, Y.: *Dynamic gating of infrared radiation in a textile*. Science **363**, 6427 (2019). DOI: 10.1126/science.aau1217.
- [16] CHEN, X., YIN, L., LV, J., GROSS, A. J., LE, M., GUTIERREZ, N. G., LI, Y., JEERAPAN, I., GIROUD, F., BEREZOVSKA, A., O'REILLY, R. K., XU, S., COSNIER, S., and WANG, J.: *Stretchable and Flexible Buckypaper-Based Lactate Biofuel Cell for Wearable Electronics*. Adv. Funct. Mater. **29**, 46 (2019). DOI: 10.1002/adfm.201905785.
- [17] HU, L., CHEN, W., XIE, X., LIU, N., YANG, Y., WU, H., YAO, Y., PASTA, M., ALSHAREEF, H. N., and CUI, Y.: *Symmetrical MnO<sub>2</sub>-Carbon Nanotube-Textile Nanostructures for Wearable Pseudocapacitors with High Mass Loading*. ACS Nano **5**, 11 (2011). DOI: 10.1021/nn203085j.
- [18] CHAND, S.: *Review Carbon fibers for composites*. J. Mater. Sci. **35**, 6 (2000). DOI: 10.1023/A:1004780301489.
- [19] LU, W., ZU, M., BYUN, J.-H., KIM, B.-S., and CHOU, T.-W.: *State of the Art of Carbon Nanotube Fibers: Opportunities and Challenges*. Adv. Mater. **24**, 14 (2012). DOI: 10.1002/adma.201104672.
- [20] MANGALGIRI, P. D.: *Composite materials for aerospace applications*. Bull. Mater. Sci. **22**, 3 (1999). DOI: 10.1007/BF02749982.
- [21] PASQUALI, M.: *A better future for fossil hydrocarbons and carbon nanomaterials*. Presentation at APS March Meeting, Boston 2019.
- [22] IIJIMA, S.: *Helical microtubules of graphitic carbon*. Nature **354**, 6348 (1991). DOI: 10.1038/354056a0.
- [23] SAITO, R., DRESSSELHAUS, G., and DRESSSELHAUS, M. S.: *Physical Properties of Carbon Nanotubes*. 1<sup>st</sup> ed. World Scientific Publishing Company, London 1998.
- [24] ZHANG, R., ZHANG, Y., ZHANG, Q., XIE, H., QIAN, W., and WEI, F.: *Growth of Half-Meter Long Carbon Nanotubes Based on Schulz-Flory Distribution*. ACS Nano **7**, 7 (2013). DOI: 10.1021/nn401995z.
- [25] MINTMIRE, J. W., DUNLAP, B. I., and WHITE, C. T.: *Are fullerene tubules metallic?* Phys. Rev. Lett. **68**, 5 (1992). DOI: 10.1103/PhysRevLett.68.631.

- 
- [26] TANS, S. J., DEVORET, M. H., DAI, H., THESS, A., SMALLEY, R. E., GEERLIGS, L. J., and DEKKER, C.: *Individual single-wall carbon nanotubes as quantum wires*. Nature **386**, 6624 (1997). DOI: [10.1038/386474a0](https://doi.org/10.1038/386474a0).
- [27] JORIO, A., DRESSELHAUS, G., and DRESSELHAUS, M. S. (eds.): *Carbon Nanotubes: Advanced Topics in the Synthesis, Structure, Properties and Applications*. Top. Appl. Phys. Springer-Verlag, Berlin, Heidelberg 2008. DOI: [10.1007/978-3-540-72865-8](https://doi.org/10.1007/978-3-540-72865-8).
- [28] BERBER, S., KWON, Y.-K., and TOMÁNEK, D.: *Unusually High Thermal Conductivity of Carbon Nanotubes*. Phys. Rev. Lett. **84**, 20 (2000). DOI: [10.1103/PhysRevLett.84.4613](https://doi.org/10.1103/PhysRevLett.84.4613).
- [29] KIM, P., SHI, L., MAJUMDAR, A., and MCEUEN, P. L.: *Thermal Transport Measurements of Individual Multiwalled Nanotubes*. Phys. Rev. Lett. **87**, 21 (2001). DOI: [10.1103/PhysRevLett.87.215502](https://doi.org/10.1103/PhysRevLett.87.215502).
- [30] YU, M.-F., LOURIE, O., DYER, M. J., MOLONI, K., KELLY, T. F., and RUOFF, R. S.: *Strength and Breaking Mechanism of Multiwalled Carbon Nanotubes Under Tensile Load*. Science **287**, 5453 (2000). DOI: [10.1126/science.287.5453.637](https://doi.org/10.1126/science.287.5453.637).
- [31] VOLDER, M. F. L. D., TAWFICK, S. H., BAUGHMAN, R. H., and HART, A. J.: *Carbon Nanotubes: Present and Future Commercial Applications*. Science **339**, 6119 (2013). DOI: [10.1126/science.1222453](https://doi.org/10.1126/science.1222453).
- [32] MINTMIRE, J. W. and WHITE, C. T.: *Electronic and structural properties of carbon nanotubes*. Carbon **33**, 7 (1995). DOI: [10.1016/0008-6223\(95\)00018-9](https://doi.org/10.1016/0008-6223(95)00018-9).
- [33] BACHILO, S. M., STRANO, M. S., KITTRELL, C., HAUGE, R. H., SMALLEY, R. E., and WEISMAN, R. B.: *Structure-Assigned Optical Spectra of Single-Walled Carbon Nanotubes*. Science **298**, 5602 (2002). DOI: [10.1126/science.1078727](https://doi.org/10.1126/science.1078727).
- [34] O'CONNELL, M. J., BACHILO, S. M., HUFFMAN, C. B., MOORE, V. C., STRANO, M. S., HAROZ, E. H., RIALON, K. L., BOUL, P. J., NOON, W. H., KITTRELL, C., MA, J., HAUGE, R. H., WEISMAN, R. B., and SMALLEY, R. E.: *Band Gap Fluorescence from Individual Single-Walled Carbon Nanotubes*. Science **297**, 5581 (2002). DOI: [10.1126/science.1072631](https://doi.org/10.1126/science.1072631).
- [35] WEISMAN, R. B. and BACHILO, S. M.: *Dependence of Optical Transition Energies on Structure for Single-Walled Carbon Nanotubes in Aqueous Suspension: An Empirical Kataura Plot*. Nano Lett. **3**, 9 (2003). DOI: [10.1021/nl034428i](https://doi.org/10.1021/nl034428i).
- [36] AVOURIS, P., FREITAG, M., and PEREBEINOS, V.: *Carbon-nanotube photonics and optoelectronics*. Nat. Photon. **2**, 6 (2008). DOI: [10.1038/nphoton.2008.94](https://doi.org/10.1038/nphoton.2008.94).

- [37] BARONE, P. W., PARKER, R. S., and STRANO, M. S.: *In Vivo Fluorescence Detection of Glucose Using a Single-Walled Carbon Nanotube Optical Sensor: Design, Fluorophore Properties, Advantages, and Disadvantages*. *Anal. Chem.* **77**, 23 (2005). DOI: [10.1021/ac0511997](https://doi.org/10.1021/ac0511997).
- [38] GLÜCKERT, J. T., ADAMSKA, L., SCHINNER, W., HOFMANN, M. S., DOORN, S. K., TRETIAK, S., and HÖGELE, A.: *Dipolar and charged localized excitons in carbon nanotubes*. *Phys. Rev. B* **98**, 19 (2018). DOI: [10.1103/PhysRevB.98.195413](https://doi.org/10.1103/PhysRevB.98.195413).
- [39] FREITAG, M., MARTIN, Y., MISEWICH, J. A., MARTEL, R., and AVOURIS, P.: *Photoconductivity of Single Carbon Nanotubes*. *Nano Lett.* **3**, 8 (2003). DOI: [10.1021/nl034313e](https://doi.org/10.1021/nl034313e).
- [40] PRADHAN, B., SETYOWATI, K., LIU, H., WALDECK, D. H., and CHEN, J.: *Carbon Nanotube-Polymer Nanocomposite Infrared Sensor*. *Nano Lett.* **8**, 4 (2008). DOI: [10.1021/nl0732880](https://doi.org/10.1021/nl0732880).
- [41] LU, R., CHRISTIANSON, C., KIRKEMINDE, A., REN, S., and WU, J.: *Extraordinary Photocurrent Harvesting at Type-II Heterojunction Interfaces: Toward High Detectivity Carbon Nanotube Infrared Detectors*. *Nano Lett.* **12**, 12 (2012). DOI: [10.1021/nl303302p](https://doi.org/10.1021/nl303302p).
- [42] LEE, J. U.: *Photovoltaic effect in ideal carbon nanotube diodes*. *Appl. Phys. Lett.* **87**, 7 (2005). DOI: [10.1063/1.2010598](https://doi.org/10.1063/1.2010598).
- [43] CHEN, C., LU, Y., KONG, E. S., ZHANG, Y., and LEE, S.-T.: *Nanowelded Carbon-Nanotube-Based Solar Microcells*. *Small* **4**, 9 (2008). DOI: [10.1002/sml.200701309](https://doi.org/10.1002/sml.200701309).
- [44] WANG, S., ZHANG, L., ZHANG, Z., DING, L., ZENG, Q., WANG, Z., LIANG, X., GAO, M., SHEN, J., XU, H., CHEN, Q., CUI, R., LI, Y., and PENG, L.-M.: *Photovoltaic Effects in Asymmetrically Contacted CNT Barrier-Free Bipolar Diode*. *J. Phys. Chem. C* **113**, 17 (2009). DOI: [10.1021/jp901282h](https://doi.org/10.1021/jp901282h).
- [45] MUELLER, T., KINOSHITA, M., STEINER, M., PEREBEINOS, V., BOL, A. A., FARMER, D. B., and AVOURIS, P.: *Efficient narrow-band light emission from a single carbon nanotube p-n diode*. *Nat. Nanotechnol.* **5**, 1 (2010). DOI: [10.1038/nnano.2009.319](https://doi.org/10.1038/nnano.2009.319).
- [46] WANG, S., ZENG, Q., YANG, L., ZHANG, Z., WANG, Z., PEI, T., DING, L., LIANG, X., GAO, M., LI, Y., and PENG, L.-M.: *High-Performance Carbon Nanotube Light-Emitting Diodes with Asymmetric Contacts*. *Nano Lett.* **11**, 1 (2011). DOI: [10.1021/nl101513z](https://doi.org/10.1021/nl101513z).
- [47] HE, X., HARTMANN, N. F., MA, X., KIM, Y., IHLY, R., BLACKBURN, J. L., GAO, W., KONO, J., YOMOGIDA, Y., HIRANO, A., TANAKA, T., KATAURA, H., HTOON, H., and DOORN, S. K.: *Tunable room-temperature single-photon emission at telecom wavelengths from  $sp^3$  defects in carbon nanotubes*. *Nat. Photon.* **11**, 9 (2017). DOI: [10.1038/nphoton.2017.119](https://doi.org/10.1038/nphoton.2017.119).

- [48] KWON, H., FURMANCHUK, A., KIM, M., MEANY, B., GUO, Y., SCHATZ, G. C., and WANG, Y.: *Molecularly Tunable Fluorescent Quantum Defects*. J. Am. Chem. Soc. **138**, 21 (2016). DOI: 10.1021/jacs.6b03618.
- [49] ICHIDA, M., MIZUNO, S., TANI, Y., SAITO, Y., and NAKAMURA, A.: *Exciton Effects of Optical Transitions in Single-Wall Carbon Nanotubes*. J. Phys. Soc. Jpn. **68**, 10 (1999). DOI: 10.1143/JPSJ.68.3131.
- [50] WANG, E., DUKOVIC, G., BRUS, L. E., and HEINZ, T. E.: *The Optical Resonances in Carbon Nanotubes Arise from Excitons*. Science **308**, 5723 (2005). DOI: 10.1126/science.1110265.
- [51] ANDO, T.: *Excitons in Carbon Nanotubes*. J. Phys. Soc. Jpn. **66**, 4 (1997). DOI: 10.1143/JPSJ.66.1066.
- [52] LÜER, L., HOSEINKHANI, S., POLLI, D., CROCHET, J., HERTEL, T., and LANZANI, G.: *Size and mobility of excitons in (6, 5) carbon nanotubes*. Nat. Phys. **5**, 1 (2009). DOI: 10.1038/nphys1149.
- [53] GEORGI, C., BÖHMLER, M., QIAN, H., NOVOTNY, L., and HARTSCHUH, A.: *Probing exciton propagation and quenching in carbon nanotubes with near-field optical microscopy*. Phys. Status Solidi B **246**, 11–12 (2009). DOI: 10.1002/pssb.200982306.
- [54] MORITSUBO, S., MURAI, T., SHIMADA, T., MURAKAMI, Y., CHIASHI, S., MARUYAMA, S., and KATO, Y. K.: *Exciton Diffusion in Air-Suspended Single-Walled Carbon Nanotubes*. Phys. Rev. Lett. **104**, 24 (2010). DOI: 10.1103/PhysRevLett.104.247402.
- [55] HERTEL, T., HIMMELEIN, S., ACKERMANN, T., STICH, D., and CROCHET, J.: *Diffusion Limited Photoluminescence Quantum Yields in 1-D Semiconductors: Single-Wall Carbon Nanotubes*. ACS Nano **4**, 12 (2010). DOI: 10.1021/nn101612b.
- [56] GHOSH, S., BACHILO, S. M., SIMONETTE, R. A., BECKINGHAM, K. M., and WEISMAN, R. B.: *Oxygen Doping Modifies Near-Infrared Band Gaps in Fluorescent Single-Walled Carbon Nanotubes*. Science **330**, 6011 (2010). DOI: 10.1126/science.1196382.
- [57] MIYAUCHI, Y., IWAMURA, M., MOURI, S., KAWAZOE, T., OHTSU, M., and MATSUDA, K.: *Brightening of excitons in carbon nanotubes on dimensionality modification*. Nat. Photon. **7**, 9 (2013). DOI: 10.1038/nphoton.2013.179.
- [58] PIAO, Y., MEANY, B., POWELL, L. R., VALLEY, N., KWON, H., SCHATZ, G. C., and WANG, Y.: *Brightening of carbon nanotube photoluminescence through the incorporation of  $sp^3$  defects*. Nat. Chem. **5**, 10 (2013). DOI: 10.1038/nchem.1711.
- [59] HE, X., GIFFORD, B. J., HARTMANN, N. F., IHLY, R., MA, X., KILINA, S. V., LUO, Y., SHAYAN, K., STRAUF, S., BLACKBURN, J. L., TRETIAK, S., DOORN, S. K., and HTOON, H.: *Low-Temperature Single Carbon Nanotube Spectroscopy of  $sp^3$  Quantum Defects*. ACS Nano **11**, 11 (2017). DOI: 10.1021/acsnano.7b03022.

- [60] HOFMANN, M. S., NOÉ, J., KNEER, A., CROCHET, J. J., and HÖGELE, A.: *Ubiquity of Exciton Localization in Cryogenic Carbon Nanotubes*. *Nano Lett.* **16**, 5 (2016). DOI: [10.1021/acs.nanolett.5b04901](https://doi.org/10.1021/acs.nanolett.5b04901).
- [61] HTOON, H., O'CONNELL, M. J., COX, P. J., DOORN, S. K., and KLIMOV, V. I.: *Low Temperature Emission Spectra of Individual Single-Walled Carbon Nanotubes: Multiplicity of Subspecies within Single-Species Nanotube Ensembles*. *Phys. Rev. Lett.* **93**, 2 (2004). DOI: [10.1103/PhysRevLett.93.027401](https://doi.org/10.1103/PhysRevLett.93.027401).
- [62] HIRORI, H., MATSUDA, K., MIYAUCHI, Y., MARUYAMA, S., and KANEMITSU, Y.: *Exciton Localization of Single-Walled Carbon Nanotubes Revealed by Femtosecond Excitation Correlation Spectroscopy*. *Phys. Rev. Lett.* **97**, 25 (2006). DOI: [10.1103/PhysRevLett.97.257401](https://doi.org/10.1103/PhysRevLett.97.257401).
- [63] HÖGELE, A., GALLAND, C., WINGER, M., and IMAMOĞLU, A.: *Photon Antibunching in the Photoluminescence Spectra of a Single Carbon Nanotube*. *Phys. Rev. Lett.* **100**, 21 (2008). DOI: [10.1103/PhysRevLett.100.217401](https://doi.org/10.1103/PhysRevLett.100.217401).
- [64] MA, X., HARTMANN, N. F., BALDWIN, J. K. S., DOORN, S. K., and HTOON, H.: *Room-temperature single-photon generation from solitary dopants of carbon nanotubes*. *Nat. Nanotechnol.* **10**, 8 (2015). DOI: [10.1038/nnano.2015.136](https://doi.org/10.1038/nnano.2015.136).
- [65] HE, X., HTOON, H., DOORN, S. K., PERNICE, W. H. P., PYATKOV, F., KRUPKE, R., JEANTET, A., CHASSAGNEUX, Y., and VOISIN, C.: *Carbon nanotubes as emerging quantum-light sources*. *Nat. Mater.* **17**, 8 (2018). DOI: [10.1038/s41563-018-0109-2](https://doi.org/10.1038/s41563-018-0109-2).
- [66] CHIASHI, S., WATANABE, S., HANASHIMA, T., and HOMMA, Y.: *Influence of Gas Adsorption on Optical Transition Energies of Single-Walled Carbon Nanotubes*. *Nano Lett.* **8**, 10 (2008). DOI: [10.1021/nl801074j](https://doi.org/10.1021/nl801074j).
- [67] HOFMANN, M. S., GLÜCKERT, J. T., NOÉ, J., BOURJAU, C., DEHMEL, R., and HÖGELE, A.: *Bright, long-lived and coherent excitons in carbon nanotube quantum dots*. *Nat. Nanotechnol.* **8**, 7 (2013). DOI: [10.1038/nnano.2013.119](https://doi.org/10.1038/nnano.2013.119).
- [68] LEFEBVRE, J., FRASER, J., HOMMA, Y., and FINNIE, P.: *Photoluminescence from single-walled carbon nanotubes: a comparison between suspended and micelle-encapsulated nanotubes*. *Appl. Phys. A* **78**, 8 (2004). DOI: [10.1007/s00339-003-2460-6](https://doi.org/10.1007/s00339-003-2460-6).
- [69] MATSUDA, K., KANEMITSU, Y., IRIE, K., SAIKI, T., SOMEYA, T., MIYAUCHI, S., and MARUYAMA, S.: *Photoluminescence intermittency in an individual single-walled carbon nanotube at room temperature*. *Appl. Phys. Lett.* **86**, 12 (2005). DOI: [10.1063/1.1894609](https://doi.org/10.1063/1.1894609).

- [70] VIALLA, F., CHASSAGNEUX, Y., FERREIRA, R., ROQUELET, C., DIEDERICHS, C., CASSABOIS, G., ROUSSIGNOL, P., LAURET, J. S., and VOISIN, C.: *Unifying the Low-Temperature Photoluminescence Spectra of Carbon Nanotubes: The Role of Acoustic Phonon Confinement*. Phys. Rev. Lett. **113**, 5 (2014). DOI: [10.1103/PhysRevLett.113.057402](https://doi.org/10.1103/PhysRevLett.113.057402).
- [71] GIFFORD, B. J., KILINA, S., HTOON, H., DOORN, S. K., and TRETIAK, S.: *Exciton Localization and Optical Emission in Aryl-Functionalized Carbon Nanotubes*. J. Phys. Chem. C **122**, 3 (2018). DOI: [10.1021/acs.jpcc.7b09558](https://doi.org/10.1021/acs.jpcc.7b09558).
- [72] SARPKEYA, I., ZHANG, Z., WALDEN-NEWMAN, W., WANG, X., HONE, J., WONG, C. W., and STRAUF, S.: *Prolonged spontaneous emission and dephasing of localized excitons in air-bridged carbon nanotubes*. Nat. Commun. **4** (2013). DOI: [10.1038/ncomms3152](https://doi.org/10.1038/ncomms3152).
- [73] WALDEN-NEWMAN, W., SARPKEYA, I., and STRAUF, S.: *Quantum Light Signatures and Nanosecond Spectral Diffusion from Cavity-Embedded Carbon Nanotubes*. Nano Lett. **12**, 4 (2012). DOI: [10.1021/nl204402v](https://doi.org/10.1021/nl204402v).
- [74] AI, N., WALDEN-NEWMAN, W., SONG, Q., KALLIAKOS, S., and STRAUF, S.: *Suppression of Blinking and Enhanced Exciton Emission from Individual Carbon Nanotubes*. ACS Nano **5**, 4 (2011). DOI: [10.1021/nn102885p](https://doi.org/10.1021/nn102885p).
- [75] HOFMANN, M. S.: *Spectroscopy of localized excitons in carbon nanotubes*. Dissertation, Ludwig-Maximilians-Universität, München 2016. URN: [urn:nbn:de:bvb:19-202117](https://nbn-resolving.org/urn:nbn:de:bvb:19-202117).
- [76] MOORE, J., STANITSKI, C., and JURIS, P.: *Principles of Chemistry: The Molecular Science*. Brooks/Cole, Cengage Learning, Belmont 2009.
- [77] BRITTIN, W. E.: *Valence angle of the tetrahedral carbon atom*. J. Chem. Educ. **22**, 3 (1945). DOI: [10.1021/ed022p145](https://doi.org/10.1021/ed022p145).
- [78] FALCAO, E. H. and WUDL, F.: *Carbon allotropes: beyond graphite and diamond*. J. Chem. Technol. Biotechnol. **82**, 6 (2007). DOI: [10.1002/jctb.1693](https://doi.org/10.1002/jctb.1693).
- [79] CHUNG, D. D. L.: *Review Graphite*. J. Mater. Sci. **37**, 8 (2002). DOI: [10.1023/A:1014915307738](https://doi.org/10.1023/A:1014915307738).
- [80] MCCLURE, J. W.: *Diamagnetism of Graphite*. Phys. Rev. **104**, 3 (1956). DOI: [10.1103/PhysRev.104.666](https://doi.org/10.1103/PhysRev.104.666).
- [81] SLONCZEWSKI, J. C. and WEISS, P. R.: *Band Structure of Graphite*. Phys. Rev. **109**, 2 (1958). DOI: [10.1103/PhysRev.109.272](https://doi.org/10.1103/PhysRev.109.272).
- [82] WALLACE, P. R.: *The Band Theory of Graphite*. Phys. Rev. **71**, 9 (1947). DOI: [10.1103/PhysRev.71.622](https://doi.org/10.1103/PhysRev.71.622).

- [83] NOVOSELOV, K. S., GEIM, A. K., MOROZOV, S. V., JIANG, D., ZHANG, Y., DUBONOS, S. V., GRIGORIEVA, I. V., and FIRSOV, A. A.: *Electric Field Effect in Atomically Thin Carbon Films*. *Science* **306**, 5696 (2004). DOI: [10.1126/science.1102896](https://doi.org/10.1126/science.1102896).
- [84] NOVOSELOV, K. S., JIANG, D., SCHEDIN, F., BOOTH, T. J., KHOTKEVICH, V. V., MOROZOV, S. V., and GEIM, A. K.: *Two-dimensional atomic crystals*. *Proc. Natl. Acad. Sci. U.S.A.* **102**, 30 (2005). DOI: [10.1073/pnas.0502848102](https://doi.org/10.1073/pnas.0502848102).
- [85] COOPER, D. R., D'ANJOU, B., GHATTAMANENI, N., HARACK, B., HILKE, M., HORTH, A., MAJLIS, N., MASSICOTTE, M., VANDSBURGER, L., WHITEWAY, E., and YU, V.: *Experimental Review of Graphene*. *ISRN Condens. Matter Phys.* **2012** (2012).
- [86] REICH, S., MAULTZSCH, J., THOMSEN, C., and ORDEJÓN, P.: *Tight-binding description of graphene*. *Phys. Rev. B* **66**, 3 (2002). DOI: [10.1103/PhysRevB.66.035412](https://doi.org/10.1103/PhysRevB.66.035412).
- [87] CASTRO NETO, A. H., GUINEA, F., PERES, N. M. R., NOVOSELOV, K. S., and GEIM, A. K.: *The electronic properties of graphene*. *Rev. Mod. Phys.* **81**, 1 (2009). DOI: [10.1103/RevModPhys.81.109](https://doi.org/10.1103/RevModPhys.81.109).
- [88] SEMENOFF, G. W.: *Condensed-Matter Simulation of a Three-Dimensional Anomaly*. *Phys. Rev. Lett.* **53**, 26 (1984). DOI: [10.1103/PhysRevLett.53.2449](https://doi.org/10.1103/PhysRevLett.53.2449).
- [89] MAK, K. F., HE, K., SHAN, J., and HEINZ, T. F.: *Control of valley polarization in monolayer MoS<sub>2</sub> by optical helicity*. *Nat. Nanotechnol.* **7**, 8 (2012). DOI: [10.1038/nnano.2012.96](https://doi.org/10.1038/nnano.2012.96).
- [90] XIAO, D., LIU, G.-B., FENG, W., XU, X., and YAO, W.: *Coupled Spin and Valley Physics in Monolayers of MoS<sub>2</sub> and Other Group-VI Dichalcogenides*. *Phys. Rev. Lett.* **108**, 19 (2012). DOI: [10.1103/PhysRevLett.108.196802](https://doi.org/10.1103/PhysRevLett.108.196802).
- [91] RYCERZ, A., TWORZYDŁO, J., and BEENAKKER, C. W. J.: *Valley filter and valley valve in graphene*. *Nat. Phys.* **3**, 3 (2007). DOI: [10.1038/nphys547](https://doi.org/10.1038/nphys547).
- [92] XIAO, D., YAO, W., and NIU, Q.: *Valley-Contrasting Physics in Graphene: Magnetic Moment and Topological Transport*. *Phys. Rev. Lett.* **99**, 23 (2007). DOI: [10.1103/PhysRevLett.99.236809](https://doi.org/10.1103/PhysRevLett.99.236809).
- [93] YAO, W., XIAO, D., and NIU, Q.: *Valley-dependent optoelectronics from inversion symmetry breaking*. *Phys. Rev. B* **77**, 23 (2008). DOI: [10.1103/PhysRevB.77.235406](https://doi.org/10.1103/PhysRevB.77.235406).
- [94] HAYASHI, T., KIM, Y. A., MATOBA, T., ESAKA, M., NISHIMURA, K., TSUKADA, T., ENDO, M., and DRESSELHAUS, M. S.: *Smallest Freestanding Single-Walled Carbon Nanotube*. *Nano Lett.* **3**, 7 (2003). DOI: [10.1021/nl034080r](https://doi.org/10.1021/nl034080r).
- [95] QIN, L.-C., ZHAO, X., HIRAHARA, K., MIYAMOTO, Y., ANDO, Y., and IJIMA, S.: *The smallest carbon nanotube*. *Nature* **408**, 6808 (2000). DOI: [10.1038/35040699](https://doi.org/10.1038/35040699).

- 
- [96] WANG, N., TANG, Z. K., LI, G. D., and CHEN, J. S.: *Single-walled 4 Å carbon nanotube arrays*. Nature **408**, 6808 (2000). DOI: 10.1038/35040702.
- [97] SVENSSON, J. and CAMPBELL, E. E. B.: *Schottky barriers in carbon nanotube-metal contacts*. J. Appl. Phys. **110**, 11 (2011). DOI: 10.1063/1.3664139.
- [98] SAITO, R., FUJITA, M., DRESSELHAUS, G., and DRESSELHAUS, M. S.: *Electronic structure of chiral graphene tubules*. Appl. Phys. Lett. **60**, 18 (1992). DOI: 10.1063/1.107080.
- [99] VAN HOVE, L.: *The Occurrence of Singularities in the Elastic Frequency Distribution of a Crystal*. Phys. Rev. **89**, 6 (1953). DOI: 10.1103/PhysRev.89.1189.
- [100] BOŽOVIĆ, I., BOŽOVIĆ, N., and DAMNJANOVIĆ, M.: *Optical dichroism in nanotubes*. Phys. Rev. B **62**, 11 (2000). DOI: 10.1103/PhysRevB.62.6971.
- [101] GRÜNEIS, A., SAITO, R., SAMSONIDZE, G. G., KIMURA, T., PIMENTA, M. A., JORIO, A., FILHO, A. G. S., DRESSELHAUS, G., and DRESSELHAUS, M. S.: *Inhomogeneous optical absorption around the K point in graphite and carbon nanotubes*. Phys. Rev. B **67**, 16 (2003). DOI: 10.1103/PhysRevB.67.165402.
- [102] MIYAUCHI, Y., OBA, M., and MARUYAMA, S.: *Cross-polarized optical absorption of single-walled nanotubes by polarized photoluminescence excitation spectroscopy*. Phys. Rev. B **74**, 20 (2006). DOI: 10.1103/PhysRevB.74.205440.
- [103] AJIKI, H. and ANDO, T.: *Aharonov-Bohm effect in carbon nanotubes*. Physica B **201** (1994). DOI: 10.1016/0921-4526(94)91112-6.
- [104] KATAURA, H., KUMAZAWA, Y., MANIWA, Y., UMEZU, I., SUZUKI, S., OHTSUKA, Y., and ACHIBA, Y.: *Optical properties of single-wall carbon nanotubes*. Synth. Met. **103**, 1 (1999). DOI: 10.1016/S0379-6779(98)00278-1.
- [105] WILDER, J. W. G., VENEMA, L. C., RINZLER, A. G., SMALLEY, R. E., and DEKKER, C.: *Electronic structure of atomically resolved carbon nanotubes*. Nature **391**, 6662 (1998). DOI: 10.1038/34139.
- [106] SUGANO, M., KASUYA, A., TOHJI, K., SAITO, Y., and NISHINA, Y.: *Resonance Raman scattering and diameter-dependent electronic states in single-wall carbon nanotubes*. Chem. Phys. Lett. **292**, 4 (1998). DOI: 10.1016/S0009-2614(98)00709-X.
- [107] KUZMANY, H., BURGER, B., HULMAN, M., KÜRTI, J., RINZLER, A. G., and SMALLEY, R. E.: *Spectroscopic analysis of different types of single-wall carbon nanotubes*. EPL **44**, 4 (1998). DOI: 10.1209/epl/i1998-00504-y.
- [108] ICHIDA, M., MIZUNO, S., SAITO, Y., KATAURA, H., ACHIBA, Y., and NAKAMURA, A.: *Coulomb effects on the fundamental optical transition in semiconducting single-walled carbon nanotubes: Divergent behavior in the small-diameter limit*. Phys. Rev. B **65**, 24 (2002). DOI: 10.1103/PhysRevB.65.241407.

- [109] SAITO, R., DRESSELHAUS, G., and DRESSELHAUS, M. S.: *Trigonal warping effect of carbon nanotubes*. Phys. Rev. B **61**, 4 (2000). DOI: [10.1103/PhysRevB.61.2981](https://doi.org/10.1103/PhysRevB.61.2981).
- [110] REICH, S. and THOMSEN, C.: *Chirality dependence of the density-of-states singularities in carbon nanotubes*. Phys. Rev. B **62**, 7 (2000). DOI: [10.1103/PhysRevB.62.4273](https://doi.org/10.1103/PhysRevB.62.4273).
- [111] LI, Z. M., TANG, Z. K., LIU, H. J., WANG, N., CHAN, C. T., SAITO, R., OKADA, S., LI, G. D., CHEN, J. S., NAGASAWA, N., and TSUDA, S.: *Polarized Absorption Spectra of Single-Walled 4 Å Carbon Nanotubes Aligned in Channels of an AlPO<sub>4</sub>-5 Single Crystal*. Phys. Rev. Lett. **87**, 12 (2001). DOI: [10.1103/PhysRevLett.87.127401](https://doi.org/10.1103/PhysRevLett.87.127401).
- [112] POPOV, V. N.: *Curvature effects on the structural, electronic and optical properties of isolated single-walled carbon nanotubes within a symmetry-adapted non-orthogonal tight-binding model*. New J. Phys. **6** (2004). DOI: [10.1088/1367-2630/6/1/017](https://doi.org/10.1088/1367-2630/6/1/017).
- [113] POREZAG, D., FRAUENHEIM, T., KÖHLER, T., SEIFERT, G., and KASCHNER, R.: *Construction of tight-binding-like potentials on the basis of density-functional theory: Application to carbon*. Phys. Rev. B **51**, 19 (1995). DOI: [10.1103/PhysRevB.51.12947](https://doi.org/10.1103/PhysRevB.51.12947).
- [114] KANE, C. L. and MELE, E. J.: *Ratio Problem in Single Carbon Nanotube Fluorescence Spectroscopy*. Phys. Rev. Lett. **90**, 20 (2003). DOI: [10.1103/PhysRevLett.90.207401](https://doi.org/10.1103/PhysRevLett.90.207401).
- [115] SPATARU, C. D., ISMAIL-BEIGI, S., BENEDICT, L. X., and LOUIE, S. G.: *Excitonic Effects and Optical Spectra of Single-Walled Carbon Nanotubes*. Phys. Rev. Lett. **92**, 7 (2004). DOI: [10.1103/PhysRevLett.92.077402](https://doi.org/10.1103/PhysRevLett.92.077402).
- [116] JORIO, A., FANTINI, C., PIMENTA, M. A., CAPAZ, R. B., SAMSONIDZE, G. G., DRESSELHAUS, G., DRESSELHAUS, M. S., JIANG, J., KOBAYASHI, N., GRÜNEIS, A., and SAITO, R.: *Resonance Raman spectroscopy ( $n, m$ )-dependent effects in small-diameter single-wall carbon nanotubes*. Phys. Rev. B **71**, 7 (2005). DOI: [10.1103/PhysRevB.71.075401](https://doi.org/10.1103/PhysRevB.71.075401).
- [117] ZHAO, H. and MAZUMDAR, S.: *Electron-Electron Interaction Effects on the Optical Excitations of Semiconducting Single-Walled Carbon Nanotubes*. Phys. Rev. Lett. **93**, 15 (2004). DOI: [10.1103/PhysRevLett.93.157402](https://doi.org/10.1103/PhysRevLett.93.157402).
- [118] SAMSONIDZE, G. G., SAITO, R., KOBAYASHI, N., GRÜNEIS, A., JIANG, J., JORIO, A., CHOU, S. G., DRESSELHAUS, G., and DRESSELHAUS, M. S.: *Family behavior of the optical transition energies in single-wall carbon nanotubes of smaller diameters*. Appl. Phys. Lett. **85**, 23 (2004). DOI: [10.1063/1.1829160](https://doi.org/10.1063/1.1829160).
- [119] MAULTZSCH, J., POMRAENKE, R., REICH, S., CHANG, E., PREZZI, D., RUINI, A., MOLINARI, E., STRANO, M. S., THOMSEN, C., and LIENAU, C.: *Erratum: Exciton binding energies in carbon nanotubes from two-photon photoluminescence [Phys. Rev. B. 72, 241402(R) (2005)]*. Phys. Rev. B **74**, 16 (2006). DOI: [10.1103/PhysRevB.74.169901](https://doi.org/10.1103/PhysRevB.74.169901).

- 
- [120] MAULTZSCH, J., POMRAENKE, R., REICH, S., CHANG, E., PREZZI, D., RUINI, A., MOLINARI, E., STRANO, M. S., THOMSEN, C., and LIENAU, C.: *Exciton binding energies in carbon nanotubes from two-photon photoluminescence*. Phys. Rev. B **72**, 24 (2005). DOI: [10.1103/PhysRevB.72.241402](https://doi.org/10.1103/PhysRevB.72.241402).
- [121] SHAVER, J. and KONO, J.: *Temperature-dependent magneto-photoluminescence spectroscopy of carbon nanotubes: evidence for dark excitons*. Laser Photonics Rev. **1**, 3 (2007). DOI: [10.1002/lpor.200710018](https://doi.org/10.1002/lpor.200710018).
- [122] WANNIER, G. H.: *The Structure of Electronic Excitation Levels in Insulating Crystals*. Phys. Rev. **52**, 3 (1937). DOI: [10.1103/PhysRev.52.191](https://doi.org/10.1103/PhysRev.52.191).
- [123] DUKOVIC, G., WANG, F., SONG, D., SFEIR, M. Y., HEINZ, T. F., and BRUS, L. E.: *Structural Dependence of Excitonic Optical Transitions and Band-Gap Energies in Carbon Nanotubes*. Nano Lett. **5**, 11 (2005). DOI: [10.1021/nl0518122](https://doi.org/10.1021/nl0518122).
- [124] PEDERSEN, T. G.: *Variational approach to excitons in carbon nanotubes*. Phys. Rev. B **67**, 7 (2003). DOI: [10.1103/PhysRevB.67.073401](https://doi.org/10.1103/PhysRevB.67.073401).
- [125] PEDERSEN, T. G.: *Exciton effects in carbon nanotubes*. Carbon **42**, 5-6 (2004). DOI: [10.1016/j.carbon.2003.12.028](https://doi.org/10.1016/j.carbon.2003.12.028).
- [126] MA, Y.-Z., VALKUNAS, L., BACHILO, S. M., and FLEMING, G. R.: *Exciton Binding Energy in Semiconducting Single-Walled Carbon Nanotubes*. J. Phys. Chem. B **109**, 33 (2005). DOI: [10.1021/jp053011t](https://doi.org/10.1021/jp053011t).
- [127] SPATARU, C. D., ISMAIL-BEIGI, S., CAPAZ, R. B., and LOUIE, S. G.: *Theory and Ab Initio Calculation of Radiative Lifetime of Excitons in Semiconducting Carbon Nanotubes*. Phys. Rev. Lett. **95**, 24 (2005). DOI: [10.1103/PhysRevLett.95.247402](https://doi.org/10.1103/PhysRevLett.95.247402).
- [128] ANDO, T.: *Effects of Valley Mixing and Exchange on Excitons in Carbon Nanotubes with Aharonov-Bohm Flux*. J. Phys. Soc. Jpn. **75**, 2 (2006). DOI: [10.1143/JPSJ.75.024707](https://doi.org/10.1143/JPSJ.75.024707).
- [129] PEREBEINOS, V., TERSOFF, J., and AVOURIS, P.: *Radiative Lifetime of Excitons in Carbon Nanotubes*. Nano Lett. **5**, 12 (2005). DOI: [10.1021/nl051828s](https://doi.org/10.1021/nl051828s).
- [130] MORTIMER, I. B. and NICHOLAS, R. J.: *Role of Bright and Dark Excitons in the Temperature-Dependent Photoluminescence of Carbon Nanotubes*. Phys. Rev. Lett. **98**, 2 (2007). DOI: [10.1103/PhysRevLett.98.027404](https://doi.org/10.1103/PhysRevLett.98.027404).
- [131] SRIVASTAVA, A., HTOON, H., KLIMOV, V. I., and KONO, J.: *Direct Observation of Dark Excitons in Individual Carbon Nanotubes: Inhomogeneity in the Exchange Splitting*. Phys. Rev. Lett. **101**, 8 (2008). DOI: [10.1103/PhysRevLett.101.087402](https://doi.org/10.1103/PhysRevLett.101.087402).
- [132] SHAVER, J., CROOKER, S. A., FAGAN, J. A., HOBBIIE, E. K., UBRIG, N., PORTUGALL, O., PEREBEINOS, V., AVOURIS, P., and KONO, J.: *Magneto-optical spectroscopy of highly aligned carbon nanotubes: Identifying the role of threading magnetic flux*. Phys. Rev. B **78**, 8 (2008). DOI: [10.1103/PhysRevB.78.081402](https://doi.org/10.1103/PhysRevB.78.081402).

- [133] LEBEDKIN, S., HENNRICH, F., SKIPA, T., and KAPPES, M. M.: *Near-Infrared Photoluminescence of Single-Walled Carbon Nanotubes Prepared by the Laser Vaporization Method*. J. Phys. Chem. B **107**, 9 (2003). DOI: [10.1021/jp027096z](https://doi.org/10.1021/jp027096z).
- [134] WANG, E., DUKOVIC, G., BRUS, L. E., and HEINZ, T. F.: *Time-Resolved Fluorescence of Carbon Nanotubes and Its Implication for Radiative Lifetimes*. Phys. Rev. Lett. **92**, 17 (2004). DOI: [10.1103/PhysRevLett.92.177401](https://doi.org/10.1103/PhysRevLett.92.177401).
- [135] LEFEBVRE, J., FINNIE, P., and HOMMA, Y.: *Temperature-dependent photoluminescence from single-walled carbon nanotubes*. Phys. Rev. B **70**, 4 (2004). DOI: [10.1103/PhysRevB.70.045419](https://doi.org/10.1103/PhysRevB.70.045419).
- [136] BERGER, S., VOISIN, C., CASSABOIS, G., DELALANDE, C., ROUSSIGNOL, P., and MARIE, X.: *Temperature Dependence of Exciton Recombination in Semiconducting Single-Wall Carbon Nanotubes*. Nano Lett. **7**, 2 (2007). DOI: [10.1021/nl062609p](https://doi.org/10.1021/nl062609p).
- [137] WALSH, A. G., NICKOLAS VAMIVAKAS, A., YIN, Y., CRONIN, S. B., SELIM ÜNLÜ, M., GOLDBERG, B. B., and SWAN, A. K.: *Scaling of exciton binding energy with external dielectric function in carbon nanotubes*. Physica E **40**, 7 (2008). DOI: [10.1016/j.physe.2007.07.007](https://doi.org/10.1016/j.physe.2007.07.007).
- [138] KANE, C. L. and MELE, E. J.: *Electron Interactions and Scaling Relations for Optical Excitations in Carbon Nanotubes*. Phys. Rev. Lett. **93**, 19 (2004). DOI: [10.1103/PhysRevLett.93.197402](https://doi.org/10.1103/PhysRevLett.93.197402).
- [139] CAPAZ, R. B., SPATARU, C. D., ISMAIL-BEIGI, S., and LOUIE, S. G.: *Diameter and chirality dependence of exciton properties in carbon nanotubes*. Phys. Rev. B **74**, 12 (2006). DOI: [10.1103/PhysRevB.74.121401](https://doi.org/10.1103/PhysRevB.74.121401).
- [140] CAPAZ, R. B., SPATARU, C. D., ISMAIL-BEIGI, S., and LOUIE, S. G.: *Excitons in carbon nanotubes: Diameter and chirality trends*. Phys. Status Solidi B **244**, 11 (2007). DOI: [10.1002/pssb.200776200](https://doi.org/10.1002/pssb.200776200).
- [141] WALSH, A. G., VAMIVAKAS, A. N., YIN, Y., CRONIN, S. B., ÜNLÜ, M. S., GOLDBERG, B. B., and SWAN, A. K.: *Screening of Excitons in Single, Suspended Carbon Nanotubes*. Nano Lett. **7**, 6 (2007). DOI: [10.1021/nl070193p](https://doi.org/10.1021/nl070193p).
- [142] MOORE, V. C., STRANO, M. S., HAROZ, E. H., HAUGE, R. H., SMALLEY, R. E., SCHMIDT, J., and TALMON, Y.: *Individually Suspended Single-Walled Carbon Nanotubes in Various Surfactants*. Nano Lett. **3**, 10 (2003). DOI: [10.1021/nl034524j](https://doi.org/10.1021/nl034524j).
- [143] PEREBEINOS, V., TERSOFF, J., and AVOURIS, P.: *Scaling of Excitons in Carbon Nanotubes*. Phys. Rev. Lett. **92**, 25 (2004). DOI: [10.1103/PhysRevLett.92.257402](https://doi.org/10.1103/PhysRevLett.92.257402).
- [144] CAPAZ, R. B., SPATARU, C. D., TANGNEY, P., COHEN, M. L., and LOUIE, S. G.: *Temperature Dependence of the Band Gap of Semiconducting Carbon Nanotubes*. Phys. Rev. Lett. **94**, 3 (2005). DOI: [10.1103/PhysRevLett.94.036801](https://doi.org/10.1103/PhysRevLett.94.036801).

- 
- [145] EHRENBERG, W. and SIDAY, R. E.: *The Refractive Index in Electron Optics and the Principles of Dynamics*. Proc. Phys. Soc. B **62**, 1 (1949). DOI: 10.1088/0370-1301/62/1/303.
- [146] AHARONOV, Y. and BOHM, D.: *Significance of Electromagnetic Potentials in the Quantum Theory*. Phys. Rev. **115**, 3 (1959). DOI: 10.1103/PhysRev.115.485.
- [147] AHARONOV, Y. and BOHM, D.: *Further Considerations on Electromagnetic Potentials in the Quantum Theory*. Phys. Rev. **123**, 4 (1961). DOI: 10.1103/PhysRev.123.1511.
- [148] AJIKI, H. and ANDO, T.: *Electronic States of Carbon Nanotubes*. J. Phys. Soc. Jpn. **62**, 4 (1993). DOI: 10.1143/JPSJ.62.1255.
- [149] ZARIC, S., OSTOJIC, G. N., KONO, J., SHAVER, J., MOORE, V. C., STRANO, M. S., HAUGE, R. H., SMALLEY, R. E., and WEI, X.: *Optical Signatures of the Aharonov-Bohm Phase in Single-Walled Carbon Nanotubes*. Science **304**, 5674 (2004). DOI: 10.1126/science.1096524.
- [150] SHAVER, J., KONO, J., PORTUGALL, O., KRSTIĆ, V., RIKKEN, G. L. J. A., MIYAUCHI, Y., MARUYAMA, S., and PEREBEINOS, V.: *Magnetic Brightening of Carbon Nanotube Photoluminescence through Symmetry Breaking*. Nano Lett. **7**, 7 (2007). DOI: 10.1021/nl070260f.
- [151] ZARIC, S., OSTOJIC, G. N., SHAVER, J., KONO, J., PORTUGALL, O., FRINGS, P. H., RIKKEN, G. L. J. A., FURIS, M., CROOKER, S. A., WEI, X., MOORE, V. C., HAUGE, R. H., and SMALLEY, R. E.: *Excitons in Carbon Nanotubes with Broken Time-Reversal Symmetry*. Phys. Rev. Lett. **96**, 1 (2006). DOI: 10.1103/PhysRevLett.96.016406.
- [152] LAMPERT, M. A.: *Mobile and Immobile Effective-Mass-Particle Complexes in Non-metallic Solids*. Phys. Rev. Lett. **1**, 12 (1958). DOI: 10.1103/PhysRevLett.1.450.
- [153] YOSHIDA, M., POPERT, A., and KATO, Y. K.: *Gate-voltage induced trions in suspended carbon nanotubes*. Phys. Rev. B **93**, 4 (2016). DOI: 10.1103/PhysRevB.93.041402.
- [154] GALLAND, C. and IMAMOĞLU, A.: *All-Optical Manipulation of Electron Spins in Carbon-Nanotube Quantum Dots*. Phys. Rev. Lett. **101**, 15 (2008). DOI: 10.1103/PhysRevLett.101.157404.
- [155] THOMAS, G. A. and RICE, T. M.: *Trions, molecules and excitons above the Mott density in Ge*. Solid State Commun. **23**, 6 (1977). DOI: 10.1016/0038-1098(77)90232-0.
- [156] KAWABATA, T., MURO, K., and NARITA, S.: *Observation of cyclotron resonance absorptions due to excitonic ion and excitonic molecule ion in silicon*. Solid State Commun. **23**, 4 (1977). DOI: 10.1016/0038-1098(77)90456-2.
- [157] STÉBÉ, B. and AINANE, A.: *Ground state energy and optical absorption of excitonic trions in two dimensional semiconductors*. Superlattices Microstruct. **5**, 4 (1989). DOI: 10.1016/0749-6036(89)90382-0.

- [158] WARBURTON, R. J., DÜRR, C. S., KARRAI, K., KOTTHAUS, J. P., MEDEIROS-RIBEIRO, G., and PETROFF, P. M.: *Charged Excitons in Self-Assembled Semiconductor Quantum Dots*. Phys. Rev. Lett. **79**, 26 (1997). DOI: [10.1103/PhysRevLett.79.5282](https://doi.org/10.1103/PhysRevLett.79.5282).
- [159] BRACKER, A. S., STINAFF, E. A., GAMMON, D., WARE, M. E., TISCHLER, J. G., PARK, D., GERSHONI, D., FILINOV, A. V., BONITZ, M., PEETERS, F., and RIVA, C.: *Binding energies of positive and negative trions: From quantum wells to quantum dots*. Phys. Rev. B **72**, 3 (2005). DOI: [10.1103/PhysRevB.72.035332](https://doi.org/10.1103/PhysRevB.72.035332).
- [160] PEETERS, F. M., RIVA, C., and VARGA, K.: *Trions in quantum wells*. Physica B **300**, 1 (2001). DOI: [10.1016/S0921-4526\(01\)00577-4](https://doi.org/10.1016/S0921-4526(01)00577-4).
- [161] KHENG, K., COX, R. T., d'AUBIGNÉ, M. Y., BASSANI, F., SAMINADAYAR, K., and TATARENKO, S.: *Observation of negatively charged excitons  $X^-$  in semiconductor quantum wells*. Phys. Rev. Lett. **71**, 11 (1993). DOI: [10.1103/PhysRevLett.71.1752](https://doi.org/10.1103/PhysRevLett.71.1752).
- [162] KHENG, K., SAMINADAYAR, K., and MAGNEA, N.: *Effect of confined electrons on the centre-of-mass quantization states of the exciton in wide modulation-doped CdTe/CdZnTe quantum wells*. J. Cryst. Growth **184-185** (1998). DOI: [10.1016/S0022-0248\(98\)80177-2](https://doi.org/10.1016/S0022-0248(98)80177-2).
- [163] MATSUNAGA, R., MATSUDA, K., and KANEMITSU, Y.: *Observation of Charged Excitons in Hole-Doped Carbon Nanotubes Using Photoluminescence and Absorption Spectroscopy*. Phys. Rev. Lett. **106**, 3 (2011). DOI: [10.1103/PhysRevLett.106.037404](https://doi.org/10.1103/PhysRevLett.106.037404).
- [164] SANTOS, S. M., YUMA, B., BERCIAUD, S., SHAVER, J., GALLART, M., GILLIOT, P., COGNET, L., and LOUNIS, B.: *All-Optical Trion Generation in Single-Walled Carbon Nanotubes*. Phys. Rev. Lett. **107**, 18 (2011). DOI: [10.1103/PhysRevLett.107.187401](https://doi.org/10.1103/PhysRevLett.107.187401).
- [165] PARK, J. S., HIRANA, Y., MOURI, S., MIYAUCHI, Y., NAKASHIMA, N., and MATSUDA, K.: *Observation of Negative and Positive Trions in the Electrochemically Carrier-Doped Single-Walled Carbon Nanotubes*. J. Am. Chem. Soc. **134**, 35 (2012). DOI: [10.1021/ja304282j](https://doi.org/10.1021/ja304282j).
- [166] GLAUBER, R. J.: *The Quantum Theory of Optical Coherence*. Phys. Rev. **130**, 6 (1963). DOI: [10.1103/PhysRev.130.2529](https://doi.org/10.1103/PhysRev.130.2529).
- [167] HANBURY BROWN, R. and TWISS, R. Q.: *A Test of a New Type of Stellar Interferometer on Sirius*. Nature **178**, 4541 (1956). DOI: [10.1038/1781046a0](https://doi.org/10.1038/1781046a0).
- [168] HANBURY BROWN, R. and TWISS, R. Q.: *Interferometry of the intensity fluctuations in light – I. Basic theory: the correlation between photons in coherent beams of radiation*. Proc. R. Soc. A **242**, 1230 (1957). DOI: [10.1098/rspa.1957.0177](https://doi.org/10.1098/rspa.1957.0177).
- [169] HANBURY BROWN, R. and TWISS, R. Q.: *Interferometry of the intensity fluctuations in light – II. An experimental test of the theory for partially coherent light*. Proc. R. Soc. A **243**, 1234 (1958). DOI: [10.1098/rspa.1958.0001](https://doi.org/10.1098/rspa.1958.0001).

- [170] FANO, U.: *Quantum Theory of Interference Effects in the Mixing of Light from Phase-Independent Sources*. Am. J. Phys. **29**, 8 (1961). DOI: 10.1119/1.1937827.
- [171] FOX, M.: *Quantum Optics: An Introduction*. Oxford University Press, Oxford, New York 2006.
- [172] HANBURY BROWN, R. and TWISS, R. Q.: *Correlation between Photons in two Coherent Beams of Light*. Nature **177**, 4497 (1956). DOI: 10.1038/177027a0.
- [173] GLAUBER, R. J.: *Coherent and Incoherent States of the Radiation Field*. Phys. Rev. **131**, 6 (1963). DOI: 10.1103/PhysRev.131.2766.
- [174] WANG, T., PUCCIONI, G. P., and LIPPI, G. L.: *Dynamical Buildup of Lasing in Mesoscale Devices*. Sci. Rep. **5**, 1 (2015). DOI: 10.1038/srep15858.
- [175] CARMICHAEL, H. J. and WALLS, D. F.: *A quantum-mechanical master equation treatment of the dynamical Stark effect*. J. Phys. B **9**, 8 (1976). DOI: 10.1088/0022-3700/9/8/007.
- [176] KIMBLE, H. J., DAGENAIS, M., and MANDEL, L.: *Photon Antibunching in Resonance Fluorescence*. Phys. Rev. Lett. **39**, 11 (1977). DOI: 10.1103/PhysRevLett.39.691.
- [177] KIMBLE, H. J. and MANDEL, L.: *Theory of resonance fluorescence*. Phys. Rev. A **13**, 6 (1976). DOI: 10.1103/PhysRevA.13.2123.
- [178] PAUL, H.: *Photon antibunching*. Rev. Mod. Phys. **54**, 4 (1982). DOI: 10.1103/RevModPhys.54.1061.
- [179] MOREAU, E., ROBERT, I., MANIN, L., THIERRY-MIEG, V., GÉRARD, J. M., and ABRAM, I.: *Quantum Cascade of Photons in Semiconductor Quantum Dots*. Phys. Rev. Lett. **87**, 18 (2001). DOI: 10.1103/PhysRevLett.87.183601.
- [180] KIRAZ, A., FÄLTH, S., BECHER, C., GAYRAL, B., SCHOENFELD, W. V., PETROFF, P. M., ZHANG, L., HU, E., and IMAMOĞLU, A.: *Photon correlation spectroscopy of a single quantum dot*. Phys. Rev. B **65**, 16 (2002). DOI: 10.1103/PhysRevB.65.161303.
- [181] SHIRANE, M., IGARASHI, Y., OTA, Y., NOMURA, M., KUMAGAI, N., OHKOUCHI, S., KIRIHARA, A., ISHIDA, S., IWAMOTO, S., YOROZU, S., and ARAKAWA, Y.: *Charged and neutral biexciton-exciton cascade in a single quantum dot within a photonic bandgap*. Physica E **42**, 10 (2010). DOI: 10.1016/j.physe.2010.02.031.
- [182] HE, Y.-M., IFF, O., LUNDT, N., BAUMANN, V., DAVANCO, M., SRINIVASAN, K., HÖFLING, S., and SCHNEIDER, C.: *Cascaded emission of single photons from the biexciton in monolayered WSe<sub>2</sub>*. Nat. Commun. **7** (2016). DOI: 10.1038/ncomms13409.
- [183] VERBERK, R. and ORRIT, M.: *Photon statistics in the fluorescence of single molecules and nanocrystals: Correlation functions versus distributions of on- and off-times*. J. Chem. Phys. **119**, 4 (2003). DOI: 10.1063/1.1582848.

- [184] GLÜCKERT, J. T.: *Optical Spectroscopy of Individual Single-Walled Carbon Nanotubes in an Electric Gate Structure: Tuning the Photoluminescence with Electric Fields*. Dissertation, Ludwig-Maximilians-Universität, München 2014. URN: urn:nbn:de:bvb:19-167678.
- [185] VOIGT, W.: *Doppelbrechung von im Magnetfelde befindlichem Natriumdampf in der Richtung normal zu den Kraftlinien*. Nachr. d. Kgl. Ges. d. Wiss. zu Göttingen, Math.-phys. Kl. **1898**, 4 (1898).
- [186] MANSURIPUR, M.: *The Faraday Effect*. Opt. Photonics News **10**, 11 (1999). DOI: 10.1364/OPN.10.11.000032.
- [187] LEFEBVRE, J., AUSTING, D. G., BOND, J., and FINNIE, P.: *Photoluminescence Imaging of Suspended Single-Walled Carbon Nanotubes*. Nano Lett. **6**, 8 (2006). DOI: 10.1021/nl060530e.
- [188] FINNIE, P., HOMMA, Y., and LEFEBVRE, J.: *Band-Gap Shift Transition in the Photoluminescence of Single-Walled Carbon Nanotubes*. Phys. Rev. Lett. **94**, 24 (2005). DOI: 10.1103/PhysRevLett.94.247401.
- [189] CAO, J., WANG, Q., and DAI, H.: *Electron transport in very clean, as-grown suspended carbon nanotubes*. Nat. Mater. **4**, 10 (2005). DOI: 10.1038/nmat1478.
- [190] FRANKLIN, A. D.: *The road to carbon nanotube transistors*. Nature **498**, 7455 (2013). DOI: 10.1038/498443a.
- [191] SANCHEZ-VALENCIA, J. R., DIENEL, T., GRÖNING, O., SHORUBALKO, I., MUELLER, A., JANSEN, M., AMSHAROV, K., RUFFIEUX, P., and FASEL, R.: *Controlled synthesis of single-chirality carbon nanotubes*. Nature **512**, 7512 (2014). DOI: 10.1038/nature13607.
- [192] YANG, F., WANG, X., ZHANG, D., YANG, J., LUO, D., XU, Z., WEI, J., WANG, J.-Q., XU, Z., PENG, F., LI, X., LI, R., LI, Y., LI, M., BAI, X., DING, F., and LI, Y.: *Chirality-specific growth of single-walled carbon nanotubes on solid alloy catalysts*. Nature **510**, 7506 (2014). DOI: 10.1038/nature13434.
- [193] AN, H., KUMAMOTO, A., TAKEZAKI, H., OHYAMA, S., QIAN, Y., INOUE, T., IKUHARA, Y., CHIASHI, S., XIANG, R., and MARUYAMA, S.: *Chirality specific and spatially uniform synthesis of single-walled carbon nanotubes from a sputtered Co-W bimetallic catalyst*. Nanoscale **8**, 30 (2016). DOI: 10.1039/C6NR02749K.
- [194] LIU, B., WU, F., GUI, H., ZHENG, M., and ZHOU, C.: *Chirality-Controlled Synthesis and Applications of Single-Wall Carbon Nanotubes*. ACS Nano **11**, 1 (2017). DOI: 10.1021/acsnano.6b06900.
- [195] ARNOLD, M. S., GREEN, A. A., HULVAT, J. F., STUPP, S. I., and HERSAM, M. C.: *Sorting carbon nanotubes by electronic structure using density differentiation*. Nat. Nanotechnol. **1**, 1 (2006). DOI: 10.1038/nnano.2006.52.

- [196] GHOSH, S., BACHILO, S. M., and WEISMAN, R. B.: *Advanced sorting of single-walled carbon nanotubes by nonlinear density-gradient ultracentrifugation*. Nat. Nanotechnol. **5**, 6 (2010). DOI: [10.1038/nnano.2010.68](https://doi.org/10.1038/nnano.2010.68).
- [197] HERSAM, M. C.: *Progress towards monodisperse single-walled carbon nanotubes*. Nat. Nanotechnol. **3**, 7 (2008). DOI: [10.1038/nnano.2008.135](https://doi.org/10.1038/nnano.2008.135).
- [198] LEFEBVRE, J., DING, J., LI, Z., FINNIE, P., LOPINSKI, G., and MALENFANT, P. R. L.: *High-Purity Semiconducting Single-Walled Carbon Nanotubes: A Key Enabling Material in Emerging Electronics*. Acc. Chem. Res. **50**, 10 (2017). DOI: [10.1021/acs.accounts.7b00234](https://doi.org/10.1021/acs.accounts.7b00234).
- [199] NISH, A., HWANG, J.-Y., DOIG, J., and NICHOLAS, R. J.: *Highly selective dispersion of single-walled carbon nanotubes using aromatic polymers*. Nat. Nanotechnol. **2**, 10 (2007). DOI: [10.1038/nnano.2007.290](https://doi.org/10.1038/nnano.2007.290).
- [200] HUI DUAN, W., WANG, Q., and COLLINS, E.: *Dispersion of carbon nanotubes with SDS surfactants: a study from a binding energy perspective*. Chem. Sci. **2**, 7 (2011). DOI: [10.1039/C0SC00616E](https://doi.org/10.1039/C0SC00616E).
- [201] VAISMAN, L., WAGNER, H. D., and MAROM, G.: *The role of surfactants in dispersion of carbon nanotubes*. Adv. Colloid Interface Sci. **128–130** (2006). DOI: [10.1016/j.cis.2006.11.007](https://doi.org/10.1016/j.cis.2006.11.007).
- [202] STREIT, J., SNYDER, C. R., CAMPO, J., ZHENG, M., SIMPSON, J. R., HIGHT WALKER, A. R., and FAGAN, J. A.: *Alkane Encapsulation Induces Strain in Small-Diameter Single-Wall Carbon Nanotubes*. J. Phys. Chem. C **122**, 21 (2018). DOI: [10.1021/acs.jpcc.8b03166](https://doi.org/10.1021/acs.jpcc.8b03166).
- [203] FAGAN, J. A., KHRIPIN, C. Y., BATISTA, C. A. S., SIMPSON, J. R., HÁROZ, E. H., WALKER, A. R. H., and ZHENG, M.: *Isolation of Specific Small-Diameter Single-Wall Carbon Nanotube Species via Aqueous Two-Phase Extraction*. Adv. Mater. **26**, 18 (2014). DOI: [10.1002/adma.201304873](https://doi.org/10.1002/adma.201304873).
- [204] FAGAN, J. A.: *Aqueous two-polymer phase extraction of single-wall carbon nanotubes using surfactants*. Nanoscale Adv. **1**, 9 (2019). DOI: [10.1039/C9NA00280D](https://doi.org/10.1039/C9NA00280D).
- [205] LIU, H., NISHIDE, D., TANAKA, T., and KATAURA, H.: *Large-scale single-chirality separation of single-wall carbon nanotubes by simple gel chromatography*. Nat. Commun. **2** (2011). DOI: [10.1038/ncomms1313](https://doi.org/10.1038/ncomms1313).
- [206] HOMMA, Y., SUZUKI, S., KOBAYASHI, Y., NAGASE, M., and TAKAGI, D.: *Mechanism of bright selective imaging of single-walled carbon nanotubes on insulators by scanning electron microscopy*. Appl. Phys. Lett. **84**, 10 (2004). DOI: [10.1063/1.1667608](https://doi.org/10.1063/1.1667608).
- [207] ZHANG, R. Y., WEI, Y., NAGAHARA, L. A., AMLANI, I., and TSUI, R. K.: *The contrast mechanism in low voltage scanning electron microscopy of single-walled carbon nanotubes*. Nanotechnology **17**, 1 (2005). DOI: [10.1088/0957-4484/17/1/046](https://doi.org/10.1088/0957-4484/17/1/046).

- [208] GOLDBERG, B. B., IPPOLITO, S. B., NOVOTNY, L., LIU, Z., and UNLU, M. S.: *Immersion lens microscopy of photonic nanostructures and quantum dots*. IEEE J. Sel. Top. Quantum Electron. **8**, 5 (2002). DOI: [10.1109/JSTQE.2002.804232](https://doi.org/10.1109/JSTQE.2002.804232).
- [209] LIU, Z., GOLDBERG, B. B., IPPOLITO, S. B., VAMIVAKAS, A. N., ÜNLÜ, M. S., and MIRIN, R.: *High resolution, high collection efficiency in numerical aperture increasing lens microscopy of individual quantum dots*. Appl. Phys. Lett. **87**, 7 (2005). DOI: [10.1063/1.2012532](https://doi.org/10.1063/1.2012532).
- [210] RAYLEIGH, F. R. S.: XXXI. *Investigations in optics, with special reference to the spectroscope*. Lond. Edinb. Dubl. Philos. Mag. J. Sci. **8**, 49 (1879). DOI: [10.1080/14786447908639684](https://doi.org/10.1080/14786447908639684).
- [211] LUAN, L., SIEVERT, P. R., WATKINS, B., MU, W., HONG, Z., and KETTERSON, J. B.: *Angular radiation pattern of electric dipoles embedded in a thin film in the vicinity of a dielectric half space*. Appl. Phys. Lett. **89**, 3 (2006). DOI: [10.1063/1.2234299](https://doi.org/10.1063/1.2234299).
- [212] KARRAI, K., LORENZ, X., and NOVOTNY, L.: *Enhanced reflectivity contrast in confocal solid immersion lens microscopy*. Appl. Phys. Lett. **77**, 21 (2000). DOI: [10.1063/1.1326839](https://doi.org/10.1063/1.1326839).
- [213] KOYAMA, K., YOSHITA, M., BABA, M., SUEMOTO, T., and AKIYAMA, H.: *High collection efficiency in fluorescence microscopy with a solid immersion lens*. Appl. Phys. Lett. **75**, 12 (1999). DOI: [10.1063/1.124833](https://doi.org/10.1063/1.124833).
- [214] LEE, K. G., CHEN, X. W., EGHLEI, H., KUKURA, P., LETTOW, R., RENN, A., SANDOGHDAR, V., and GÖTZINGER, S.: *A planar dielectric antenna for directional single-photon emission and near-unity collection efficiency*. Nat. Photon. **5**, 3 (2011). DOI: [10.1038/nphoton.2010.312](https://doi.org/10.1038/nphoton.2010.312).
- [215] HELLEN, E. H. and AXELROD, D.: *Fluorescence emission at dielectric and metal-film interfaces*. J. Opt. Soc. Am. B **4**, 3 (1987). DOI: [10.1364/JOSAB.4.000337](https://doi.org/10.1364/JOSAB.4.000337).
- [216] NUTZ, M.: *Optoelectronic Studies of Molybdenum Disulfide Field-Effect Devices*. Master's Thesis, Ludwig-Maximilians-Universität, München 2014.
- [217] FORD, G. W. and WEBER, W. H.: *Electromagnetic interactions of molecules with metal surfaces*. Phys. Rep. **113**, 4 (1984). DOI: [10.1016/0370-1573\(84\)90098-X](https://doi.org/10.1016/0370-1573(84)90098-X).
- [218] COGNET, L., TSYBOULSKI, D. A., ROCHA, J.-D. R., DOYLE, C. D., TOUR, J. M., and WEISMAN, R. B.: *Stepwise Quenching of Exciton Fluorescence in Carbon Nanotubes by Single-Molecule Reactions*. Science **316**, 5830 (2007). DOI: [10.1126/science.1141316](https://doi.org/10.1126/science.1141316).
- [219] YOSHIKAWA, K., MATSUDA, K., and KANEMITSU, Y.: *Exciton Transport in Suspended Single Carbon Nanotubes Studied by Photoluminescence Imaging Spectroscopy*. J. Phys. Chem. C **114**, 10 (2010). DOI: [10.1021/jp911518h](https://doi.org/10.1021/jp911518h).

- 
- [220] XIE, J., INABA, T., SUGIYAMA, R., and HOMMA, Y.: *Intrinsic diffusion length of excitons in long single-walled carbon nanotubes from photoluminescence spectra*. Phys. Rev. B **85**, 8 (2012). DOI: 10.1103/PhysRevB.85.085434.
- [221] CROCHET, J. J., DUQUE, J. G., WERNER, J. H., LOUNIS, B., COGNET, L., and DOORN, S. K.: *Disorder Limited Exciton Transport in Colloidal Single-Wall Carbon Nanotubes*. Nano Lett. **12**, 10 (2012). DOI: 10.1021/nl301739d.
- [222] ISHII, A., YOSHIDA, M., and KATO, Y. K.: *Exciton diffusion, end quenching, and exciton-exciton annihilation in individual air-suspended carbon nanotubes*. Phys. Rev. B **91**, 12 (2015). DOI: 10.1103/PhysRevB.91.125427.
- [223] HÖGELE, A., NOÉ, J. C., HOFMANN, M. S., and GLÜCKERT, J. T.: *Cryogenic Spectroscopy of Carbon Nanotubes: The Role of Exciton Localization*. In: *Handbook of Carbon Nanomaterials* **9**, pp. 223–268. Ed. by WEISMAN, R. B. and KONO, J. Red. by d'SOUZA, F. and KADISH, K. M. World Scientific Series on Carbon Nanoscience. World Scientific, Singapore 2017. DOI: 10.1142/10862.
- [224] JEANTET, A., CHASSAGNEUX, Y., RAYNAUD, C., ROUSSIGNOL, P., LAURET, J. S., BESGA, B., ESTÈVE, J., REICHEL, J., and VOISIN, C.: *Widely Tunable Single-Photon Source from a Carbon Nanotube in the Purcell Regime*. Phys. Rev. Lett. **116**, 24 (2016). DOI: 10.1103/PhysRevLett.116.247402.
- [225] HAGEN, A., STEINER, M., RASCHKE, M. B., LIENAU, C., HERTEL, T., QIAN, H., MEIXNER, A. J., and HARTSCHUH, A.: *Exponential Decay Lifetimes of Excitons in Individual Single-Walled Carbon Nanotubes*. Phys. Rev. Lett. **95**, 19 (2005). DOI: 10.1103/PhysRevLett.95.197401.
- [226] KRUMMHEUER, B., AXT, V. M., and KUHN, T.: *Theory of pure dephasing and the resulting absorption line shape in semiconductor quantum dots*. Phys. Rev. B **65**, 19 (2002). DOI: 10.1103/PhysRevB.65.195313.
- [227] GALLAND, C., HÖGELE, A., TÜRECI, H. E., and IMAMOĞLU, A.: *Non-Markovian Decoherence of Localized Nanotube Excitons by Acoustic Phonons*. Phys. Rev. Lett. **101**, 6 (2008). DOI: 10.1103/PhysRevLett.101.067402.
- [228] WILSON-RAE, I., GALLAND, C., ZWERGER, W., and IMAMOĞLU, A.: *Exciton-assisted optomechanics with suspended carbon nanotubes*. New J. Phys. **14**, 11 (2012). DOI: 10.1088/1367-2630/14/11/115003.
- [229] SARPKEYA, I., AHMADI, E. D., SHEPARD, G. D., MISTRY, K. S., BLACKBURN, J. L., and STRAUF, S.: *Strong Acoustic Phonon Localization in Copolymer-Wrapped Carbon Nanotubes*. ACS Nano **9**, 6 (2015). DOI: 10.1021/acsnano.5b01997.

- [230] JEANTET, A., CHASSAGNEUX, Y., CLAUDE, T., LAURET, J. S., and VOISIN, C.: *Interplay of spectral diffusion and phonon-broadening in individual photo-emitters: the case of carbon nanotubes*. *Nanoscale* **10**, 2 (2018). DOI: [10.1039/C7NR05861F](https://doi.org/10.1039/C7NR05861F).
- [231] FRÖHLICH, H., PELZER, H., and ZIENAU, S.: *XX. Properties of slow electrons in polar materials*. *Lond. Edinb. Dubl. Philos. Mag. J. Sci.* **41**, 314 (1950). DOI: [10.1080/14786445008521794](https://doi.org/10.1080/14786445008521794).
- [232] FRÖHLICH, H.: *Electrons in lattice fields*. *Adv. Phys.* **3**, 11 (1954). DOI: [10.1080/00018735400101213](https://doi.org/10.1080/00018735400101213).
- [233] YU, P. Y. and CARDONA, M.: *Fundamentals of Semiconductors*. Springer, Berlin, Heidelberg 2005.
- [234] HOLSTEIN, T.: *Studies of polaron motion: Part I. The molecular-crystal model*. *Ann. Phys. (N. Y.)* **8**, 3 (1959). DOI: [10.1016/0003-4916\(59\)90002-8](https://doi.org/10.1016/0003-4916(59)90002-8).
- [235] HOLSTEIN, T.: *Studies of polaron motion: Part II. The "small" polaron*. *Ann. Phys. (N. Y.)* **8**, 3 (1959). DOI: [10.1016/0003-4916\(59\)90003-X](https://doi.org/10.1016/0003-4916(59)90003-X).
- [236] WILSON, E. B., DECIUS, J. C., and CROSS, P. C.: *Molecular Vibrations: The Theory of Infrared and Raman Vibrational Spectra*. McGraw-Hill Book Company, New York, Toronto, London 1955.
- [237] ARDIZZONE, V., CHASSAGNEUX, Y., VIALLA, F., DELPORT, G., DELCAMP, C., BELABAS, N., DELEPORTE, E., ROUSSIGNOL, P., ROBERT-PHILIP, I., VOISIN, C., and LAURET, J. S.: *Strong reduction of exciton-phonon coupling in single-wall carbon nanotubes of high crystalline quality: Insight into broadening mechanisms and exciton localization*. *Phys. Rev. B* **91**, 12 (2015). DOI: [10.1103/PhysRevB.91.121410](https://doi.org/10.1103/PhysRevB.91.121410).
- [238] MA, X., ADAMSKA, L., YAMAGUCHI, H., YALCIN, S. E., TRETIAK, S., DOORN, S. K., and HTOON, H.: *Electronic Structure and Chemical Nature of Oxygen Dopant States in Carbon Nanotubes*. *ACS Nano* **8**, 10 (2014). DOI: [10.1021/nn504553y](https://doi.org/10.1021/nn504553y).
- [239] VAGOV, A., AXT, V. M., and KUHN, T.: *Electron-phonon dynamics in optically excited quantum dots: Exact solution for multiple ultrashort laser pulses*. *Phys. Rev. B* **66**, 16 (2002). DOI: [10.1103/PhysRevB.66.165312](https://doi.org/10.1103/PhysRevB.66.165312).
- [240] PENNINGTON, G., GOLDSMAN, N., AKTURK, A., and WICKENDEN, A. E.: *Deformation potential carrier-phonon scattering in semiconducting carbon nanotube transistors*. *Appl. Phys. Lett.* **90**, 6 (2007). DOI: [10.1063/1.2437127](https://doi.org/10.1063/1.2437127).
- [241] NOÉ, J. C.: *Environmental effects in the photophysics of cryogenic carbon nanotubes*. Dissertation, Ludwig-Maximilians-Universität, München 2019. URN: [urn:nbn:de:bvb:19-240029](https://nbn-resolving.org/urn:nbn:de:bvb:19-240029).

- 
- [242] HOPFIELD, J. J.: *Theory of the Contribution of Excitons to the Complex Dielectric Constant of Crystals*. Phys. Rev. **112**, 5 (1958). DOI: [10.1103/PhysRev.112.1555](https://doi.org/10.1103/PhysRev.112.1555).
- [243] GERACE, D. and ANDREANI, L. C.: *Quantum theory of exciton-photon coupling in photonic crystal slabs with embedded quantum wells*. Phys. Rev. B **75**, 23 (2007). DOI: [10.1103/PhysRevB.75.235325](https://doi.org/10.1103/PhysRevB.75.235325).
- [244] PANZARINI, G. and ANDREANI, L. C.: *Quantum theory of exciton polaritons in cylindrical semiconductor microcavities*. Phys. Rev. B **60**, 24 (1999). DOI: [10.1103/PhysRevB.60.16799](https://doi.org/10.1103/PhysRevB.60.16799).
- [245] HILBORN, R. C.: *Einstein coefficients, cross sections,  $f$  values, dipole moments, and all that*. Am. J. Phys. **50**, 11 (1982). DOI: [10.1119/1.12937](https://doi.org/10.1119/1.12937).
- [246] JACKSON, J. D.: *Classical Electrodynamics*. 3<sup>rd</sup> ed. Wiley, New York, Chichester, Weinheim, Brisbane, Singapore, Toronto 1998.
- [247] STOKES, G. G.: *On the Change of Refrangibility of Light*. In: *Philosophical Transactions of the Royal Society of London for the year MDCCCLII 1*, pp. 463–561. Richard Taylor and William Francis, London 1852.
- [248] THOMAS, D. C. and CHRISTIAN, S. D.: *Micellar and surface behavior of sodium deoxycholate characterized by surface tension and ellipsometric methods*. J. Colloid Interface Sci. **78**, 2 (1980). DOI: [10.1016/0021-9797\(80\)90585-8](https://doi.org/10.1016/0021-9797(80)90585-8).
- [249] MA, X., CAMBRÉ, S., WENSELEERS, W., DOORN, S. K., and HTOON, H.: *Quasiphase Transition in a Single File of Water Molecules Encapsulated in (6, 5) Carbon Nanotubes Observed by Temperature-Dependent Photoluminescence Spectroscopy*. Phys. Rev. Lett. **118**, 2 (2017). DOI: [10.1103/PhysRevLett.118.027402](https://doi.org/10.1103/PhysRevLett.118.027402).
- [250] STAVRINO, P. N., RYU, G., CAMPOY-QUILES, M., and BRADLEY, D. D. C.: *The change in refractive index of poly(9,9-dioctylfluorene) due to the adoption of the  $\beta$ -phase chain conformation*. J. Phys. Condens. Matter **19**, 46 (2007). DOI: [10.1088/0953-8984/19/46/466107](https://doi.org/10.1088/0953-8984/19/46/466107).
- [251] PEREVEDENTSEV, A., SONNEFRAUD, Y., BELTON, C. R., SHARMA, S., CASS, A. E. G., MAIER, S. A., KIM, J.-S., STAVRINO, P. N., and BRADLEY, D. D. C.: *Dip-pen patterning of poly(9,9-dioctylfluorene) chain-conformation-based nano-photonic elements*. Nat. Commun. **6** (2015).
- [252] YANG, L. and HAN, J.: *Electronic Structure of Deformed Carbon Nanotubes*. Phys. Rev. Lett. **85**, 1 (2000). DOI: [10.1103/PhysRevLett.85.154](https://doi.org/10.1103/PhysRevLett.85.154).
- [253] HUANG, M., WU, Y., CHANDRA, B., YAN, H., SHAN, Y., HEINZ, T. F., and HONE, J.: *Direct Measurement of Strain-Induced Changes in the Band Structure of Carbon Nanotubes*. Phys. Rev. Lett. **100**, 13 (2008). DOI: [10.1103/PhysRevLett.100.136803](https://doi.org/10.1103/PhysRevLett.100.136803).

- [254] GAO, J., LOI, M. A., de CARVALHO, E. J. F., and dos SANTOS, M. C.: *Selective Wrapping and Supramolecular Structures of Polyfluorene-Carbon Nanotube Hybrids*. ACS Nano **5**, 5 (2011). DOI: [10.1021/nn200564n](https://doi.org/10.1021/nn200564n).
- [255] GOMULYA, W., GAO, J., and LOI, M. A.: *Conjugated polymer-wrapped carbon nanotubes: physical properties and device applications*. Eur. Phys. J. B **86**, 10 (2013). DOI: [10.1140/epjb/e2013-40707-9](https://doi.org/10.1140/epjb/e2013-40707-9).
- [256] YANG, H., BEZUGLY, V., KUNSTMANN, J., FILORAMO, A., and CUNIBERTI, G.: *Diameter-Selective Dispersion of Carbon Nanotubes via Polymers: A Competition between Adsorption and Bundling*. ACS Nano **9**, 9 (2015). DOI: [10.1021/acsnano.5b03051](https://doi.org/10.1021/acsnano.5b03051).
- [257] PERDEW, J. P.: *Density-functional approximation for the correlation energy of the inhomogeneous electron gas*. Phys. Rev. B **33**, 12 (1986). DOI: [10.1103/PhysRevB.33.8822](https://doi.org/10.1103/PhysRevB.33.8822).
- [258] BECKE, A. D.: *Density-functional exchange-energy approximation with correct asymptotic behavior*. Phys. Rev. A **38**, 6 (1988). DOI: [10.1103/PhysRevA.38.3098](https://doi.org/10.1103/PhysRevA.38.3098).
- [259] PERDEW, J. P.: *Erratum: Density-functional approximation for the correlation energy of the inhomogeneous electron gas [Phys. Rev. B 33, 8822 (1986)]*. Phys. Rev. B **34**, 10 (1986). DOI: [10.1103/PhysRevB.34.7406.3](https://doi.org/10.1103/PhysRevB.34.7406.3).
- [260] BECKE, A. D.: *Density-functional thermochemistry. III. The role of exact exchange*. J. Chem. Phys. **98**, 7 (1993). DOI: [10.1063/1.464913](https://doi.org/10.1063/1.464913).
- [261] STEPHENS, P. J., DEVLIN, F. J., CHABALOWSKI, C. F., and FRISCH, M. J.: *Ab Initio Calculation of Vibrational Absorption and Circular Dichroism Spectra Using Density Functional Force Fields*. J. Phys. Chem. **98**, 45 (1994). DOI: [10.1021/j100096a001](https://doi.org/10.1021/j100096a001).
- [262] HTOON, H., O'CONNELL, M. J., DOORN, S. K., and KLIMOV, V. I.: *Single Carbon Nanotubes Probed by Photoluminescence Excitation Spectroscopy: The Role of Phonon-Assisted Transitions*. Phys. Rev. Lett. **94**, 12 (2005). DOI: [10.1103/PhysRevLett.94.127403](https://doi.org/10.1103/PhysRevLett.94.127403).
- [263] RUDIN, S., REINECKE, T. L., and BAYER, M.: *Temperature dependence of optical linewidth in single InAs quantum dots*. Phys. Rev. B **74**, 16 (2006). DOI: [10.1103/PhysRevB.74.161305](https://doi.org/10.1103/PhysRevB.74.161305).
- [264] STOCK, E., DACHNER, M.-R., WARMING, T., SCHLIWA, A., LOCHMANN, A., HOFFMANN, A., TOROPOV, A. I., BAKAROV, A. K., DEREBEZOV, I. A., RICHTER, M., HAISLER, V. A., KNORR, A., and BIMBERG, D.: *Acoustic and optical phonon scattering in a single In(Ga)As quantum dot*. Phys. Rev. B **83**, 4 (2011). DOI: [10.1103/PhysRevB.83.041304](https://doi.org/10.1103/PhysRevB.83.041304).
- [265] GRIMME, S.: *Supramolecular Binding Thermodynamics by Dispersion-Corrected Density Functional Theory*. Chem. Eur. J. **18**, 32 (2012). DOI: [10.1002/chem.201200497](https://doi.org/10.1002/chem.201200497).

- [266] SYNDER, R. G. and SCHACHTSCHNEIDER, J. H.: *A valence force field for saturated hydrocarbons*. Spectrochim. Acta **21**, 1 (1965). DOI: 10.1016/0371-1951(65)80115-1.
- [267] SHARP, K. and MATSCHINSKY, F.: *Translation of Ludwig Boltzmann's Paper "On the Relationship between the Second Fundamental Theorem of the Mechanical Theory of Heat and Probability Calculations Regarding the Conditions for Thermal Equilibrium"* *Sitzungsberichte der Kaiserlichen Akademie der Wissenschaften. Mathematisch-Naturwissen Classe. Abt. II, LXXVI 1877, pp 373-435 (Wien. Ber. 1877, 76:373-435). Reprinted in Wiss. Abhandlungen, Vol. II, reprint 42, p. 164-223, Barth, Leipzig, 1909.* Entropy **17**, 4 (2015). DOI: 10.3390/e17041971.
- [268] BAYER, M. and FORCHEL, A.: *Temperature dependence of the exciton homogeneous linewidth in  $In_{0.60}Ga_{0.40}As/GaAs$  self-assembled quantum dots*. Phys. Rev. B **65**, 4 (2002). DOI: 10.1103/PhysRevB.65.041308.
- [269] RUDIN, S., REINECKE, T. L., and SEGALL, B.: *Temperature-dependent exciton linewidths in semiconductors*. Phys. Rev. B **42**, 17 (1990). DOI: 10.1103/PhysRevB.42.11218.
- [270] FAVERO, I., CASSABOIS, G., FERREIRA, R., DARSON, D., VOISIN, C., TIGNON, J., DELALANDE, C., BASTARD, G., ROUSSIGNOL, P., and GÉRARD, J. M.: *Acoustic phonon sidebands in the emission line of single InAs/GaAs quantum dots*. Phys. Rev. B **68**, 23 (2003). DOI: 10.1103/PhysRevB.68.233301.
- [271] KAMMERER, C., VOISIN, C., CASSABOIS, G., DELALANDE, C., ROUSSIGNOL, P., KLOPF, F., REITHMAIER, J. P., FORCHEL, A., and GÉRARD, J. M.: *Line narrowing in single semiconductor quantum dots: Toward the control of environment effects*. Phys. Rev. B **66**, 4 (2002). DOI: 10.1103/PhysRevB.66.041306.
- [272] ARAUJO, P. T., MACIEL, I. O., PESCE, P. B. C., PIMENTA, M. A., DOORN, S. K., QIAN, H., HARTSCHUH, A., STEINER, M., GRIGORIAN, L., HATA, K., and JORIO, A.: *Nature of the constant factor in the relation between radial breathing mode frequency and tube diameter for single-wall carbon nanotubes*. Phys. Rev. B **77**, 24 (2008). DOI: 10.1103/PhysRevB.77.241403.
- [273] LIM, Y.-S., NUGRAHA, A. R. T., CHO, S.-J., NOH, M.-Y., YOON, E.-J., LIU, H., KIM, J.-H., TELG, H., HÁROZ, E. H., SANDERS, G. D., BAIK, S.-H., KATAURA, H., DOORN, S. K., STANTON, C. J., SAITO, R., KONO, J., and JOO, T.: *Ultrafast Generation of Fundamental and Multiple-Order Phonon Excitations in Highly Enriched (6, 5) Single-Wall Carbon Nanotubes*. Nano Lett. **14**, 3 (2014). DOI: 10.1021/nl404536b.
- [274] TOBIN, R. G.: *Vibrational linewidths of adsorbed molecules: Experimental considerations and results*. Surf. Sci. **183**, 1 (1987). DOI: 10.1016/S0039-6028(87)80347-3.

- [275] LAZZERI, M., PISCANEC, S., MAURI, F., FERRARI, A. C., and ROBERTSON, J.: *Phonon linewidths and electron-phonon coupling in graphite and nanotubes*. Phys. Rev. B **73**, 15 (2006). DOI: [10.1103/PhysRevB.73.155426](https://doi.org/10.1103/PhysRevB.73.155426).
- [276] BIRKEDAL, D., LEOSON, K., and HVAM, J. M.: *Long Lived Coherence in Self-Assembled Quantum Dots*. Phys. Rev. Lett. **87**, 22 (2001). DOI: [10.1103/PhysRevLett.87.227401](https://doi.org/10.1103/PhysRevLett.87.227401).
- [277] GAMMON, D., RUDIN, S., REINECKE, T. L., KATZER, D. S., and KYONO, C. S.: *Phonon broadening of excitons in GaAs/Al<sub>x</sub>Ga<sub>1-x</sub>As quantum wells*. Phys. Rev. B **51**, 23 (1995). DOI: [10.1103/PhysRevB.51.16785](https://doi.org/10.1103/PhysRevB.51.16785).
- [278] ROBINSON, H. D. and GOLDBERG, B. B.: *Light-induced spectral diffusion in single self-assembled quantum dots*. Phys. Rev. B **61**, 8 (2000). DOI: [10.1103/PhysRevB.61.R5086](https://doi.org/10.1103/PhysRevB.61.R5086).
- [279] LIFSHITZ, E.: *Evidence in Support of Exciton to Ligand Vibrational Coupling in Colloidal Quantum Dots*. J. Phys. Chem. Lett. **6**, 21 (2015). DOI: [10.1021/acs.jpcllett.5b01567](https://doi.org/10.1021/acs.jpcllett.5b01567).
- [280] HARRAH, D. M. and SWAN, A. K.: *The Role of Length and Defects on Optical Quantum Efficiency and Exciton Decay Dynamics in Single-Walled Carbon Nanotubes*. ACS Nano **5**, 1 (2011). DOI: [10.1021/nn1031214](https://doi.org/10.1021/nn1031214).
- [281] MA, X., BALDWIN, J. K. S., HARTMANN, N. F., DOORN, S. K., and HTOON, H.: *Solid-State Approach for Fabrication of Photostable, Oxygen-Doped Carbon Nanotubes*. Adv. Funct. Mater. **25**, 39 (2015). DOI: [10.1002/adfm.201502580](https://doi.org/10.1002/adfm.201502580).
- [282] DRESSELHAUS, M. S., DRESSELHAUS, G., and JORIO, A.: *Raman Spectroscopy of Carbon Nanotubes in 1997 and 2007*. J. Phys. Chem. C **111**, 48 (2007). DOI: [10.1021/jp071378n](https://doi.org/10.1021/jp071378n).
- [283] DILLON, A. C., PARILLA, P. A., ALLEMAN, J. L., GENNETT, T., JONES, K. M., and HEBEN, M. J.: *Systematic inclusion of defects in pure carbon single-wall nanotubes and their effect on the Raman D-band*. Chem. Phys. Lett. **401**, 4 (2005). DOI: [10.1016/j.cplett.2004.11.104](https://doi.org/10.1016/j.cplett.2004.11.104).
- [284] KÜRTI, J., ZÓLYOMI, V., GRÜNEIS, A., and KUZMANY, H.: *Double resonant Raman phenomena enhanced by van Hove singularities in single-wall carbon nanotubes*. Phys. Rev. B **65**, 16 (2002). DOI: [10.1103/PhysRevB.65.165433](https://doi.org/10.1103/PhysRevB.65.165433).
- [285] KOYAMA, T., SHIMIZU, S., MIYATA, Y., SHINOHARA, H., and NAKAMURA, A.: *Ultrafast formation and decay dynamics of trions in p-doped single-walled carbon nanotubes*. Phys. Rev. B **87**, 16 (2013). DOI: [10.1103/PhysRevB.87.165430](https://doi.org/10.1103/PhysRevB.87.165430).

- [286] BROZENA, A. H., LEEDS, J. D., ZHANG, Y., FOURKAS, J. T., and WANG, Y.: *Controlled Defects in Semiconducting Carbon Nanotubes Promote Efficient Generation and Luminescence of Trions*. ACS Nano **8**, 5 (2014). DOI: [10.1021/nn500894p](https://doi.org/10.1021/nn500894p).
- [287] TAFT, R. W.: *Linear Free Energy Relationships from Rates of Esterification and Hydrolysis of Aliphatic and Ortho-substituted Benzoate Esters*. J. Am. Chem. Soc. **74**, 11 (1952). DOI: [10.1021/ja01131a010](https://doi.org/10.1021/ja01131a010).
- [288] TAFT, R. W.: *Polar and Steric Substituent Constants for Aliphatic and o-Benzoate Groups from Rates of Esterification and Hydrolysis of Esters*. J. Am. Chem. Soc. **74**, 12 (1952). DOI: [10.1021/ja01132a049](https://doi.org/10.1021/ja01132a049).
- [289] TAFT, R. W.: *Linear Steric Energy Relationships*. J. Am. Chem. Soc. **75**, 18 (1953). DOI: [10.1021/ja01114a044](https://doi.org/10.1021/ja01114a044).
- [290] HANSCH, C., LEO, A., and TAFT, R. W.: *A survey of Hammett substituent constants and resonance and field parameters*. Chem. Rev. **91**, 2 (1991). DOI: [10.1021/cr00002a004](https://doi.org/10.1021/cr00002a004).
- [291] CHERKASOV, A. R., GALKIN, V. I., and CHERKASOV, R. A.: *The problem of the quantitative evaluation of the inductive effect: correlation analysis*. Russ. Chem. Rev. **65**, 8 (1996). DOI: [10.1070/RC1996v065n08ABEH000227](https://doi.org/10.1070/RC1996v065n08ABEH000227).
- [292] HARTMANN, N. F., VELIZHANIN, K. A., HAROZ, E. H., KIM, M., MA, X., WANG, Y., HTOON, H., and DOORN, S. K.: *Photoluminescence Dynamics of Aryl  $sp^3$  Defect States in Single-Walled Carbon Nanotubes*. ACS Nano **10**, 9 (2016). DOI: [10.1021/acsnano.6b02986](https://doi.org/10.1021/acsnano.6b02986).
- [293] GOKUS, T., HARTSCHUH, A., HARUTYUNYAN, H., ALLEGRINI, M., HENNRICH, F., KAPPES, M., GREEN, A. A., HERSAM, M. C., ARAÚJO, P. T., and JORIO, A.: *Exciton decay dynamics in individual carbon nanotubes at room temperature*. Appl. Phys. Lett. **92**, 15 (2008). DOI: [10.1063/1.2913009](https://doi.org/10.1063/1.2913009).
- [294] DUQUE, J. G., PASQUALI, M., COGNET, L., and LOUNIS, B.: *Environmental and Synthesis-Dependent Luminescence Properties of Individual Single-Walled Carbon Nanotubes*. ACS Nano **3**, 8 (2009). DOI: [10.1021/nn9003956](https://doi.org/10.1021/nn9003956).
- [295] BERCIAUD, S., COGNET, L., and LOUNIS, B.: *Luminescence Decay and the Absorption Cross Section of Individual Single-Walled Carbon Nanotubes*. Phys. Rev. Lett. **101**, 7 (2008). DOI: [10.1103/PhysRevLett.101.077402](https://doi.org/10.1103/PhysRevLett.101.077402).
- [296] GOKUS, T., COGNET, L., DUQUE, J. G., PASQUALI, M., HARTSCHUH, A., and LOUNIS, B.: *Mono- and Biexponential Luminescence Decays of Individual Single-Walled Carbon Nanotubes*. J. Phys. Chem. C **114**, 33 (2010). DOI: [10.1021/jp1049217](https://doi.org/10.1021/jp1049217).
- [297] LEFEBVRE, J., FRASER, J. M., FINNIE, P., and HOMMA, Y.: *Photoluminescence from an individual single-walled carbon nanotube*. Phys. Rev. B **69**, 7 (2004). DOI: [10.1103/PhysRevB.69.075403](https://doi.org/10.1103/PhysRevB.69.075403).

- [298] ZEEMAN, P.: *On the influence of magnetism on the nature of the light emitted by a substance*. Lond. Edinb. Dubl. Philos. Mag. J. Sci. **43**, 262 (1897). DOI: [10.1080/14786449708620985](https://doi.org/10.1080/14786449708620985).
- [299] ZEEMAN, P.: *The Effect of Magnetisation on the Nature of Light Emitted by a Substance*. Nature **55**, 1424 (1897). DOI: [10.1038/055347a0](https://doi.org/10.1038/055347a0).
- [300] KUEMMETH, F., ILANI, S., RALPH, D. C., and MCEUEN, P. L.: *Coupling of spin and orbital motion of electrons in carbon nanotubes*. Nature **452**, 7186 (2008). DOI: [10.1038/nature06822](https://doi.org/10.1038/nature06822).
- [301] LI, Y., LUDWIG, J., LOW, T., CHERNIKOV, A., CUI, X., AREFE, G., KIM, Y. D., van der ZANDE, A. M., RIGOSI, A., HILL, H. M., KIM, S. H., HONE, J., LI, Z., SMIRNOV, D., and HEINZ, T. F.: *Valley Splitting and Polarization by the Zeeman Effect in Monolayer MoSe<sub>2</sub>*. Phys. Rev. Lett. **113**, 26 (2014). DOI: [10.1103/PhysRevLett.113.266804](https://doi.org/10.1103/PhysRevLett.113.266804).
- [302] SRIVASTAVA, A., SIDLER, M., ALLAIN, A. V., LEMBKE, D. S., KIS, A., and IMAMOĞLU, A.: *Valley Zeeman effect in elementary optical excitations of monolayer WSe<sub>2</sub>*. Nat. Phys. **11**, 2 (2015). DOI: [10.1038/nphys3203](https://doi.org/10.1038/nphys3203).
- [303] JARILLO-HERRERO, P., SAPMAZ, S., DEKKER, C., KOUWENHOVEN, L. P., and ZANT, H. S. J. van der: *Electron-hole symmetry in a semiconducting carbon nanotube quantum dot*. Nature **429**, 6990 (2004). DOI: [10.1038/nature02568](https://doi.org/10.1038/nature02568).
- [304] DENG, S., ZHANG, Y., BROZENA, A. H., MAYES, M. L., BANERJEE, P., CHIOU, W.-A., RUBLOFF, G. W., SCHATZ, G. C., and WANG, Y.: *Confined propagation of covalent chemical reactions on single-walled carbon nanotubes*. Nat. Commun. **2** (2011). DOI: [10.1038/ncomms1384](https://doi.org/10.1038/ncomms1384).
- [305] GIFFORD, B. J., HE, X., KIM, M., KWON, H., SAHA, A., SIFAIN, A. E., WANG, Y., HTOON, H., KILINA, S., DOORN, S. K., and TRETIAK, S.: *Optical Effects of Divalent Functionalization of Carbon Nanotubes*. Chem. Mater. **31**, 17 (2019). DOI: [10.1021/acs.chemmater.9b01438](https://doi.org/10.1021/acs.chemmater.9b01438).
- [306] SANTORI, C., PELTON, M., SOLOMON, G., DALE, Y., and YAMAMOTO, Y.: *Triggered Single Photons from a Quantum Dot*. Phys. Rev. Lett. **86**, 8 (2001). DOI: [10.1103/PhysRevLett.86.1502](https://doi.org/10.1103/PhysRevLett.86.1502).
- [307] SANTORI, C., FATTAL, D., VUČKOVIĆ, J., SOLOMON, G. S., WAKS, E., and YAMAMOTO, Y.: *Submicrosecond correlations in photoluminescence from InAs quantum dots*. Phys. Rev. B **69**, 20 (2004). DOI: [10.1103/PhysRevB.69.205324](https://doi.org/10.1103/PhysRevB.69.205324).
- [308] SALLEN, G., TRIBU, A., AICHELE, T., ANDRÉ, R., BESOMBES, L., BOUGEROL, C., RICHARD, M., TATARENKO, S., KHENG, K., and POIZAT, J.-P.: *Subnanosecond spectral diffusion measurement using photon correlation*. Nat. Photon. **4**, 10 (2010). DOI: [10.1038/nphoton.2010.174](https://doi.org/10.1038/nphoton.2010.174).

- [309] PIĘTKA, B., SUFFCZYŃSKI, J., GORYCA, M., KAZIMIERCZUK, T., GOLNIK, A., KOSSACKI, P., WYSMOLEK, A., GAJ, J. A., STEPNIIEWSKI, R., and POTEMSKI, M.: *Photon correlation studies of charge variation in a single GaAlAs quantum dot*. Phys. Rev. B **87**, 3 (2013). DOI: [10.1103/PhysRevB.87.035310](https://doi.org/10.1103/PhysRevB.87.035310).
- [310] CHANG, W.-H., CHANG, H.-S., CHEN, W.-Y., HSU, T. M., HSIEH, T.-P., CHYI, J.-I., and YEH, N.-T.: *Optical control of the exciton charge states of single quantum dots via impurity levels*. Phys. Rev. B **72**, 23 (2005). DOI: [10.1103/PhysRevB.72.233302](https://doi.org/10.1103/PhysRevB.72.233302).
- [311] QIN, H., MENG, R., WANG, N., and PENG, X.: *Photoluminescence Intermittency and Photo-Bleaching of Single Colloidal Quantum Dot*. Adv. Mater. **29**, 14 (2017). DOI: [10.1002/adma.201606923](https://doi.org/10.1002/adma.201606923).
- [312] MENG, R., QIN, H., NIU, Y., FANG, W., YANG, S., LIN, X., CAO, H., MA, J., LIN, W., TONG, L., and PENG, X.: *Charging and Discharging Channels in Photoluminescence Intermittency of Single Colloidal CdSe/CdS Core/Shell Quantum Dot*. J. Phys. Chem. Lett. **7**, 24 (2016). DOI: [10.1021/acs.jpcllett.6b02448](https://doi.org/10.1021/acs.jpcllett.6b02448).
- [313] ISHII, A., UDA, T., and KATO, Y. K.: *Room-Temperature Single-Photon Emission from Micrometer-Long Air-Suspended Carbon Nanotubes*. Phys. Rev. Appl. **8**, 5 (2017). DOI: [10.1103/PhysRevApplied.8.054039](https://doi.org/10.1103/PhysRevApplied.8.054039).
- [314] LUO, Y., AHMADI, E. D., SHAYAN, K., MA, Y., MISTRY, K. S., ZHANG, C., HONE, J., BLACKBURN, J. L., and STRAUF, S.: *Purcell-enhanced quantum yield from carbon nanotube excitons coupled to plasmonic nanocavities*. Nat. Commun. **8**, 1 (2017). DOI: [10.1038/s41467-017-01777-w](https://doi.org/10.1038/s41467-017-01777-w).
- [315] KHAMINSKAYA, S., PYATKOV, E., SŁOWIK, K., FERRARI, S., KAHL, O., KOVALYUK, V., RATH, P., VETTER, A., HENNRICH, F., KAPPES, M. M., GOL'TSMAN, G., KORNEEV, A., ROCKSTUHL, C., KRUPKE, R., and PERNICE, W. H. P.: *Fully integrated quantum photonic circuit with an electrically driven light source*. Nat. Photon. **10**, 11 (2016). DOI: [10.1038/nphoton.2016.178](https://doi.org/10.1038/nphoton.2016.178).
- [316] JEANTET, A., CHASSAGNEUX, Y., CLAUDE, T., ROUSSIGNOL, P., LAURET, J. S., REICHEL, J., and VOISIN, C.: *Exploiting One-Dimensional Exciton-Phonon Coupling for Tunable and Efficient Single-Photon Generation with a Carbon Nanotube*. Nano Lett. **17**, 7 (2017). DOI: [10.1021/acs.nanolett.7b00973](https://doi.org/10.1021/acs.nanolett.7b00973).
- [317] MIURA, R., IMAMURA, S., OHTA, R., ISHII, A., LIU, X., SHIMADA, T., IWAMOTO, S., ARAKAWA, Y., and KATO, Y. K.: *Ultralow mode-volume photonic crystal nanobeam cavities for high-efficiency coupling to individual carbon nanotube emitters*. Nat. Commun. **5**, 1 (2014). DOI: [10.1038/ncomms6580](https://doi.org/10.1038/ncomms6580).

- [318] ELSHAARI, A. W., PERNICE, W., SRINIVASAN, K., BENSON, O., and ZWILLER, V.: *Hybrid integrated quantum photonic circuits*. Nat. Photon. **14**, 5 (2020). DOI: [10.1038/s41566-020-0609-x](https://doi.org/10.1038/s41566-020-0609-x).
- [319] BECKE, A. D.: *Perspective: Fifty years of density-functional theory in chemical physics*. J. Chem. Phys. **140**, 18 (2014). DOI: [10.1063/1.4869598](https://doi.org/10.1063/1.4869598).
- [320] BORN, M. and OPPENHEIMER, R.: *Zur Quantentheorie der Molekeln*. Ann. Phys. (Leipzig) **389**, 20 (1927). DOI: [10.1002/andp.19273892002](https://doi.org/10.1002/andp.19273892002).
- [321] SLATER, J. C.: *Note on Hartree's Method*. Phys. Rev. **35**, 2 (1930). DOI: [10.1103/PhysRev.35.210.2](https://doi.org/10.1103/PhysRev.35.210.2).
- [322] FOCK, V.: *Näherungsmethode zur Lösung des quantenmechanischen Mehrkörperproblems*. Z. Physik **61**, 1 (1930). DOI: [10.1007/BF01340294](https://doi.org/10.1007/BF01340294).
- [323] FOCK, V.: *„Selfconsistent field“ mit Austausch für Natrium*. Z. Physik **62**, 11 (1930). DOI: [10.1007/BF01330439](https://doi.org/10.1007/BF01330439).
- [324] HARTREE, D. R. and HARTREE, W.: *Self-consistent field, with exchange, for beryllium*. Proc. R. Soc. A **150**, 869 (1935). DOI: [10.1098/rspa.1935.0085](https://doi.org/10.1098/rspa.1935.0085).
- [325] HOHENBERG, P. and KOHN, W.: *Inhomogeneous Electron Gas*. Phys. Rev. **136** (1964). DOI: [10.1103/PhysRev.136.B864](https://doi.org/10.1103/PhysRev.136.B864).
- [326] KOHN, W. and SHAM, L. J.: *Self-Consistent Equations Including Exchange and Correlation Effects*. Phys. Rev. **140** (1965). DOI: [10.1103/PhysRev.140.A1133](https://doi.org/10.1103/PhysRev.140.A1133).
- [327] LEVY, M.: *Universal variational functionals of electron densities, first-order density matrices, and natural spin-orbitals and solution of the  $v$ -representability problem*. Proc. Natl. Acad. Sci. U.S.A. **76**, 12 (1979). DOI: [10.1073/pnas.76.12.6062](https://doi.org/10.1073/pnas.76.12.6062).
- [328] SLATER, J. C.: *Atomic Shielding Constants*. Phys. Rev. **36**, 1 (1930). DOI: [10.1103/PhysRev.36.57](https://doi.org/10.1103/PhysRev.36.57).
- [329] BOYS, S. F. and EGERTON, A. C.: *Electronic wave functions – I. A general method of calculation for the stationary states of any molecular system*. Proc. R. Soc. A **200**, 1063 (1950). DOI: [10.1098/rspa.1950.0036](https://doi.org/10.1098/rspa.1950.0036).
- [330] GILL, P. M. W.: *Molecular integrals Over Gaussian Basis Functions*. In: *Adv. Quantum Chem.* **25**, pp. 141–205. Ed. by SABIN, J. R. and ZERNER, M. C. Academic Press, San Diego, New York, Boston, London, Sydney, Tokyo, Toronto 1994. DOI: [10.1016/S0065-3276\(08\)60019-2](https://doi.org/10.1016/S0065-3276(08)60019-2).
- [331] DAVIDSON, E. R. and FELLER, D.: *Basis set selection for molecular calculations*. Chem. Rev. **86**, 4 (1986). DOI: [10.1021/cr00074a002](https://doi.org/10.1021/cr00074a002).

- [332] HERMAN, F, VAN DYKE, J. P., and ORTENBURGER, I. B.: *Improved Statistical Exchange Approximation for Inhomogeneous Many-Electron Systems*. Phys. Rev. Lett. **22**, 16 (1969). DOI: [10.1103/PhysRevLett.22.807](https://doi.org/10.1103/PhysRevLett.22.807).
- [333] HERMAN, F, ORTENBURGER, I. B., and DYKE, J. P. V.: *A method for improving the physical realism of first-principles band structure calculations*. Int. J. Quantum Chem. **4** (1969). DOI: [10.1002/qua.560040746](https://doi.org/10.1002/qua.560040746).
- [334] NEUMANN, R., NOBES, R. H., and HANDY, N. C.: *Exchange functionals and potentials*. Mol. Phys. **87**, 1 (1996). DOI: [10.1080/00268979600100011](https://doi.org/10.1080/00268979600100011).
- [335] ADAMO, C., ERNZERHOF, M., and SCUSERIA, G. E.: *The meta-GGA functional: Thermochemistry with a kinetic energy density dependent exchange-correlation functional*. J. Chem. Phys. **112**, 6 (2000). DOI: [10.1063/1.480838](https://doi.org/10.1063/1.480838).
- [336] LEE, C., YANG, W., and PARR, R. G.: *Development of the Colle-Salvetti correlation-energy formula into a functional of the electron density*. Phys. Rev. B **37**, 2 (1988). DOI: [10.1103/PhysRevB.37.785](https://doi.org/10.1103/PhysRevB.37.785).
- [337] KRISTYÁN, S. and PULAY, P.: *Can (semi)local density functional theory account for the London dispersion forces?* Chem. Phys. Lett. **229**, 3 (1994). DOI: [10.1016/0009-2614\(94\)01027-7](https://doi.org/10.1016/0009-2614(94)01027-7).
- [338] EISENSCHITZ, R. and LONDON, F.: *Über das Verhältnis der van der Waalschen Kräfte zu den homöopolaren Bindungskräften*. Z. Physik **60**, 7 (1930). DOI: [10.1007/BF01341258](https://doi.org/10.1007/BF01341258).
- [339] LONDON, F.: *Zur Theorie und Systematik der Molekularkräfte*. Z. Physik **63**, 3 (1930). DOI: [10.1007/BF01421741](https://doi.org/10.1007/BF01421741).
- [340] NEESE, F.: *The ORCA program system*. WIREs Comput. Mol. Sci. **2**, 1 (2012). DOI: [10.1002/wcms.81](https://doi.org/10.1002/wcms.81).
- [341] HANWELL, M. D., CURTIS, D. E., LONIE, D. C., VANDERMEERSCH, T., ZUREK, E., and HUTCHISON, G. R.: *Avogadro: an advanced semantic chemical editor, visualization, and analysis platform*. J. Cheminform. **4**, 1 (2012). DOI: [10.1186/1758-2946-4-17](https://doi.org/10.1186/1758-2946-4-17).
- [342] BROYDEN, C. G.: *The Convergence of a Class of Double-rank Minimization Algorithms – I. General Considerations*. IMA J. Appl. Math. **6**, 1 (1970). DOI: [10.1093/imamat/6.1.76](https://doi.org/10.1093/imamat/6.1.76).
- [343] FLETCHER, R.: *A new approach to variable metric algorithms*. Comput. J. **13**, 3 (1970). DOI: [10.1093/comjnl/13.3.317](https://doi.org/10.1093/comjnl/13.3.317).
- [344] GOLDFARB, D.: *A family of variable-metric methods derived by variational means*. Math. Comp. **24**, 109 (1970). DOI: [10.1090/S0025-5718-1970-0258249-6](https://doi.org/10.1090/S0025-5718-1970-0258249-6).

- [345] SHANNO, D. F.: *Conditioning of quasi-Newton methods for function minimization*. Math. Comp. **24**, 111 (1970). DOI: [10.1090/S0025-5718-1970-0274029-X](https://doi.org/10.1090/S0025-5718-1970-0274029-X).
- [346] GOERIGK, L. and GRIMME, S.: *A thorough benchmark of density functional methods for general main group thermochemistry, kinetics, and noncovalent interactions*. Phys. Chem. Chem. Phys. **13**, 14 (2011). DOI: [10.1039/C0CP02984J](https://doi.org/10.1039/C0CP02984J).
- [347] BURKE, K.: *Perspective on density functional theory*. J. Chem. Phys. **136**, 15 (2012). DOI: [10.1063/1.4704546](https://doi.org/10.1063/1.4704546).
- [348] WEIGEND, F. and AHLRICH, R.: *Balanced basis sets of split valence, triple zeta valence and quadruple zeta valence quality for H to Rn: Design and assessment of accuracy*. Phys. Chem. Chem. Phys. **7**, 18 (2005). DOI: [10.1039/B508541A](https://doi.org/10.1039/B508541A).
- [349] PROYNOV, E., SHAO, Y., and KONG, J.: *Efficient self-consistent DFT calculation of non-dynamic correlation based on the B05 method*. Chem. Phys. Lett. **493**, 4 (2010). DOI: [10.1016/j.cplett.2010.05.029](https://doi.org/10.1016/j.cplett.2010.05.029).
- [350] PROYNOV, E., LIU, F., and KONG, J.: *Modified Becke'05 method of nondynamic correlation in density functional theory with self-consistent implementation*. Chem. Phys. Lett. **525-526** (2012). DOI: [10.1016/j.cplett.2011.12.069](https://doi.org/10.1016/j.cplett.2011.12.069).
- [351] PROYNOV, E., LIU, F., SHAO, Y., and KONG, J.: *Improved self-consistent and resolution-of-identity approximated Becke'05 density functional model of nondynamic electron correlation*. J. Chem. Phys. **136**, 3 (2012). DOI: [10.1063/1.3676726](https://doi.org/10.1063/1.3676726).
- [352] WEIGEND, F.: *A fully direct RI-HF algorithm: Implementation, optimised auxiliary basis sets, demonstration of accuracy and efficiency*. Phys. Chem. Chem. Phys. **4**, 18 (2002). DOI: [10.1039/B204199P](https://doi.org/10.1039/B204199P).
- [353] JUNG, Y., SODT, A., GILL, P. M. W., and HEAD-GORDON, M.: *Auxiliary basis expansions for large-scale electronic structure calculations*. Proc. Natl. Acad. Sci. U.S.A. **102**, 19 (2005). DOI: [10.1073/pnas.0408475102](https://doi.org/10.1073/pnas.0408475102).
- [354] NEESE, F., WENNMOHS, F., HANSEN, A., and BECKER, U.: *Efficient, approximate and parallel Hartree-Fock and hybrid DFT calculations. A 'chain-of-spheres' algorithm for the Hartree-Fock exchange*. Chem. Phys. **356**, 1 (2009). DOI: [10.1016/j.chemphys.2008.10.036](https://doi.org/10.1016/j.chemphys.2008.10.036).
- [355] IZSÁK, R. and NEESE, F.: *An overlap fitted chain of spheres exchange method*. J. Chem. Phys. **135**, 14 (2011). DOI: [10.1063/1.3646921](https://doi.org/10.1063/1.3646921).
- [356] KOSSMANN, S. and NEESE, F.: *Comparison of two efficient approximate Hartree-Fock approaches*. Chem. Phys. Lett. **481**, 4 (2009). DOI: [10.1016/j.cplett.2009.09.073](https://doi.org/10.1016/j.cplett.2009.09.073).
- [357] WEIGEND, F.: *Accurate Coulomb-fitting basis sets for H to Rn*. Phys. Chem. Chem. Phys. **8**, 9 (2006). DOI: [10.1039/B515623H](https://doi.org/10.1039/B515623H).

- 
- [358] GRIMME, S., ANTONY, J., EHRLICH, S., and KRIEG, H.: *A consistent and accurate ab initio parametrization of density functional dispersion correction (DFT-D) for the 94 elements H-Pu*. J. Chem. Phys. **132**, 15 (2010). DOI: [10.1063/1.3382344](https://doi.org/10.1063/1.3382344).
- [359] GRIMME, S., EHRLICH, S., and GOERIGK, L.: *Effect of the damping function in dispersion corrected density functional theory*. J. Comput. Chem. **32**, 7 (2011). DOI: [10.1002/jcc.21759](https://doi.org/10.1002/jcc.21759).
- [360] BOUGUER, P.: *Essai d'optique, sur la gradation de la lumière*. Claude Jombert, Paris 1729.
- [361] LAMBERT, J. H.: *Photometria sive de mensura et gradibus luminis, colorum et umbrae*. Eberhardt Klett, Augsburg 1760.
- [362] BEER, A.: *Bestimmung der Absorption des rothen Lichts in farbigen Flüssigkeiten*. Ann. Phys. (Leipzig) **162**, 5 (1852). DOI: [10.1002/andp.18521620505](https://doi.org/10.1002/andp.18521620505).
- [363] MARKOV, A. A.: *An Example of Statistical Investigation of the Text Eugene Onegin Concerning the Connection of Samples in Chains*. Sci. Context **19**, 4 (2006). DOI: [10.1017/S0269889706001074](https://doi.org/10.1017/S0269889706001074).
- [364] Van KAMPEN, N. G.: *Stochastic Processes in Physics and Chemistry*. Elsevier, Amsterdam, Oxford 2007.
- [365] GOODMAN, J. and WEARE, J.: *Ensemble samplers with affine invariance*. Comm. App. Math. Comp. Sci. **5**, 1 (2010). DOI: [10.2140/camcos.2010.5.65](https://doi.org/10.2140/camcos.2010.5.65).
- [366] FOREMAN-MACKEY, D., HOGG, D. W., LANG, D., and GOODMAN, J.: *emcee: The MCMC Hammer*. Publ. Astron. Soc. Pac. **125**, 925 (2013). DOI: [10.1086/670067](https://doi.org/10.1086/670067).
- [367] NEESE, F.: *An improvement of the resolution of the identity approximation for the formation of the Coulomb matrix*. J. Comput. Chem. **24**, 14 (2003). DOI: [10.1002/jcc.10318](https://doi.org/10.1002/jcc.10318).



## List of Publications

A list of the author's publications is provided below. Publications related to this dissertation are labeled [P1–P3, P6, P8].

- [P1] NUTZ, M., ZHAO, S., NOÉ, J. C., FAGAN, J. A., GOVOROV, A. O., and HÖGELE, A.: *Asymmetry of cryogenic photoluminescence spectra of carbon nanotubes mediated by dipolar coupling to surfactant polymers*. In preparation.
- [P2] KWON, H., KIM, M., NUTZ, M., HARTMANN, N. F., PERRIN, V., MEANY, B., HOFMANN, M. S., CLARK, C. W., HTOON, H., DOORN, S. K., HÖGELE, A., and WANG, Y.: *Probing Trions at Chemically Tailored Trapping Defects*. ACS Cent. Sci. **5**, 11 (2019). DOI: [10.1021/acscentsci.9b00707](https://doi.org/10.1021/acscentsci.9b00707).
- [P3] NUTZ, M., ZHANG, J., KIM, M., KWON, H., WU, X., WANG, Y., and HÖGELE, A.: *Photon Correlation Spectroscopy of Luminescent Quantum Defects in Carbon Nanotubes*. Nano Lett. **19**, 10 (2019). DOI: [10.1021/acs.nanolett.9b02553](https://doi.org/10.1021/acs.nanolett.9b02553).
- [P4] MEIER, S., HIGUCHI, T., NUTZ, M., HÖGELE, A., and HOMMELHOFF, P.: *High spatial coherence in multiphoton-photoemitted electron beams*. Appl. Phys. Lett. **113**, 14 (2018). DOI: [10.1063/1.5045282](https://doi.org/10.1063/1.5045282).
- [P5] NEUMANN, A., LINDLAU, J., NUTZ, M., MOHITE, A. D., YAMAGUCHI, H., and HÖGELE, A.: *Signatures of defect-localized charged excitons in the photoluminescence of monolayer molybdenum disulfide*. Phys. Rev. Materials **2**, 12 (2018). DOI: [10.1103/PhysRevMaterials.2.124003](https://doi.org/10.1103/PhysRevMaterials.2.124003).
- [P6] NOÉ, J. C., NUTZ, M., RESCHAUER, J., MORELL, N., TSIOUTSIOS, I., RESERBAT-PLANTEY, A., WATANABE, K., TANIGUCHI, T., BACHTOLD, A., and HÖGELE, A.: *Environmental Electrometry with Luminescent Carbon Nanotubes*. Nano Lett. **18**, 7 (2018). DOI: [10.1021/acs.nanolett.8b00871](https://doi.org/10.1021/acs.nanolett.8b00871).
- [P7] NEUMANN, A., LINDLAU, J., COLOMBIER, L., NUTZ, M., NAJMAEI, S., LOU, J., MOHITE, A. D., YAMAGUCHI, H., and HÖGELE, A.: *Opto-valleytronic imaging of atomically thin semiconductors*. Nat. Nanotechnol. **12**, 4 (2017). DOI: [10.1038/nnano.2016.282](https://doi.org/10.1038/nnano.2016.282).
- [P8] HOFMANN, M. S., NOÉ, J., NUTZ, M., KNEER, A., DEHMEL, R., SCHAFFROTH, L., and HÖGELE, A.: *Synthesis and cryogenic spectroscopy of narrow-diameter single-wall carbon nanotubes*. Carbon **105** (2016). DOI: [10.1016/j.carbon.2016.04.073](https://doi.org/10.1016/j.carbon.2016.04.073).



# Danksagung

Am Ende meiner Dissertation möchte ich mich bei all denen bedanken, die mich in den letzten Jahren begleitet und unterstützt haben und mir über manche frustrierende Phase hinweg geholfen haben.

Allen voran möchte ich Alexander Högele danken für die Betreuung und die Möglichkeit, in seiner Gruppe zu forschen. Vielen Dank, Alex, für deinen freundschaftlichen Umgang auf Augenhöhe, deinen Rat bei allen Herausforderungen und dein stets offenes Ohr bei allen Anliegen. Die wissenschaftlichen Diskussionen mit dir haben mir immer wieder vor Augen geführt, wo es mir selbst noch an Verständnis gemangelt hatte. Bedanken möchte ich mich auch bei Jörg Kotthaus für den Aufbau eines Lehrstuhls mit hervorragendem wissenschaftlichen Umfeld und dennoch lockerer Arbeitsatmosphäre.

Mein Dank gilt auch meinen Kollegen, die mich in die Welt der Nanoröhren eingeführt haben. Matthias Hofmann und Jonathan Noé haben mir unschätzbare Wissen über die Spektroskopie und den Umgang mit Kryostaten vermittelt. Jonathan, dir möchte ich besonders für die jahrelange hervorragende Zusammenarbeit nicht nur bei der Spektroskopie auf Bornitrid und über Gräben, sondern auch für alle Diskussionen und Scherze und nicht zuletzt für starke Nerven bei der Justage des Etalons danken.

Bedanken möchte ich mich auch bei allen weiteren, über die Jahre wechselnden Bürokollegen, namentlich Michael Förg, Jonathan Förste, Victor Funk, Jessica Lindlau, Enrico Schubert und Samarth Vadia, für die immer gute Stimmung und die vielen gemeinsamen Mittagessen, die Kaffeepausen und bereichernde Diskussionen. Auch allen anderen Mitstreitern in der Nanophotonik gebührt mein Dank. Besonders hervorheben möchte ich Léo Colombier, Matthias Hauck, Andre Neumann, Sarah Wittig und Shen Zhao. Bei meiner Bachelorstudentin Lilian Schaffroth und meinem Praktikanten Vivien Perrin bedanke ich mich für die gute Zusammenarbeit in Labor und Reinraum.

Weiterhin danke ich allen Kollaborateuren, ohne die diese Arbeit nicht möglich gewesen wäre. Danke an Jeffrey Fagan vom National Institute of Standards and Technology für die Bereitstellung von tensidumhüllten Kohlenstoffnanoröhren, an die Gruppe von YuHuang Wang von der University of Maryland für die Bereitstellung funktionalisierter Kohlenstoffnanoröhren und an die Gruppe von Stephen Doorn vom Los Alamos National Laboratory für deren Charakterisierung. Ich danke außerdem Alexander Govorov von der Ohio University für Diskussionen über dipolare Wechselwirkungen zwischen Exzitonen und Molekülschwingungen.

Bert Lorenz danke ich für die reibungslose Organisation am Lehrstuhl und Martina Edenhofer und ihrer Nachfolgerin Dayse Ferreira e Silva für die Unterstützung im Sekretariat. Bei Philipp Altpeter bedanke ich mich für die unschätzbare Unterstützung bei allen Prozessen im Reinraum und bei Reinhold Rath und Christian Obermayer für die Hilfe mit allen Belangen rund um Pumpen, Gasleitungen und sonstiger Technik. Danke an Anton Heindl für die stete Versorgung mit Stickstoff und Helium sowie für gelegentliche Hilfe in der Werkstatt. Zu guter Letzt möchte ich Stephan Manus für die Unterstützung mit seinem unglaublichen Wissen rund um alle Belange der Elektronik danken.

Vielen Dank an die feinmechanische Werkstatt mit ihren Leitern Jürgen Aust und Thomas Großhauser und allen Mitarbeitern für die immer bereitwillige Anfertigung manchmal auch ausgefallener Bauteile. Danke auch an Klaus Steinberger und Matthias Tischler in der IT, ohne deren stete Hilfsbereitschaft meine Tätigkeit als Lehrstuhladministrator nicht möglich gewesen wäre.

Für das Korrekturlesen und für Verbesserungsvorschläge zu dieser Arbeit danke ich Alexander Högele, Jonathan Förste, Jonathan Noé und Samarth Vadia.

Zuletzt möchte ich meinen Eltern Robert und Elisabeth danken, dass sie mir meinen langen Ausbildungsweg ermöglicht haben und mich bei all meinen Projekten stets unterstützten.

Sarah, dir möchte ich dafür danken, dass du immer für mich da bist, mich bei manchem Durchhänger wieder aufgebaut hast, ertragen hast, dass ich manchmal auch zu unmöglichen Zeiten irgendetwas für meine Forschung erledigen musste und mich bei der Anfertigung dieser Arbeit bei vielen nervigen Fragen zu Struktur und Gestaltung unterstützt hast.